



Transformations de phase des Sulfures de Nickel dans les verres trempés

O. Yousfi

► To cite this version:

O. Yousfi. Transformations de phase des Sulfures de Nickel dans les verres trempés. Génie des procédés. Institut National Polytechnique de Grenoble - INPG, 2009. Français. NNT: . tel-00526605

HAL Id: tel-00526605

<https://theses.hal.science/tel-00526605>

Submitted on 15 Oct 2010

HAL is a multi-disciplinary open access archive for the deposit and dissemination of scientific research documents, whether they are published or not. The documents may come from teaching and research institutions in France or abroad, or from public or private research centers.

L'archive ouverte pluridisciplinaire **HAL**, est destinée au dépôt et à la diffusion de documents scientifiques de niveau recherche, publiés ou non, émanant des établissements d'enseignement et de recherche français ou étrangers, des laboratoires publics ou privés.

INSTITUT POLYTECHNIQUE DE GRENOBLE

N° attribué par la bibliothèque

|_|_|_|_|_|_|_|_|_|_|_|_|_|_|_|

THESE

pour obtenir le grade de

DOCTEUR DE L'Institut polytechnique de Grenoble

Spécialité : «Matériaux, Mécanique, Génie civil, Electrochimie»

préparée au laboratoire Science et Ingénierie des Matériaux et Procédés

dans le cadre de l'**Ecole Doctorale**

« Ingénierie-Matériaux Mécanique Energétique Environnement Procédés Production »

présentée et soutenue publiquement

par

Oussama YOUSFI

Le 4 juin 2009

TITRE

Transformations de phase des Sulfures de Nickel dans les verres trempés

DIRECTEUR DE THESE : Patricia DONNADIEU

CO-DIRECTEUR DE THESE : Yves BRECHET

JURY

M.	Gary PURDY	, Président
M.	Dominique MANGELINCK	, Rapporteur
M.	Philippe MAUGIS	, Rapporteur
Mme.	Patricia DONNADIEU	, Directeur de thèse
M.	Yves BRECHET	, Co-directeur
M.	Andreas KASPER	, Examineur

Résumé :

Le sulfure de Nickel (NiS) peut former des inclusions dans les verres trempés conduisant à une fracture due à la transformation de phase avec changement de volume. Un traitement thermique, provoquant cette transformation de phase, est actuellement utilisé afin de réduire cet effet. Pour proposer des traitements plus efficaces, une étude allant des mécanismes de transformation jusqu'à la modélisation a été menée. Selon la composition et la température, deux mécanismes de transformation (avec ou sans partition) ont été mis en évidence par l'étude microstructurale et calorimétrique donne les lignes directrices de la modélisation. Une étude *in situ* en microscope optique a fourni les informations complémentaires indispensables (taux de germination, mobilité des interfaces) pour construire des modèles cinétiques. La modélisation décrit la transformation en condition isotherme pourra être adaptée aux conditions anisothermes proches du traitement industriel.

Mots clés : sulfure de Nickel, transformation de phase, transformation massive, transformation avec partition, modélisation, verre trempé

Abstract:

Nickel sulphide (NiS) can form inclusions in tempered glass which lead to fracture due to a phase transformation with volume change. A heat treatment, aiming to provoke this phase transformation, is currently used to reduce this effect. In order to propose more efficient treatments, a complete study going from identification of the transformation mechanisms to the modelling of the transformation was carried out. Depending on stoichiometry and temperature, two mechanisms for the transformation (partitioned or partitionless) have been evidenced by detailed microstructural and calorimetric studies which give the main lines for the modelling. An *in situ* following of the transformation by optical microscopy has provided information (like nucleation rate and interface migration velocity) necessary to build the kinetic models. This modelling which described the transformation under isothermal treatment can be further extended to anisothermal condition closer to the industrial one.

Key words: Nickel sulphide, phase transformation, massive transformation, partitioned transformation, modelling, tempered glass

Remerciements

بسم الله الرحمن الرحيم
الحمد لله رب العالمين

J'aimerais remercier Jean-Marc Chaix et Michel Pons, directeurs successifs du LTPCM, aujourd'hui devenu SIMaP, pour m'avoir accueilli durant ces trois dernières années au sein de leur laboratoire.

Je remercie les membres du jury et plus particulièrement le Professeur Gary Purdy de l'université McMaster à Hamilton au Canada pour avoir présidé le jury et pour les diverses discussions pertinentes sur cette étude. Je remercie également Mr. Philippe Maugis du CIRIMAT et Mr. Dominique Mangelinck de l'IM2NP d'avoir accepté d'être rapporteurs de ce mémoire.

Mes plus grands remerciements vont à mes directeurs de thèse Patricia Donnadieu et Yves Bréchet qui ont largement contribué à la bonne orientation et au bon déroulement de cette étude. Merci à eux deux pour avoir fait que tous les jours je devienne un peu plus autonome et efficace, et merci pour tout ce qu'ils m'ont appris tant sur le plan scientifique qu'humain. Ils ont toujours été très disponibles pour répondre à mes questions. Merci à Yves pour tous les repas très réussis, mais aussi pour m'avoir fait goûter pour la première fois du champ.....omy.

J'adresse mes remerciements à Mr. Loic Jourdain, directeur de Saint Gobain Glass CRDC, pour m'avoir accueilli au sein de l'entreprise et permis de bénéficier d'une bourse CIFRE pour cette étude.

Je tiens aussi à remercier les responsables Saint Gobain CRDC qui ont été successivement impliqués dans ce travail : Yves Demars, Francis Serruys et Maurice Lemaître. Je tiens à remercier tout particulièrement PD. Dr. Andreas Kasper de Saint Gobain HRDC qui est à l'origine de cette thèse pour tout son soutien scientifique ainsi que pour ses conseils et ses suggestions éclairés qui m'ont permis de mieux comprendre l'histoire des inclusions NiS et de mieux orienter l'étude. Merci à Francis Serruys qui a veillé régulièrement au bon déroulement de la thèse.

Un grand merci aussi à Petra Vehres du HRDC pour avoir élaboré tous les échantillons nécessaires à cette étude.

Remerciements

Je remercie aussi toutes les personnes qui ont participé à cette étude, l'équipe du CMTC et tout particulièrement Florence Robaut, Alexandre Crisci, Frédéric Charlot et Stéphane Coindeau pour leur aide précieuse dans la caractérisation de mes échantillons (EBSD, Analyse Microsonde et DRX). Merci aussi à Isabelle Paintrand du CERMAV, Francois Brisset de l'ICMMO et Anne Cécile Grillet du LMOPS pour leur aide dans la réalisation de certaines expériences de cette étude.

Un grand merci à tous les permanents que j'ai côtoyé au cours de ma thèse :

Marie, Jean-Paul, Bruno, Françoise, Joël, Guillaume, Mireille, Muriel, Marc², Frédéric², Jean-Louis², Jean-Marc, Béatrice, Jacqueline, Jessica, Virginie, Sabine, Sandrine, Luce, Alain, Pierre, Nathalie, Jean-Jacques, Catherine, Annie, Michel, Rolland, Graziella, Francine...

Et aussi à tous mes ami(e)s :

Coraline, Mazen, Benjamin, Béchir, Sylvain, Guilhem, Aurélie, Jean-Joël, Malika, Laurent, Gregory, Valérie, Céline, Ian, Emre, Guillaume, Nicolas, Sébastien, Sami, Fabiola, Jamel, Ramzi, Sinh, Thors-ten, Jean-Louis, Muhammad, Manu, Fatima, Benoit, Walid, Haithem, Fehmi, Khalil, Zaid, Mohamed, Hatem, Brahim, Housseem...

Un merci particulier à mes collègues de bureau Valérie, Coraline et Guilhem qui grâce à leur différentes passions ont su entretenir une ambiance très conviviale dans notre bureau durant ces trois années.

Un remerciement très chaleureux bien entendu pour mes ami(e)s de la sacrée pause café de midi (ils se reconnaîtront bien). Merci pour toute votre bonne humeur...

Des remerciements personnels à Marie pour ses conseils, nos nombreuses discussions chargées d'humour, pour son aide dans l'organisation du pot de thèse et surtout pour m'avoir suggérer la destination de mon voyage de noce.....en Tunisie !!!!

Un remerciement particulier à mes amis et frères Béchir, Mazen et Brahim sur lesquels j'ai toujours pu compter pour trouver le réconfort nécessaire dans tous les moments difficiles au cours de ces années.

Merci à ma famille qui m'a soutenu tout au long de cette thèse. Mustapha, Ghalia, Sofian, Souhaieb, Rathouan, Hamza, Zoubaier, Olfa, Fatma, Houda, et les petit(e)s, Bilel, Anissa, Farouk, Mariem, Khalil et Aymen.

Enfin, un très très grand merci à ma chère et tendre épouse Sarra pour son soutien quotidien durant ces trois années...

Table des matières

Résumé :	i
Abstract:	iii
Remerciements	v
Table des matières	1
Chapitre I. Introduction	5
I.1 Sulfures de Nickel dans les verres trempés	5
I.2 Mode de formation des inclusions de sulfures de Nickel	6
I.3 Inclusions NiS et rupture des verres trempés	9
I.4 Le Heat Soak Test	12
I.5 Plan de thèse	14
Chapitre II. Phase transformations in Nickel sulphide (NiS): microstructure and mechanisms	15
II.1 Introduction:	15
II.2 Materials and methods:	17
II.2.1 Materials	17
II.2.2 Heat treatments	18
II.2.3 Microstructural characterization	20
II.3 DSC characterization of the phase transformation	20
II.4 Microstructural signature of the transformation: influence of temperature, stoichiometry and Fe impurities	22
II.4.1 Typical morphologies of the phase transformations	22
II.4.2 Effect of composition and temperature	25

Table des matières

II.5	Morphology and related α/β orientation relationships	28
II.5.1	Lamellar morphology	29
II.5.2	Globular morphology	29
II.5.3	Coarse lamellar morphology	30
II.5.4	Block morphology	31
II.6	Composition analysis	31
II.6.1	Composition analysis of α and β grain and profile at the α/β interface	32
II.6.2	Composition analysis of β phase and post-transformation with precipitation of Ni_3S_4	34
II.7	Fine scale microstructure for the lamellar and globular morphology	35
II.7.1	Early stages	35
II.7.2	β fine structure in lamellar morphology	36
II.8	Summary and discussion:	37
II.8.1	Parallels with phase transformations in the Fe-C system	39
II.8.2	From morphology to kinetic law	42
II.9	Conclusion:	44
Chapitre III.	Calorimetric study of phase transformations in Nickel sulphide (NiS)	47
III.1	Introduction:	47
III.2	Materials and methods:	49
III.2.1	Materials	49
III.2.2	Heat treatments and measurement cycles	50
III.3	The $\alpha \rightarrow \beta$-NiS transformation and phase diagram validation	51
III.3.1	DSC signature during non isothermal heat treatment	51
III.3.2	β phase composition and evolution of the Ni_3S_4 volume fraction with temperature and α phase composition	52
III.4	Kinetic aspect of the $\alpha \rightarrow \beta$-NiS transformation:	56
III.4.1	DSC scans at constant heating rate and partial transformation evidence	56
III.4.2	TTT diagrams	60
III.4.3	JMAK analysis:	63
III.5	Discussion:	66
III.6	Conclusion:	70
Chapitre IV.	Measurements of interdiffusion coefficients in α NiS.	71
IV.1	Introduction:	71
IV.2	Diffusion couple and interdiffusion coefficient measurement	72
IV.2.1	Diffusion couple : qualitative observations	72
IV.2.2	Interdiffusion coefficient in α -NiS	74
IV.3	Discussion and concluding remarks	76

Table des matières

Chapitre V. NiS phase transformations: <i>in situ</i> observation and modelling under isothermal conditions.....	77
V.1 Introduction:	77
V.2 Experimental conditions of the <i>in situ</i> optical microscopy observations.....	78
V.3 <i>In situ</i> observations of the phase transformations	80
V.3.1 Qualitative description of the evolution of the different morphologies	81
V.3.2 Quantitative study of the phase transformation for the different morphologies	84
V.4 Modelling of the phase transformation	90
V.4.1 Modelling of the Interface velocity.....	91
V.4.2 Modelling of transformed volume fraction on isothermal heat treatment.....	93
V.5 Discussion and concluding remarks:.....	98
 Chapitre VI. Proposition to improve the efficiency of the Heat Soak Test	 101
VI.1 Introduction:	101
VI.2 Microstructures and mechanism for the $\alpha \rightarrow \beta$-NiS transformation.....	102
VI.3 Kinetic law of NiS phase transformation and HST optimization	102
VI.3.1 Kinetics aspect of the $\alpha \rightarrow \beta$ -NiS transformation: TTT diagram.....	105
VI.3.2 Kinetic results on two stage heat treatments.....	106
VI.4 Summary and conclusion:.....	108
 Chapitre VII. Conclusion	 111
 Bibliographie.....	 115
 Annexes.....	 119
 Annexe A : Composition and microstructure of Nickel sulphide stones found in tempered glass	 121
A.I. Introduction:	121
A.II. Characterization of Nickel sulphide stones	122
A.II.1 Phases and microstructure in Nickel sulphide stones	122
A.II.2 Phase compositions.....	126
A.III. Discussion.....	126
A.IV. Conclusion	129
 Annexe B : Cristallographie et relation structurale entre les phases α et β	 131
 Annexe C : Observation en Microscopie électronique (MEB) avec chauffage <i>in situ</i> de la transformation $\alpha \rightarrow \beta$-NiS.....	 137

Table des matières

Annexe D : Caractérisation par dilatométrie de la transformation de phase.....	139
Annexe E : Transformation de phase des sulfures de Nickel et évolution à température ambiante.....	143
E.I. Effet de la composition sur la cinétique de Transformation de phase à température ambiante	143
E.II. Effet de la composition sur la microstructure de la Transformation de phase à température ambiante.....	146
Annexe F : Illustration de la microstructure lamellaire à différentes températures.....	149

Chapitre I. Introduction

Ce chapitre introduira le contexte industriel de la thèse, présentera une synthèse des connaissances sur les sulfures de Nickel dans les verres trempés et explicitera le plan de rédaction de la thèse ainsi que les principaux points abordés dans chacun des chapitres de thèse.

I.1 Sulfures de Nickel dans les verres trempés

Les inclusions de sulfure de Nickel présentes en très faible proportion dans un verre (1 particule par 300m²) peuvent conduire après plusieurs années, dans certaines situations, à l'explosion des vitrages. Ce problème concerne essentiellement les verres trempés qui sont connus pour leurs propriétés mécaniques et esthétiques. Ces matériaux sont confrontés, depuis leurs développements, au phénomène de la rupture différée due à des inclusions de NiS. Cet effet est lié aux transformations de phase avec augmentation de volume qui se produisent dans les inclusions de NiS. En effet, les verres industriels contiennent en impuretés du Soufre et du Nickel qui ne sont pas solubles dans la matrice vitreuse et qui proviennent de la matière première utilisée (en particulier les verres recyclés), ainsi que des débris d'aciers inoxydables contenant du Nickel et résultant de l'usure des outils par la silice abrasive. Il se forme à haute température des inclusions de sulfure de Nickel de taille micronique, dans la majorité des cas de forme sphérique. Après trempe, les inclusions présentent la structure cristallographique dite α -NiS, stable à haute température mais métastable à la température ambiante.

La rupture résulte du changement de volume occasionné par la transformation de la phase α -NiS haute température vers la phase β -NiS basse température. Cette transformation peut se produire spontanément à température ambiante. Ce phénomène de fracture des verres trempés due aux inclusions de sulfure de Nickel est connu depuis les années 60. Il a été reporté pour la première fois par Ballantyne [1, 2] en 1961. Les producteurs de verre ont essayé de résoudre ce problème par des mesures de réduction du taux d'impuretés en Nickel et Soufre. Ces améliorations n'ont pas permis la

résolution du problème. Cette question reste un problème d'actualité vu l'augmentation du nombre des vitrages installés dans les bâtiments modernes. Certains panneaux de verres trempés peuvent se casser sans l'influence de facteurs extérieurs, quelques temps voir plusieurs années après leur mise en place. C'est pourquoi plusieurs études ont été conduites de façon à éviter la rupture des verres trempés pour le bâtiment, ou au moins à limiter leur casse à la période avant la pose.

La solution appliquée actuellement pour remédier à ce problème consiste à faire un traitement thermique pour provoquer la rupture avant installation des vitres. Ce traitement thermique qui est appelé Heat Soak Test (HST) fait l'objet d'une norme reconnue par les industriels européens et avec des variantes d'application dans chaque pays. A l'issue du traitement HST, les verriers estiment que 98,5% des vitrages défectueux, c'est-à-dire comportant des inclusions critiques, sont éliminés. Cependant ce test est coûteux par sa durée et par la température de maintien assez élevée et il risque en outre de nuire à la qualité du verre trempé. C'est dans ce cadre qu'est menée cette étude qui a pour objectif l'amélioration du HST par une étude approfondie de la transformation (expérience et modélisation). Une connaissance de la cinétique de transformation mais aussi du mécanisme de germination de la transformation pourrait permettre de modifier le traitement. Ainsi on pourrait rendre ce test qui est intrinsèquement destructif :

- plus efficace au sens où un maximum de vitrage à problème pourrait être éliminé.
- plus court si des paliers adaptés permettent d'accélérer la transformation.
- plus adapté aux verres trempés si la température du test peut être réduite.

La connaissance de la transformation de phase du sulfure de Nickel sera donc au centre de ce travail de thèse. L'objectif est de mieux comprendre les caractéristiques de la transformation de phase de ces inclusions, en particulier les mécanismes, pour aller jusqu'à une modélisation de la loi cinétique de la transformation.

I.2 Mode de formation des inclusions de sulfures de Nickel

Les verres industriels contiennent en impuretés du Soufre et du Nickel qui ne sont pas solubles dans la matrice vitreuse et forment alors des inclusions de sulfure de Nickel de taille micronique. Les inclusions de NiS sont dispersées d'une manière hétérogène dans les verres avec une moyenne de 1 inclusion / 300m². Ces inclusions ont une forme sphérique avec un diamètre variable, typiquement entre 50µm et 550µm (Figure 1). L'hétérogénéité de la répartition spatiale et de la distribution en taille des inclusions dans les verres sont dues à la variation de la quantité du Soufre et du Nickel présente dans un lot de verre. Sur une section de verre trempé (après fracture due à des inclusions de NiS), les inclusions se répartissent selon l'histogramme de la Figure 3. Les inclusions de NiS sont localisées essentiellement, mais pas seulement, dans le cœur de la plaque de verre.

I.2 Mode de formation des inclusions de sulfures de Nickel

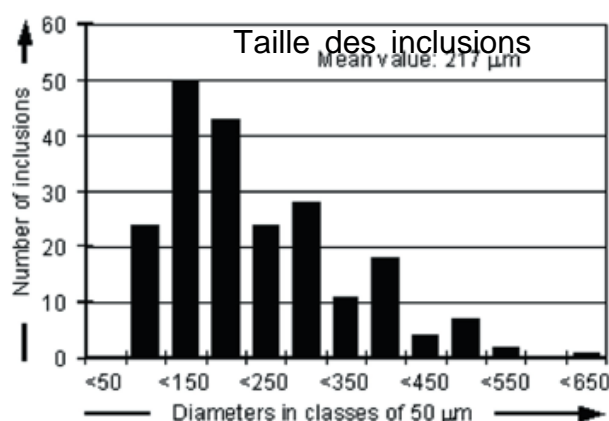


Figure 1: Distribution des diamètres des inclusions NiS mesurés sur les vitrages cassés [3].

En raison du mode de formation des inclusions résumé ci-dessous, la composition des inclusions en sulfure de Nickel est variable typiquement entre 40at% et 60at%S. Cependant, l'intérêt se concentre le plus souvent sur les inclusions de composition NiS ou proches de cette stœchiométrie car seules celles-ci ont des transformations de phases avec changement de volume responsables de rupture des vitrages.

Après la trempe, les inclusions de sulfure de Nickel occupent des cavités présentant un espace libre dans le verre. Ceci est dû à la différence de coefficient de dilatation entre le verre et NiS (Table 1). Le mélange Ni-S a un coefficient de dilatation plus important que le verre, donc il se contracte plus que celui-ci lors du refroidissement. Le verre devient rigide à partir de 600°C. Ainsi, l'inclusion NiS qui se forme à environ 1000°C, se trouve à partir de 600°C au centre d'une cavité. L'espace vide est estimé à quelques microns suivant la taille des inclusions de NiS (de l'ordre de 1%).

	Verre	α -NiS	β -NiS
Module de Youngs, E (GNm⁻²)	70	80	70
Coeff. de Poisson, ν	0,23	0,27	0,20
Masse volumique, ρ (Kgm⁻³)	2,51 10 ³	5,46 10 ³	5,25 10 ³
Coeff. de dilatation thermique, α	88 10 ⁻⁷	163 10 ⁻⁷	145 10 ⁻⁷

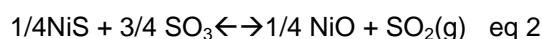
Table 1: Paramètres caractéristiques du verre et des phases α et β -NiS [4].

Le sulfure de Nickel a été étudié d'un point de vue cristallographique et thermodynamique par Laffitte *et al* [5, 6]. L'étude plus spécifique de la formation des inclusions de NiS a été réalisée essentiellement par Kasper *et al* [7, 8] et Lin *et al* [9]. Kasper [7, 8], a montré que les inclusions ont pour origine la matière première utilisée : calcite, dolomite et verre recyclé. La manutention des matériaux, en particulier pour le verre recyclé, introduit des particules métalliques qui contribuent à la teneur en impuretés Fe et Ni du verre. Pendant l'élaboration du verre, le mélange initial est chauffé jusqu'à 1200-1400°C. À cette température, le mélange fond. Mais le Nickel n'étant pas soluble dans le verre, il se forme dans le verre des petites zones de métal fondu qui réagissent avec O₂ et SO₃ dissous dans le verre fondu formant ainsi des oxydes et des sulfures de Nickel.

On peut ainsi décrire la formation des sulfures de Nickel suivant les réactions:



Les oxydes de Nickel sont dissous dans la matrice vitreuse et y diffusent alors que les sulfures de Nickel, qui ne sont pas solubles dans la matrice vitreuse, forment des inclusions insolubles. Comme les métaux les plus nobles réagissent en premier, les sulfures qui se forment sont à base de Fer ou de Nickel (NiS et FeS). Le sulfure de Fer s'oxyde le premier suivi du sulfure de Nickel qui s'oxyde à son tour en restant en équilibre avec NiO.

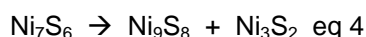


Ce processus conduit directement à la formation des inclusions de NiS à l'état fondu (riche en Ni)- avec un faible pourcentage en Fe en solution solide qui cristallise par la suite quand le verre est refroidi.

Du point de vue thermodynamique, les sulfures de Nickel contenant une quantité en Soufre supérieure à la stœchiométrie 1 :1 ne sont pas stables à l'état liquide dans le verre fondu ce qui engendre leur décomposition pour former des sulfures riches en Nickel. La nature des phases qui peuvent exister dans une inclusion dépend du ratio Ni : S au moment où le liquide NiS commence à cristalliser. Généralement, une phase liquide riche en Ni en se refroidissant se transforme suivant la réaction :



La phase Ni₇S₆ se décompose pendant le refroidissement pour former :



La présence de ces diverses phases (NiS, Ni₇S₆, Ni₉S₈, Ni₃S₂) dans les inclusions de sulfures de Nickel issues de vitrages cassés (soit dans les fours, soit après montage en façade) est confirmée par des caractérisations par diffraction des Rayons X, par imagerie MEB et par analyses chimiques EDX (Figure 2).

1.3 Inclusions NiS et rupture des verres trempés

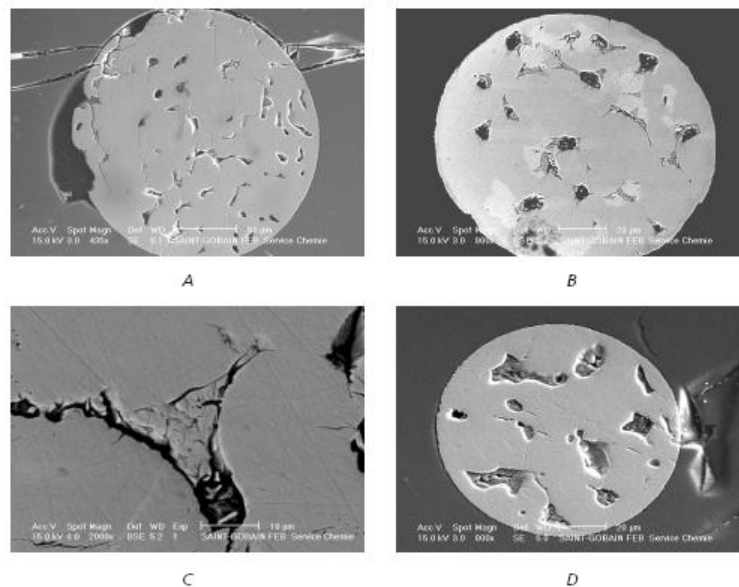


Figure 2: Observation MEB des inclusions NiS d'après Kasper *et al* [10] :

Figure2 A : Inclusion homogène en composition Figure2 B : inclusion comportant deux phases (le contraste entre les deux phases est bien révélé en mode d'imagerie d'électrons rétrodiffusés au MEB). Figure2 C : A fort grandissement mise en évidence de zones riches en fer dans les inclusions de NiS. Figure2 D : inclusion issue des vitres teintées (vert) formé d'une seule phase mais avec des pores riches en Fer mis en évidence grâce à un nettoyage avec 10% H_2SO_4 . L'inclusion contient 1,5% at-Fe les pores contiennent plus de 48% at en Fe

Ces observations mettent en évidence la complexité des inclusions qui se forment dans les vitrages industriels. Bien que la composition reste au voisinage de NiS, plusieurs phases autres que la phase α -NiS sont présentes. D'autre part, le Fer est présent dans les inclusions : - en solution solide dans la phase α -NiS jusqu'à 1,5-2%at Fe, - le reste du Fer (présent initialement dans les inclusions à l'état liquide) migre vers les pores à l'intérieur des inclusions NiS pendant le refroidissement. Ces observations sur la composition des inclusions nous amèneront à nous intéresser à l'influence de la stoechiométrie mais aussi à celle de la teneur en Fer.

1.3 Inclusions NiS et rupture des verres trempés

Le verre s'impose de plus en plus dans le marché du bâtiment où il peut être utilisé actuellement comme des pièces de structure. L'augmentation de son utilisation est due essentiellement à ses propriétés esthétiques (impact visuel, teinte) mais aussi acoustiques, énergétiques et mécaniques. Il existe plusieurs types de verre selon leurs domaines d'applications. Les verres trempés, sont développés depuis les années 50. Ils sont utilisés comme vitrages dans les bâtiments. Ils sont reconnus pour leur résistance à des facteurs extérieurs comme les contraintes exercées par les structures et la pression du vent. Ces propriétés mécaniques sont obtenues par un traitement thermique de trempe. Ce traitement consiste à réchauffer les panneaux de verre à une

température entre 500-600°C puis les refroidir rapidement jusqu'à température ambiante. On obtient ainsi des verres thermiquement durcis appelés verres trempés.

A la fin de la trempe la plaque de verre possède en section un profil de contrainte tel que décrit par la Figure 3 b. La trempe induit une zone en compression au voisinage des faces extérieures et une zone en traction dans la zone centrale. L'écart entre la contrainte dans la zone centrale et celle des faces extérieures du verre sera d'autant plus grand que la température de traitement et la vitesse de trempe sont élevées. De ce fait, les propriétés mécaniques des verres trempés, qui sont directement liées avec l'état de contrainte dans les zones en compression, sont influencées par les conditions du cycle de trempe.

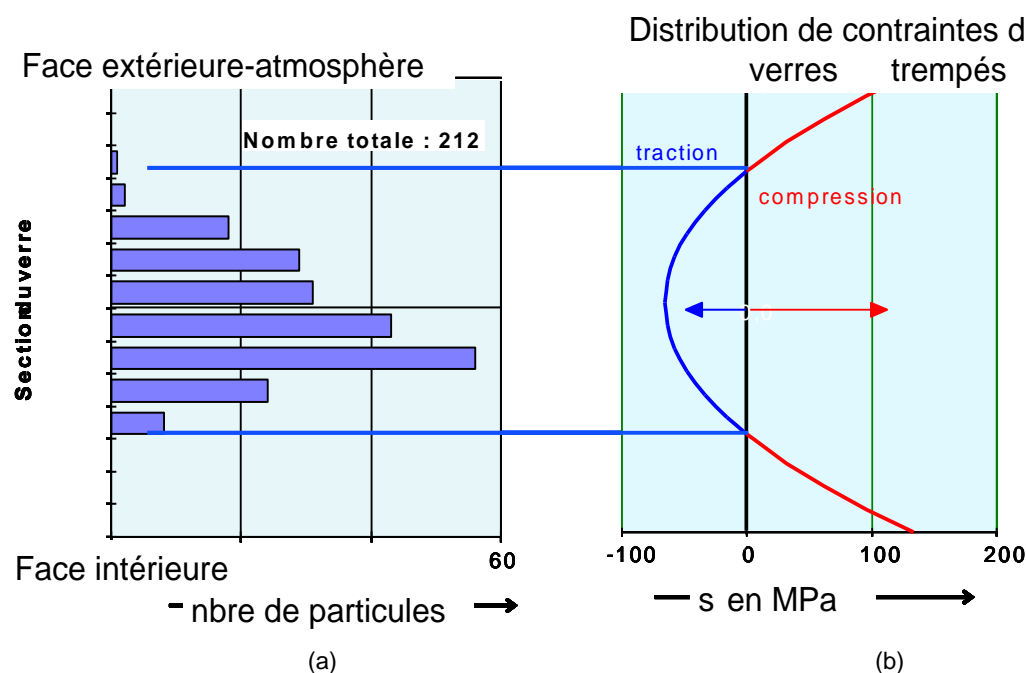


Figure 3: (a) Répartition des inclusions NiS sur une section du verre trempé ; (b) Profil des contraintes dans une section de verre trempé.

La Figure 3 a donne un histogramme du nombre de particules NiS en fonction de leur position dans l'épaisseur du verre. Cette répartition est à comparer avec la Figure 3 b qui donne un profil calculé de la tension à l'intérieur du vitrage (Hsiao [11]).

Les inclusions de NiS existent dans tous les verres mais elles ne posent problème que dans les verres trempés. En effet, les contraintes de traction existant à l'intérieur du verre trempé constituent un facteur de rupture. Au cours de la fabrication du verre, les inclusions de NiS sont trempées à partir d'une haute température et se trouvent donc à l'ambiante dans leur structure de haute température (dite α -NiS). Le refroidissement est assez rapide pour empêcher la transformation α -NiS \rightarrow β -NiS attendue par le diagramme de phase. La phase α -NiS à l'ambiante est donc métastable et tendra à passer à sa structure d'équilibre à l'ambiante (structure dite β -NiS). Cette transition de phase s'accompagne d'une augmentation de volume, de l'ordre de 2-4%, supérieure à l'espace libre autour de l'inclusion (Figure 4). Ce changement de volume provoque des fissures dans la matrice vitreuse autour de l'inclusion. Les contraintes de traction présentes dans l'intérieur du vitrage conduisent à une

1.3 Inclusions NiS et rupture des verres trempés

rupture brutale du vitrage. Ainsi la dangerosité des inclusions est fortement liée au profil de contrainte dans le verre. Il a été observé (Figure 3) que les ruptures provoquées par des inclusions de NiS sont plus nombreuses quand elles sont localisées dans la zone de forte traction.

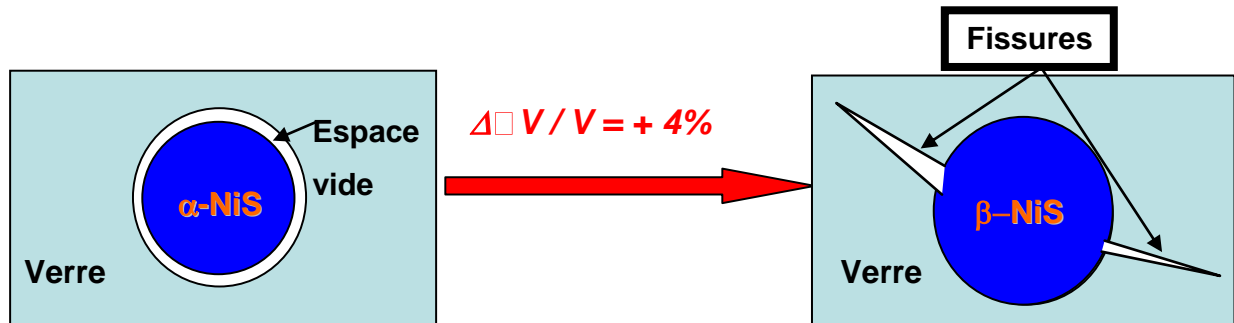


Figure 4: Sulfure de Nickel – rupture des verres trempés.

Cette figure résume le problème posé par les transformations de phase dans les inclusions de sulfures de Nickel. L'espace vide dû à la dilatation au cours de la formation des inclusions est de l'ordre de 1% alors que la transformation produit une augmentation de volume de 2-4%.

L'espace vide qui entoure les inclusions de sulfure de Nickel engendre un délai pour le début de la rupture. En effet, lorsque la transformation a lieu, l'inclusion de NiS grossit et remplit d'abord l'espace vide (Figure 4). Le changement de volume estimé à partir des mesures cristallographiques varie entre 2 et 4 % suivant les auteurs : 3,93% Hsiao [11], 2,4% Barry [12]. La différence entre ces calculs basés sur la cristallographie est due aux écarts entre les paramètres de maille utilisés dans chaque étude. Par dilatométrie, Kim *et al* [13] ont mesuré une valeur de 4,67% sur un sulfure de Nickel synthétique. Swain [4, 14] ont déduit de l'étude des densités respectives de α et β -NiS, une valeur de 4%. Il faut souligner que le calcul à partir de la cristallographie ne prend pas en compte l'effet des microstructures liées à la transformation et risque d'être moins réalistes que les valeurs issues de la dilatométrie (Annexe D) et la mesure de densité.

La taille critique des inclusions NiS qui peuvent provoquer la rupture est directement liée à l'état de contrainte et peut être calculé par un modèle mécanique dans le cas d'une inclusion au cours d'un traitement thermique Swain [4, 14]. Ce modèle prend en compte un changement de volume de 4% à la transformation, la dilatation au cours d'un traitement thermique ainsi que la présence d'un espace libre autour de l'inclusion. Il aboutit à une valeur de diamètre critique D_c :

$$D_c = \frac{\pi K_{1c}^2}{3.55 \sqrt{P_0} \sigma_0^{1.5}} \quad \text{eq 5}$$

avec $K_{1c}=0,76 \text{ MPa.m}^{1/2}$ le facteur de concentration de contrainte du verre, σ_0 la contrainte résiduelle autour de l'inclusion, $P_0=615 \text{ MPa}$ la pression hydrostatique résultante après la transformation $\alpha \rightarrow \beta$ -NiS et de la différence entre les coefficients de dilatation thermique.

Ce modèle montre que les inclusions de taille supérieure à $60\mu\text{m}$ pour $\sigma_{\text{traction}}(\text{max}) = 50 \text{ MPa}$ (Swain [4, 14]) peuvent provoquer la rupture. Compte tenu de la distribution des contraintes de traction (Figure 3b) dans les verres trempés et de la dispersion en taille des inclusions (50 à 500 microns), au centre des plaques ($\sigma_{\text{traction}} = 50\text{MPa}$), toutes les inclusions de sulfure de Nickel dépassent la taille critique. Comme il y a peu de possibilités de réduction de la taille des inclusions et de diminution de la contrainte de traction dans les verres trempés, il est indispensable de développer la détection des inclusions, soit par des méthodes d'imagerie, soit par des traitements thermiques provoquant la rupture anticipée.

I.4 Le Heat Soak Test

La solution industrielle utilisée pour remédier à la rupture spontanée des verres trempés consiste à provoquer par un traitement thermique approprié la transformation de phase et donc la fracture des vitrages avant montage. Ce test destructif appelé « Heat Soak Test » (HST) réalise un recuit des vitrages à une température inférieure à 400°C donc dans le domaine de stabilité de la phase $\beta\text{-NiS}$ (Figure 5). Il vise ainsi à accélérer la transformation de phase haute température $\alpha\text{-NiS}$ (hors équilibre dans le verre après trempe) en phase stable à basse température $\beta\text{-NiS}$. Ce test compte trois étapes : chauffage jusqu'à la température du traitement, maintien pendant une durée adaptée et finalement refroidissement jusqu'à l'ambiante. La durée ainsi que la température du palier ont été déterminée d'une manière empirique. En Europe, la norme « EN14179-1 » correspond aux conditions résumées par la Figure 5. Selon les pays, la norme appliquée aux vitrages varie en termes de température et de temps de maintien.

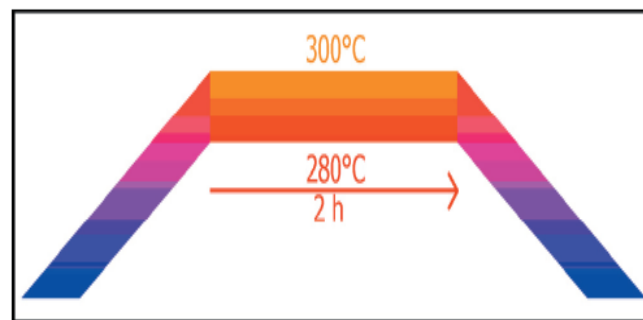


Figure 5: Schéma du cycle thermique lors d'un Heat Soak Test (HST) selon la Norme européenne EN14179-1.

L'application d'un tel test à l'échelle industrielle est soumise à plusieurs contraintes notamment sur le procédé de chauffage pour atteindre une température (entre 280 et 300°C) au niveau de tous les vitrages. Cette étape est généralement lente : selon la nature du four, elle peut durer entre 3h et 6h. De plus selon la position des vitrages dans le four, les vitesses de chauffage et refroidissement peuvent varier notablement : entre 1 et $2^\circ\text{C}/\text{mn}$.

I.4 Le Heat Soak Test

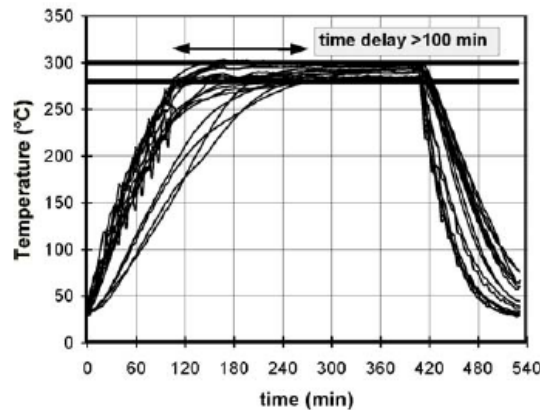


Figure 6: Courbe de température enregistrée en différents points d'un ensemble de panneaux de vitrage au cours d'un HST [3].

La Figure 6 donne l'évolution de la température pendant la phase de chauffage enregistrée à la surface d'un ensemble de vitrage. Des thermocouples sont placés à plusieurs endroits sur les vitrages et différentes positions dans le four. On remarque qu'il faut attendre 240 mn pour atteindre une température homogène ($280 < T < 300^{\circ}\text{C}$ imposée par la Norme EN14179-1) au niveau de tous les vitrages. Les vitesses de chauffage minimales et maximales enregistrées sont respectivement de 1 et $2,2^{\circ}\text{C}/\text{mn}$. Un délai de 100 mn, dû à la différence des vitesses de chauffage, est enregistré entre le premier et le dernier point, pour atteindre la température minimale du HST qui est de 280°C . La réalisation en conditions industrielles du HST impose donc certaines conditions quant aux vitesses de chauffage et de refroidissement ainsi que de durée minimale du traitement thermique.

Après ce test, les panneaux déficients, c'est-à-dire comportant des inclusions critiques, sont détruits avec un taux de fiabilité de 98,5%. Cependant le test est onéreux par sa durée et par la température de maintien assez élevée qui risque de nuire à la qualité du verre trempé. Les profils de contraintes désirés dans les verres trempés résultent de traitement thermique vers 500°C - 600°C . Ceci motive une étude de la cinétique de transformation visant à optimiser ce HST en obtenant par exemple le même taux de sécurité avec des températures et des durées de palier inférieures à celles utilisées actuellement.

Dans notre étude au laboratoire, nous serons amenés à conduire des études en condition isotherme et à des vitesses variables de montée en température. Cependant, la gamme de vitesse que nous explorerons est destinée à conduire l'étude cinétique conduisant à une modélisation. Ensuite, sur cette base pourra être abordée la modélisation en condition anisotherme adaptée aux conditions industrielles.

I.5 Plan de thèse

La thèse se composera d'une partie expérimentale associée à une partie modélisation. Dans cette démarche, les résultats expérimentaux devront servir de base à une modélisation de la transformation permettant à terme une mise au point de traitement thermique adapté. L'étude a été ainsi conduite afin d'atteindre progressivement les objectifs suivants : identifier les mécanismes de transformation, étudier l'impact de la composition en Soufre et la teneur en impureté (Fe) sur les mécanismes et la cinétique de transformation, déterminer les lois cinétiques qui contrôlent la transformation et enfin modéliser la cinétique de transformation.

1. Le premier chapitre sera centré essentiellement sur les aspects microstructuraux de la transformation. La transformation de phase $\alpha \rightarrow \beta$ -NiS a été étudiée dans le passé essentiellement d'un point de vue macroscopique en suivant la cinétique par calorimétrie différentielle. La caractérisation microstructurale de la transformation de phase a été conduite à travers des observations en microscopies optique et électronique sur des échantillons partiellement transformés. La combinaison de la microscopie optique et électronique (MEB, EBSD et MET) permettra d'étudier l'évolution microstructurale au cours de la transformation ainsi que les premiers stades de transformation, les relations d'orientation entre phases. L'influence de la stœchiométrie du sulfure et la teneur en impureté (Fe) sur la microstructure de transformation sont aussi examinées. L'étude microstructurale permettra de dégager les mécanismes associés à la transformation de phase selon les domaines de composition et température.
2. Le deuxième chapitre sera centré sur une étude de la transformation de phase par calorimétrie différentielle à balayage (DSC -Differential Scanning Calorimetry). D'une part, les résultats de cette étude seront utilisés pour valider le diagramme de phase dans notre domaine d'étude. D'autre part, on dégagera de cette étude des informations cinétiques sur la transformation notamment à travers la construction du diagramme TTT (Temps-Température-Transformation) à différentes compositions. Une analyse des données sur l'évolution de la fraction volumique transformée sera réalisée avec un formalisme de type Johnson-Mehl-Avrami-Kolmogorov (JMAK).
3. Le troisième chapitre rapporte l'étude des coefficients de diffusion des éléments Ni, S et Fe à travers des expériences de couple de diffusion. Ces coefficients de diffusion sont indispensables dans la suite de l'étude pour modéliser les cinétiques de la transformation de phase $\alpha \rightarrow \beta$ -NiS.
4. Dans le quatrième chapitre, sera développée la modélisation de la cinétique de transformation de phase pour des traitements isothermes. Une partie des données expérimentales nécessaires à la modélisation a été déjà présentée dans les chapitres précédents. Les paramètres manquant à la modélisation seront complétés, dans ce chapitre, à travers une étude cinétique *in situ* en microscopie optique de la transformation.
5. Le dernier chapitre rassemble les résultats qui associés à la modélisation permettent de proposer des traitements thermique alternatifs pour le HST.

Chapitre II. Phase transformations in Nickel sulphide (NiS): microstructure and mechanisms

II.1 Introduction:

Tempered glasses are known for their mechanical properties obtained after quenching from high temperature. This quenching leads to the creation of compression strain near the surface and tensile strain in the inner zone. However, such thermally toughened glass occasionally suffers from the so-called “spontaneous cracking” due to the presence of Nickel sulphide inclusions. This problem was first reported by Ballantyne[2] in the late fifties. In tempered glasses, the inclusions quenched from high temperature display the hexagonal α -NiS structure. The α -NiS phase is metastable at room temperature and will later transform into its stable form at low temperature, known as the β phase, which has a rhombohedral structure. This phase transformation is accompanied by a volume change of about 4%[2, 14]. This volume increase is known to be the origin of this fracture. Inclusions located in compressive zone do not cause any problem but inclusions situated in the inner tensile zone of tempered glasses provoke increased stresses leading to the creation of cracks. Fracture happens when the pressure in the glass around the NiS inclusions is high enough to initiate the first crack. This delayed fracture mechanism could take months to years for at least two reasons. First the phase transformation is slow at room temperature; second, due to the difference in thermal expansion coefficient between NiS inclusions and the glass, at room temperature, there is a gap of about $1\mu\text{m}$ around the inclusions and this gap can accommodate a part of the volume change. This is the reason that the spontaneous breakage on buildings can be delayed by one to two years.

Different inclusions are found in glasses but only NiS containing inclusions are known to cause the delayed fracture. The inclusions result from glass processing and originate from Nickel impurities

Chapitre II. Phase transformations in Nickel sulphide (NiS): microstructure and mechanisms

found in raw materials and from materials handling. These impurities are not soluble in the glass matrix and cause the formation of micronic inclusions, 50-600 μ m, with spherical shape. Generally, these inclusions contain two major elements Ni and S, and small quantities of Fe and Cu. The average composition of these inclusions varies between 50.10 and 52.7at%S (Annex A). The iron quantity varies between 0.11 and 1.62at%. The majority of the inclusions possess a Fe content close to 0,2at%.

Glass producers have tried to solve this problem, first by the elimination of the origin of impurities, but this was not completely successful, only a reduction of the quantity of the inclusions was possible. The second solution was to develop a heat treatment, the so called HST, to provoke the NiS phase transformation before installation of the glasses on buildings.

Previous microstructural results obtained on this system were limited to an optical microscopy study with Nomarski contrast [13]. This study concluded that a martensitic mechanism was possible for this phase transformation: i.e. the crystallographic structure change could be obtained by a displacive mechanism [13]. On the other hand, several investigations of the $\alpha \rightarrow \beta$ -NiS phase transformation by differential Calorimetry [3, 7, 8, 15-19] clearly disagree with a martensitic mechanism. These studies show an exothermic peak for $\alpha \rightarrow \beta$ -NiS phase transformation and an endothermic peak for the inverse reaction. In addition, the transformation is not instantaneous. It was also noticed that a slowing down of the transformation occurred with increasing overstoichiometry and Fe content. The slowing down of transformation with stoichiometry was associated with the precipitation of the Ni₃S₄ phase, (also called polydymite) [3] for overstoichiometric composition which is in conformity with phase diagram. Consequently, all the DSC results suggest that the transformation is controlled by a diffusive mechanism. In fact, different authors seem to have supported diffusive or martensitic mechanisms because they observed Nickel sulphide of different composition (overstoichiometric or stoichiometric one). Therefore stoichiometry is very important aspect to take in account in the study of the phase transformation.

Regarding the phase domains, the α -NiS phase has a relatively large composition field from 50 to 52 at%S in the temperature range 400-800°C while the β -phase has a narrow composition field. At room temperature β phase is a stoichiometric compound, at 260°C its maximum Sulphur concentration is about 50.45 at%S. Therefore, depending on the α initial composition, the $\alpha \rightarrow \beta$ -NiS phase transformation could be allotropic (composition constant transformation) or diffusive. During allotropic transformation, crystallographic structure change could be obtained by small range diffusion or by a displacive mechanism [20, 21]. When the initial α phase composition is overstoichiometric, long range diffusion is necessary to form the β phase and is expected to occur following classical diffusion mechanisms. Hence this phase transformation should conform to the classical mechanisms as found in other common systems.

The phase transformation in NiS inclusion is of great interest with respect to industrial HST, i.e. the heat treatment design in glass industry to eliminate the contaminated glasses. According to the European standard EN14179-1, the HST consists in heating to 280-300°C and holding 2h at this temperature. Heating rate is set in the range 1 to 4°C/min rate depending on the furnace and the allowed thermal strain in glass. During this thermal treatment all inclusions are expected to transform. But as the kinetics depends on the composition [3, 10], the optimization of the HST needs to take in

II.2 Materials and methods:

account the composition of the NiS inclusion. Thus inclusions with composition close to stoichiometric NiS should be the most rapid to transform while the overstoichiometric inclusions and those containing high amount of iron may take so long to transform so as to never break the glass during the HST or the lifetime of the building. It means that optimization of the HST requires, first a good knowledge of the phase diagram and second the understanding of the mechanism to model the kinetics in order to determine the composition limit to be considered for transformation. The knowledge of the phase diagram gives the maximal temperature permitted for $\alpha \rightarrow \beta$ -NiS transformation. This temperature limit has been confirmed to be 320°C [3]. On the other hand, the transformation mechanisms and related modelling remain an open question.

The present study aims at a better understanding of these mechanisms, based on microstructural features occurring during phase transformation (morphologies, interface behavior, precipitation) and their evolution according to temperature and Sulphur composition. Microstructural investigation of the $\alpha \rightarrow \beta$ -NiS phase transformation was carried out on isothermally heat treated samples. This allows one to separate temperature and time effects on microstructural evolution. In addition, all heat treatments were carried out in a DSC furnace, which provides a continuous following and better control of the transformed volume fraction. The effect of the composition was studied by means of a series of α -NiS samples of different composition. In the present study, the nucleation stage happened to be difficult to study and we have focussed on microstructures corresponding to the growth regime and on the kinetic aspects of the transformation. Contrary to previous studies of the α to β -NiS phase transformation which were essentially based on a macroscopic point of view, we have tried to investigate details as finely as possible. In this study, the microstructural changes due to the transformation were followed using a combination of several techniques: polarized light microscopy and Scanning Electron Microscopy (SEM) imaging using the crystalline contrast of the backscattered electrons complemented by Electron Back Scattered Diffraction (EBSD), Transmission Electron Microscopy (TEM) and X ray diffraction (XRD).

II.2 Materials and methods:

II.2.1 Materials

Natural NiS inclusion can be found in glasses but for this study which requires controlled composition and large samples, synthetic Nickel sulphide have been prepared. All samples were prepared starting from Nickel and Sulphur fine-powder mixed in the required proportions and agitated to obtain a good homogeneity. Nickel powder was previously heat treated at 500°C during 6h under an argon flow with 5% H₂ in order to remove any oxygen impurities. After this reduction, Nickel shows a clear gray aspect instead of its initial dark one. The powder was inserted in a quartz tube, sealed under vacuum to prevent a secondary reaction with the oxygen. It was then slowly heated ($\sim 5^\circ\text{C}.\text{min}^{-1}$) to 800°C to bind components and to obtain the master alloy. The tube was maintained at this temperature for 2 days and then cooled to 600°C. After 4 days at 600°C, the tube was cooled to 410°C during 2 hours, then quenched by immersion in water. The tube was broken under protective

Chapitre II. Phase transformations in Nickel sulphide (NiS): microstructure and mechanisms

atmosphere of argon and pieces of NiS are collected for the analyses. This initial material was kept under argon at -20°C to slow down its oxidation.

A series of NiS samples was processed with the following target composition: NiS; NiS_{1.01}; NiS_{1.02}; NiS_{1.04}; NiFe_{0.01}S. The aim was to produce NiS samples of different stoichiometry and with iron content. Bulk samples, with 20 g weight, were prepared for each composition. Phase identification and homogeneity were tested with X-Ray diffraction (XRD) and SEM observations. Composition analyses were carried out with Electron Probe Micro-Analysis (EPMA): results are summarized in Table 2 below.

It should be noticed here that composition is the average of 10 analysis measured in different areas of the sample. All samples have shown a spatial fluctuation of about $\pm 0.14\text{at\%}$ to average composition.

Composition	Target			Effective (at%)		
stoichiometry	Ni	Fe	S	Ni	Fe	S
NiS	50	0	50	49.87	0	50.13\pm0.14
NiS	50	0	50	49.6	0	50.4\pm0.14
Ni₁S_{1.01}	49.75	0	50.25	49.13	0	50.87\pm0.12
Ni₁S_{1.02}	49.5	0	50.5	48.86	0	51.14 \pm 0.17
Ni₁S_{1.04}	49	0	51	48.72	0	51.28\pm 0.14
NiFe_{0.01}S_{1.01}	49.5	0.5	50	48.88	0.60\pm0.03	50.52\pm0.12
NiFe_{0.01}S	49.5	0.5	50	49.08	0.38\pm0.05	50.56\pm0.14

Table 2: Sample compositions measured by EPMA: difference between targeted and effective of α -NiS. In the following, the reported sample composition will be the one measured by EPMA (effective composition).

Many samples show a difference between effective and target composition. This is due to experimental procedure. When mixing Ni and S, a small part of Sulphur and Nickel stick to the tube. Besides some Sulphur, which has a very low evaporating temperature, may be found at the bottom of the quartz tube. In the following, the measured composition is considered as the sample composition.

II.2.2 Heat treatments

A DSC equipment measures the heat flow due to a phase transformation. If there is only one mechanism, the heat flow is proportional to the volume fraction transformation rate. In case of a complex transformation, involving several mechanisms with different enthalpy, the heat flow estimates only an equivalent volume fraction. However, it is possible, for endothermic or exothermic transformation, to follow the transformed volume fraction by monitoring transformation enthalpy. In addition, DSC equipment is able to perform either a rapid heating, a rapid quenching as well as

II.2 Materials and methods:

permitting a continuous following of the transformed volume fraction as a function of time ($F_v(t)$). This is the reasons all of heat treatments were carried out using the DSC furnace.

Microstructure evolution was studied on different isothermal heat treatments stopped at times corresponding to different stages of transformation. NiS samples are first annealed at 450°C during 20min then quenched to room temperature in order to obtain the α structure. After that, they were rapidly ($\sim 300^\circ\text{C}/\text{min}$) heated to high temperature (200-300°C) and held at this temperature for a time during which the $\alpha \rightarrow \beta$ -NiS transformation occurred. After this step, the sample was quenched ($\sim 100^\circ\text{C}/\text{min}$) to room temperature in order to keep the resulting microstructure. The range of temperature, (200-300°C) was chosen in order to study the microstructural evolution in different field of the phase diagram around the NiS stoichiometry: β , $\beta + \text{Ni}_3\text{S}_4$ and $\alpha + \beta$ (Figure 7). The magnification of the Ni-S phase diagram around NiS stoichiometry in Figure 7b shows that below 280°C $\beta + \text{Ni}_3\text{S}_4$ are stable from stoichiometric to 51.5at%S composition and above 280°C α and β phases become stable. All the heat treatment were carried out under Argon using the Diamond DSC-Perkin Elmer equipment. Heating and cooling rate were chosen to avoid transformation during these steps. The maximum of DSC heating rates and cooling rate were used.

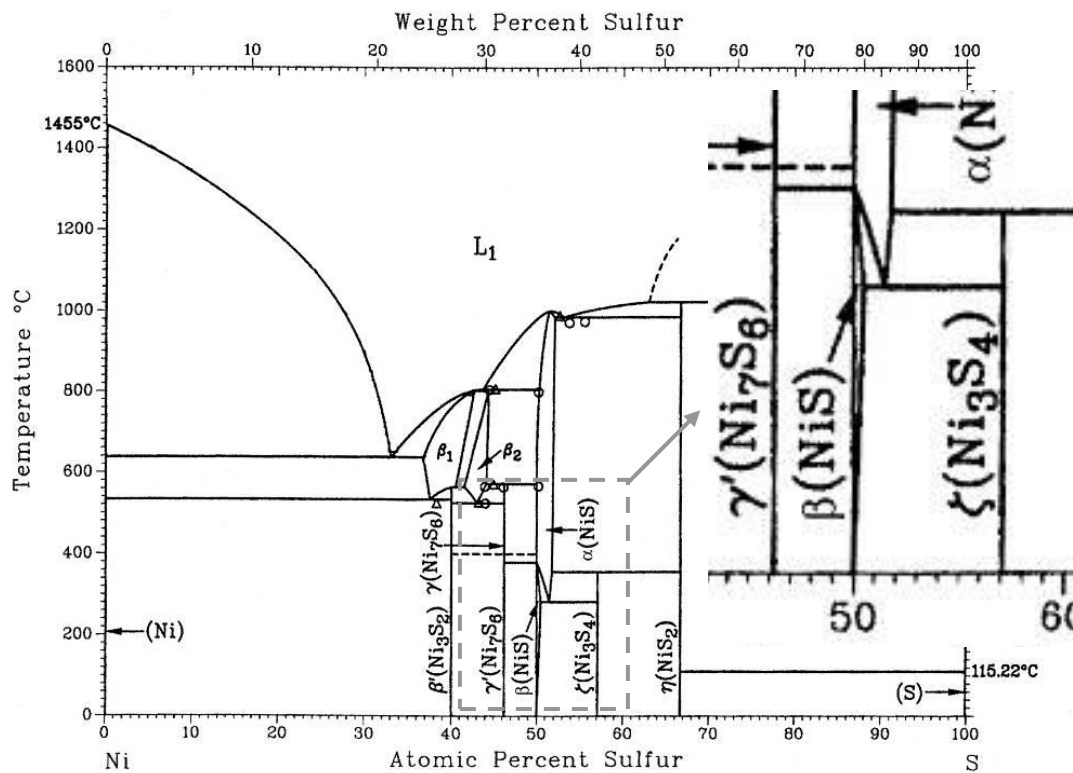


Figure 7: Ni – S phase diagram after Nash.P *et al* (1991)[22].

Around the NiS stoichiometric composition, four phases exist: α & β -NiS, Ni_3S_4 and Ni_7S_6 . These phases have respectively, hexagonal, rhombohedral, cubic and orthorhombic crystallographic structures. Ni_7S_6 and Ni_3S_4 are stoichiometric compounds as well as β -NiS at low temperature. But the β phase presents some overstoichiometry at high temperature ($\sim 0.45\text{at } \%$). The α -NiS phase shows a large composition field from 50 to 52 at%S for $T > 400^\circ\text{C}$. (A detailed description of α and β crystallographic structures is provided in Annex B)

II.2.3 Microstructural characterization

The microstructural study was carried out using different techniques such as optical microscopy, SEM for macroscopic characterization and EBSD technique and TEM for fine characterization. Metallographic observations were carried out on mechanically polished sample (1 or $\frac{1}{4}$ μm) using optical and scanning electron microscopy. Samples can be conveniently observed using optical microscopy between crossed polarizer and analyzer because of the crystallographic anisotropy of the α and β structure. This anisotropy makes possible a contrast between α and β and between the different orientations of the same phase. This color contrast allows for a qualitative identification of phases when the transformation proceeds. The interpretation of the polarized light microscopy has been tested using the EBSD technique which confirms the identification of the structures. After that SEM imaging using the backscattered electrons (BSE) mode and EDX analysis complete the phase characterization.

In SEM microscopy (BSE mode), the α and β phase cannot be distinguished by chemical contrast using the backscattered electrons because they have no or a too small difference in composition. Nevertheless, α and β NiS phases have different crystalline structure. So using the so called in lens QBSD detectors, a contrast can be obtained because this detector, compared to classical detectors, has an enhanced sensitivity to crystalline orientation. In this imaging condition, probe intensity have to be optimized to get better resolution (2 pA in FEG SEM typically) and the working distance should be as close as possible to the surface. The drawback of using such a small probe size is that the field of view will be limited to about 500 μm . Optical microscopy is carried out first in order to select an area then SEM observation is made for high resolution imaging to get detailed information on microstructure.

Crystallographic characterization of the α and β phases and their orientation relationship are obtained by the EBSD technique (SEM FEG). TEM observations have also been carried out to get fine scale description. However the investigation was here limited because NiS samples suitable for observations are difficult to obtain. TEM samples are prepared by ultramicrotomy which allows a direct cutting of thin samples using diamond knives. It has been rather successful for preparing β phase samples but α phase samples or samples with coexisting α and β phases could not be prepared by this method because the α phase was not hard enough for ultramicrotomy preparation. Good TEM results are then obtained only for the β phase.

II.3 DSC characterization of the phase transformation

This DSC study was carried out under isothermal heat treatment for the following reason. First, it allows one to estimate the time range of transformation depending on composition (stoichiometry and iron impurities content) and temperature. Second the symmetry or asymmetry of a peak can give information on the number of mechanisms involved.

Figure 8 shows DSC curves recorded during isothermal Heat treatment at 200°C for five different compositions: two near stoichiometric samples NiS (50.13 and 50.4at%S) two overstoichiometric

II.3 DSC characterization of the phase transformation

samples NiS (50.87 and 51.14at%S)) and iron contained sample NiFeS (50.56at%S, 0.38at%Fe). Figure 8b shows an example of transformed volume fraction evolution plotted against time.

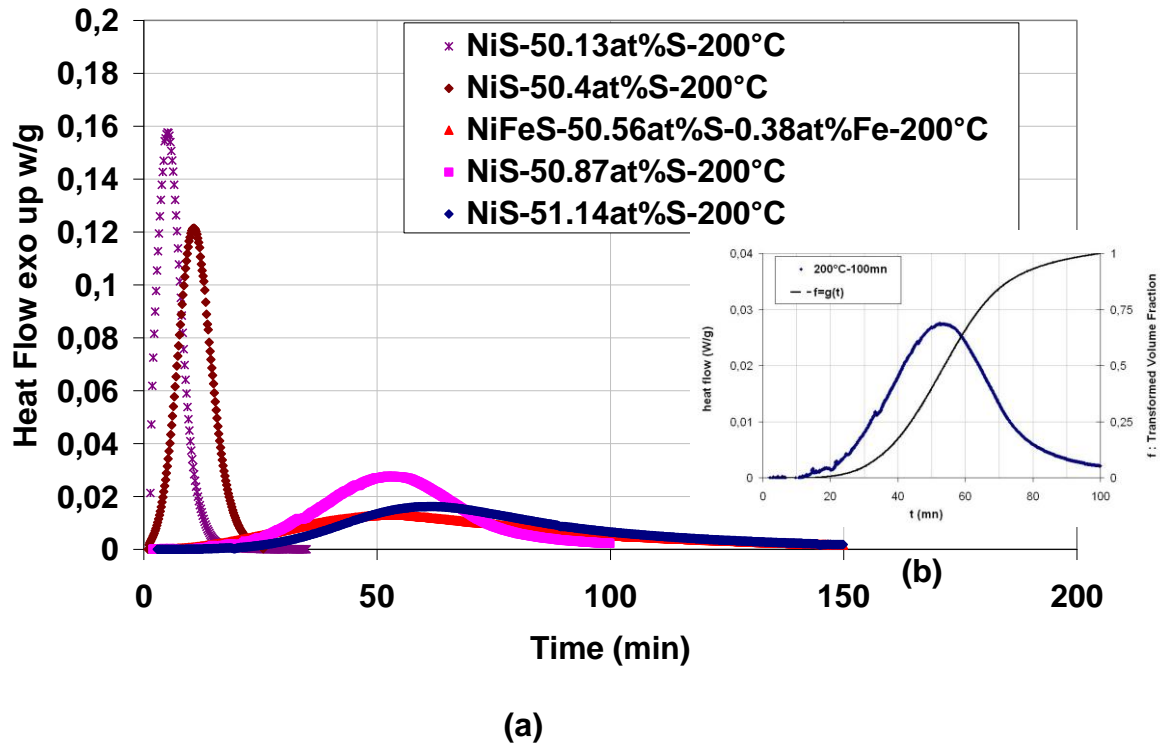


Figure 8: (a) DSC curves recorded after $\alpha \rightarrow \beta$ -NiS transformation at 200°C for different Sulphur composition and iron content: NiS (50.13, 50.4, 50.87, 51.14at%S) and NiFeS (50.56at%S, 0.38at%Fe). (b) Graphs showing the transformed volume fraction extracted from the DSC for the overstoichiometric sample $\text{Ni}_{49.13}\text{S}_{50.87}$. Increasing Sulphur composition slows down the transformation. The same effect is observed with the iron content sample.

First, all composition shows exothermic phase transformation. This is in agreement with previous studies [3, 7, 8, 15-19]. Complete transformation takes from 13 to ~120 min for the studied compositions. Times for complete transformation increase with overstoichiometry. This confirms the slowing down of the transformation, due to overstoichiometry and Fe impurities. This effect was already reported in a previous study [3] using DSC anisothermal treatments. The present study allows one to demonstrate the slowing down on isothermal heat treatment for very small composition differences. Since EPMA was used for measuring the composition, we can confirm the high impact of stoichiometry on the kinetic of the transformation.

The transformation peak shows symmetric shape for an almost stoichiometric sample ($\text{Ni}_{49.87}\text{S}_{50.13}$) which indicates that one mechanism is controlling the whole transformation. But for the overstoichiometric and iron containing samples, some dissymmetry of the peak shape can be observed. This is the signature of mechanism change during phase transformation.

However, since the DSC technique is limited to macroscopic information of the transformation, to obtain more details concerning on the mechanisms and the composition effects (overstoichiometry and iron impurities), a microstructural characterization is required in order to go further.

II.4 Microstructural signature of the transformation: influence of temperature, stoichiometry and Fe impurities

Metallographic images have been recorded from samples thermally treated within the DSC to observe different stages of transformation. The as quenched α -NiS samples were rapidly heated and held at high temperature (200-300°C). The holding time in the DSC was chosen to yield a specific volume fraction. The studied composition and temperature have been selected to explore the Ni-S phase diagram around the NiS stoichiometry: i.e. the three phase fields β , β +Ni₃S₄ or β + α .

II.4.1 Typical morphologies of the phase transformations

Repeated observations have allowed one to identify, for the growth regime, 3 typical morphologies which are referred to as globular, lamellar or block morphology.

a. Globular morphology

Figure 9, shows the morphology observed for a sample and heat treatment corresponding to the β phase field. The areas with different colors in Figure 9 correspond to the α and β -NiS phases. The color contrast results from the nature of the phase (α or β) and of the crystallographic orientations as explained in part II.2.3. The dark lines in Figure 9 are fractures in the sample. This fracture may be due to the mechanical polishing or to the volume change induced by the phase transformation.

According to Figure 9 a and b, after transformation, the microstructure consists of two phases α and β . The β grains (yellow and blue area in Figure 9 a and b) which can have very different sizes (from few μm to about 100 μm) display relatively isotropic shapes. Therefore this morphology is called in the following a globular one.

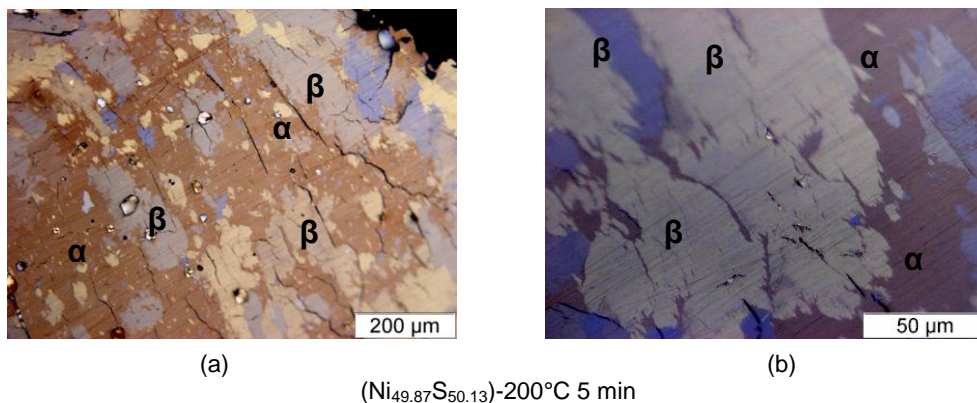


Figure 9: Globular morphology: the characteristic morphology in the β field of the phase diagram. In a single α grain several β grains at different stage of the growth regime can be observed. β grains are homogeneously nucleated inside the grains.

II.4 Microstructural signature of the transformation: influence of temperature, stoichiometry and Fe impurities

A remarkable feature illustrated by the high magnification image in Figure 9 b is that small β grains are homogeneously dispersed inside the α grain and coexist with large β grains. In addition, the β grain growth is limited inside the α grain. In other words, when growing, the β grain did not invade all of the α grain. Though this observation was made on sample corresponding to quite short time experiments, such a partial transformation with small β grains and limited growth indicate that the transformation is not as rapid as expected if it were a martensitic transformation. As the transformation occurs in the β field of the phase diagram, i.e with no composition change, the transformation should then be termed a massive one: a massive transformation is generally known as diffusive and partitionless phase transformation [23-32]. In addition, the massive transformation mechanism is in agreement with the homogenous nucleation mode implied for this globular morphology. This typical globular morphology has been observed in the metallographic study of the β phase domain, namely for near stoichiometric sample and temperature from 200 to 300°C.

It is worth mentioning that coexistence of β phase with very different sizes implies that nucleation has been possible during the entire transformation. It means that the evolution of the transformed volume fraction followed by DSC gives a transformation law which is an average over several stages of the growth regime.

b. Lamellar morphology

The micrographs in Figure 10 (and Annexe F) illustrate the morphology of samples and heat treatment corresponding to the β +Ni₃S₄ phase field. The β grains always display elongated shapes, either embedded in the α grains or starting from grain boundaries. Repeated observations always show such an elongated morphology for the β grain independently the α grain orientation which is consistent with a lamellar or plate morphology for β grain. In the following this morphology will be referred to as lamellar. The β lamellae could reach 20 μ m in thickness and 200 μ m in length. However, the β plates size range is very large: length varies from about 20 μ m to about 200 μ m. As illustrated by Figure 10b and c, lamellae nucleation occurs at the grain boundary as well as inside the grains. In case of β phase nucleating at grain boundaries, we observe that the β plates grow only from one side of the grain boundary. Figure 10c shows small β plates nucleated inside the grain and already showing a definite anisotropic shape similar to well developed lamellae. This observation reminds one of that made for the globular morphology and suggests again that the transformed states display different stages of the growth regime.

In contrast with the globular morphology, the lamellar morphology indicates that the growth in the direction parallel to the β plate is faster than in perpendicular direction. This could result from different mechanisms controlling the lengthening and thickening.

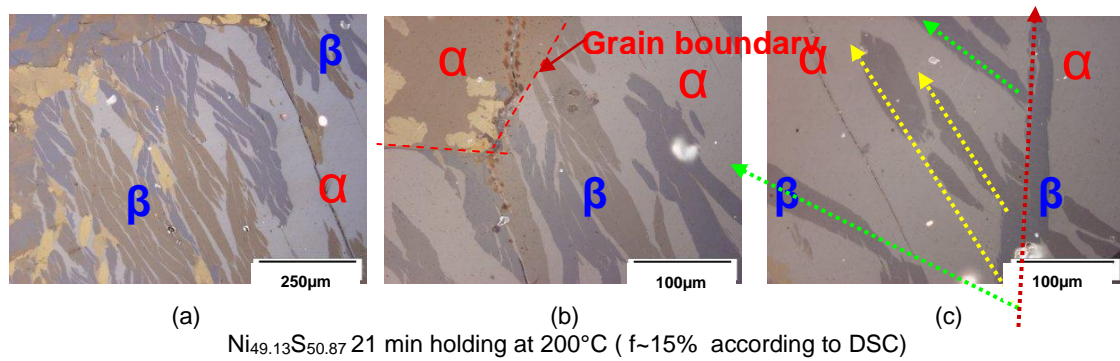


Figure 10: (a) lamellar morphology the typical morphology in the $\beta + \text{Ni}_3\text{S}_4$ field of the phase diagram (b) illustration of β lamella growth on one side of the grain boundary (c) specific orientations between β plate's growing inside the grain.

Figure 10c indicates that β plates have specific orientations with respect to each other. Preferential growth along selected directions has been observed frequently for the transformation occurring in the $\beta + \text{Ni}_3\text{S}_4$ field. This specific orientation reveals that crystallography should play a part in the phase transformation. To go further in the crystallographic aspect, EBSD cartography was recorded and analyzed to determine the α/β orientation relationships.

Repeated observations on overstoichiometric sample, $\text{Ni}_{48.86}\text{S}_{51.14}$ and $\text{Ni}_{49.13}\text{S}_{50.87}$, have confirmed that lamellar morphology is the major one in the $\beta + \text{Ni}_3\text{S}_4$ phase field. We estimate that the lamellar morphology corresponds to stoichiometry from 50.5 to 51.14at%S. The main difference between the lamellar and globular morphology is the characteristic preferential orientation of β plates in contrast to precipitates with the globular morphology which have isotropic growth. An EBSD study was also carried out on the globular morphology to compare crystallographic aspects.

c. Block morphology

In the $\alpha + \beta$ high temperature domain, the micrographs (Figure 11) show β grains with no specific shape. This quite isotropic grains which could reach $150\mu\text{m}$ in size could either form block located at the grain boundary or within the α grain. Remarkably, the interfaces between α and β for this block morphology are very irregular as illustrated in Figure 11b. In addition, β phase grains growing within one α grain (Figure 11b) present only one color contrast unlike the globular and lamellar morphology. This suggests that the block morphology should have different crystallographic aspect different from the other morphology. This point was further investigated by EBSD.

II.4 Microstructural signature of the transformation: influence of temperature, stoichiometry and Fe impurities

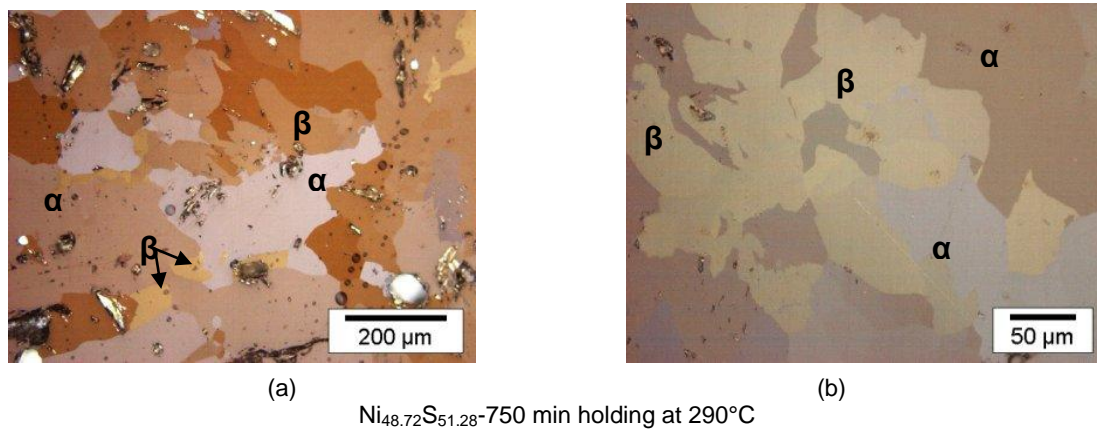


Figure 11: Block morphology: the characteristic morphology in the $\alpha+\beta$ field of the phase diagram for the low relative supersaturation.

The microstructure shown in Figure 11 corresponds to long holding time and possibly to an equilibrium state since the NiS phase diagram predicts a $\alpha+\beta$ equilibrium at this temperature and for this composition. Therefore, this block morphology should be characteristic of the two-phase field ($\alpha+\beta$) for lower relative supersaturation.

The complete metallographic study of transformed states has revealed a strong sensitivity of the morphology to the temperature and composition. This has motivated then a detailed investigation of temperature and composition effect for each morphology presented below.

II.4.2 Effect of composition and temperature

a. Globular morphology

Since the globular morphology is observed in a narrow domain of composition close to stoichiometry, no composition dependence can be actually studied. For these near stoichiometric samples, according to DSC and confirmed by optical micrography, the increase of temperature accelerates the transformation but the microstructure maintains the same globular aspect.

b. Lamellar morphology

Figure 12 corresponds to very overstoichiometric sample at two temperatures. Figure 12a strongly reminds one of the lamellar morphology shown in Figure 10. But the periphery of the lamellae appears quite ill-defined which suggests the presence of a second phase. Further investigations with SEM were necessary to clarify this point. Regarding temperature effects, the micrography in Figure 12b shows coarse and ill-defined lamella, the β grains being somewhat thicker and shorter than those in Figure 10. Their size could reach about 50 μm for thickness and 100 μm in length. In addition, in contrast to the lamella in Figure 10b, the β phase grains display few color contrasts. This suggests

Chapitre II. Phase transformations in Nickel sulphide (NiS): microstructure and mechanisms

that the transformation crystallographic characteristics have changed with increasing temperature, a point that required further investigation by EBSD.

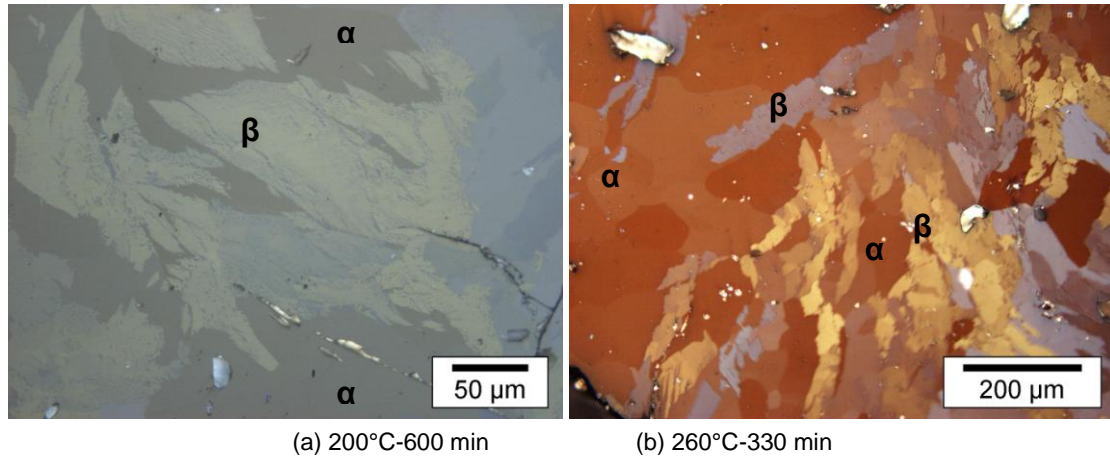


Figure 12: Optical observation of lamellar and coarse lamellar morphology in very overstoichiometric sample $\text{Ni}_{48.72}\text{S}_{51.28}$. Note in Figure 6a the dark contrast and ill defined β grain contours which may be due to Ni_3S_4 precipitation.

Figure 13 a and b give the microstructures observed for low and high overstoichiometric samples after isothermal heat treatment at 200°C. In both cases, a dark contrast is observed either decorating the α/β interface in the less overstoichiometric sample (Figure 13a) or forming alternate lamella with the β phase in the highly overstoichiometric sample (Figure 13b). Local chemical analysis with EDX in the dark zones indicated an enrichment in Sulphur. In addition X-Ray diffraction pattern indexation was consistent with three crystallographic structures: the α and β phases and a small volume fraction of the Ni_3S_4 structure which in agreement with the phase diagram.

In the less overstoichiometric sample (Figure 13a), the Ni_3S_4 phase forms small precipitates ($\sim 0.5\mu\text{m}$) along the α/β interface. In the high overstoichiometry, Figure 13b shows alternating β and Ni_3S_4 lamella respectively with about $3\mu\text{m}$ and $\sim 0.5\mu\text{m}$ width. Thus, at low overstoichiometry, the β phase forms with precipitation of Ni_3S_4 phase at the α/β -NiS interface; at high overstoichiometry, β and Ni_3S_4 phases forming at the β lamellar periphery grow according to an eutectoid morphology.

II.4 Microstructural signature of the transformation: influence of temperature, stoichiometry and Fe impurities

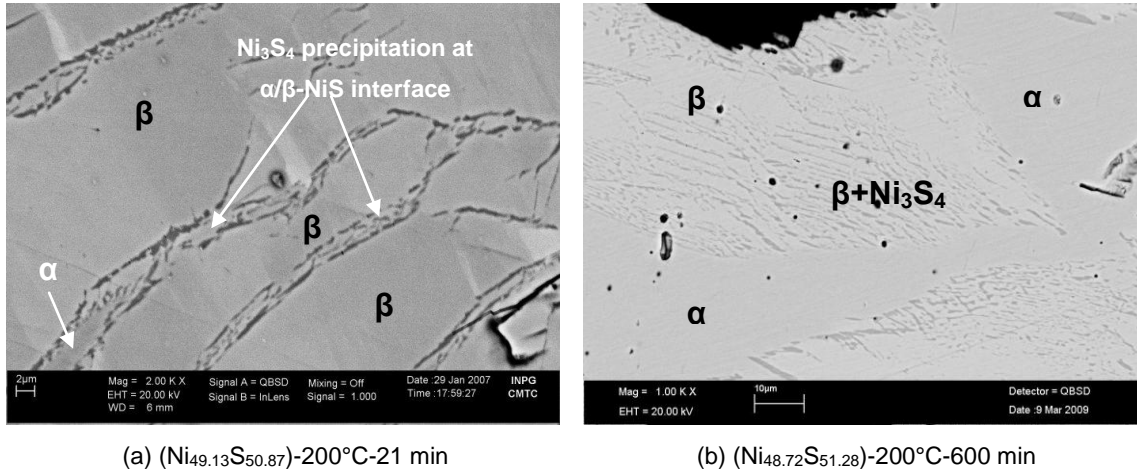


Figure 13: Effect of Sulphur composition on microstructures at 200°C (a) precipitation of Ni_3S_4 at α/β interface (b) eutectoid microstructures made of $\beta + \text{Ni}_3\text{S}_4$ lamella at the periphery of initial β lamella. At constant temperature increasing Sulphur composition slows down the transformation and leads to Ni_3S_4 precipitation. For very high overstoichiometry the morphology of the growth regime changes from lamellar toward eutectoid $\beta + \text{Ni}_3\text{S}_4$ lamella.

The DSC study reported in previous sections has already shown that the presence of Fe slows down the transformation as overstoichiometry does. In order to compare the morphology, metallography has been carried out on a Fe containing sample ($\text{Ni}_{48.88}\text{Fe}_{0.60}\text{S}_{50.52}$ -200°C-60min). According to Figure 14a, the transformed state displays a lamellar morphology. The SEM image in Figure 14b shows the precipitation Ni_3S_4 at α/β interface.

According to optical microscopy on a series of heat treatment at long times, we conclude that for the Fe containing sample the transformation remains partial which is interpreted in terms of the slowing down effect due to Fe impurities. This is similar to the effect of overstoichiometry.

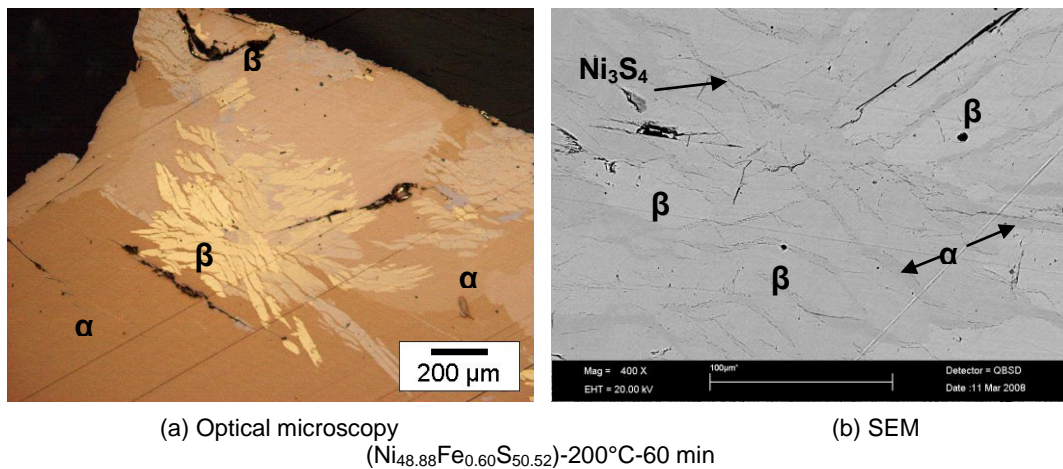


Figure 14: Effect of Fe impurities on microstructures: (a) lamellar morphology is also observed in the Fe containing sample $\text{Ni}_{48.84}\text{Fe}_{0.60}\text{S}_{50.56}$ (b) precipitation of Ni_3S_4 phase at α/β interface. The iron containing sample displays the same microstructure as the overstoichiometric sample.

c. Block morphology

The block morphology has been observed in small domain of composition and temperature: close to equilibrium line on the α phase side of the $\alpha+\beta$ field. In fact this equilibrium line being curved, the domain corresponding to the block morphology is better defined by a constant relative supersaturation than by a composition-temperature domain. The relative supersaturation, characteristic of the block morphology can be estimated from metallographic observations, composition analysis and the phase diagram using the state shown in Figure 11. One estimates a relative supersaturation of about 24%.

Figure 15 (a) illustrate the block morphology developed in a state corresponding to this level of supersaturation. When the temperature is decreased by 20°C, staying in $\alpha+\beta$ field, the morphology (Figure 15b) is no longer a block one but a lamellar one. Ni_3S_4 precipitation is not observed which is in agreement with the phase diagram.

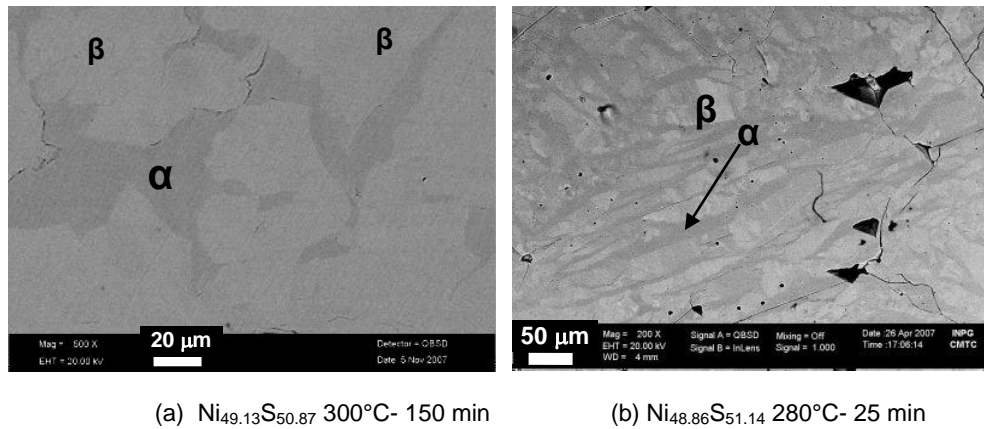


Figure 15 : SEM FEG observations: Increasing temperature leads morphology changes from lamellar to block one (no Ni_3S_4 precipitate are observed).

Microstructural characterization with optical microscopy allowed macroscopic description of typical morphology of specific mechanism either partitionless mechanism for the massive transformation or partitioned mechanism when diffusion is involved (for instance to precipitate the Ni_3S_4 phase). Nevertheless, several aspects of phase transformation such as crystallography, fine scale microstructures and composition near the α/β interface remain unknown. They were further investigated using FEG SEM, EBSD and EPMA analysis.

II.5 Morphology and related α/β orientation relationships

To further investigate orientation relationships, EBSD cartography has been carried out on all the morphologies identified in the section II.4. This crystallographic study provided the orientation relation between α and β and when possible the identification of the interface plane.

II.5 Morphology and related α/β orientation relationships

II.5.1 Lamellar morphology

EBSD cartographies recorded on one area show separately the α phase zone (Figure 16a) and the β phase zone (Figure 16b). As α and β phases respectively have hexagonal and rhombohedral structure, they can be schematically described using an hexagonal prism. Figure 16a shows three α grains (red, green and purple). The orientation of the grain in green is given on the schematic representation by the C axis in plane. Figure 16b displays the β grains in different colors corresponding to their orientations. For instance, the β grains in blue and red are respectively described by hexagonal prism having the prismatic facet of normal $(1-10)$ in plane. Within one α grain (in green in Figure 16a), we note that the β phase lamella show 6 different orientations.

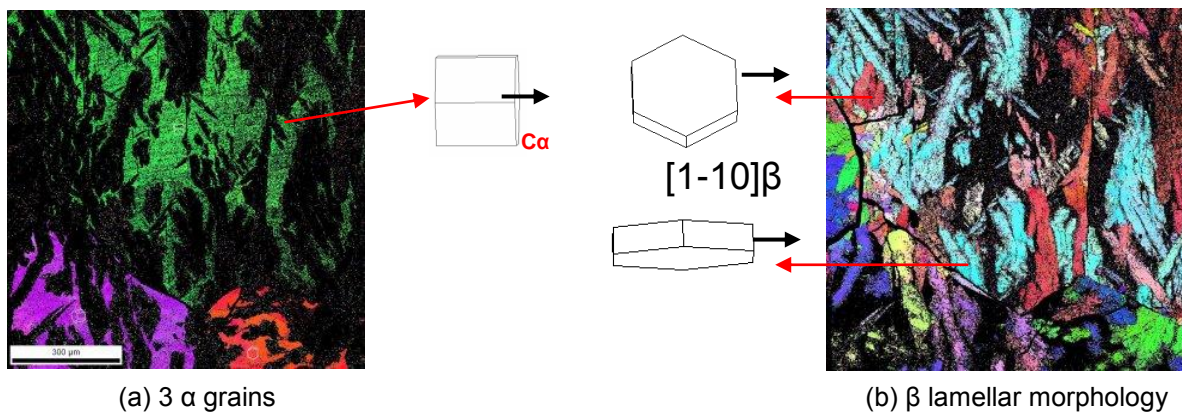
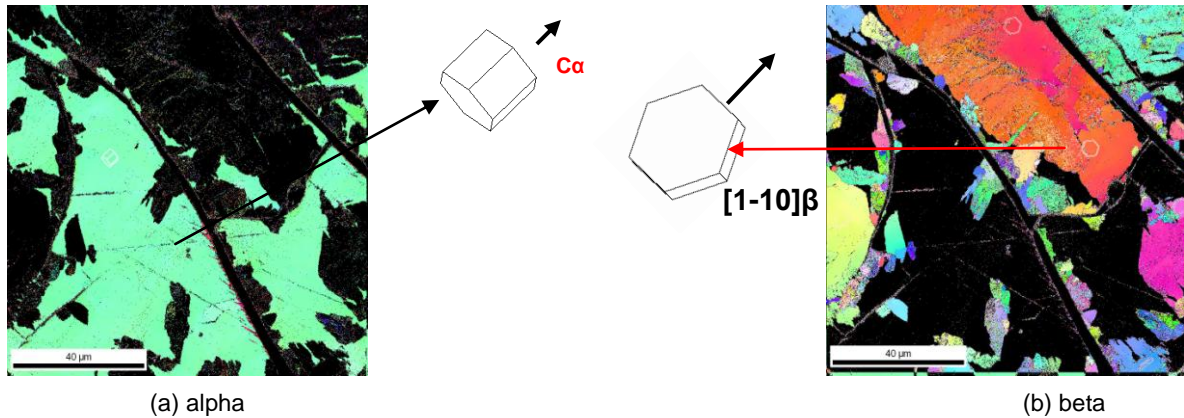


Figure 16: EBSD cartography for the lamellar morphology case: Figure 16a displays the α phase grains and their one schematic representation. Figure 16b shows several β phase grains with different orientation and their schematic representation. The corresponding orientation relationship is: $(001) \alpha \parallel (1-10) \beta$; $[450] \alpha \parallel [110] \beta$. (A detailed description of the α/β of the orientation relationship is provided in Annex B) (Partially transformed $\text{Ni}_{49.13}\text{S}_{50.87}$ after 21min hold at 200°C .)

From the EBSD cartography the following orientation relationships between α and β -lamella were obtained: $(001) \alpha \parallel (1-10) \beta$; $[450] \alpha \parallel [110] \beta$. The six β grain mentioned above are indeed crystallographic variants of this orientation relationship. The simplest feature of this orientation relationship is the parallelism of the basal plane of the α phase with the prismatic plan of the β phase: $(0001)_\alpha \parallel (1-100)_\beta$. This result is not the usually expected one because orientation relationship often shows the parallelism of high symmetry axes (for instance c_α/c_β).

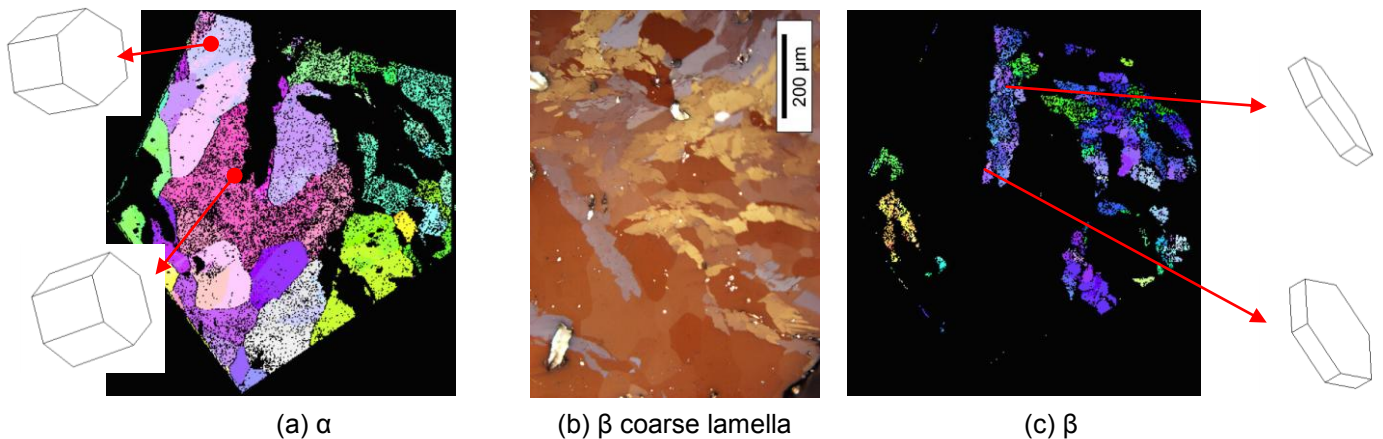
II.5.2 Globular morphology

On a sample showing the globular morphology, EBSD cartography (Figure 17) has shown that the large β grains present an orientation relation identical to what observed for the lamellar morphology i.e. $(001) \alpha \parallel (1-10) \beta$; $[450] \alpha \parallel [110] \beta$. But for small grains (less than $5\mu\text{m}$) in Figure 17b which are imaged in different color than the larger ones, no specific orientation relationship with the α phase could be identified. In contrast to the lamellar case, these small grains do not correspond to variants of a unique orientation relationship.



II.5.3 Coarse lamellar morphology

Figure 18 shows an example of EBSD cartography obtained on partially transformed samples with coarse lamellar morphology (very high overstoichiometry at high temperature in the $\beta + \text{Ni}_3\text{S}_4$ phase field II.4.2.). In contrast to the lamellar case, no specific orientation relationship has been identified. As illustrated by the schematic presentation in Figure 18, we frequently observed that there is an average orientation which sets the α and β phase C axes at about 30-45°.



II.6 Composition analysis

II.5.4 Block morphology

The EBSD cartography in Figure 19 has been obtained on partially transformed samples showing the block morphology (very high overstoichiometry at high temperature in the $\alpha+\beta$ phase field II.4.1). Here again, no specific orientation relationship has been identified. As illustrated by the schematic presentation in Figure 18, we frequently observed an average orientation which sets the α and β phase C axes at about 30-45° as in the coarse lamellar morphology.

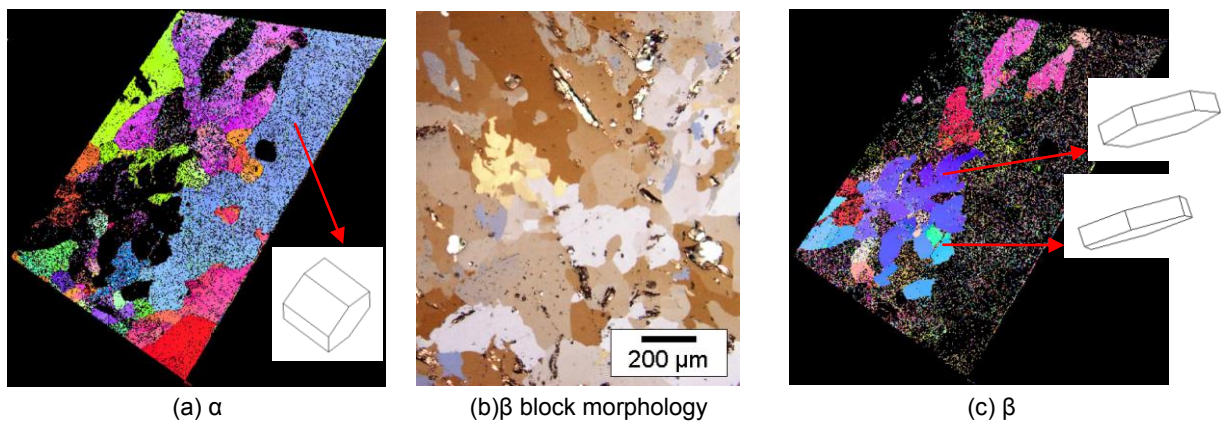


Figure 19: EBSD cartography for the block morphology case: as for the coarse lamellar morphology, no simple and well defined orientation is observed but on average we frequently observed the unspecific orientation illustrated by the schematic representation of α and β grain orientation. (Partially transformed $\text{Ni}_{48.72}\text{S}_{51.28}$ after 750 min hold at 290°C)..

The EBSD investigations have been successful in the identification of α/β orientation relationships in some of the morphologies. It became clear that increasing overstoichiometry leads to change of the orientation relation. This is an important observation which can be related to the morphology changes with stoichiometry and possibly to the kinetics. But to explain the overstoichiometry effect, at this point, a detailed composition analysis study was required.

II.6 Composition analysis

The identification of the microscopic mechanisms controlling the kinetics of phase transformation requires an accurate description of the behavior of the various chemical elements. In order to discriminate between displacive and diffusive mechanisms, we have to consider both the growth kinetics and the possible partitioning of the elements. For that purpose, a chemical composition analysis, both in the various phases and across the interphases has been carried out.

II.6.1 Composition analysis of α and β grain and profile at the α/β interface

In partially transformed sample, composition analysis of the α and β phases were carried out for the identified morphologies. Table 3 summarizes the composition measured after different heat treatment starting from α sample of different compositions.

System	Phase Morphology	T (°C)	α	β	Ni ₃ S ₄
NiS	Globular	300	49.97±0.09	50.09 ±0.09	-
	Lamellar	200	50.9 ±0.14	50.04 ±0.07	-
		260	50.75±0.08	50.07±0.13	
	Block	300	51.46 ±0.37 (*) 50.63±0.15	50.19 ±0.16	-
NiFeS	Lamellar	200	50.47 ±0.09 0.42 ±0.01(**)	50.06 ±0.09 0.49 ±0.09(**)	55.47 0.57(**)

(*) near α/β interface or in small α phase island between transformed β zones; (**) Fe impurities

Table 3: Compositions analysis by EPMA of α , β and Ni₃S₄ phases (Composition in at%S). α and β have the same composition only in globular morphology. Iron containing sample shows that Fe is soluble in β and Ni₃S₄ phases.

We note that for the globular morphology the α and β phases have the same compositions. In other words, the transformation is done without Sulphur partition between phases. Since the transformation is not instantaneous, this confirms the massive mechanism earlier proposed for this transformation in section II.4.1.

For the other morphologies, α and β phases present different compositions. This indicates that the transformation is done with Sulphur partition between α and β and is then controlled by a diffusive mechanism. We note that the composition of the α phase near α/β interface or in small α phase islands between transformed β zones, is richer in Sulphur than in the non-transformed zones (Table 3). This local enrichment of the α phase can be due to the Sulphur partition between α and β which has not been yet homogenized by diffusion. Composition profiles reported below will examine in more detail the behavior at the interface. Such composition profile will be useful to draw conclusion concerning partitioned or partitionless mechanism as well as on the local equilibrium state of the transformation.

It is worth noting that, regarding the effect of the Fe content, one can wonder whether Fe iron is localized preferentially in one phase. The analysis reported in Table 3 shows that Fe is soluble in the α and β -NiS phase and even more soluble in Ni₃S₄ phase.

Composition profiles were recorded on globular lamellar and block morphology using EPMA with 2 μ m step analysis. Figure 20 shows a composition profile corresponding to globular morphology. Small

II.6 Composition analysis

fluctuations in composition are observed inside the α and β phase grains. The mean values of composition inside α and β phases are the same which confirms a massive transformation for this morphology. According to Hillert [27, 28, 33], for massive transformation, a spike is expected at the interface because phase transformation occurs under equilibrium condition. If this equilibrium is not established totally, it should occur locally at interface. However, the width of the spike being of the order D/v due to the large growth rate of this transformation, the spike should here extend only a few atomic distances. However this spike which is theoretically predicted has never been observed. In addition, since the composition profile in Figure 20 are taken with $2\ \mu\text{m}$ step, such a spike would never be observed.

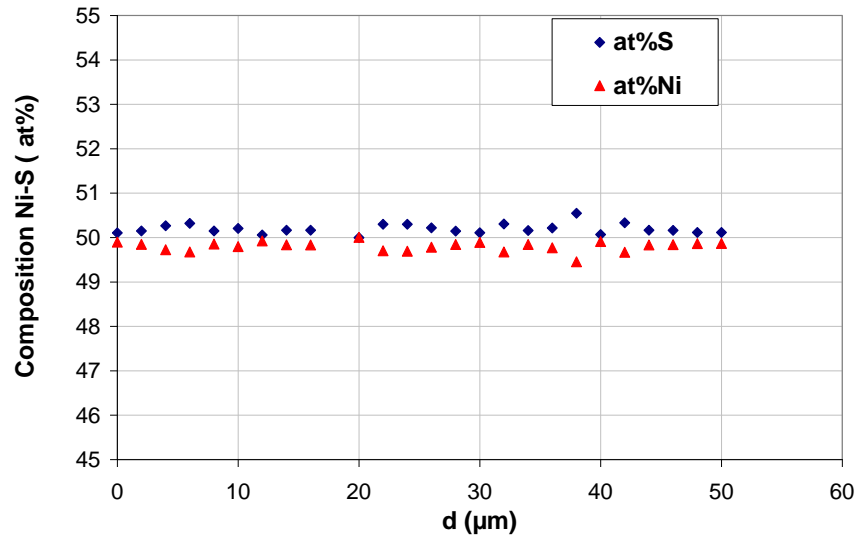
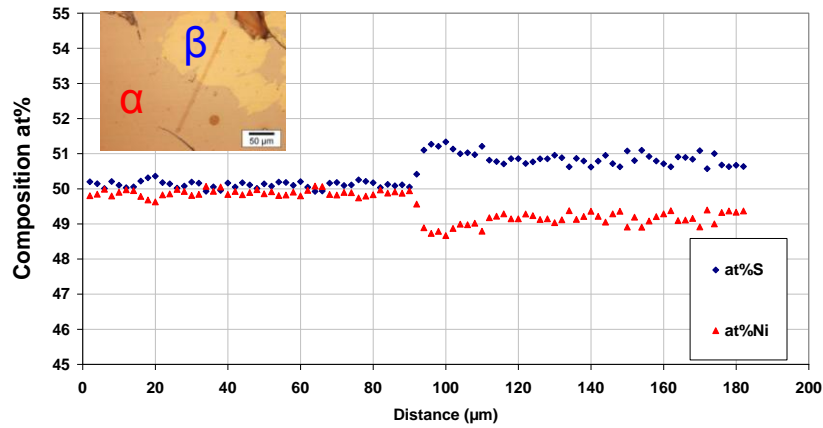


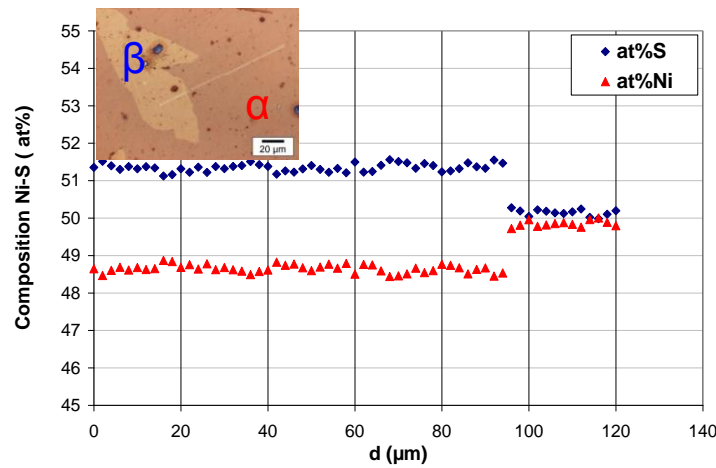
Figure 20: Composition profile at α/β interface for globular morphology: constant profile confirms partitionless transformation. Composition analysis performed by EPMA with $2\ \mu\text{m}$ step. ($\text{Ni}_{49.87}\text{S}_{50.13}$ 2min 200°C)

Figure 21 shows composition profile corresponding to lamellar and block morphology. The composition profile in Figure 21a shows a Sulphur enrichment on a range of about $20\ \mu\text{m}$ in the α phase. This indicates that the final product of the transformation is not at equilibrium. In addition, a $20\ \mu\text{m}$ diffusion length is observed which is quite large in comparison with the $80\ \mu\text{m}$ thickness of the β phase grain. This implies that the transformation leading to the lamellar morphology has required long range diffusion.

For the block morphology, the profile in Figure 21b shows different composition for the α and β phases but a constant profile within each grain. The composition difference means that the mechanism must be a diffusive one. The constant profile in the α phase indicates that the equilibrium state has been reached. Therefore, even if the mechanism is diffusive, no diffusion profile can be observed.



(a) $\text{Ni}_{49.13}\text{S}_{50.87}$ 20 min at 260°C



(b) $\text{Ni}_{48.72}\text{S}_{51.28}$ 750 min at 290°C

Figure 21: Composition profile at α/β interface for lamellar and block morphology (a) lamellar morphology: smooth profile confirms partitioned transformation (b) constant profile signature of equilibrium state. Composition analysis performed by EPMA with $2\mu\text{m}$ step.

II.6.2 Composition analysis of β phase and post-transformation with precipitation of Ni_3S_4

We note that the compositions of the β phase (Table 3) are slightly lower (about 0.3 at % in S) than those predicted by phase diagram. This could be due first to the limited precision of EPMA analysis, or to inaccuracy of the phase diagram. However, observations made in a near stoichiometric sample can provide another explanation. Figure 22 shows SEM FEG micrographs of the globular morphology developed in a near stoichiometric sample $\text{Ni}_{49.87}\text{S}_{50.13}$ heat treated at 200°C for 5 min. This micrograph reveals β zones grains separated by lines of Ni_3S_4 fine precipitates. According to the phase diagram, during the isothermal plateau, the sample was in the β phase field in which the precipitation of Ni_3S_4 phase could not take place. It is thus highly possible that precipitation has occurred during cooling after the isothermal plateau. Such post-transformation precipitation could

II.7 Fine scale microstructure for the lamellar and globular morphology

explain why the compositions of the β phase measured after different heat treatments are different from those predicted by the phase diagram. Consequently, though the β phase domain is slightly larger at high temperature than at low temperatures, it will be difficult to measure the composition of the β phase in the high temperature domain in order to test for the mechanism signature.

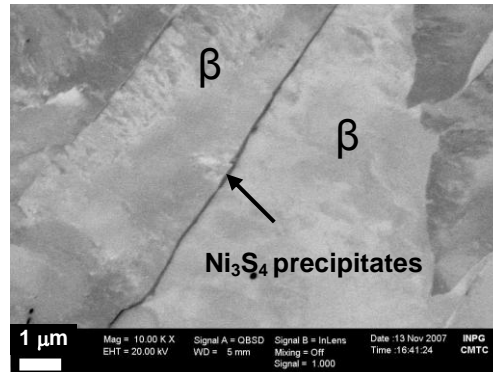


Figure 22: SEM observation of globular morphology in near stoichiometric sample (Ni_{49.87}S_{50.13} 200°C – 5 min) showing precipitation of Ni₃S₄ probably due to a post-transformation mechanism.

II.7 Fine scale microstructure for the lamellar and globular morphology

Optical microscopy has given a lot of information of the growth regime. In order to get some information about the nucleation stage, a fine scale investigation has been carried out only on the lamellar and globular morphology case, mainly by FEG SEM and TEM. The block morphology which shows rather coarse features appears quite unsuitable for such a fine scale study.

II.7.1 Early stages

Figure 23 (a) shows a FEG SEM image of the globular morphology at high magnification. The β grains have acicular shape. They are homogeneously distributed inside the grain and exhibit a remarkably wide range of size. Small grains (~ 50nm thick; 200nm length) coexist with large grains (up to 100 μ m). It means that, in one state, early stage are present together with advanced one. Consequently, even in the 60% transformed state (for instance the near stoichiometric sample Ni_{49.87}S_{50.13} heat treated 5 min at 200°C in Figure 23a), when looking closely, one can get information on the nucleation stage. It emerges that very small β grains present in the α grain indicate homogeneous nucleation (Figure 23a). In addition, examination of the grain boundary (Figure 23b and c) reveals small β phase grains spaced at about 100 nm and regularly nucleated along the boundary between two α grains. These precipitates reflect the anisotropic morphology of the β phase (~200nm for greatest dimension and 50 nm for smallest dimension). As indicated by the dotted line in Figure 23 b and c, the direction of β phase precipitates correspond to the α/β interface of larger β phase grains. We also note that the nuclei grow only on one side of the grain boundary.

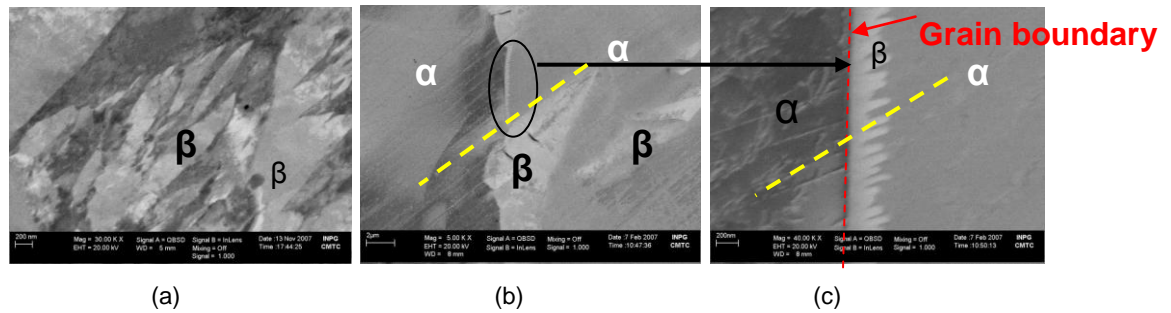


Figure 23 : Morphology of early stages (SEM FEG): a) Acicular nuclei with homogeneous distribution inside the α grain; the smallest is $\sim 50\text{nm}$ thick - 200nm length (5 min at 200°C of $\text{Ni}_{49.87}\text{S}_{50.13}$) (b) grain boundary nucleation: Nanometric grains of β phase distant of about 100 nm and regularly dispersed along a α grain boundary. Their growth occurs only on one side of the grain boundary ($\text{Ni}_{48.86}\text{S}_{51.14}$, 30 min, partially transformed $f \sim 10\%$).

II.7.2 β fine structure in lamellar morphology

The study of the α/β interface is of interest for the understanding of the transformation kinetics. However, a detailed study requires one to have edge-on interfaces and is therefore accessible only for the lamellar morphology. Figure 24a shows a FEG-SEM image of the α/β interface. The high magnification image in Figure 24c shows that the α/β interface is not straight but contains ledges ($\sim 200\text{nm}$ large and $\sim 20\text{nm}$ high). These ledges are decorated by a fine dark line. Complementary XRD diffraction analyses having revealed the presence of Ni_3S_4 phase, these dark lines are interpreted by the precipitation of Ni_3S_4 at the interface. EBSD (Figure 24b) carried out on the lamella has indicated that the interface is parallel to the α basal plane and to (010) plane in β phase. TEM investigation of the β lamella (Figure 24d) showed that, in the lamella state, β grain is formed of small and parallel plates of about 50nm thickness. According to the diffraction pattern indexation (Figure 24d), the β thin plates are parallel to the prismatic planes (1-100) and present twinning. A high resolution image (Figure 24e) shows that the ledges are characterized by two scales: steps of about 20nm thick consistent with FEG SEM observation and numerous small kinks of about few atomic planes in height. It could be noted that the contrast on the TEM image in Figure 24d is typical of small disorientations and strains between the β fine plates. Such disorientations provide an explanation for the slightly striated crystalline contrast of the β plates observed in FEG SEM (Figure 24a).

II.8 Summary and discussion:

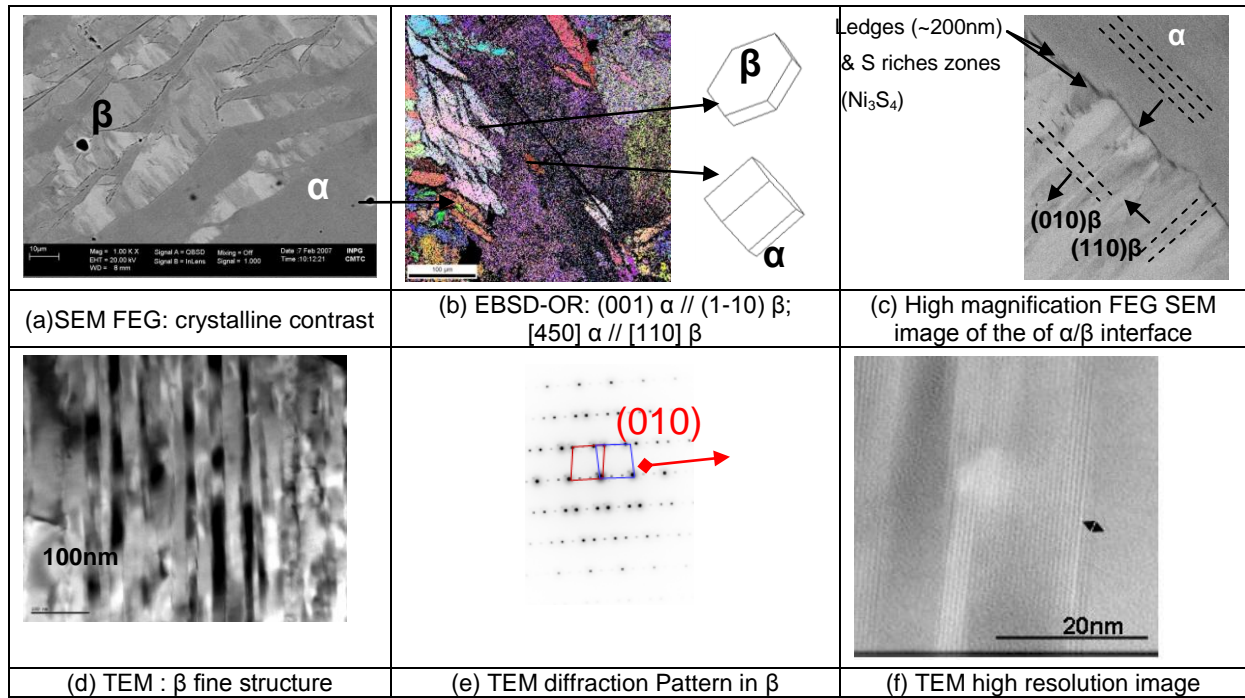


Figure 24: β fine microstructure and α/β interface characterization obtained by combining SEM FEG, EBSD and TEM observations.

II.8 Summary and discussion:

The $\alpha \rightarrow \beta$ -NiS phase transformation was studied for samples with different overstoichiometry of the α phase and for the temperature range from 200 \rightarrow 300°C. It was shown that, according to temperature and initial α -NiS composition, 4 main morphologies (or 5 taking in account sub morphologies for the lamellae case) can be identified as characteristic of the $\alpha \rightarrow \beta$ phase transformation:

- Globular morphology in the β phase field i.e. for lower overstoichiometric α -phase.
- Lamellar morphology with precipitation of Ni_3S_4 phase at α/β interface in the $\beta + \text{Ni}_3\text{S}_4$ phase field, and for overstoichiometric α -phase up to 51.14at%S.
- Lamellar morphology without precipitation of Ni_3S_4 phase at α/β interface, in the $\beta + \alpha$ phase field, and for middle overstoichiometric α -phase.
- Coarse lamellar morphology with precipitation of Ni_3S_4 phase at α/β interface, in the $\beta + \text{Ni}_3\text{S}_4$ phase field, and for high overstoichiometry >51.28at%S and for $T > 260^\circ\text{C}$
- Block morphology without precipitation of Ni_3S_4 , in the $\beta + \alpha$ phase field and for highly overstoichiometric α -phase 51.28at%S.

As the characteristic morphologies are often specific of some phase field of the NiS phase diagram, they are presented in Figure 25 below, together with the phase diagram, by typical micrographs reported in a (T, composition) sketch.

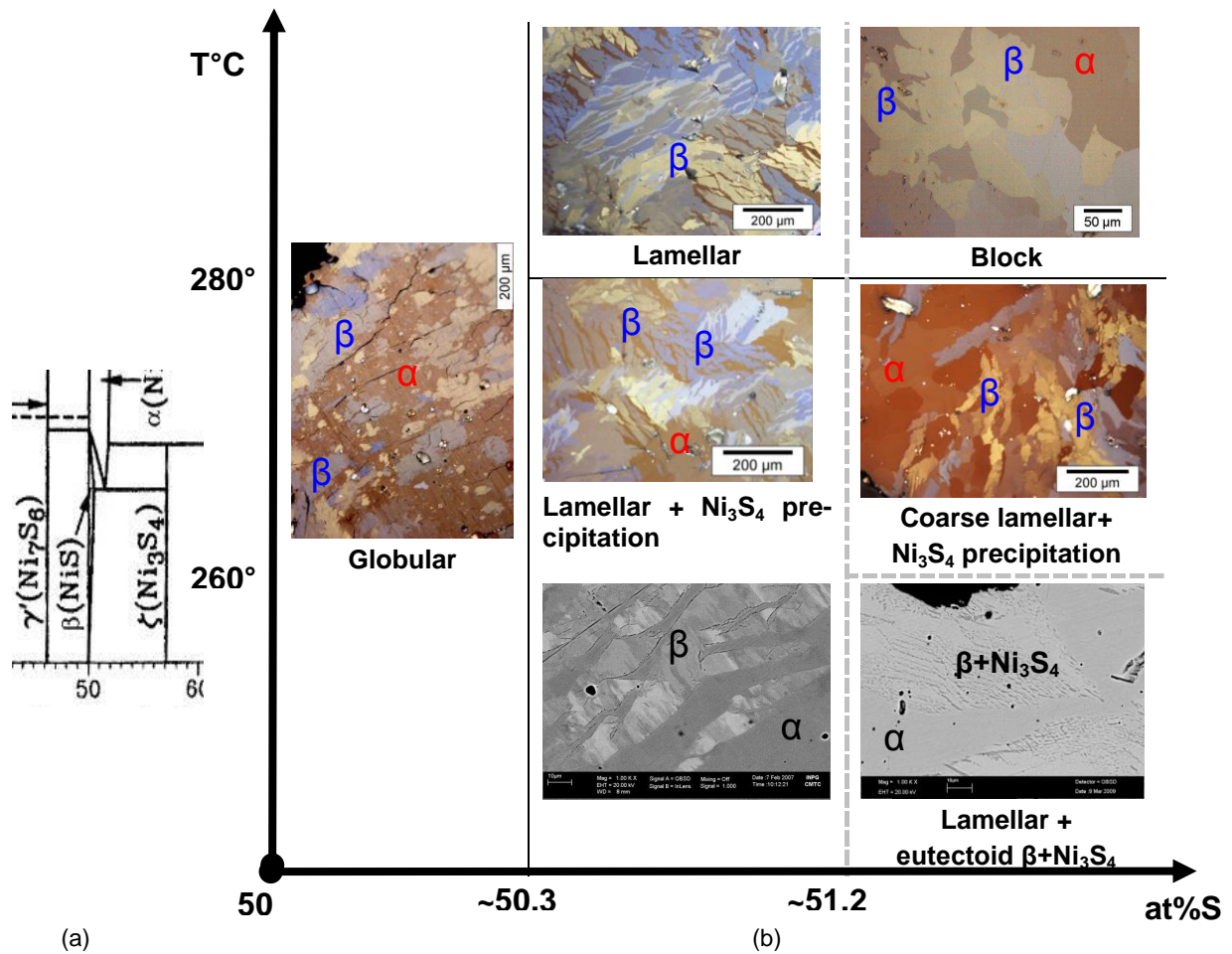


Figure 25 : (a) Ni – S phase diagram after Nash.P *et al* (1991)[22]. (b) Typical morphologies of the phase transformation observed in the different field of the phase diagram for temperature from 200-300°C and composition from 50 to 51.28at%S.

The effect of Sulphur composition on microstructural aspect of transformation can be summarized by the following points. First, for $T < 280^\circ\text{C}$ increasing Sulphur composition leads to Ni_3S_4 precipitation at the α/β -NiS interface and to an increase of their size and volume fraction. Second, when increasing overstoichiometry, the morphology changes from globular to lamellar and then to coarse lamellar morphology for $T = 260^\circ\text{C}$ or to eutectoid $\beta + \text{Ni}_3\text{S}_4$ lamella for $T = 200^\circ\text{C}$. Finally, increasing the Sulphur content reduces the nucleation rate.

Regarding the temperature effect, it was observed that, for near stoichiometric sample, the increase of temperature accelerates the transformation but the microstructure maintains the same aspect i.e. globular. In the $\beta + \text{Ni}_3\text{S}_4$ phase field, increasing the temperature leads to a decrease of the Ni_3S_4 volume fraction. For stoichiometry $< 51.14\text{at}\%\text{S}$, the morphology keeps the same aspect as at low temperature (i.e. 200°C). But for overstoichiometry $> 51.28\text{at}\%\text{S}$, the morphology turns to a coarse lamella one with a change in crystallographic aspect.

II.8 Summary and discussion:

II.8.1 Parallels with phase transformations in the Fe-C system

The variety of morphologies characteristic of the phase transformation in the NiS system reminds one of those observed in the classical Fe-C one. Indeed, the parallel between Ni-S and other common systems could help to identify common parameters in order to model $\alpha \rightarrow \beta$ phase transformation kinetic as Fe-C system which is one of the most studied from the experimental point of view as well as modelling. In addition the Ni-S phase diagram near the stoichiometric composition is very similar to the Fe-C one.

The most evident analogy between NiS and Fe-C system is illustrated by the globular morphology in Ni-S and the massive morphology in Fe-C. Figure 26a shows an example of massive morphology in Fe-C system. The main common points are the irregular shape of the second phase grains and the evidence of homogeneous nucleation.

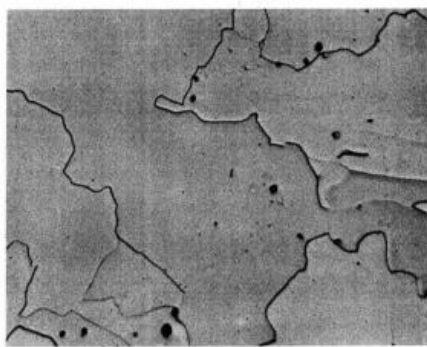
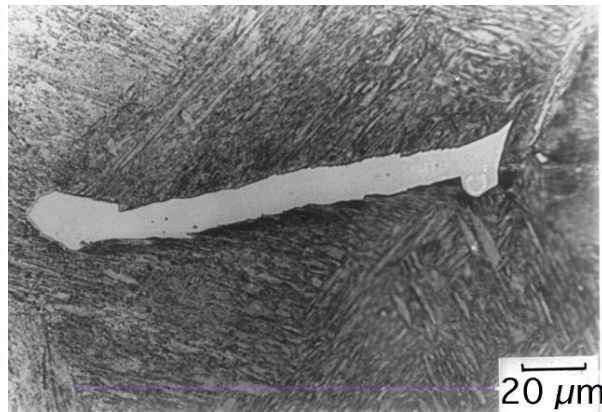


Fig. 5.80 Massive α in an Fe-0.002 wt% C quenched into iced brine from 1000 °C. Note the irregular α/α boundaries. (After T.B. Massalski in *Metals Handbook*, 8th edn., Vol. 8, American Society for Metals, 1973, p. 186.)

(a) Massive [34]



(b) allotriomorphic ferrite in Fe-0.5W-0.23C wt% [35]

Figure 26 : Example of massive and allotriomorphic morphology observed in Fe-C system

On the other hand, the coarse lamellar and block morphologies remind one of the allotriomorphic morphology in Fe-C system (Figure 26b). In both cases, the phase transformation is slow and the second phase shows no specific orientation relationship with the mother phase. The excess of solute is rejected at the interface and, depending on composition, could lead to the precipitation of Ni_3S_4 or Fe_3C .

Regarding the lamellar morphology, quite an analogy can be found with the upper bainite morphology in Fe-C system. Both transformations seem to result from similar elementary mechanisms which are schematically presented in Figure 27.

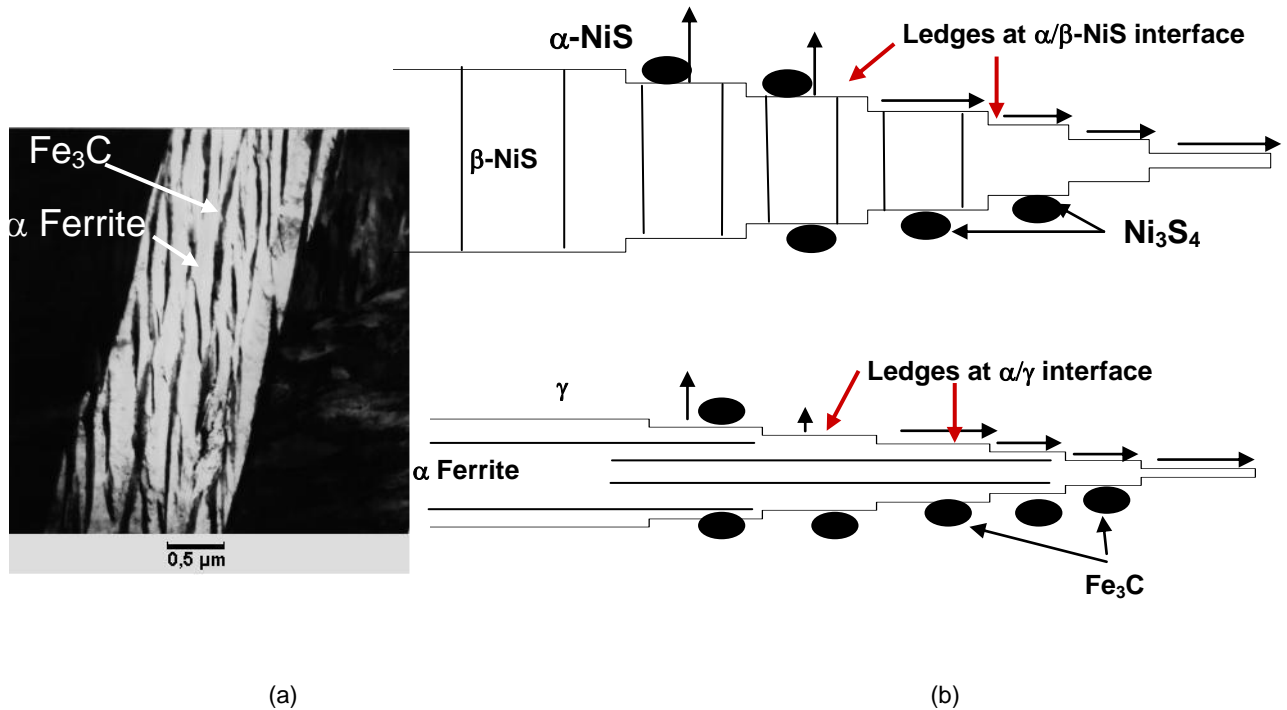


Figure 27: (a) Upper bainite in Fe-C system, (b) Schematic representation of lamellar and upper bainite morphology in the Ni-S and Fe-C system showing the strong analogy between these morphologies.

The main obvious analogy, between these morphologies, is the development of β plates with Ni_3S_4 precipitation at α/β interface similar to the growth of α ferrite plates with Fe_3C precipitation at the α/γ interface. This lamella morphology is consistent with very different growth rates in the two directions which are responsible in both cases for marked anisotropic shape. In both NiS and FeC, we note that the β lamella and the ferrite lamella grow as plates parallel to the dense plane of the mother phase (respectively the basal plane of the α phase and the (111) plane in the austenite).

A more complete comparison between Ni-S and Fe-C system is summarized in Table 4 which gives similarities and differences between globular, lamellar, block, coarse lamellar and eutectoid morphology of Ni-S system and their equivalent in the Fe-C system.

II.8 Summary and discussion:

NiS	FeC
Globular $\alpha \rightarrow \beta$	Massive $\gamma \rightarrow \alpha$
<ul style="list-style-type: none"> -Relatively rapid -Homogeneous nucleation -Irregular phase joint -Coherent interface. -OR for growth regime -No β phase formation during quenching. 	<ul style="list-style-type: none"> -Rapid -Homogeneous nucleation -Irregular phase -Occurs during quenching and at isothermal heat treatment.
Fine lamella $\alpha \rightarrow \beta + \text{Ni}_3\text{S}_4$	Upper-Bainite $\gamma \rightarrow \alpha + \text{Fe}_3\text{C}$
<ul style="list-style-type: none"> -β plates+Ni_3S_4 precipitation at α/β interface -Nucleation inside the grain and at the grain boundary -Anisotropic growth -Do not cross grain boundary. -Coherent interface. -Growth by ledges mechanism with OR between α and β 	<ul style="list-style-type: none"> -α-Ferrite plates + Fe_3C precipitation at α/γ interface -Anisotropic growth -Do not cross grain boundary. -Coherent interface. -Growth by ledges mechanism with OR between γ and α
Block $\alpha \rightarrow \beta$	Allotriomorphic ferrite $\gamma \rightarrow \alpha$
<ul style="list-style-type: none"> -Isotropic shape of β phase -Long range diffusion -No specific OR -Grain boundary and inside the grain nucleation 	<ul style="list-style-type: none"> -Isotropic shape of α phase -Long range diffusion -No specific OR -Grain boundary nucleation.
Coarse lamella $\alpha \rightarrow \beta (+\text{Ni}_3\text{S}_4)$	Allotriomorphic ferrite $\gamma \rightarrow \alpha (+\text{Fe}_3\text{C})$
<ul style="list-style-type: none"> -Slow kinetics -Irregular grain boundary -$\alpha \rightarrow \beta$ +excess Sulphur rejected in α leading to Ni_3S_4 precipitation at α/β interface -Grain boundary and inside the grain nucleation. 	<ul style="list-style-type: none"> -Slow kinetics -Irregular grain boundary -$\gamma \rightarrow \alpha$ +excess carbon rejected in austenite or Fe_3C precipitation at the γ/α interface. -No specific OR -Grain boundary nucleation.
Eutectoid lamella $\alpha \rightarrow \beta + \text{Ni}_3\text{S}_4$	Pearlitic $\gamma \rightarrow \alpha + \text{Fe}_3\text{C}$
<ul style="list-style-type: none"> -Lamellar $\beta + \text{Ni}_3\text{S}_4$ -Occurs in very overstoichiometric α phase 	<ul style="list-style-type: none"> -Lamellar $\alpha + \text{Fe}_3\text{C}$ -Occurs while cooling γ austenite below eutectoid plateau

Table 4: Comparison between phase transformation in the Ni-S and Fe-C system [20, 23, 24, 26, 27, 30, 31, 34-36]: similarities and differences are reported concerning mainly morphologies (shape, interface), orientation relationship (OR), nucleation and growth kinetic, each morphology in NiS has its equivalent in Fe-C system. This strong analogy gives bases for understanding of transformation mechanisms and further kinetic modelling of NiS phase transformation.

Chapitre II. Phase transformations in Nickel sulphide (NiS): microstructure and mechanisms

Table 4 shows striking similarities between the two systems Fe-C and Ni-S. Each morphology in NiS has its equivalent in Fe-C system. In the Fe-C system, phase transformation can be separated in partitioned and partition less transformation. The same description can be used for the Ni-S system: the globular morphology will correspond to massive or partitionless transformation and all other morphology correspond to diffusive or partitioned transformation. The concept of partitioned vs partitionless will be used in the following to devise kinetic models for the different morphologies of the phase transformation in the NiS system.

As in Fe-C system, in some cases, partitioned transformations progress in several steps with enrichment of the mother phase. As illustrated by Figure 28, small islands of α phase show a lamellar $\beta + \text{Ni}_3\text{S}_4$ morphology which corresponds to the end of transformation while the β lamellae correspond to the beginning of the transformation. It means that the phase transformation occurs in two steps: 1- the formation and growth of β plates with rejection of Sulphur in the α phase, 2- when the composition of the α phase reach the eutectoid composition $\beta + \text{Ni}_3\text{S}_4$ plates grow. According to the phase diagram, the volume fraction of the Ni_3S_4 is about 10% for the temperature range of interest here for application. Thus the main part of the transformed volume fraction is achieved during the first step which will be essentially considered in the following section.

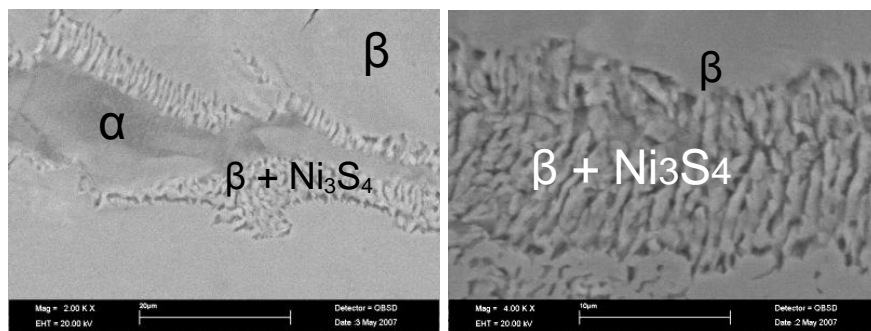


Figure 28 : eutectoid morphology with alternated $\beta + \text{Ni}_3\text{S}_4$ lamellar observed in α island and near α/β interface. ($\text{Ni}_{49.13}\text{S}_{50.87}$ heat treated at 200°C during 21 min (transformed fraction~15%)

II.8.2 From morphology to kinetic law

From experimental characterization of phase transformation, we concluded that two classes of mechanisms are involved in the $\alpha \rightarrow \beta$ phase transformation: a massive mechanism for the globular morphology and diffusive one for all other morphologies. The strong relation observed between morphology and mechanism will help to understand elementary mechanism and further model the kinetic of phase transformation. According to [20, 33-36], various microstructures can be accounted for by the occurrence of partitioned and partitionless transformation depending on composition and then by free energy considerations. Generally, in phase transformation, the system disposes of a quantity of free energy. This free energy will be dissipated during phase transformation in nucleation, interface motion and diffusion. The system tends to create morphology which minimize its free energy e.g. minimize the interface for a given volume (isotropic morphology).

Among partitionless transformation, the massive transformation occurs without long range diffusion as the second phase keeps the same composition of the mother phase. Thus, all of the free

II.8 Summary and discussion:

energy is dissipated in nucleation and interface motion. This favours homogenous nucleation and morphology of small scale. In addition, the growth kinetic along different direction being isotropic, the resulting morphology is globular. In general, there is no specific orientation relationship between phases but, in certain cases, orientation relationships have been observed [23, 31, 32]. For instance in the NiS system for the globular morphology, it was observed that the orientation relationship varies with the size of β grains. This can be interpreted in terms of preferential growth for particular orientation relations. In that case, nucleation may occur with several orientation relationships but during the growth regime, only grains with orientation energetically favoured or with a large interface mobility will develop. In other words, orientation relationship is not a critical aspect to identify the massive transformation. Indeed there is a good agreement between the characteristics expected for a partitionless transformation and the observations made on the globular morphology that we associated to a massive transformation. It was already established [20, 23, 34, 36] that, for massive transformations, the kinetic law is linear in time. This linear dependence being known, modelling the kinetic of the globular morphology requires then essentially to have the proportionality coefficient and the nucleation rate. Both can be determined with *in situ* observation of the phase transformation.

Regarding the lamellar morphologies, if the composition of the second phase is different from that of the mother phase, then a partitioned mechanism must have occurred. In that case, free energy is dissipated in diffusion, nucleation and creation and motion of interfaces. The nearer the composition of the mother phase to the composition of the second phase, the higher is the free energy of the transformation. Generally, the interface formation is limited during phase transformation as it costs a lot of free energy. However, when the transformation free energy is high, a morphology with high energy interfaces is allowed. In addition, in diffusive transformation with OR, the growth kinetics is frequently anisotropic. For instance, in overstoichiometric NiS samples, a lamellar morphology with orientation relationship between β and α grains is observed. Apparently, in these conditions, few nuclei have grown and, for this stoichiometry, the transformation free energy was high. This allows the development of morphology with large interface (lamellar) and high interface energy i.e. coherent interface. This morphology is more efficient for Sulphur evacuation inside the α phase which is consistent with the observation of lamellar morphology in the β +Ni₃S₄ and β + α phase field. It was already established [37-39] that for the lamellar morphology the kinetic law for lengthening is linear in time and for thickening it is quadratic in time [20, 35, 36, 40]. Hence, the dependence on time being known from the morphology, in the NiS case the modelling of the kinetics of the lamellar morphology requires essentially the proportionality coefficients describing interface motion, the nucleation rate and the interdiffusion coefficient in the α phase. Hence regarding some of the missing information required for modelling (nucleation rate and proportionality coefficients), as in the previous case, these can be determined with *in situ* observation of phase transformation. The interdiffusion coefficient could be measured using diffusion couple (Ni₃S₂/NiS).

Block and coarse lamellar morphologies are also produced by a partitioned transformation. The transformation free energy in these cases is lower as the composition is very overstoichiometric. As a consequence, the nucleation rate is expected to be low and low energy interfaces are preferred to the high energy one (coherent one). These energy considerations are consistent with the observation of an isotropic morphology of the β phase. For instance, in overstoichiometric NiS samples, coarse lamellar and block morphology are found, respectively, in the β +Ni₃S₄ and β + α phase field with no

Chapitre II. Phase transformations in Nickel sulphide (NiS): microstructure and mechanisms

specific OR between β grains and α phase. In addition, low energy interfaces are observed for the block and coarse lamellar morphology which confirm that crystallography does not play a significant part. Therefore, diffusion being the controlling mechanism, growth in all directions will follow a quadratic law. As mentioned previously, only the proportionality coefficient, the nucleation rate and the Sulphur coefficient in the α phase are required to model the kinetic law. They will be determined using *in situ* observation of phase transformation and using diffusion couple ($\text{Ni}_3\text{S}_2/\text{NiS}$) to measure the interdiffusion coefficient.

The thermodynamic analysis of phase transformation was successful in explaining the morphology of the second phase and in giving the basis of the modelling of the kinetic law of transformation. In the first step of the transformation, partitioning concern the α and β phase. At the end of the transformation, for overstoichiometric samples, the partitioning involves three phases α , β and Ni_3S_4 . Regarding the transformed volume fraction, the Ni_3S_4 precipitation step corresponds to a small volume fraction. In any case, the larger part of the volume change is due to β phase formation. Consequently modelling the transformation must be focused on the β phase formation.

Finally the microstructural study of NiS transformation and the parallel with Fe-C phase transformation gives some orientation in order to model the transformation kinetic law. First, it will be necessary to complete the experimental information on the kinetic law. This will be done with *in situ* studies of the transformation. Optical microscopy will be carried out to estimate the interface velocity, the nucleation rate and volume fraction evolution. However a calorimetric study will be also done to provide more global information on the evolution of the transformed volume fraction. In addition the DSC study will give a set of experimental information for comparison with modelling on the basis mentioned above. Regarding the interdiffusion coefficients, they will be measured with appropriate diffusion couples.

II.9 Conclusion:

This detailed qualitative investigation of the microstructural characteristics of the phase transformations in NiS was the first necessary step in order to identify the transformation mechanisms. Several morphologies have been identified using a combination of mainly microscopy techniques at different scales. From the typical morphologies, further confirmed by composition analysis, we have first been able to identify the existence of partitioned and partitionless phase transformation depending on the temperature and the initial α -NiS composition, i.e. the domain in the NiS phase diagram. More precisely a globular morphology for lower over stoichiometric α -phase was recognized as the signature of a massive transformation. Then, depending on composition and temperature, there are several morphologies corresponding to a partitioned (or diffusional) mechanism: i. a lamellar morphology for the highly overstoichiometric α -phase (50.55 -51.2at%S), the excess of Sulphur is rejected at α/β interface leading to significant Ni_3S_4 precipitation, i.i. a coarse lamellar morphology for very high overstoichiometry >51.2at%S characterized by $\beta + \text{Ni}_3\text{S}_4$ microstructures, i.i.i. Block morphology for very overstoichiometric composition and $T > 280^\circ\text{C}$.

Comparison between the phase transformation developed in Ni-S and Fe-C system shows many interesting similarities. The parallel between these two systems is very useful to identify the appropriate kinetic model developed in Fe-C system which will be relevant for the Ni-S one. Actually, it

II.9 Conclusion:

provides the main lines to follow to progress in the direction of modelling. For instance, it has appeared very fruitful to separate the partitioned and partitionless mechanisms, as frequently done for the Fe-C since each one leads to a specific time dependence of the growth law (linear for partitionless, quadratic for a diffusion control). From this discussion, based on the mechanisms, it develops out that to devise a modelling of the phase transformation, once the time dependence is known, quantities like the nucleation rate, the interface velocity etc remain to be determined. The point is that *in situ* observation of the transformation is able to provide this information. However, for the quantification of diffusion controlled growth, one is obliged to have a measurement or at least a reasonable estimation of the interdiffusion coefficient. It is also worth mentioning that the present study has made significant use of an earlier established phase diagram which seems globally correct but may need to be tested at some point. Therefore, the next step will be to carry out a detailed DSC study to examine the validity of phase diagram and to gather data on the evolution of the transformed volume fraction which will be of interest for comparison with the modelled kinetic law. In parallel, it will be necessary to make diffusion couples and obtain as much information as possible on interdiffusion in NiS. Finally, *in situ* observation of the phase transformation will be the last experimental step before starting to build the models to account for the transformation kinetic laws in the relevant composition and temperature domains.

Chapitre III. Calorimetric study of phase transformations in Nickel sulphide (NiS)

III.1 Introduction:

The microstructural study of the $\alpha \rightarrow \beta$ -NiS phase transformation reported in the previous chapter for isothermal heat treatment, has shown that the phase transformation occurs according to thermally activated mechanisms such as partitionless massive or diffusion controlled partitioning transformations ones. The study of NiS phase transformations, around the stoichiometric composition, and for the temperature range 170-300°C, have pointed out that several microstructural aspects of phase transformations (example: Ni₃S₄ precipitation, partial transformation for overstoichiometric sample and for T>280°C) are in a good agreement with the Ni-S phase diagram. Nevertheless, the measured Sulphur composition of the β phase does not change with temperature contrary to what would be expected from the phase diagram. This disagreement with the phase diagram predictions can be attributed to post-transformation precipitation of the Ni₃S₄ phase as proposed in previous chapter. However such an interpretation raises the very question of the validity of the published phase diagram itself.

The Ni-S phase diagram has been established mainly after three studies [9, 22, 41]. In our domain of interest, no detailed microstructural characterization of phase transformation was carried out to cross check the statements made concerning equilibrium conditions. Hence the first objective of the calorimetric study presented here will be to assess the validity of the NiS phase diagram and in particular to clarify the deviation of the composition of the β phase. This validation will be done through a detailed study of peak positions and of the evolution of their area depending on composition and temperature.

Chapitre III. Calorimetric study of phase transformations in Nickel sulphide (NiS)

The second objective is to obtain quantitative information on the time evolution of the transformed volume fraction. The microstructural study presented in the previous chapter has already provided information on the morphological aspects and the possible mechanisms controlling the phase transformations. Modelling the kinetic law requires experimental data at the macroscopic level concerning the evolution of the transformed volume fraction $F_v(t)$, as a function of temperature and composition. We have observed that, in a given sample, the $\alpha \rightarrow \beta$ phase transformation shows different stages of advancement in different locations, and that this is more and more prominent when the overstoichiometry is increased. This motivates one then to use the DSC method in order to follow the global evolution of the transformed volume fraction (F_v).

The DSC investigation was achieved through isothermal and non isothermal heat treatment. The methods of analysis of the DSC results used here are standard in physical metallurgy, but had never been applied to the transformation of NiS, which is more familiar to the culture of glass-makers. First a qualitative description will be given by a study of the transformation behavior at various heating rate and for different compositions. Second, a quantitative study based on the isothermal heat treatment allows one to build the Time Temperature Transformation (TTT) diagram. This diagram allows the gathering and synthesizing of all the kinetic information on the same graph. A TTT diagram describes quantitatively the advancement of the transformation in a given time as function of temperature. The effect of overstoichiometry and Fe impurities on the TTT curve will be also studied. After that isothermal DSC curves are analyzed using Johnson Mehl Avrami Kolmogorov (JMAK) model. This provides a determination of the Avrami exponent which can give an indication on the active transformation mechanism.

The calorimetric study of the $\alpha \rightarrow \beta$ -NiS phase transformation on isothermal and non isothermal heat treatment has been already investigated by several authors [3, 7, 8, 15-19]. The non-isothermal studies [3, 7, 10, 12, 13, 15-17, 42] documented the slowing down of the transformation with increasing overstoichiometry and Fe content. All these conclusions were drawn from a purely macroscopic point of view, i.e. analyzing the thermograms, without being supported by a microstructural study of the transformation. In addition the few DSC study [13, 16, 17] claiming a relation with transformation mechanism were carried out essentially on near stoichiometric samples. Therefore the overstoichiometry effect on isothermal and non isothermal heat treatment still has to be investigated.

In the present work, the study of the heating rate effect on the transformation kinetics has been carried out from 25°C to 450°C at several heating rates (1 to 32°C/min) and for different compositions (50.13at%S to 51.28at%S) and iron contents (up to 50.5at%S and 0.6at%Fe). The temperature field is chosen to be 25°C \rightarrow 450°C because in this domain occur the $\alpha \rightarrow \beta$ transformation and the inverse $\beta \rightarrow \alpha$ one. As for the microstructural study of the transformation presented in the previous chapter, the isothermal study concerns the temperature range from 170°C to 300°C and for different overstoichiometry. These conditions allow one to test different fields of the phase diagram around the NiS stoichiometry (domain: β , β +Ni₃S₄ and α + β in the diagram Figure 25a).

III.2 Materials and methods:

III.2.1 Materials

In order to obtain a consistent picture of the transformations and to benefit from previous microstructural observations, the same samples used in the previous microstructural study were studied by DSC in the present work. Some additional samples with different compositions were added for the sake of completeness. Only one NiS (50.4at%S) sample which is monocrystalline was obtained from a different process. Bulk sample, of the hexagonal α -NiS phase, weighting 20 g, was prepared for each composition. The nature of the phases present in the sample and their homogeneity were monitored with X-Ray diffraction and SEM observations. Composition analyses were performed with electron microprobe analysis (EMPA). The results are summarized in Figure 29b:

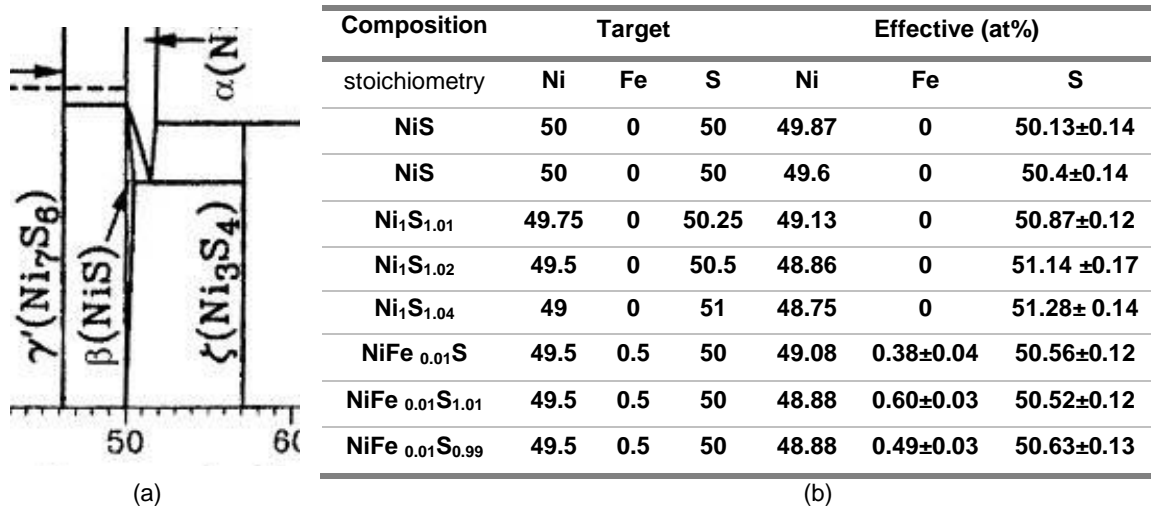


Figure 29: (a) Ni – S phase diagram after Nash.P et al (1991)[22].

Around stoichiometric composition 4 phases exist: α & β -NiS, Ni_3S_4 and Ni_7S_6 . Ni_7S_6 and Ni_3S_4 are stoichiometric compounds as well as β -NiS for low temperatures. But β field presents some over-stoichiometry at high temperature (~0.4at %). α -NiS presents a composition field from 50 to 52 at%S for $T > 400^\circ\text{C}$.

(b) Samples: difference between aimed and real composition of α -NiS (Measured by Castaing micro-probe). The effective composition is considered as reference for different samples.

III.2.2 Heat treatments and measurement cycles

Calorimetric investigation of the transformation was carried out using different isothermal and non isothermal heat treatments. The non isothermal DSC study allows one to identify the calorimetric signature of NiS transformations during heating. According to the phase diagram, the α phase is stable for temperature above 380°C for stoichiometric sample and above 280°C for overstoichiometric samples (51.5at%S). That is why the non-isothermal study was done in the temperature range 25°C to 450°C.

For a given composition, the effect of the heating rate on the thermogram was studied. Efficient comparison requires that these heat treatments with different heating rates are carried out on samples with the same composition. Since sample composition (Figure 29b) shows fluctuations of about 0.14 at%, it is more appropriate to use the same α sample for the different heat treatments. Thus, during the DSC study, the α phase was regenerated using a thermal cycle referred to here as a “ α regenerating step”. This cycle is composed by a heating at 8°Cmin⁻¹ from 25°C until 450°C follows by an isothermal stage at this temperature during 20 min and finishes with a rapid cooling (100°Cmin⁻¹) to 25°C which allows to quench the α phase. After that a measurement cycle can be done under isothermal conditions. During the measurement cycle, the transformation $\alpha \rightarrow \beta$ occurred and during the regeneration cycle the sample was completely transformed back into the α phase. Figure 30 gives a sketch of the thermal cycles alternating measurement sequences and α regeneration cycles.

For isothermal study, the measurement cycle (Figure 30) consisted of an isothermal step during which the $\alpha \rightarrow \beta + \text{Ni}_3\text{S}_4$ transformation occurred. The α sample was rapidly heated (~300°C/min) to high temperature (200-300°C) and held at this temperature. After that the sample was quenched (~100°C/min) to room temperature in order to retain the microstructural state obtained at the end of the high temperature isothermal treatment. The heating and cooling rate, before and after isothermal steps, were chosen to avoid transformation during these steps (maximum of DSC heating rate and cooling rate were here used). After quenching, the α regenerating step was carried out. These “measurement sequence -regeneration steps” were repeated to study the transformation at different temperatures.

Regarding the non-isothermal study, the measurement cycle consisted of heating from 25°C to 450°C, with heating rates between 1 and 32°C/min. During this heating, the quenched α phase first decomposed to $\beta + \text{Ni}_3\text{S}_4$, which itself transformed to α when the temperature was increased. It is worth noticing that the DSC curves recorded during the α regenerating step, which follows isothermal steps, corresponds the $\beta + \text{Ni}_3\text{S}_4 \rightarrow \alpha$ transformation. The comparative analysis of the $\beta + \text{Ni}_3\text{S}_4 \rightarrow \alpha$ peak following different isothermal treatments served as a good indicator of the state of the transformation at the end of the isotherms.

For all these experiments, we have used a Diamond DSC-Perkin Elmer equipment under Argon flow (20mm³/min). NiS Samples were put in aluminium pans and placed in the sample compartment using an empty pan as the reference. In this study DSC calibration curve was made for 8°C/min heating rate using indium and zinc as the standard.

III.3 The α (β -NiS transformation and phase diagram validation

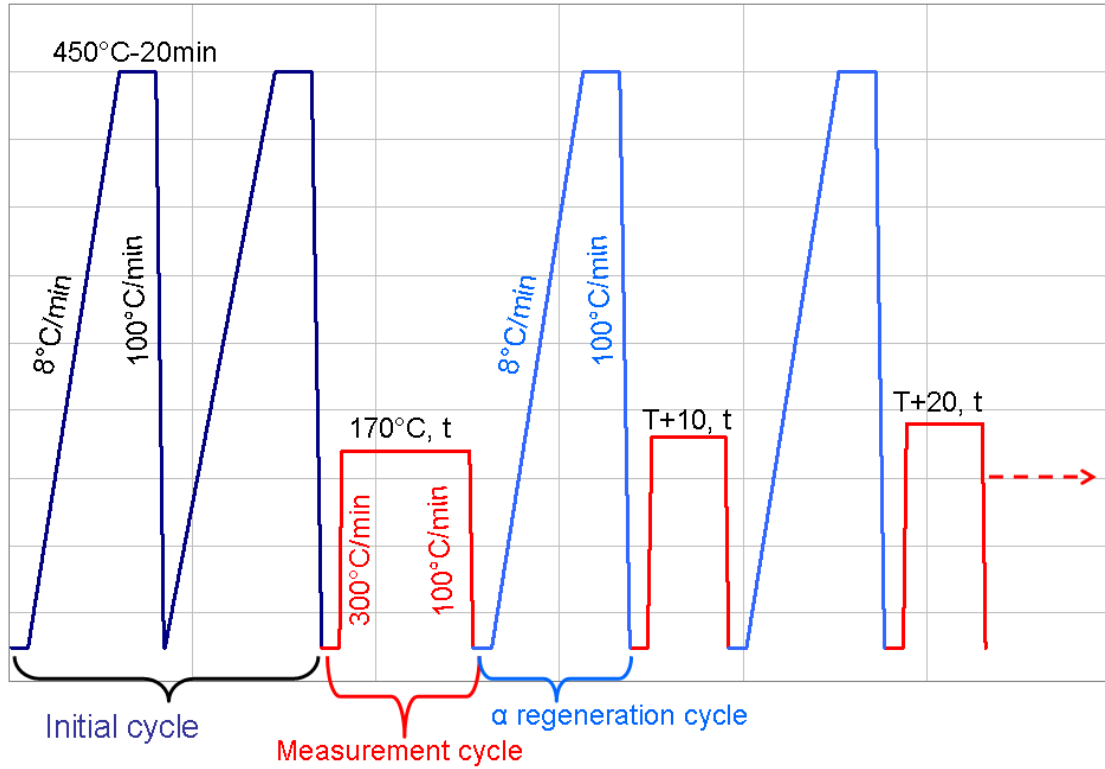


Figure 30: Thermal cycle used in DSC during isothermal study: plateau temperature varies between 170°C and 300°C.

III.3 The $\alpha \rightarrow \beta$ -NiS transformation and phase diagram validation

III.3.1 DSC signature during non isothermal heat treatment

Figure 31 shows DSC curves recorded during heating at 2°C/min from 25 to 450°C on two samples with different overstoichiometry. At such a low heating rate, the transformation sequence should be close to equilibrium path. For low overstoichiometric sample, the DSC curves (in red in Figure 31) display two peaks. XRD characterization on samples quenched after each peak confirms that these peaks correspond respectively to α -NiS \rightarrow β -NiS transformation for the exothermic peak (199°C) and to β -NiS \rightarrow α -NiS inverse transformation for the endothermic peak (395°C). These features were already observed in previous studies [3, 10, 16, 17] and are consistent with the phase diagram. For very overstoichiometric sample (curve in blue in Figure 31), the peak position is shifted to high temperature for the first transformation (around 250°C) and to the low temperature for the second one (around 380°C). In addition, the DSC curve displays a second endothermic peak.

Chapitre III. Calorimetric study of phase transformations in Nickel sulphide (NiS)

It was already established, from the microstructural study, that depending on the initial composition of α phase, the transformation $\alpha \rightarrow \beta$ occurs for low overstoichiometry while $\alpha \rightarrow \beta + \text{Ni}_3\text{S}_4$ occurs for high overstoichiometry. A sample quenched during the transformation at the maximum of this new endothermic peak was analyzed by X-ray diffraction, which indicated the coexistence of three phases α -NiS, β -NiS and Ni_3S_4 . Therefore the new endothermic peak should be related to the precipitation of the Ni_3S_4 phase. According to the Ni-S phase diagram, three transformations occur upon heating from 25°C to 450°C for overstoichiometric sample: $\alpha \rightarrow \beta + \text{Ni}_3\text{S}_4$ till the eutectoid plateau, followed by the $\beta + \text{Ni}_3\text{S}_4 \rightarrow \alpha$ transformation at the eutectoid plateau. In the latter case, a part of β phase reacts with Ni_3S_4 to form α phase. Above the eutectoid plateau, the $\beta \rightarrow \alpha$ transformation will take place. As shown previously the first and third peaks on DSC curve, correspond respectively to the $\alpha \rightarrow \beta + \text{Ni}_3\text{S}_4$ and to the $\beta \rightarrow \alpha$ inverse transformation. Thus the new endothermic peak corresponds to the $\beta + \text{Ni}_3\text{S}_4 \rightarrow \alpha$ transformation which is consistent with the presence of the eutectoid plateau in the Ni-S phase diagram.

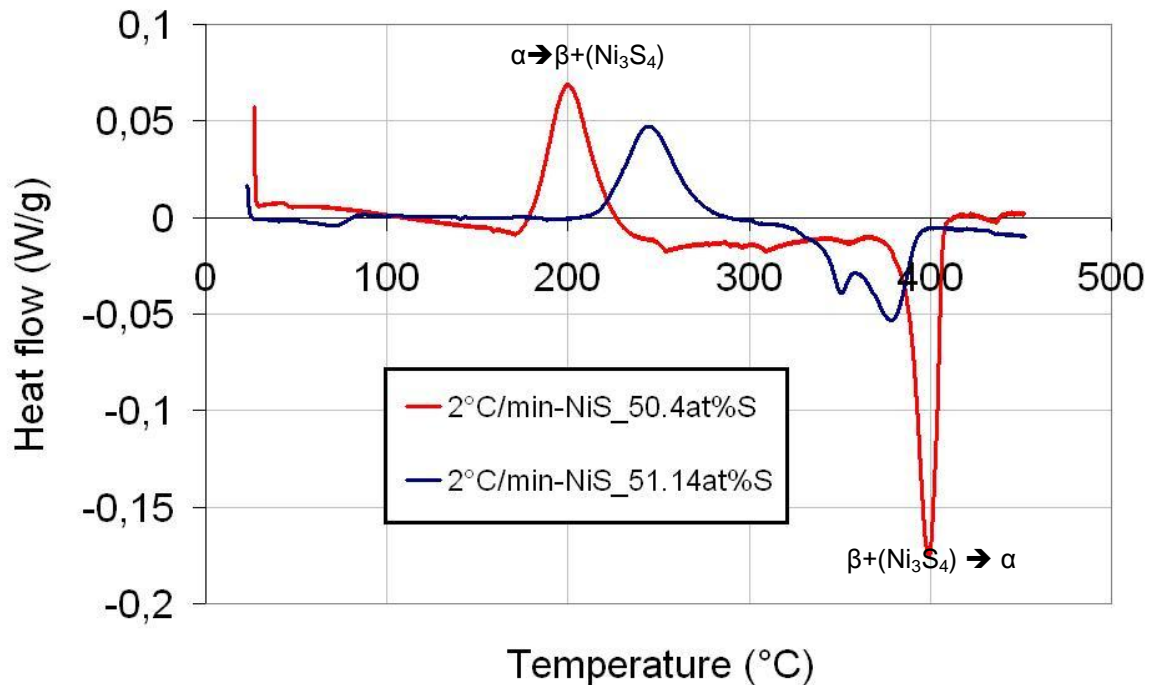


Figure 31 : DSC (heat flow=f(T)) obtained during heating rate at 2°C/min between 25 and 450°C sample Ni_{49.6}S_{50.4}, and Ni_{48.86}S_{51.14}

III.3.2 β phase composition and evolution of the Ni_3S_4 volume fraction with temperature and α phase composition

The issue here was to check the accuracy of the equilibrium line $\beta/(\beta + \text{Ni}_3\text{S}_4)$. According to the published Ni-S phase diagram, this equilibrium line is curved. Hence the Sulphur content of the equilibrium β phase should increase for increasing temperature. However, as reported in the EMPA analysis (in the previous chapter), the Sulphur composition of the β phase measured after different

III.3 The α - β -NiS transformation and phase diagram validation

isothermal heat treatments shows a near stoichiometric composition even under changing heat treatment conditions. According to phase diagram, the Sulphur content of β phase is expected to be about 50.33 at% at 200°C and 50.45at% at 260°C while it was always measured to be around 50.1at% regardless of the heat treatment. In the previous microstructural study, it was proposed that this disagreement may result from a post transformation precipitation of the Ni_3S_4 phase. Thus before challenging the accuracy of the equilibrium line, it is necessary to first examine the post transformation precipitation.

We know from the calorimetric study (heating from 25°C to 450°C) that the first endothermic peak is a signature of the presence of the Ni_3S_4 phase. Therefore the possibility of a post transformation precipitation can be tested by a measurement cycle recorded after an isothermal step during which only the β phase is formed. For overstoichiometric composition, this is possible for isothermal heat treatment at temperatures above 280°C. Figure 32 shows the measurements (from 25°C to 450°C at 8°C/min) recorded after total transformation at 5 different temperatures on one overstoichiometric sample (50.87at%S). Two peaks, respectively related to $\beta + \text{Ni}_3\text{S}_4 \rightarrow \alpha$ and to $\beta \rightarrow \alpha$, are observed during the heating cycle for all temperatures (Figure 32). The presence of the first endothermic peak $\beta + \text{Ni}_3\text{S}_4 \rightarrow \alpha$, after the isotherm treatment at 280°C and 300°C, confirms the precipitation of the Ni_3S_4 phase. According to the published phase diagram, at this temperature only α and β phases could exist. Therefore the precipitation of Ni_3S_4 has not occurred during the isothermal step but during further cooling. According to the phase diagram, since the transformation is partial at high temperature, the precipitation could occur during the cooling in two ways: either the α phase transforms to $\beta + \text{Ni}_3\text{S}_4$ or the Ni_3S_4 forms from the β phase decomposition. For temperatures above 280°C, since the equilibrium α phase composition is very overstoichiometric (more than 51.33at%S), the kinetics being very slow, the transformation can not happen during cooling. In addition the peak area for $\beta + \text{Ni}_3\text{S}_4 \rightarrow \alpha$ is slightly larger at 280°C than at 300°C, we concluded then that the Ni_3S_4 precipitation originates from the supersaturated β phase and not from the transformation of the residual α phase since the Sulphur content of the β phase is higher at 280°C than at 300°C (according to phase diagram).

The post transformation precipitation therefore explains why the composition of the β phase is different from the equilibrium one but does not confirm that the equilibrium line is curved (i.e. Sulphur composition of the β phase increasing with the temperature). Alternatively we can check the validity of the $\beta/\beta + \text{Ni}_3\text{S}_4$ equilibrium line. According to the phase diagram, the quantity of Ni_3S_4 directly depends on the β phase composition and the volume fraction of Ni_3S_4 is expected to decrease while increasing temperature. Therefore, for a given α phase composition, the evolution of the quantity of Ni_3S_4 phase with temperature provide information to test the shape of the $\beta/\beta + \text{Ni}_3\text{S}_4$ equilibrium line. The Ni_3S_4 volume fraction can be studied using the measurement cycle recorded after each isothermal step since at the end of isothermal step, the α phase is completely transformed to β or $\beta + \text{Ni}_3\text{S}_4$ phase. According to the DSC curves at different temperatures (Figure 32), the area of the first endothermic peak which is related to the eutectoid plateau decreases while increasing temperature. During an eutectoid plateau, the transformation $\beta + \text{Ni}_3\text{S}_4 \rightarrow \alpha$ is expected to occur with constant volume fraction (for instance ~38% for sample 50.87at%S). The experimental observations are in contradiction to a constant volume fraction of transformed β and Ni_3S_4 . Since the fraction of $\beta + \text{Ni}_3\text{S}_4$ should be constant at the eutectoid plateau, this can be interpreted to mean that β and Ni_3S_4 have different enthalpies of formation and that the volume fraction of β and Ni_3S_4 phases changes with temperature. We deduced

then that the equilibrium line is likely to be curved and that the Sulphur content of the β phase increases with temperature. It is important to notice that the enthalpy, for a constant fraction of $\beta + \text{Ni}_3\text{S}_4$, slightly increases with increasing Ni_3S_4 volume fraction, hence the Ni_3S_4 phase has a slightly higher formation enthalpy than the β phase.

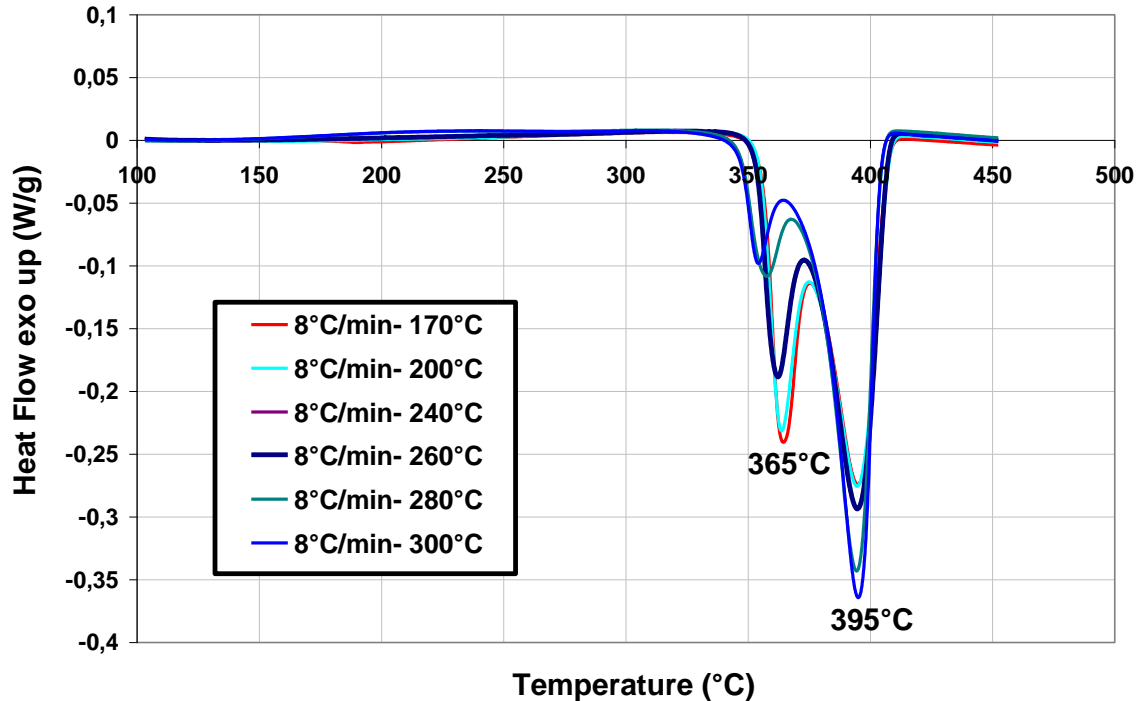


Figure 32 : Recorded DSC curves (heat flow against temperature) obtained during heating cycle (heating rate at 8K/min from 25 to 450°C) after isotherms at 170, 200, 240, 260, 280 and 300°C. Sample $\text{Ni}_{49.13}\text{S}_{50.87}$

The third question to address concerning the NiS phase diagram is the equilibrium condition of the eutectoid plateau. This is important because, for overstoichiometric sample, as shown in the microstructural study reported in the first chapter, the transformation is partial above the eutectoid temperature. Moreover, the equilibrium conditions in our domain of interest (maximum temperature 300°C) are close to the eutectoid one. The study of these equilibrium conditions is done by comparison of the volume fraction of the α phase decomposed during the eutectoid plateau expected by phase diagram to those obtained from DSC curves. The fraction is here estimated from DSC curves by the ratio of the area of peaks corresponding respectively to the $\beta \rightarrow \alpha$ and $\beta + \text{Ni}_3\text{S}_4 \rightarrow \alpha$ transformation. It is important to mention that the estimation using the peak area requires that the formed phases have the same enthalpy. Indeed, it was concluded in the previous that the enthalpy of the Ni_3S_4 phase is slightly higher than the one of the β phase. Since the volume fraction of the Ni_3S_4 phase is at maximum about 10%, in the studied domain of temperature, the ratio of peak area provide an estimation which should be close to the effective one.

According to the Ni-S phase diagram the volume fraction of the α phase decomposed during eutectoid plateau depends only on the initial composition of the α phase. This fraction is about 60% for sample 51.14at%S, but about 39% for 50.87at%S. Such a dependence on initial α composition should be then evident from the volume fraction (or from the peak area of the DSC curves). Figure 33 shows the

III.3 The α (β -NiS transformation and phase diagram validation

peaks relative to $\beta + \text{Ni}_3\text{S}_4 \rightarrow \alpha$ and $\beta \rightarrow \alpha$, recorded during heating after total transformation at 170°C for 4 samples of different composition. According to these DSC curves, the area under the first endothermic peak increases with overstoichiometry. This is interpreted in terms of the quantity of $\beta + \text{Ni}_3\text{S}_4$ increasing with composition, which is consistent with the phase diagram. In addition, for the sample with 51.14at%S, the area under the first endothermic peak is higher than the one relative to $\beta \rightarrow \alpha$ transformation and for sample 50.87at%S, the first peak area is lower than the second one. This is in agreement with a volume fraction of the $\beta + \text{Ni}_3\text{S}_4$ phases transforming during the first endothermic peak being higher than that of the β phase transformed in the second peak for sample 51.14at%S (and a lower volume fraction for the sample 50.87at%S). This feature is consistent with the tendency of volume fraction expected from the phase diagram. On the other hand, the area of peaks relative to $\beta \rightarrow \alpha$ on the DSC curves (Figure 32) remains constant for $T < 260^\circ\text{C}$. This is interpreted in terms of a constant volume fraction of the β phase which transforms during this peak as expected for an eutectoid transformation. Regarding the first endothermic peak, Figure 33 shows that it keeps the same position for all composition (around 365°C). This is also in agreement with an eutectoid transformation which always occurs at a constant temperature regardless of the composition. However the position of this peak is slightly different from what expected from the phase diagram (280°C). This is likely due to a kinetic effect and is not an important issue in what follows (60°C difference).

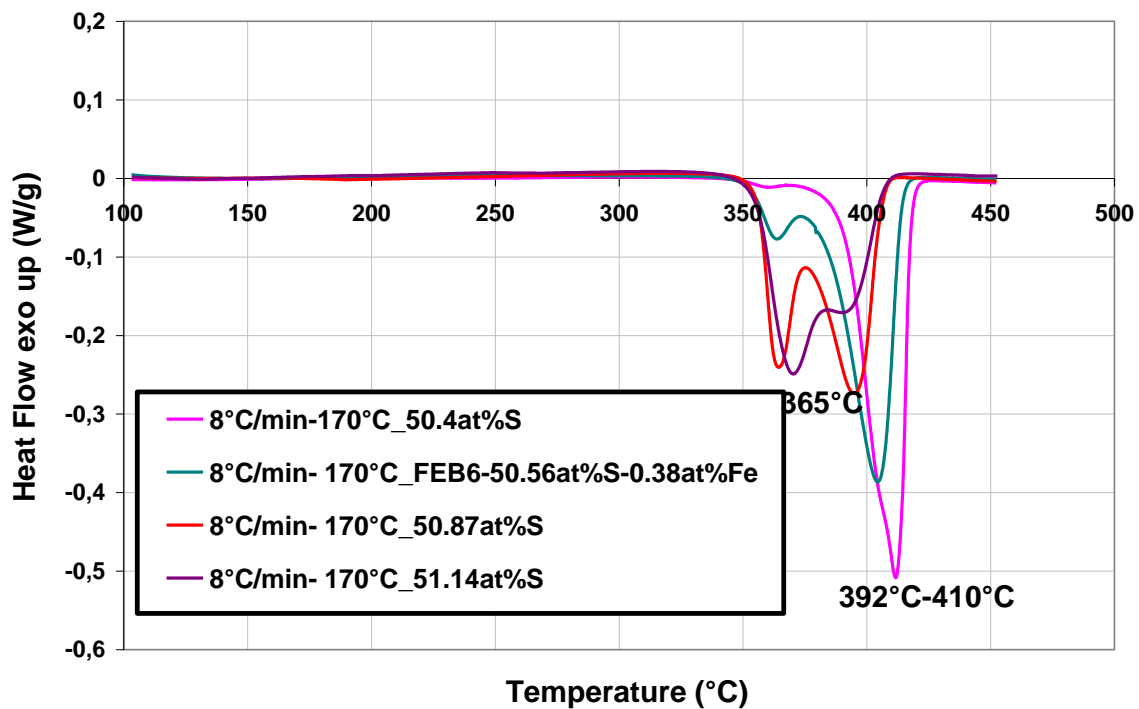


Figure 33 : Recorded DSC curves (heat flow against temperature) obtained during heating cycle (heating rate at 8K/min from 25 to 450°C) after isotherms at 170. Samples $\text{Ni}_{49.6}\text{S}_{50.4}$, $\text{Ni}_{49.13}\text{S}_{50.87}$, $\text{Ni}_{48.86}\text{S}_{51.14}$ and $\text{Ni}_{49.08}\text{Fe}_{0.38}\text{S}_{50.56}$.

One can be concerned about possible Sulphur evaporation during the DSC experiment which would lead to changes in the stoichiometry. DSC curves (Figure 32) which were recorded on one sample at different temperature, shows that the peak maintains the same position. We consider this as an indication that the α phase composition does not change along the cycle. Hence no significant desulphurization is expected. On the other hand, some shift to lower temperatures has been observed

as illustrated by the DSC curves in Figure 32 relative to $T=280^{\circ}\text{C}$ and 300°C where the first endothermic peak shifts to lower temperature in contrast to curves recorded for $T<260^{\circ}\text{C}$. As Ni_3S_4 phase is here formed by post transformation precipitation, thus only $\text{Ni}_3\text{S}_4 \rightarrow \alpha$ transformation has occurred which explains this shift to lower temperature.

The present DSC investigations have confirmed qualitatively the validity of the Ni-S phase diagram in the field of interest. Therefore this phase diagram can now confidently be used to extract the equilibrium data necessary for further kinetic modelling. In the following section, the DSC study will be focused on gathering quantitative kinetic information on the $\alpha \rightarrow \beta$ phase transformation.

III.4 Kinetic aspect of the $\alpha \rightarrow \beta$ -NiS transformation:

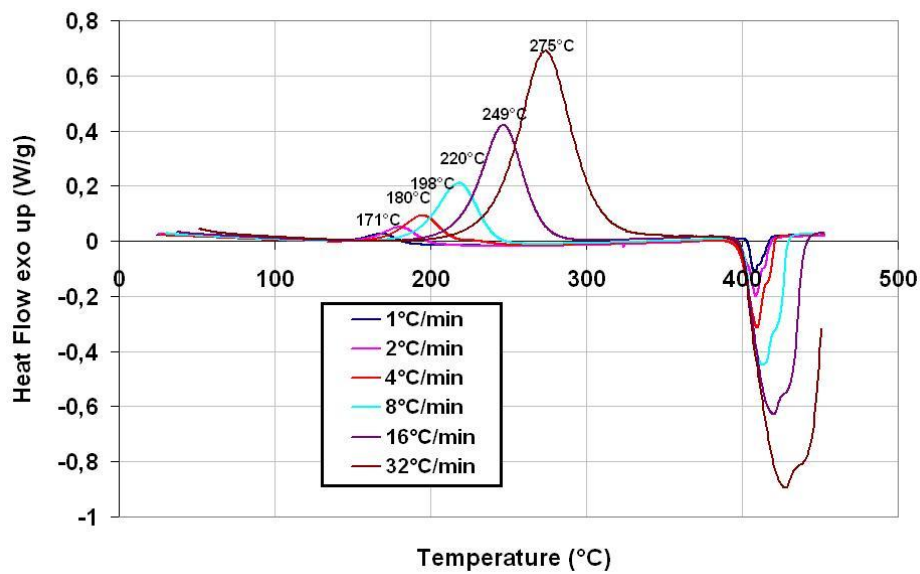
The main point of this kinetic study is to determine the degree of completion of the transformation with time. However, since it was already pointed out in the microstructural study (Chapter 2) that the overstoichiometry and iron impurities slow down the transformation, we will consider first qualitatively the effect of heating rate on transformation behavior to examine whether the transformation is complete or partial. In a second step, the TTT diagram will be built using the transformation time range determination derived from isothermal heat treatment. TTT curves for different overstoichiometry and iron impurity content will be reported. Finally, a quantitative analysis of the isothermal DSC curves will be developed using the Johnson Mehl formalism (JMAK model).

III.4.1 DSC scans at constant heating rate and partial transformation evidence

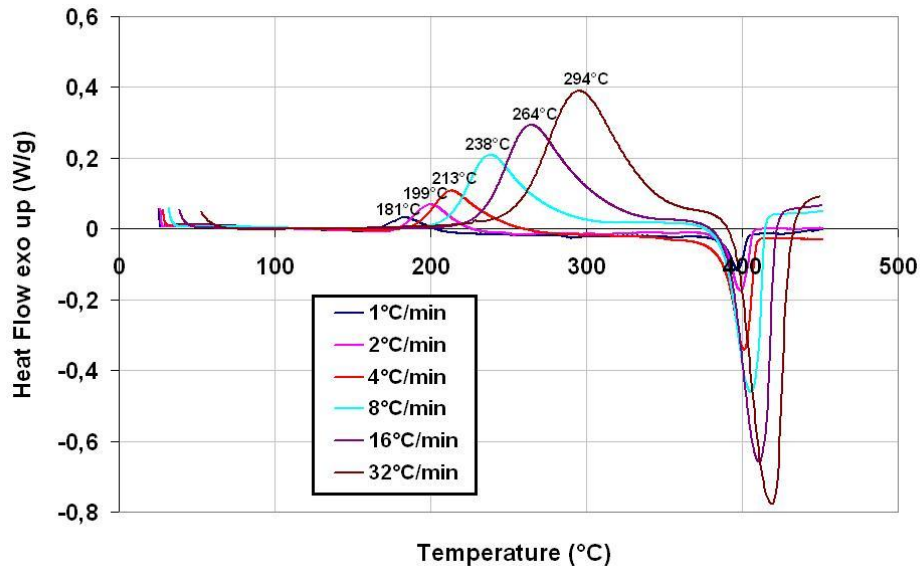
Non-isothermal heat treatments are appropriate to study the influence of heating rate on transformation kinetics and also to evidence partial or complete transformation.

Figure 34 a and b display DSC curves recorded after different heating rates (1, 2, 4, 8, 16 and $32^{\circ}\text{C}/\text{min}$) from 25°C to 450°C on low overstoichiometric samples (50.13at% and 50.4at%S). For a given heating rate, the DSC curve shows two peaks corresponding to $\alpha \rightarrow \beta$ -NiS and the $\beta \rightarrow \alpha$ -NiS inverse transformation. We note that the area under the peak increases while increasing heating rate (Figure 34a). This increase is not significant since, in all DSC experiments and for slow phase transformations, when heat flow is plotted against temperature increasing heating rate always tends to increase the peak area. Figure 34a also shows that the positions of peaks relative to α -NiS $\rightarrow \beta$ -NiS phase transformation are shifted to high temperature. For the near stoichiometric sample (Figure 34a) the transformation is complete for all the heating rates since the transformation peak ends within the temperature range of stability of the β phase (below 380°C). In the following, the DSC results obtained on sample 50.13at%S (the nearest composition to the stoichiometry 50:50) will be used as reference in the study of the evolution of the transformation kinetics.

III.4 Kinetic aspect of the $\alpha \rightarrow \beta$ -NiS transformation:



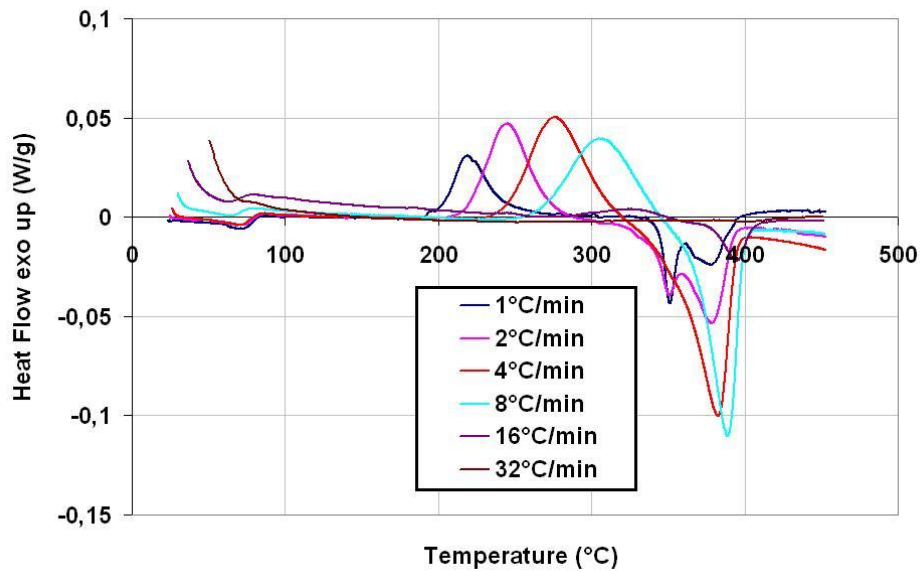
(a) sample $\text{Ni}_{49.87}\text{S}_{50.13}$



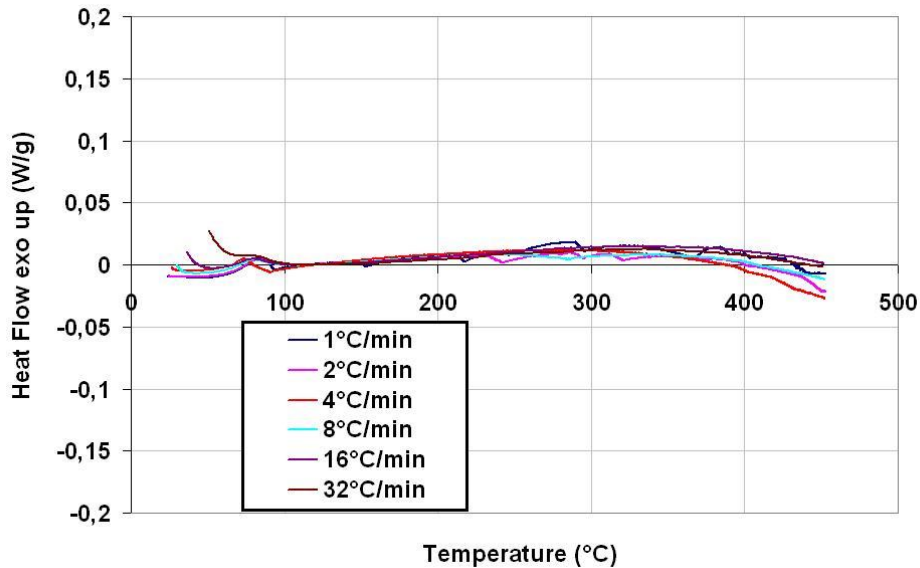
(b) sample $\text{Ni}_{49.6}\text{S}_{50.4}$

Figure 34 : Recorded DSC curves (heat flow against temperature) obtained after several heating rate (1, 2, 4, 8, 16 and 32K/min) from 25 to 450 $^{\circ}\text{C}$. Near stoichiometric samples.

Regarding highly overstoichiometric sample, Figure 35a and b give the DSC curves recorded for samples of composition 51.14at%S and 51.28at%S, respectively. For heating rates $< 4^{\circ}\text{C}/\text{min}$, DSC curves (Figure 35a) display the expected endothermic peaks but the exothermic peaks related to the $\alpha \rightarrow \beta$ -NiS transformation are shifted towards higher temperatures. Comparison of Figure 35a and Figure 34a shows that, for a same heating rate, the shift of the peak is larger for the high overstoichiometric than the near stoichiometric one. Added to that, in overstoichiometric sample (Figure 35a), for high heating rate (8, 16 and 32 $^{\circ}\text{C}/\text{min}$), the peak area decreases when the heating rate increases.



(a) sample $\text{Ni}_{48.86}\text{S}_{51.14}$



(b) sample $\text{Ni}_{48.72}\text{S}_{51.28}$

Figure 35 : Recorded DSC curves (heat flow against temperature) obtained after several heating rate (1, 2, 4, 8, 16 et 32K/min) from 25 to 450°C. Overstoichiometric samples.

Generally speaking, on DSC curves, the peak shifts are all the more pronounced when the transformation rate is small in comparison with the heating rate. The fact that the DSC peak shift is larger for overstoichiometric composition indicates that overstoichiometry causes the slowing down of the transformation. Figure 35b clearly confirms that, for very high overstoichiometry, the transformation becomes so slow that no peak is detected for all heating rates. In addition, the absence of the $\beta \rightarrow \alpha$ peak in Figure 35b confirms that no $\alpha \rightarrow \beta$ transformation has occurred.

The decrease of the peak area, observed on Figure 35a, indicates that for heating rates larger than 4°C/min the transformation is partial since peak areas are always expected to increase for non isothermal heat treatment. However, for lower heating rates, one can wonder whether the

III.4 Kinetic aspect of the α (β -NiS transformation:

transformation was not already partial. For fully transformed states (for instance sample 51.14at%S- Figure 33), the DSC curves display the two characteristic endothermic peaks with the first peak area being larger than the second one. In Figure 35a, this feature is only observed for heating rate at 1°C/min. Consequently, the transformation becomes partial for heating rate higher than 2°C/min on sample of high overstoichiometry (51.14at%S).

The peak shifts for different heating rates have been measured for the two near stoichiometric samples (DSC curves in Figure 34 a and b). Using the Kissinger [43] method, activation energies of about 57 kJmol⁻¹ and 56 kJmol⁻¹ are obtained. This activation energy indicates that the transformation is thermally activated and that its high value may allow the compensation for the effect of deceleration due to the overstoichiometry. This explains why the peaks, corresponding to $\alpha \rightarrow \beta$ phase transformation, shift to high temperature (for instance in Figure 31 : a shift from 181°C to 230°C at 2°C/min) with increasing overstoichiometry.

Regarding the effect of iron impurity content on the kinetics of transformation, DSC curves corresponding to a sample (Ni_{48.88}Fe_{0.49}S_{50.63}) (Figure 36), display the same features as the overstoichiometric sample (Figure 35b) : i. large peak shifts to the high temperature, i.e. peak surface decreasing when the heating rate increases. Consequently the Fe content has an effect on the kinetics similar to that of overstoichiometry.

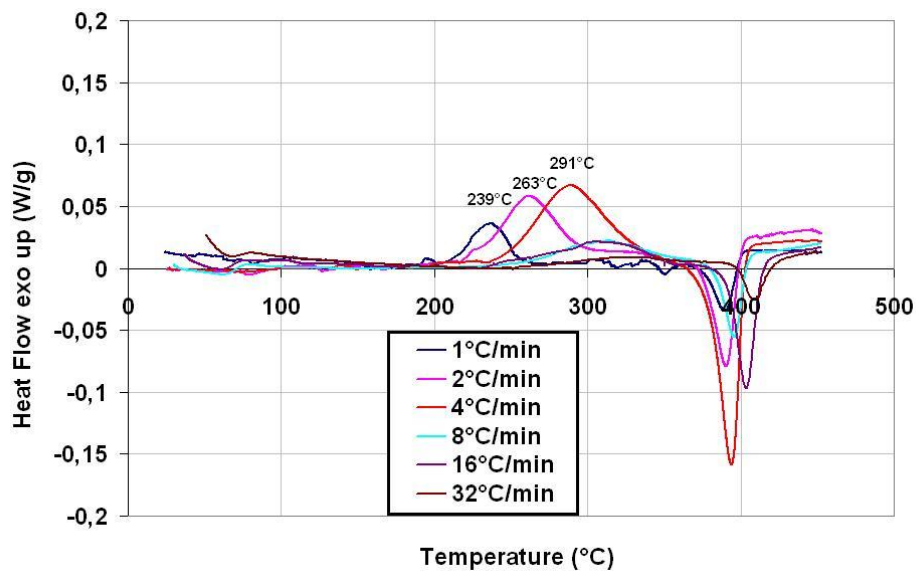
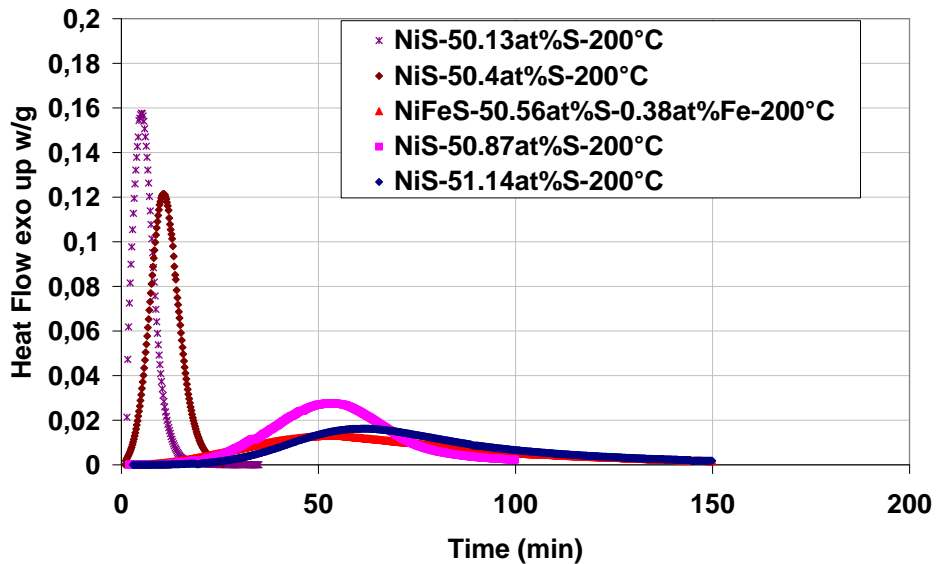


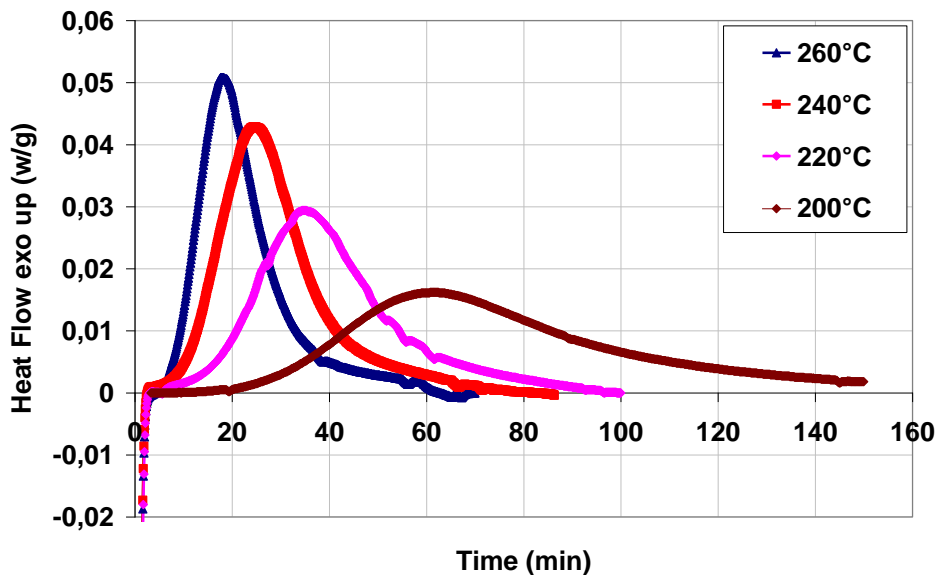
Figure 36 : Recorded DSC curves (heat flow against temperature) obtained after several heating rate (1, 2, 4, 8, 16 et 32K/min) from 25 to 450°C. Iron contained sample Ni_{48.88}Fe_{0.49}S_{50.63}.

III.4.2 TTT diagrams

Isothermal DSC runs were performed in order to build the TTT diagrams. As shown in the previous section, the transformation slows down significantly with overstoichiometry. Therefore, in addition to the set of curves at different temperatures, isothermal curves for different stoichiometry are necessary. The first step is then to acquire such a series of DSC curves for different stoichiometry and temperature as illustrated in Figure 37a and b.



(a) Composition effect, (plateau temperature T_p : 200°C).



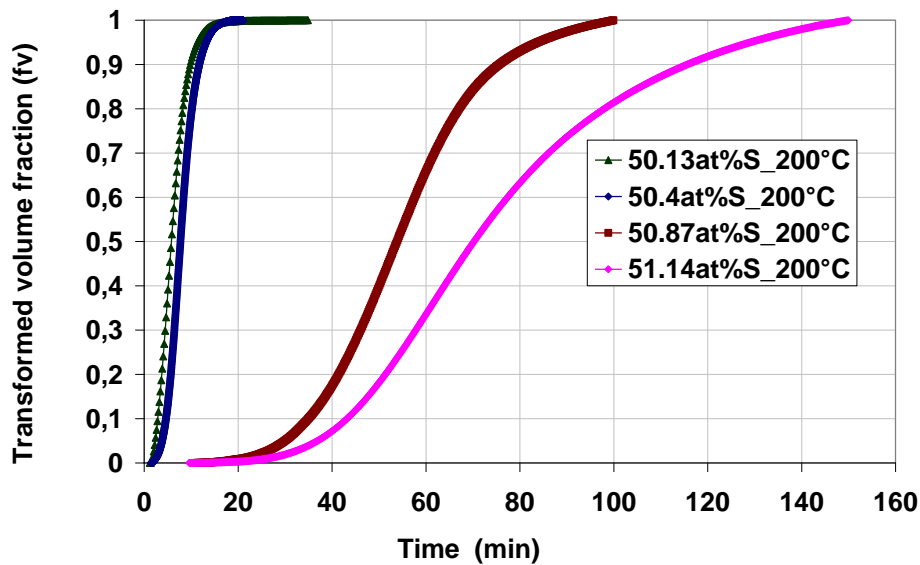
(b) Temperature effect (sample composition 51.14at%S)

Figure 37 : Recorded DSC curves $\Delta H=f(t)$ during isothermal heat treatment at different temperature and composition conditions illustrating the slow down of the transformation when increasing overstoichiometry and decreasing temperature. These curves provide the transformation time range necessary to build the TTT diagram.

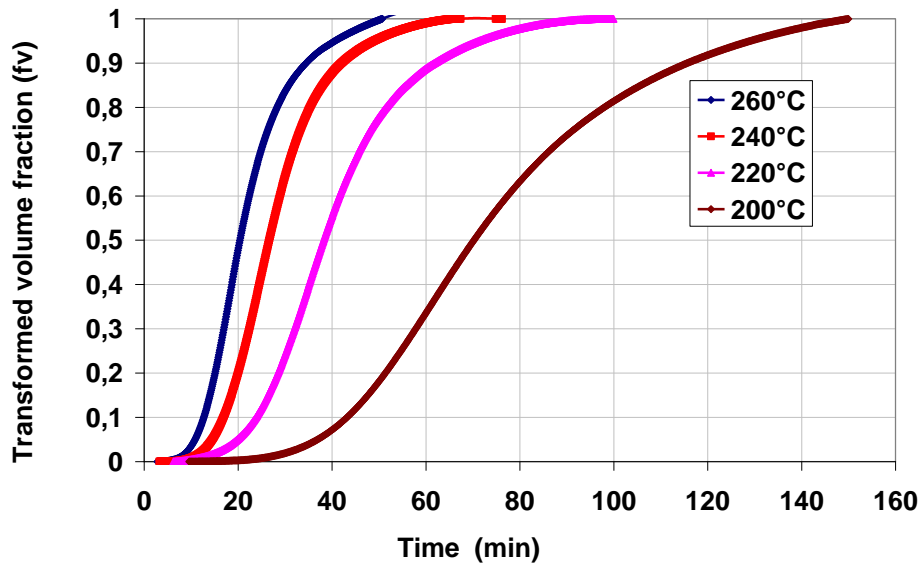
III.4 Kinetic aspect of the α (β -NiS) transformation:

On Figure 37a, it is worth noticing that, for low stoichiometry, the peak shows symmetric shape while, for high overstoichiometry its shape is assymmetric. This can be due to change in the nucleation and growth morphology with overstoichiometry. It can also result from the precipitation of the Ni_3S_4 which volume fraction increases with overstoichiometry. This point is specifically important with respect to the extraction of the transformed volume fraction from the isothermal DSC curves. Actually, the volume fraction can be readily obtained from DSC curves when a single phase is formed but this becomes questionable when two phases are formed. However, in the present case, the volume fraction of the Ni_3S_4 phase is known from the phase diagram to be at maximum $\sim 10\%$. In addition, from the comparison of peak area in DSC curves (section III.3.2), we have concluded that the enthalpy of $\alpha \rightarrow \beta$ and $\alpha \rightarrow \beta + \text{Ni}_3\text{S}_4$ transformation were close. Therefore, in the following, we will consider that the DSC curves provide a reliable estimation of the transformed volume fraction.

Figure 38 gives the evolution of the transformed volume fraction derived from the DSC curves: for different compositions (Figure 38a) and temperatures (Figure 38b). These curves provide the transformation time ranges which are necessary to build the TTT diagrams. For instance, Figure 38a shows that total transformation is obtained for about 150 min at 200°C in an overstoichiometric sample (51.14at%S) and for about 10 min in a near stoichiometric sample (50.13at%S). Figure 38b shows the evolution of the transformed volume fraction for different temperatures on overstoichiometric sample (51.14at%S). For this stoichiometry, the transformation time range for complete transformation significantly varies with temperature: from about 150 min at 200°C to about 45 min at 260°C .



(a) Composition effect on Fv evolution (plateau temperature T_p : 200°C).



(b) Temperature effect on Fv evolution (sample composition 51.14at%S)

Figure 38 : Evolution of the transformed volume fraction with time, derived from isothermal DSC curves, at different temperature and composition conditions. These curves are used to determine the transformation time range for a given transformed volume fraction.

Using the information on transformation time range and related volume fraction at different composition, a TTT curve can be built: see for instance, the TTT curve in Figure 39 which corresponds to a 90% transformed volume fraction, for different overstoichiometry and iron content. It is worth noting that it is not necessary here to investigate temperatures higher than 280°C since we know from the phase diagram and the microstructural study (Chapter 2) that the transformation is not complete except for near stoichiometric compositions.

Indeed the set of TTT curves is very appropriate tool to synthesise all the information on the temperature and composition effect. For near stoichiometric sample (50.4at%S), Fv~90% is reached after about 17 min at 200°C and 3 min at 260°C. For the overstoichiometric sample 51.14at%S after 115 min at 200°C and about 40 min at 260°C. The acceleration with temperature increase is clearly illustrated by the reduction of the time range: from 125 min at 200°C to 50 min at 260°C. The same remark holds for the composition effect: for an increase of 1 at%S the transformation time range increases from about 20 min to about 110 min. According to the TTT curves in Figure 39, the transformation time range is less than 60 min for temperature between 240°C and 280°C and for all studied compositions. Of course, at temperature high than 280°C, as the transformation becomes partial, the time of transformation is not reported.

The rather flat shape of the TTT curve at low temperature indicates a strong influence of the temperature. On the contrary, the curved shape at higher temperature corresponds to a smaller effect of the temperature on the transformation time range. Such behavior can be related to the shape of the TTT curve which correspond to half of a C shape (the high temperature domain being not investigated because of non complete transformation). In solid state phase transformation, the C shape of TTT curve is known to result from competition of two mechanisms which have inverse evolution according to

III.4 Kinetic aspect of the α (β -NiS) transformation:

temperature: a driving force for nucleation and growth which increases with decreasing temperature, in competition with the mobility of species which decreases with an Arrhenius law when temperature is decreasing. Such mechanisms should be involved for the $\alpha \rightarrow \beta$ transformation.

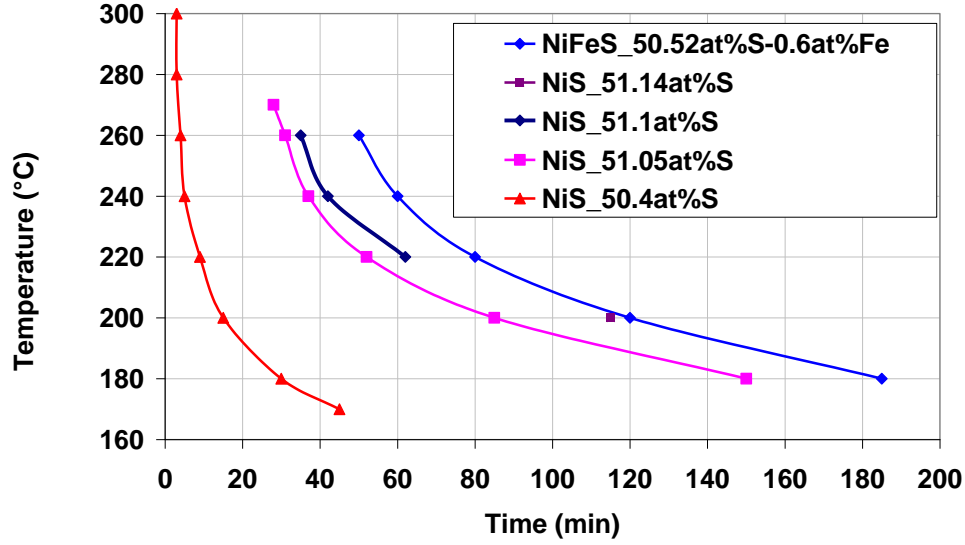


Figure 39: Time Temperature Transformation (TTT) diagram for Ni(Fe)S sample of different composition for Fv=90%: the transformation time range, corresponding to Fv=90%, is less than 1h for T>240°C for the studied compositions

III.4.3 JMAK analysis:

The isothermal DSC data will be now used to extract some information on mechanisms as can be done with the help of JMAK kinetic model. Although this is essentially a phenomenological model, this analysis will give in particular the so called Avrami exponent which is related to the transformation mechanism and the morphology of the growing particles. One cannot prove a mechanism via these arguments, but one can say that a proposed mechanism is or is not consistent with the observed Avrami exponent.

For the isothermal transformations with a nucleation and growth mechanism, Avrami [44] showed that the transformed volume fraction according to time can be expressed according to the following equation:

$$\alpha = 1 - \exp(-Kt^n) \quad \text{eq 6}$$

where α is the fraction of the transformed phase at time t , n the Avrami exponent which depends on the transformation mechanism and the morphology of the growing particles. The coefficient K depends on the temperature often according to an Arrhenius law:

$$K = K_0 \exp\left[-\frac{nE}{kT}\right] \quad \text{eq 7}$$

K_0 is the frequency factor, E the activation energy, k the Boltzmann constant and T the temperature: The relation between α and t can be rewritten in the following form:

$$\ln(\ln(1 - \alpha)) = n \ln(t) + \ln(K) \quad \text{eq 8}$$

Chapitre III. Calorimetric study of phase transformations in Nickel sulphide (NiS)

The value of K and the Avrami exponent can be then obtained from the plot of $\ln(-\ln(1-\alpha))$ as a function of $\ln(t-t_0)$. Figure 40 shows this plot together with the evolution of transformed volume fraction for two samples of different overstoichiometry (near stoichiometric sample in Figure 40a and overstoichiometric one in Figure 40b). Figure 40 clearly shows that the slope of curves related to Avrami exponent change during the phase transformation. When, comparing Figure 40a and Figure 40b, we note a more pronounced change of the Avrami exponent for the overstoichiometric sample than for the near stoichiometric one which remains almost constant. For a more quantitative follow up of the change during the transformation, it will be more convenient to plot the evolution of the Avrami exponent with the transformed volume fraction (or time).

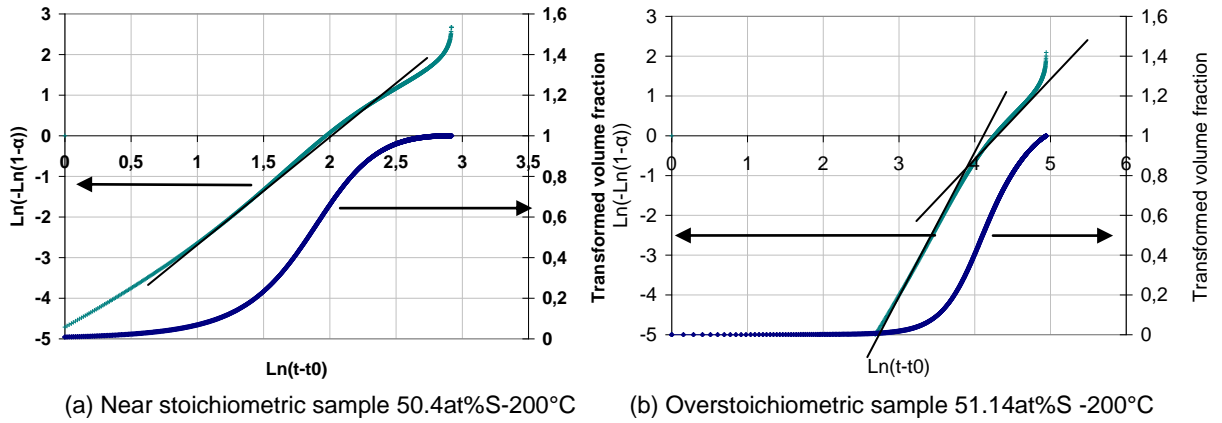


Figure 40 : Blue curves show the evolution of transformed volume fraction for two samples of different overstoichiometry ($T_p=200^\circ\text{C}$) ; Green curves show the plot of $\ln(-\ln(1-\alpha))$ as a function of $\ln(t-t_0)$, the Avrami exponent is obtained from the slope of this curve.

The Avrami exponent (n) can be derived from relation (eq8) just by a rewriting to derive n as a function of volume fraction:

$$n = \frac{\ln(\ln(1-\alpha)) - \ln(K)}{\ln(t)} \quad \text{eq 9}$$

Strictly speaking, in the original model JMAK with the simplest hypothesis, as summarized in the classic book by J.W.Christian [20], the exponent is constant. We will consider however a “local Avrami exponent” which may change while the transformation proceeds. This can be the case for instance when there is a progressive activation of a limited number of potential sites for nucleation.

Figure 41 shows the evolution of Avrami exponent during phase transformation for different stoichiometry from 50.13 to 51.14at%S. For the sample 50.13at%S, the Avrami exponent is constant (equal to 2) during the whole transformation. For high overstoichiometry (51.14at%S), the phase transformation is described by two exponents: about 3-3.5 and around 2. The transformation begins with a relatively high Avrami exponent (3.5) and finished with a smaller one (2). The slope change occurs after about 70% Fv for near stoichiometric sample and after about 30% for overstoichiometric one.

III.4 Kinetic aspect of the α (β -NiS) transformation:

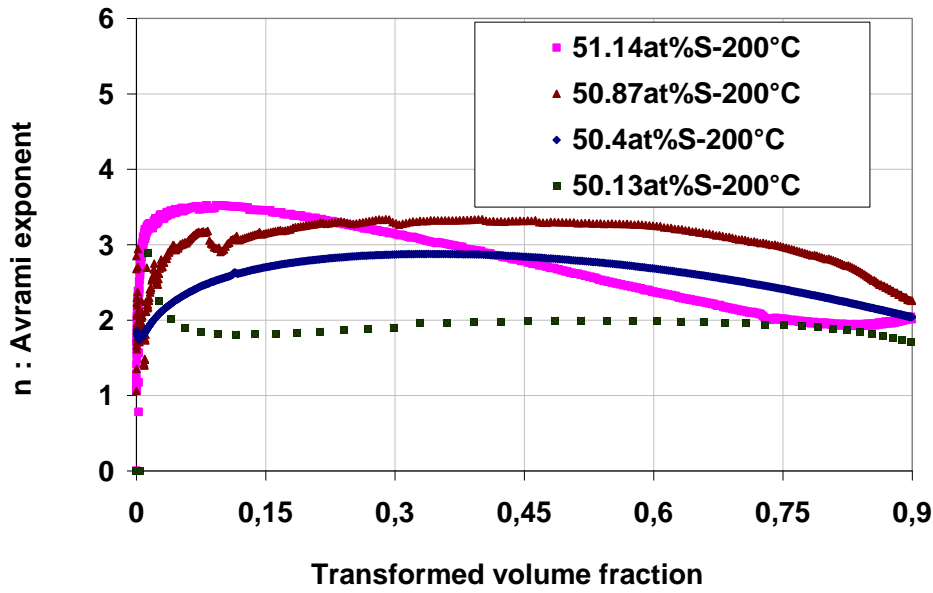
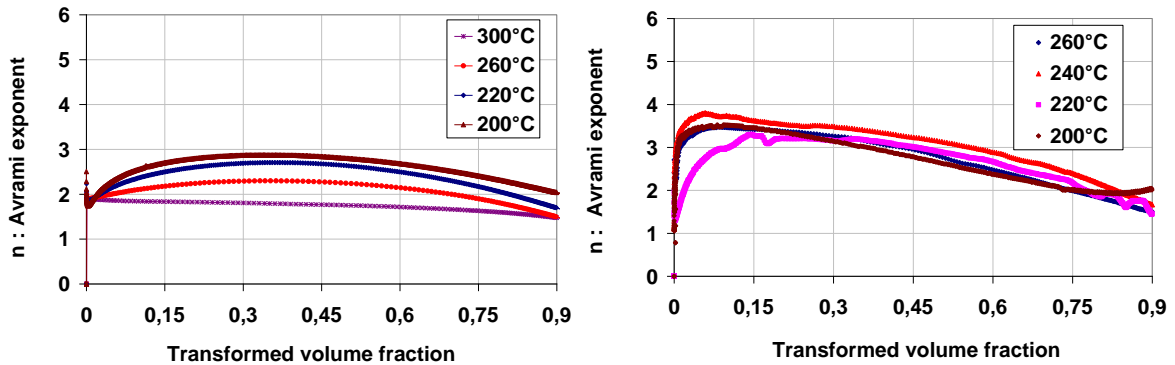


Figure 41 : Effect of composition on the Avrami exponent evolution during phase transformation for isothermal treatment at 200°C: Avrami exponent is obtained through JMAK analysis of the isothermal DSC curves

The evolution of Avrami exponent has also been studied at different temperatures and two compositions: near stoichiometric (Figure 42a) and overstoichiometric (Figure 42b). For the near stoichiometric sample, at high temperature (Figure 42a), the Avrami exponent is constant (1.5-2) during transformation. But at low temperature, it changes from 3 to 2. Regarding the overstoichiometric sample (Figure 42b) the Avrami exponent varies between 3.5 and 2 for all temperatures. In all cases, higher Avrami exponents are observed in the beginning of the transformation and the lowest one at the end. Avrami exponent values will be discussed in the following section with respect to the transformation mechanism. However, one has to keep in mind that though Avrami exponents provide valuable information to discuss on possible mechanism, they are not unambiguously related to a unique transformation mechanism.



(a) Near stoichiometric sample 50.4at%S

(b) Overstoichiometric sample 51.14at%S

Figure 42 : Effect of temperature on the Avrami exponent evolution during phase transformation in near stoichiometric and overstoichiometric sample: Avrami exponent is obtained through JMAK analysis of the isothermal DSC curves ($200 < T < 300^{\circ}\text{C}$).

Chapitre III. Calorimetric study of phase transformations in Nickel sulphide (NiS)

Since the Avrami exponent changes during transformation, for overstoichiometric samples, two JMAK models are necessary to describe the time evolution of the volume fraction F_v . An example of simulation of the F_v , measured from DSC curves, with JMAK model is shown in Figure 43a and b. Figure 43b clearly illustrates that two JMAK models are necessary to describe the F_v evolution for overstoichiometric sample, with an exponent $n=3.5$ at short times, and $n=2$ for longer treatments. However, for a near stoichiometric sample, a complete description of F_v is possible with a JMAK model with a single exponent $n=2$ (Figure 43a). Hence, for overstoichiometric sample, two activation energies corresponding to the first JMAK model and the second one are measured (respectively 150KJ/mol and 87.6 KJ/mol). The measured activation energies E_a indicate that the second step, which consists in the precipitation of the Ni_3S_4 phase reported in the microstructural study (Chapter 2) is slower and less temperature dependant than the first step (i.e. growth of lamellar of the β phase observed in the microstructural study (Chapter 2))

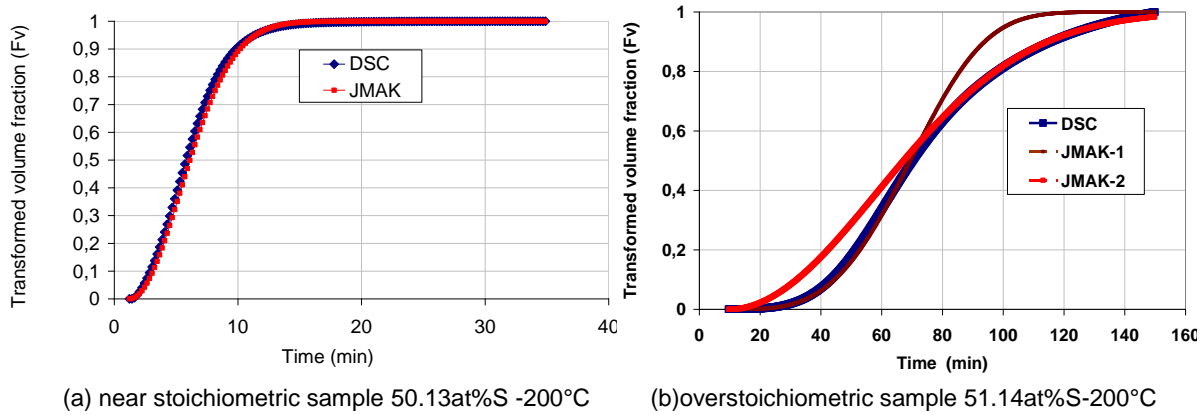


Figure 43: JMAK modelling of the evolution of the transformed volume fraction: for overstoichiometric sample two JMAK model are necessary for total description of the $F_v(t)$ curves.

III.5 Discussion:

The activation energies we have measured are relatively high and vary along the transformation and with stoichiometry by almost a factor of 2. We can compare this result to earlier DSC studies which had also provided kinetic parameters, using Kissinger model [43], for near stoichiometric composition. For instance, the activation energy found in the present study, 57KJ/mol, are close to those found by Bishop *et al* [16] 62kJmol⁻¹ and Kasper *et al* [3] 60KJ/mol. In addition our results are in agreement with [3] that reports an increase of activation energies with increasing overstoichiometry. However some differences are observed between the different authors, but this could be due to difficulties of accurately controlling sample composition. Owing to the reasonable agreement between independent measurements for the near stoichiometry sample, in further modelling of the phase transformation this value of the activation energy (57KJ/mol) will be used to account for temperature dependence.

III.5 Discussion:

The second important result from the DSC study is the indirect information on mechanisms contained in the Avrami exponent which describes the evolution of the volume fraction. In the understanding of the solid state phase transformation, Avrami coefficients can be related to the morphology of the second phase, the growth kinetic law and the nucleation rate. Christian [20] has shown that the evolution of the transformed volume fraction, during the reaction, is given by the volume increase of the pre-existing growing particle plus the volume corresponding to the formation of new nucleus. Therefore modelling the evolution of F_v depends on the nucleation rate and the kinetic law controlling the volume increase of the growing particle. Hence for a given particle shape, nucleation rate and growth law, it is possible to predict the expected Avrami exponent. As detailed in Christian [20] numerous shapes and growth laws can be considered. However, the present discussion will be limited to case relevant for the NiS transformation since the microstructural study has already allowed to identify the morphologies and possible mechanisms involved in NiS transformation. At this stage of the study, the evolution of the nucleation rate and the particle growth law remain to be determined to complete the sets of parameters required for modelling. Nevertheless, a comparison of the experimental Avrami exponent and the one expected for the NiS transformation can be useful in view of further modelling since it can help to discriminate as far as possible among mechanisms consistent with observations.

According to the microstructural study of NiS phase transformation (Chapter 2), depending on composition and temperature, four typical morphologies (globular, block, lamellar and coarse lamellar) are observed which can be described by two representative shapes: globular and lamellar. In addition, the microstructural study (Chapter 2) has also shown that two mechanisms are involved in the particle growth: a partitionless massive transformation and a diffusion controlled partitioning one. The growth rate is constant in time, for a massive mechanism and is parabolic in time for a diffusion controlled mechanism [20, 34-36]. Therefore in the determination of the expected Avrami exponent two morphologies (globular and lamellar) growing with either constant or parabolic kinetics will be considered. As we ignore the nucleation rate, several hypotheses will be considered. Table 5 summarizes the expected Avrami exponent and in particular points out the impact of the nucleation rate on the Avrami exponent for a given growth kinetics.

The first obvious remark on the expected Avrami exponents gathered in Table 5 is that a value is not associated to a unique solution. On the other hand, as illustrated by Table 5, for one given morphology, depending on growth law and nucleation rate, the expected Avrami can change. For instance, for globular morphology growing with linear kinetic from constant number of pre-existing nuclei, the volume fraction is described by an Avrami exponent $n=3$. But for a decreasing nucleation rate, an Avrami exponent of $3 < n < 4$ is expected. This exponent will be equal to 4 for transformation with constant nucleation rate or even higher than 4 for increasing nucleation rate. However, a tendency can be derived from Table 5: for spherical morphology growing with diffusion controlled mechanism, Table 5 indicates that the Avrami exponent is expected to be $1\frac{1}{2}$, $1\frac{1}{2}-2\frac{1}{2}$, $2\frac{1}{2}$, i.e. experimental values close half integer should be associated to diffusion controlled mechanisms.

Analyses of DSC curves have shown an Avrami exponent close to 3 (Figure 42a) for globular morphology in near stoichiometric sample. According to Table 5, this Avrami exponent is consistent with two possibilities: a linear growth from a constant number of pre-existing nuclei or diffusion controlled growth with increasing nucleation rate (which give $n > 2\frac{1}{2}$). However, we know from the

Chapitre III. Calorimetric study of phase transformations in Nickel sulphide (NiS)

microstructural observations that the transformation is a massive one in this case. In addition explosive nucleation rates (which reflect autocatalytic processes) are rather unusual, the latter hypothesis is rejected.

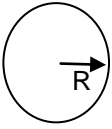
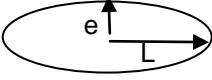
Morphology in NiS		Growth law	Nucleation rate	Expected Avrami exponent
Globular 		Linear growth $R \sim t \rightarrow V \sim t^3$	Zero nucleation rate	3
			Decreasing //	3-4
			Constant //	4
			Increasing //	>4
		Parabolic growth $R \sim t^{1/2} \rightarrow V \sim t^{3/2}$	Zero nucleation rate	1½
			Decreasing //	1½-2½
			Constant //	2½
			Increasing //	>2½
Lamellar 	Needle	Linear lengthening $\left. \begin{matrix} L \sim t \\ e \sim t^{1/2} \end{matrix} \right\} \rightarrow V \sim t^2$	Zero nucleation rate	2
			Decreasing //	2-3
			Constant //	3
			Increasing //	>3
	Plates	Linear lengthening $\left. \begin{matrix} L \sim t \\ e \sim t^{1/2} \end{matrix} \right\} \rightarrow V \sim t^{5/2}$	Zero nucleation rate	2½
			Decreasing //	2½-3½
			Constant //	3½
			Increasing //	>3½

Table 5: Expected Avrami exponent for Morphology observed in NiS transformation as function of different nucleation rates. (V=Volume)

In Table 5 the lamellar case has been divided in two subcases (needle and plate) since the observations of lamellar shape does not necessarily correspond to an isotropic shape. Hence the two subcases, needle and plates are more appropriate to account for anisotropic shape. For the needle shape when the lengthening and thickening are controlled respectively by linear and parabolic law, the volume fraction is described by Avrami exponents like $n=2$, 2-3, 3 and n larger than 3 for the different nucleation conditions. On the other hand, the expected Avrami exponents for the plate shape are 2½, 2½-3½, 3½ or larger than 3. Regarding experimental Avrami exponents determined with the DSC, for overstoichiometric samples, n varies between 3 and 3.5 (Figure 41 and Figure 42b). Again, these values are consistent with two possible mechanisms: needle growth with increasing nucleation rate or plates growth with constant nucleation rate. These two solutions are consistent with our microstructural observations i.e. lamellar morphology and not instantaneous nucleation (Chapter 2). Hence in order to discriminate between these two solutions, further investigation of the nucleation rate is necessary and will be carried out in this study using *in situ* observation of the phase transformation (reported here in Chapter 5).

III.5 Discussion:

JMAK analysis, in the NiS system, has also shown that during one isothermal treatment, the Avrami exponent changes continuously from 3.5 to 2 for overstoichiometric samples (Figure 42b). This change of the Avrami exponent could result from two effects: either a change in the growing mechanism or in the growing morphology. As it was pointed out from our previous microstructural study of phase transformation (Chapter 2) in the first stage of the transformation, the morphology of the growth regime consists in β phase lamella while in the last stage occurs the precipitation of Ni_3S_4 . Therefore there is a significant change in the morphology which can explain the Avrami exponent change. These two mechanisms, corresponding respectively to $n=2$ and $n=3.5$, coexist for a large part of the transformation, but they can be well separated at the beginning of the transformation (high Avrami exponent) and at the end of the transformation (low Avrami exponent). The continuous variation observed in between, can be here explained by the fact that nuclei of β phase appear continuously as the transformation proceeds.

Regarding isothermal treatment at different temperature, a decreasing Avrami exponent, from 3.5 to 2, is observed in overstoichiometric sample (51.14 at%S) for the studied range (Figure 42b). Generally speaking, the temperature has no effect on the Avrami exponent for most of the transformation since it depends only on the growth geometry, and then changes only with this geometry. For instance, in the overstoichiometric sample, the morphological evolution during the transformation is almost the same for all temperatures: growth of β phase lamella is followed by the precipitation of the Ni_3S_4 phase as shown in Chapter 2. Hence no temperature effect on Avrami exponent would be observed, which is consistent with the DSC results. However, for the near stoichiometric sample 50.4at%S, the Avrami exponent changes with temperature: $n=3$ at low temperature and $n\sim 2$ at high temperature. $n=2$ does not correspond to any mechanism with linear growth as expected for the globular morphology. The origin of such an Avrami exponent could be explained by the fact that at high temperature the transformation, which is very rapid, could occur during the heating stage. Therefore further growth would be taking place for already existing small grains of the β phase, with non negligible volume.

The Avrami exponents, obtained from analysis of the DSC curves, considered together with microstructural aspect of the NiS phase transformation, were fruitful confirming possible transformation mechanisms. At this stage, modelling the phase transformation requires a detailed study of the nucleation rate and the time dependence of the interface motion; this motivated a further study of the nucleation rate evolution and interface velocity, according to temperature and composition, which was carried out through *in situ* observation of phase transformation in optical microscopy; these results are reported in Chapter 5.

III.6 Conclusion:

DSC experiments, both with a constant heating rate and obtained isothermally, have allowed us to get a better knowledge of the NiS phase diagram. The observed transformation kinetics, synthesized in a series of TTT diagrams for different S and Fe content, can be accurately described within the JMAK formalism, and the measured Avrami exponent are consistent with the morphologies observed and with the various diffusive mechanisms, partitioned or partitionless, which have been proposed in previous works. A full modelling of the transformation kinetics, incorporating an appropriate nucleation model, was the next step in this study. However before the modelling itself, since diffusion controlled mechanisms had been identified, it was essential to have some data on diffusion coefficient for the Ni-S system. Hence next step in the study was to carry out diffusion couple experiments (Chapter 4). Then as announced in the discussion above, an *in situ* follow up of the transformation and the modelling became possible (Chapter 5).

Chapitre IV. Measurements of interdiffusion coefficients in α NiS.

IV.1 Introduction:

As concluded in the previous chapters (2-3), the phase transformation in overstoichiometric sample occurs with long range partitioned mechanism. Modelling the kinetic of such diffusion controlled phase transformation requires a knowledge of the interdiffusion coefficient in the α -NiS phase. Such evaluation of the interdiffusion coefficient could be obtained from appropriate diffusion couple in which Sulphur and Nickel controls the kinetics of the growing reaction zones [45, 46]. More precisely, the measurement of the intermetallic growth or diffusion depth thickness allows one to derive interdiffusion coefficient values. It was established in the previous chapters that the transformation kinetics is thermally activated and that iron impurities slow down the kinetics. Therefore the interdiffusion coefficient in the α -phase was investigated as function of temperature and of the iron impurities content.

According to the NiS phase diagram [22] , the interdiffusion coefficient in α phase can be extracted from several diffusion couples with Ni, Ni_3S_2 or Ni_7S_6 , on one side and, on the other side, Ni_3S_4 , NiS_2 or very overstoichiometric α -NiS phase. Among all possibilities, the $\text{Ni}_7\text{S}_6/\text{NiS}_2$ should be the most appropriate diffusion couple for a direct measurement since only the α phase would be formed at the interface. But it was not possible to prepare good NiS_2 samples. Thus another diffusion couple ($\text{Ni}_3\text{S}_2/\text{NiS}$) had to be used. Unfortunately, since the α phase is metastable for $T < 400^\circ\text{C}$ and tends to transform at low temperatures to β NiS, the $\text{Ni}_3\text{S}_2/\text{NiS}$ diffusion couples are necessarily studied for $T > 400^\circ\text{C}$. Regarding the temperature field of interest for the phase transformation ($200\text{--}300^\circ\text{C}$), the measured interdiffusion coefficient would then be extrapolated to low temperature using an Arrhenius law. Diffusion couples with different α phase compositions have been studied: namely a very overstoichiometric α sample (51.28at%S) and an iron containing sample ($\text{Ni}_{48.88}\text{Fe}_{0.6}\text{S}_{50.52}$). In the

following, we will first present a qualitative description of the diffusion couple experiments and then report the measurement of the interdiffusion coefficient.

IV.2 Diffusion couple and interdiffusion coefficient measurement

Diffusion couple experiments require preliminary preparation to obtain, for each sample, flat and smooth surfaces in order to have the best contact on the largest possible area. Thereafter the two samples were maintained in contact using a specific mounting with a spring exerting a pressure (about ~ 5 MPa) [47]. The whole device was introduced into a furnace for isothermal treatment at different temperatures, during times sufficient to have significant diffusion effects. These experiments were carried out under an argon flux to prevent possible oxidation of the surface. Figure 44 shows the Ni-S phase diagram and a schematic representation of the studied diffusion couple. According to the phase diagram, it is expected that the $\text{Ni}_3\text{S}_2/\text{NiS}$ diffusion couple will form at $T=400^\circ\text{C}$ a Ni_9S_8 layer and a diffusion layer near the $\text{Ni}_9\text{S}_8/\alpha\text{-NiS}$ interface showing a concentration profile reflecting the Sulphur and Nickel diffusion. For each diffusion couple, the thickness of the Ni_9S_8 layer, the depth of the diffusion layer, the Sulphur composition along the diffusion profile was measured. All the compositions were measured using Electron Probe Microanalysis (EPMA). The analysis of this set of data then yielded the interdiffusion coefficient measurement.

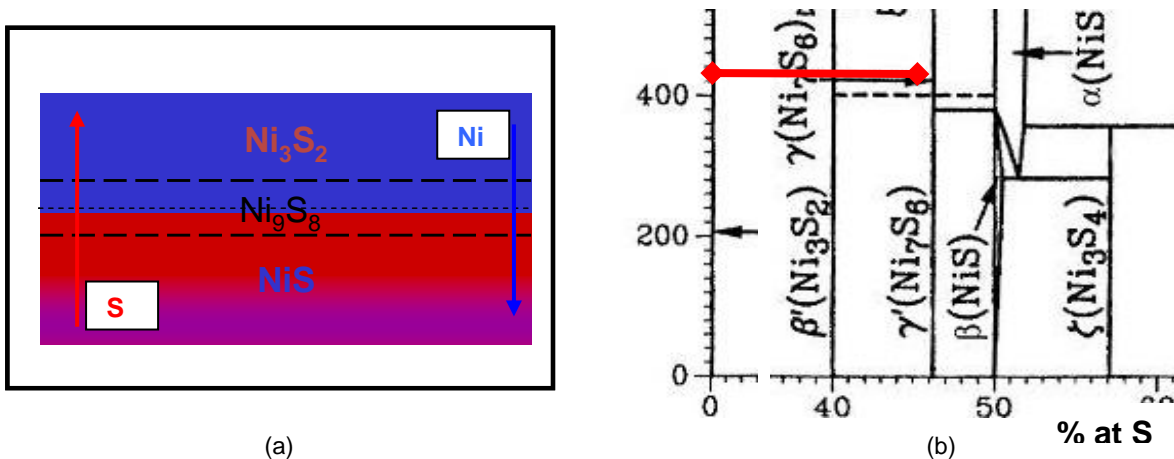


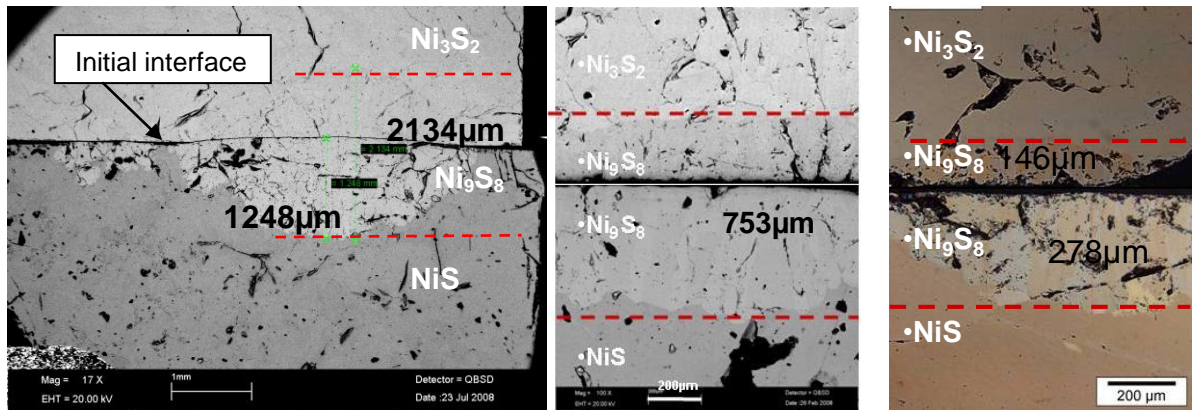
Figure 44 : (a) : Schematics of a diffusion couple (b) : Ni-S phase Diagram: after Nash. P *et al* (1991)

IV.2.1 Diffusion couple : qualitative observations

Figure 45a shows a micrograph of the diffusion couple near the interdiffusion interface after a heat treatment at 500°C for 6h30. It should be first noted that the starting samples (Ni_3S_2 and NiS phases) being rather brittle, after heat treatment the samples showed many cracks. The porosity originated from the initial Ni_3S_2 and NiS samples which were prepared following the method described in Chapter 2. However on the micrograph Figure 45a, three layers of different grey contrast can be identified. The intermediate layer, i.e. the grey contrast zone, does not show a very constant thickness, a feature which is certainly due to poor surface contact. Hence in the following the measured thicknesses always correspond to the maximum observed ones. The average Sulphur compositions within each layer are respectively: 60at% (clear grey layer), 52.9at% (grey layer) and 50.5at% (dark layer). These compositions correspond respectively Ni_3S_2 , Ni_9S_8 and $\alpha\text{-NiS}$ phases as

IV.2 Diffusion couple and interdiffusion coefficient measurement

expected from the phase diagram. The formation of the Ni_9S_8 layer on both sides of the initial interface implies that the two elements are involved in the diffusion mechanism. The thickness of the Ni_9S_8 layer is higher on the NiS side than that in Ni_3S_2 one. In addition we note a displacement of the initial interface towards the Ni_3S_2 . This is an indication that the elements Ni and S do not have the same diffusion coefficient. From the cross section in Figure 45a, we can measure the Ni_9S_8 layer total thickness and the thickness of the Ni_9S_8 phase formed in the α phase. This value (1248 μm) will be further used together with the diffusion depth in the α phase.



(a) Ni_3S_2 / $\text{Ni}_{48.75}\text{S}_{51.28}$ 500°C - 6h30 (b) Ni_3S_2 / $\text{Ni}_{48.75}\text{S}_{51.28}$ 400°C - 16h (c) Ni_3S_2 / $\text{Ni}_{48.88}\text{Fe}_{0.6}\text{S}_{50.52}$ 400°C - 16h

Figure 45 : (a) : SEM micrograph showing the formation of Ni_9S_8 layer on both side of the initial interface, (b) and (c) comparison of the thickness of the Ni_9S_8 layer obtained with NiS and NiFeS sample.

Regarding the effect of the iron content, the micrographs of Figure 45b and c allow one to compare the diffusion couple obtained respectively with α -NiS sample (Figure 45b) and NiFeS sample (Figure 45c). In both cases, a Ni_9S_8 layer is formed but its thickness is significantly affected by the presence of Fe impurities: 753 μm (Figure 45b) for the $\text{Ni}_3\text{S}_2/\text{Ni}_{48.75}\text{S}_{51.28}$ couple, 424 μm (Figure 45c), for the $\text{Ni}_3\text{S}_2/\text{Ni}_{48.88}\text{Fe}_{0.6}\text{S}_{50.52}$ one. By simple comparison of the Ni_9S_8 layer thicknesses, we can conclude that the diffusion is faster in the NiS samples. The addition of Fe causes a slowing down of the diffusion.

The second relevant information given by the diffusion couple experiment, in addition to the thickness of the Ni_9S_8 layer, is the composition profile along a normal to the interface. Figure 46 shows a EPMA composition profile carried out with a 15 μm step, for the couple shown in Figure 45b. Three composition fields are observed, which correspond, from the left to the right, respectively to Ni_3S_2 , Ni_9S_8 and α phase. Constant composition is observed in the Ni_3S_2 and Ni_9S_8 layers which are indeed line compounds. Nevertheless the Ni_3S_2 layer composition is about 41at% in S which is slightly different from the expected 40at%S. This cannot be explained by Sulphur diffusion because Ni_3S_2 is a supposed to be a line compound, and this difference may be due to analysis imprecision. On the other hand, the composition in the α side is not constant (Figure 46) but shows a diffusion profile on a depth of 750 μm in the NiS layer. This is in good agreement with the Ni-S phase diagram which presents a large composition field for the α phase. The NiS part of the diffusion couple (profile together with the thickness of the Ni_9S_8 phase) makes it possible to calculate the interdiffusion coefficients in the α phase as reported in the following section.

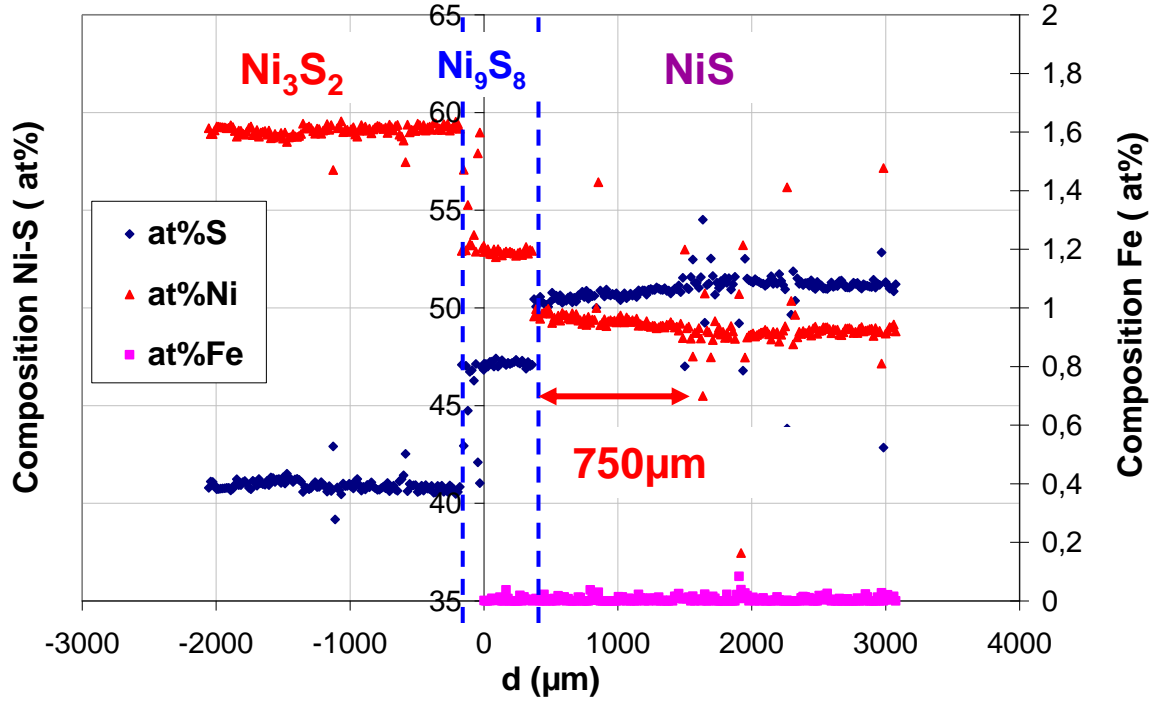


Figure 46: Diffusion couple Ni_3S_2 / NiS ($\text{Ni}_{48,72}\text{S}_{51,28}$) 400°C 16h: EPMA composition analysis.

IV.2.2 Interdiffusion coefficient in α -NiS

The objective here is to obtain not only the interdiffusion coefficient but also its temperature dependence which is assumed to follow an Arrhenius law ($D = D_0 \exp(-Q/RT)$).

The interdiffusion coefficient in the α phase can be measured using the classical relation between the diffusion coefficient (D) and the diffusion depth (X): $X^2 = 4Dt$. In the NiS diffusion couple, we assumed that the depth value correspond to the thickness affected by diffusion in the α phase (i.e. the thickness of the Ni_9S_8 in the α side added to the depth of the diffusion profile in the α -phase). However, this assumption requires first to check that the evolution of the thickness of the Ni_9S_8 , during isothermal holding, is controlled by a diffusive mechanism. Figure 47 shows the evolution of the thickness of the Ni_9S_8 layer at 400°C and for different holding time. It appears clearly from this curve that the thickness shows a quadratic evolution and therefore its growth is considered to be diffusion controlled. It is then reasonable to use the classical relation between the diffusion depth and the time ($X^2 = 4Dt$) to measure the interdiffusion coefficient.

IV.2 Diffusion couple and interdiffusion coefficient measurement

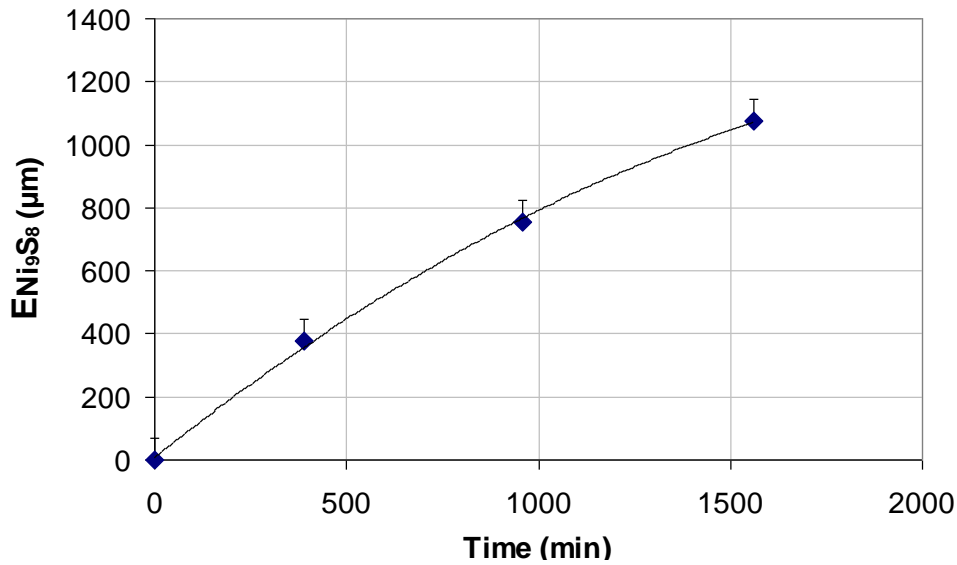
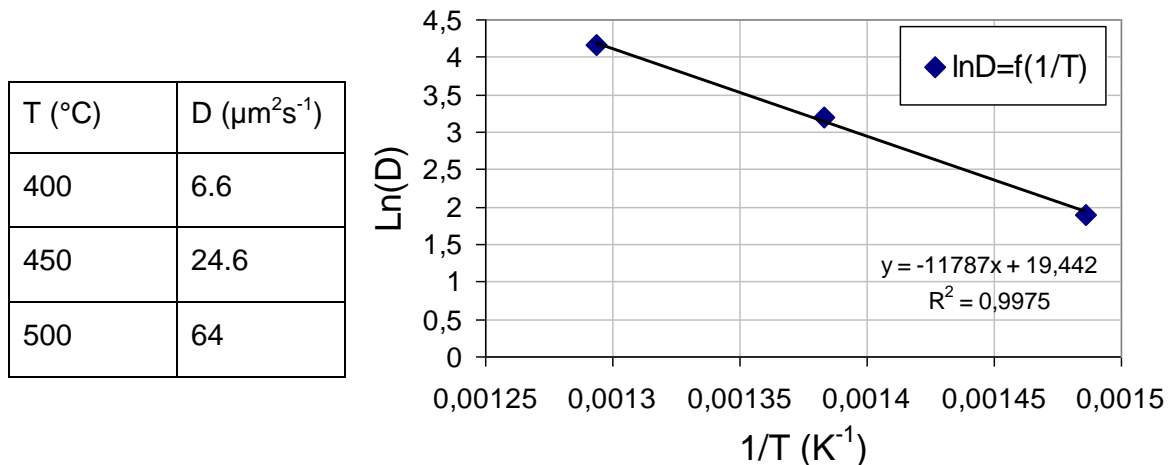


Figure 47 : Ni_3S_2 / NiS ($\text{Ni}_{48.72}\text{S}_{51.28}$) diffusion couple at 400°C holding time 6h30-16h and 26h: the thickness of the Ni_9S_8 shows a quadratic evolution as function of time.

Regarding the temperature dependence of the interdiffusion coefficient, the values of Q and D_0 for the Arrhenius law $D = D_0 \exp(-Q/RT)$, can be derived from the measurement of the interdiffusion coefficient D at different temperatures. Q corresponds to the slope of $\ln D = f(1/T)$ and D to the intercept with the y-axis.

Figure 48b summarizes on an Arrhenius plot the experimental results on the interdiffusion coefficients measured at three temperatures (400-450-500°C). The interdiffusion coefficients are also reported in Figure 48a. Since the experimental data are accurately described on a semilog plot as function of $1/T$ as a linear function (Figure 48) the activation energy can be extracted from the slope: $Q = 98 \text{ kJ/mol}$. In addition, the intercept with the y-axis gives the value of $D_0 = 2.8 \cdot 10^8 \mu\text{m}^2\text{s}^{-1}$.



(a) Interdiffusion coefficient at three temperatures

(b) Arrhenius plot $\ln D = f(1/T)$.

Figure 48 : Determination of Q and D_0 through Ni_3S_2 / NiS ($\text{Ni}_{48.72}\text{S}_{51.28}$) diffusion couple: $Q = 98 \text{ kJ/mol}$, $D_0 = 2.8 \cdot 10^8 \mu\text{m}^2\text{s}^{-1}$

IV.3 Discussion and concluding remarks

Concerning the present results, a number of experimental difficulties have to be mentioned. The experiments have been carried out on those samples with the best possible quality for the Ni-S system. However, because mainly of the brittleness of the starting samples, it was difficult to have high quality surface contact: the cross sections of the diffusion couple often showed irregular interfaces. The present results correspond to a selection made on the area for which we estimate that a good contact between phases was achieved. In addition, for the thin Ni₉S₈ layer, the interdiffusion zone was not sufficiently developed to maintain contact the two parts of the diffusion couple. Then frequently the diffusion couples break before observations.

In spite of these technical problems, the results are consistent with what is expected for the evolution of diffusion depths and reaction zone thickness controlled by diffusion. It was possible to estimate the interdiffusion coefficient in the α phase and to derive experimentally the parameters of the Arrhenius law governing this diffusion.

Since the interdiffusion coefficient of interest in the NiS phase transformation are those at T=200-300°C, an extrapolation of the diffusion coefficient to low temperature is necessary. From the measured Arrhenius law, the interdiffusion coefficient at 260°C should be about $0.07\mu\text{m}^2\text{s}^{-1}$ which corresponds to a diffusion depth of 18 μm . According to the composition profile at the α/β interface for a heat treatment at 260°C as reported in Chapter 2, at this temperature a diffusion depth was estimated to be 60 μm . This value is actually significantly different from the depth value estimated with the extrapolated diffusion coefficient at 260°C (18 μm). Assuming that the activation energy is correct, this discrepancy could be related to the poor extrapolation employed to estimate D_0 . In order to have a more reliable interdiffusion coefficient in the low temperature field, we have modified the D_0 parameter to correspond with the low temperature value for D. Then the corrected interdiffusion coefficient parameters in the Arrhenius law are $D_0=2.9 \cdot 10^9\mu\text{m}^2\text{s}^{-1}$ and $Q=98 \text{ kJ/mol}$.

Regarding the effect of iron impurities on diffusion, the experimental observation indicated that Fe slows down the diffusion. It is worth remembering that iron occupies the same sites as Ni and that overstoichiometry in the α structure originates from structural vacancies in the Ni crystalline [5, 48, 49] structure. Then adding iron reduces the vacancy density and thus causes the deceleration of the Ni diffusion. In addition, the Fe atomic volume, which is larger than that of Ni may also contribute to the slowing down of the S diffusion.

Chapitre V. NiS phase transformations: *in situ* observation and modelling under isothermal conditions

V.1 Introduction:

In Chapter 2, which was devoted to the microstructures typical of the NiS phase transformation, we identified the different characteristic morphologies and the related mechanisms, i.e. partitioned or partitionless growth corresponding to different compositions and temperatures. In addition, for several cases, the evolution of the transformed volume fraction has been obtained using calorimetric measurements (Chapter 3). The macroscopic study of the kinetics, analyzed via a phenomenological Johnson Mehl Avrami Kolmogorov (JMAK) approach, provided a convenient description of the phase transformation but with the limits inherent to this kind of modelling: the composition and temperature effects are not accounted for on a physical understanding of the governing mechanisms, and as a consequence, the parameters of JMAK law are purely fitting parameters. The present contribution aims at a more physically based description of the transformation kinetics.

In addition to the identification of mechanisms, the provision of the morphology (globular or lamellar) of the daughter phase, and the expected growth rate of the linear dimensions (linear or quadratic in time), a quantitative modelling requires i) the values of the interdiffusion coefficient (or at least a reasonable estimation), and ii) a proper description of the nucleation rate for each morphology. The interdiffusion coefficients have been determined using diffusion couples as reported in Chapter 4. The nucleation rate and the interface velocity of the growing particles, for each morphology, was experimentally studied here using *in situ* follow up of the transformation by optical microscopy during an isothermal treatment. This set of experiments provided the interface velocity, to be analyzed according to the mechanisms proposed: globular or lamellar growth, controlled by diffusion, (with Sulphur partition or partitionless), and the nucleation rate which was used as an input in a macroscopic model for the transformation kinetics.

It is worth noticing that *in situ* following of the transformation allows the acquisition of several qualitative and quantitative pieces of informations on the transformation. On the one hand, it gives direct information on the spatial distribution of the nucleation sites and on their morphological evolution. On the other hand, the evolution of the nuclei number, the interface velocities and the transformed volume fraction as function of time can be measured.

This chapter is organized as follows. In section V.2, the experimental set up employed to carry out the Optical *in situ* experiment will be presented. In section V.3, the experimental results concerning isothermal treatments at various temperatures and for different compositions will be presented, first qualitatively to identify the different morphologies, then quantitatively as far as transformed volume fraction, nucleation rate, and growth kinetics are concerned. In section V.4, a physically based model will be proposed for the growth kinetics, and coupled with the observed nucleation rates, will provide a global macroscopic model to be compared with the kinetics already obtained by DSC experiments (chapter 3).

V.2 Experimental conditions of the *in situ* optical microscopy observations

An *in situ* study of the phase transformation in the NiS sample was carried out with polarized light microscopy using a hot stage with controlled heating. The Linkam LTS 350 hot stage was operating under air and allowed for observation at 100 X magnifications during heat treatment. The heating was achieved by convection mode using Linkam TMS94 temperature controller. The maximum heating rate was used (30°C/min) in order to avoid transformation during the heating step.

Metallographic observations were carried out on mechanically polished samples (1µm). Microstructure evolution was observed during different isothermal heat treatments starting from NiS samples in the hexagonal α phase. The range of temperature studied was limited to 200-300°C which corresponds to evolution time compatible with optical microscopy observation and hot stage stability.

Microscopy images (640X480 pixels) have been recorded at a magnification of 100X which corresponds to a spatial resolution of about 3µm (however a better resolution was obtained in the following because interface migration corresponds to relative measurement). The recording frequency depends on the transformation kinetics and was the same during one transformation. The transformations have been followed to completion except for the very high overstoichiometric sample, because of the slowing down of the transformation.

In principle, owing to the color contrast exhibited by the α and the β phase grains under polarized light, image analysis can be used. Nevertheless, the automatic identification of phases was possible only when the transformation occurred in one α grain. Hence to have statistics on many grains, a manual counting has been preferred. In addition, the surface relief, which appears during transformation, because of the volume change, tends to blur the images which would prevent following of the whole transformation with an automatic analysis. Of course this manual counting method forces one to make the measurement only on a set of images selected at different stage of the transformation.

V.2 Experimental conditions of the in situ optical microscopy observations

The α phase samples were heated at $\sim 30^\circ\text{C}/\text{min}$ up to the holding temperature at which the transformation kinetics were studied for a duration depending on the $\alpha \rightarrow \beta$ -NiS transformation rate. After this high temperature holding, the sample was cooled down to room temperature.

As usual with *in situ* microscopy using a hot stage, care must be taken to avoid experimental artefacts. There is a risk that the transformation observed on the surface does not correspond to the bulk behavior because, for instance, a higher nucleation rate can operate at the surface. However, cross sections taken from 5 of the investigated samples have clearly indicated that in the present case the surface observations obtained by *in situ* optical microscopy were representative of the behavior of the bulk material. A second risk for *in situ* observation comes from the possibility of desulphurization of the NiS samples. Some desulphurization has indeed occurred because we observed a thin Sulphur pollution on the hot stage window. But composition measurement after *in situ* experiment do not show a significant loss of Sulphur compared to the usual local sample fluctuation ($\pm 0.14\text{at}\%$ according to microprobe analysis). Finally, to ensure the validity of the hot stage experiment, the evolution of volume fraction derived from the *in situ* observation can also be compared to the one obtained by the earlier DSC measurements. The good agreement observed allowed us to confirm the reliability of the present hot stage microscopy results.

The surface fraction gives a representative transformed volume fraction since the initial α phase is polycrystalline. Then the transformed volume fraction is extracted from the images using the intercept method. This method consists of the measurement of the number of intersections between a grid node and β phase in a given image. Then the estimation of the transformed volume fraction is given from the ratio between the number of intersections and to the total node number. Regarding the precision of the analysis method, using the intercept method the error in the measured transformed volume fraction is about $\pm 5\%$. In the NiS transformation, as it occurs with a volume change, the quality of the image degrades as the transformation progresses, therefore only the zones with the best contrast are considered in the measurement.

The nucleation rate was measured from the evolution of the number of nuclei appearing during the phase transformation between two images taken at successive times. All new β grains appearing at the surface, even if they could correspond to emerging grains growing from the volume, are considered as new nuclei. Of course this effect should be taken into account when calculating the nucleation density (in volume) from that observed at the surface.

Regarding the interface velocity, it is worth noticing that, for anisotropic growing particles (here lamella), the apparent interface velocity is dependant on the growth direction. The measurement of interface velocity corresponding to a given direction requires knowledge of the orientation relation ship between the growing particle and the mother phase. Since the sectioning direction is randomly chosen then the β grains which are more likely to correspond to the shape identified for the transformation are chosen for study. A set of 3 β lamellas was chosen for the measurement of the interface velocity in this work. In addition it is known from the study of the phase transformation (Chapter 2) that the growth of a given grain of the second phase could be influenced by other growing particles. Hence the measurements were done, when possible, on β lamella growing far enough from the other lamella to limit the impingement effects. The interface velocity was determined by following the growth of one β

lamella and consisted of the measurement of the interface position at different time of transformation. The measurement of the interface velocity is done on the image using 2000X1500pixel (1pixel ~1 μ m) resolution.

V.3 *In situ* observations of the phase transformations

The objective was to measure the evolution of the nucleation rate, interface velocity and the volume fraction corresponding to the typical morphologies identified for the NiS phase transformations: namely the globular, lamellar, coarse lamellar and block morphology as reported in Chapter 2. These characteristic morphologies correspond to specific domains of the NiS phase diagrams as summarized in Figure 49. Since the transformation is known to slow down considerably when the overstoichiometry increases (Chapter 2, Chapter 3), it was not possible to achieve *in situ* observation for the lamellar + eutectoid β +Ni₃S₄ morphology case. For this composition, the transformed volume fraction is only 30% after 10 hours holding at 200°C.

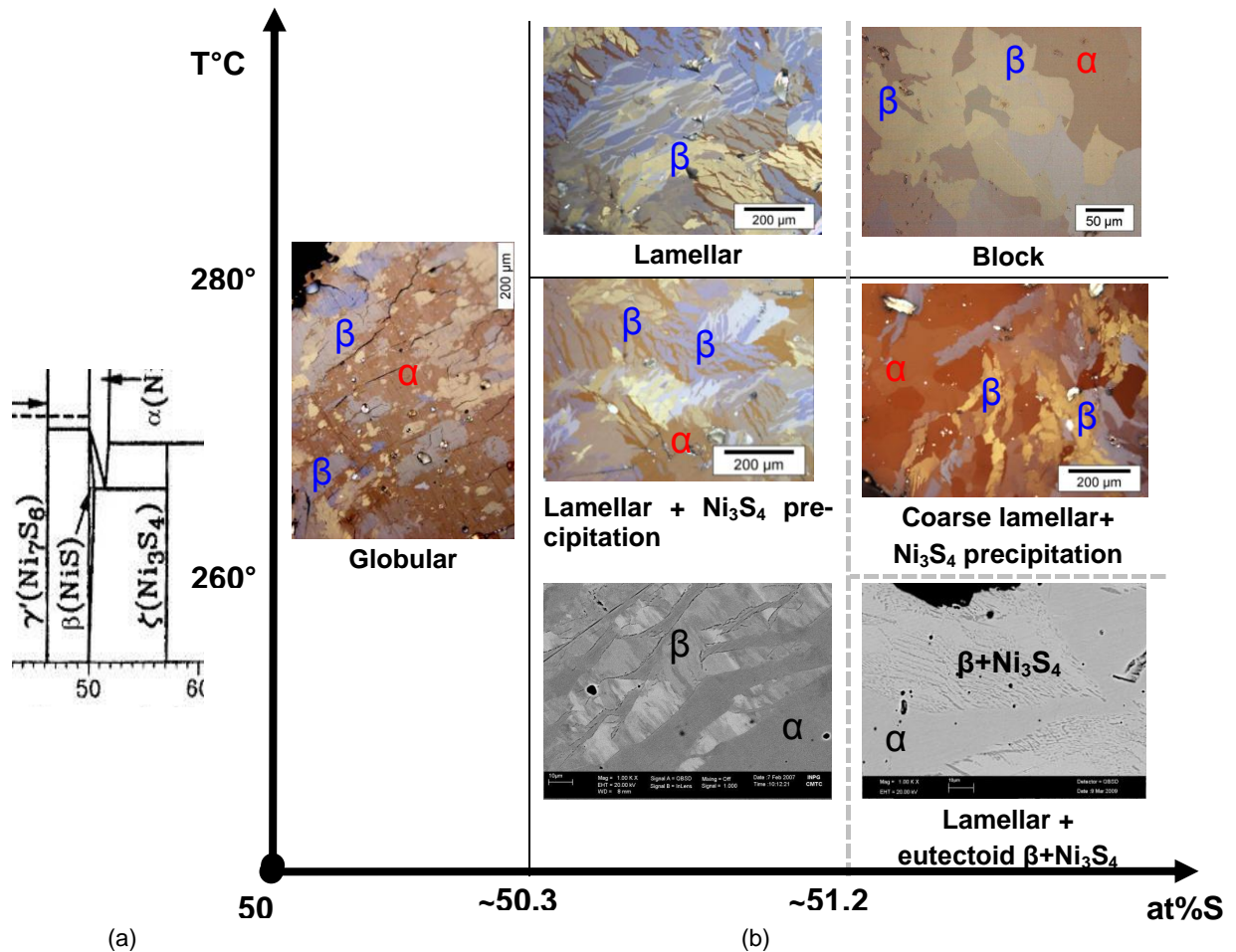


Figure 49: (a) Ni – S phase diagram after Nash.P *et al* (1991)[22]. (b) Typical transformation morphologies observed in the different field of the phase diagram for temperature from 200-300°C and composition from 50 to 51.28at%S.

V.3 *In situ* observations of the phase transformations

V.3.1 Qualitative description of the evolution of the different morphologies

Before deriving quantitative information from the *in situ* sequences, we present a qualitative description of the microstructural evolution which will emphasize on the details related to the mechanisms associated to the morphologies of interest here (globular, lamellar, coarse lamellar and block).

a. Globular morphology

Figure 50 shows micrographs recorded after different transformation times on near stoichiometric sample known to display a globular morphology. According to the sequence of images in Figure 50, we note that a large number of β phase grains appeared homogeneously distributed appear in the different α phase grains. This simultaneous nucleation is in agreement with the mechanism proposed from the analysis of DSC curves: i.e. linear growth of spheroidal grains from pre-existing nuclei. The β phase grains show isotropic shape and maintain such a shape when growing. When β grains nucleate close to a α phase grain boundary, the β phases, when they grow, cross the grain boundary. This observation is consistent with the massive transformation mechanism which was already suggested from our microstructural study (Chapter 2). After 10 minutes, total transformation is achieved as expected for the massive transformation operating for this near stoichiometric sample.

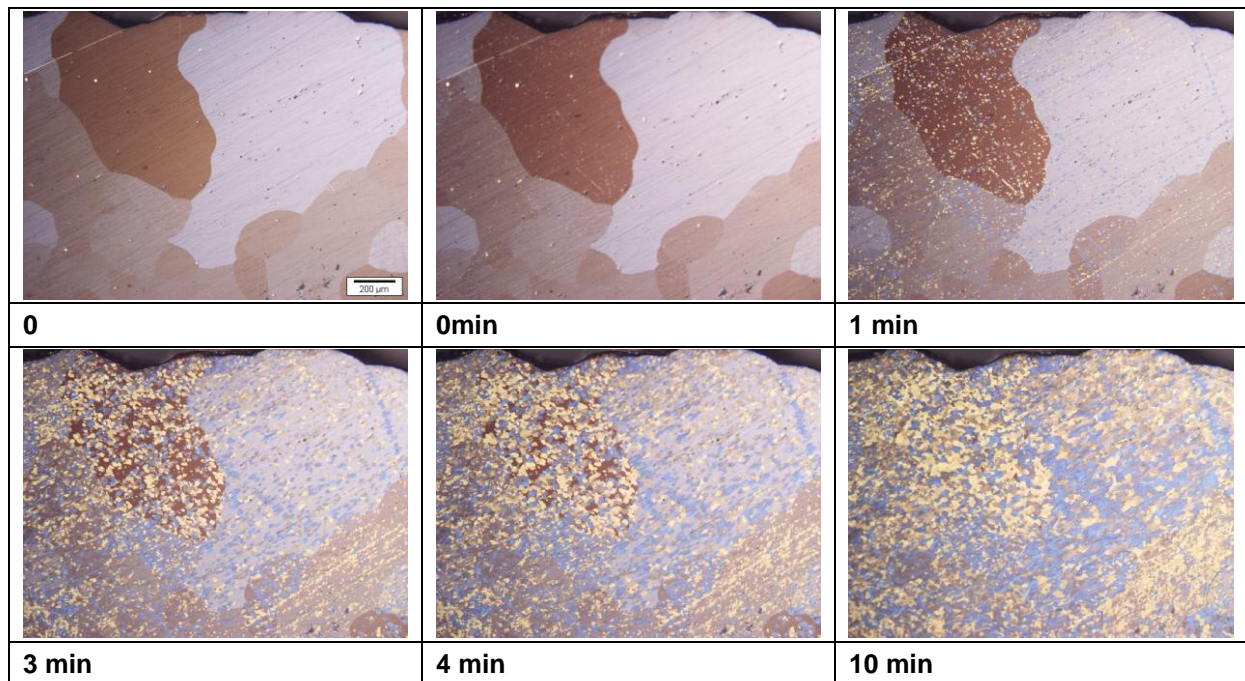


Figure 50: *In situ* observation of the Globular morphology growth: complete transformation after 10min. Near stoichiometric NiFeS sample (49.7at%S-0.5 at%Fe) at 200°C

b. Lamellar morphology

Figure 51 shows a sequence of images corresponding to the growth of the β grain in a case expected to give a lamellar morphology. It is remarkable that here the first β grains are observed after a delay of about 5 min. The nucleation does not occur simultaneously but is observed continuously throughout the transformation. The observation of continuous nucleation is important information for the transformation mechanism; it is consistent with the constant or increasing nucleation rate proposed from the JMAK analysis of DSC curves (Chapter 3). The β phase grains are not distributed very homogeneously from one α grain to another and frequently β grain nucleation occurs at a grain boundary. The β grains grow without crossing the grain boundary. After 140 minutes, a total transformation seems to be achieved (though the small volume fraction of Ni_3S_4 phase formed at the end of the transformation cannot be observed in optical microscopy).

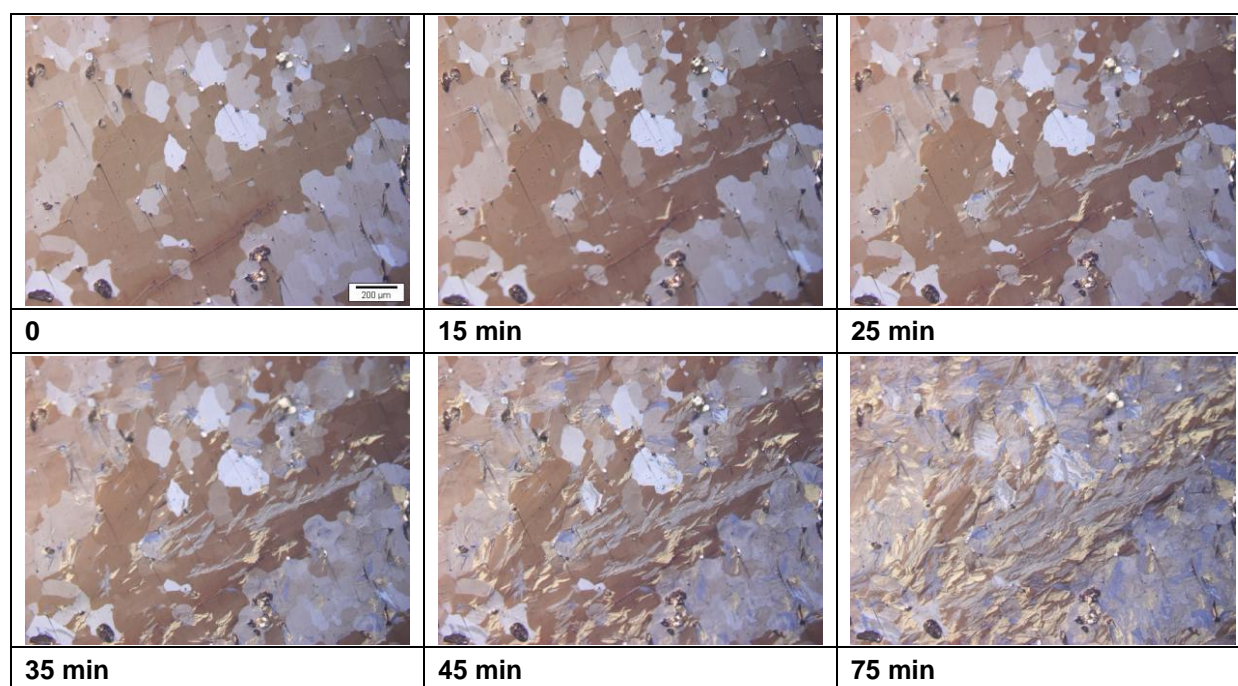


Figure 51: *In situ* observation of the lamellar morphology growth: complete transformation after 140min. The lamellar morphology is well illustrated in the central zone of the micrograph, and is ill-defined in other grains because of the random sectioning. Overstoichiometric NiS sample (51.18at%S) at 200°C 140min

c. Coarse lamellar morphology

Figure 52 displays a sequence of image of the transformation for the composition and temperature corresponding to the coarse lamellar morphology. The nucleation of β phase grain was also heterogeneous and occurred continuously during the transformation. However, the β phase grains are less numerous and larger than in the lamellar morphology case. In the present case, when growing, the β grains do not cross the grain boundary. This indicates that the growth mechanism is dependent on the orientation relation and then the orientation relationship is relevant for both nucleation and growth steps.

V.3 *In situ* observations of the phase transformations

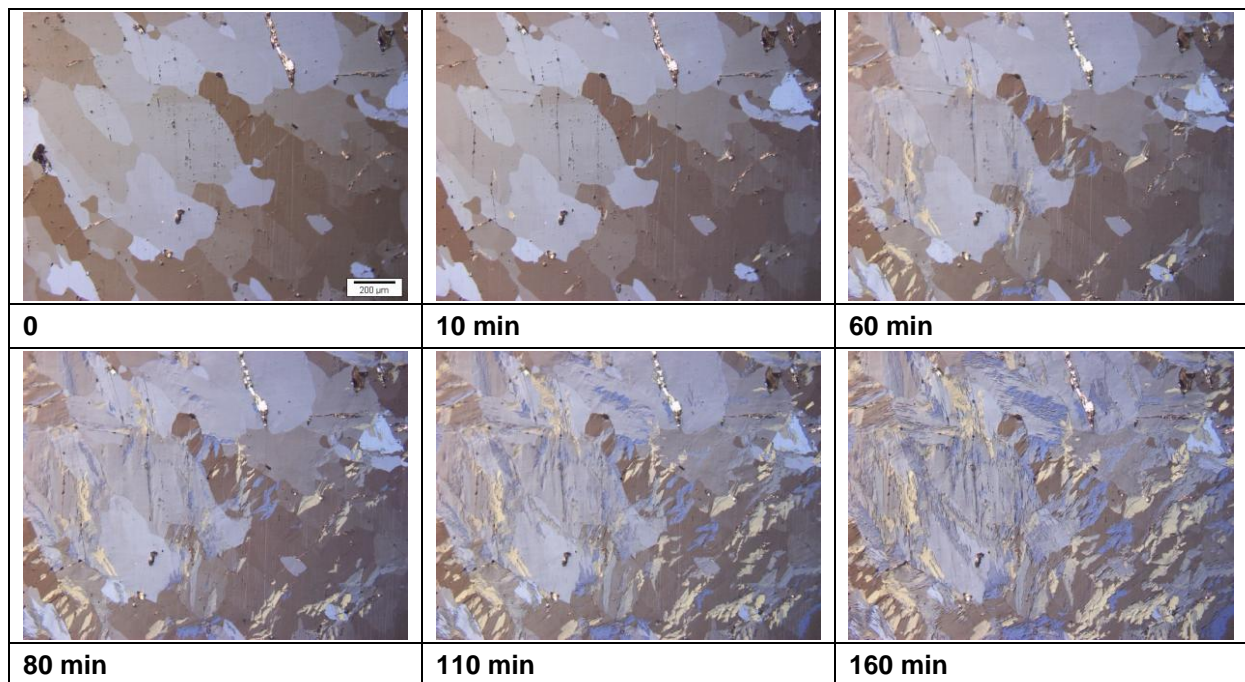


Figure 52: *In situ* observation of the coarse lamellar morphology growth: The microstructure at the end of the heat treatment shows $\alpha+\beta$ domain because the heat treatment is stopped before the end of the transformation since the transformation is very slow.

NiS very overstoichiometric sample at 260°C: partial transformation after 160min

d. Block morphology

The sequence of images in Figure 52 illustrates the transformation for the domain associated to the block morphology. The first β phase grains were observed after a delay of about 10 min. The nucleation occurred continuously during the transformation. The nucleation was heterogeneous and occurred mainly on grain boundaries. When they grew, the β phase grains crossed the grain boundaries. At the end of the transformation, a coexistence of α and β phases is observed as expected from the phase diagram. The growth mechanism in this case should be independent of the orientation relation between α and β grains and the orientation relation is then only relevant for the nucleation step.

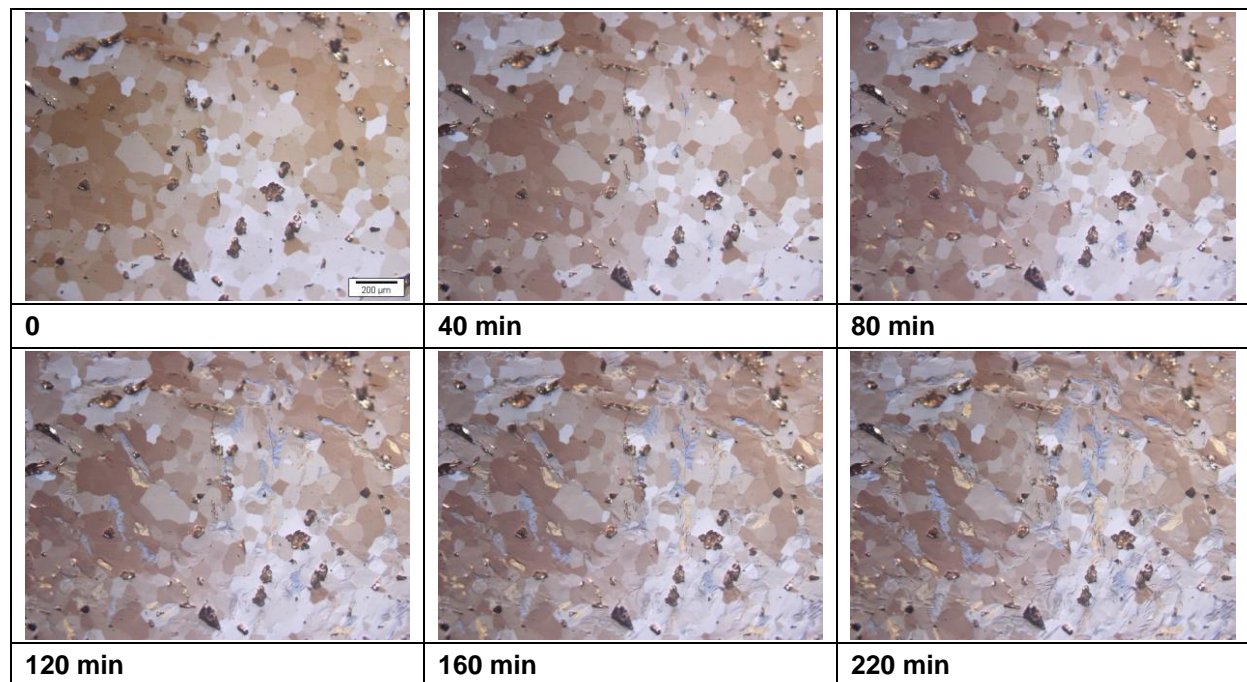


Figure 53: *In situ* observation of the block morphology growth: The microstructure at the end of the heat treatment shows $\alpha+\beta$ domain because the heat treatment is stopped before the end of the transformation since the transformation is very slow.

Very overstoichiometric NiS sample: 220min holding at 290°C

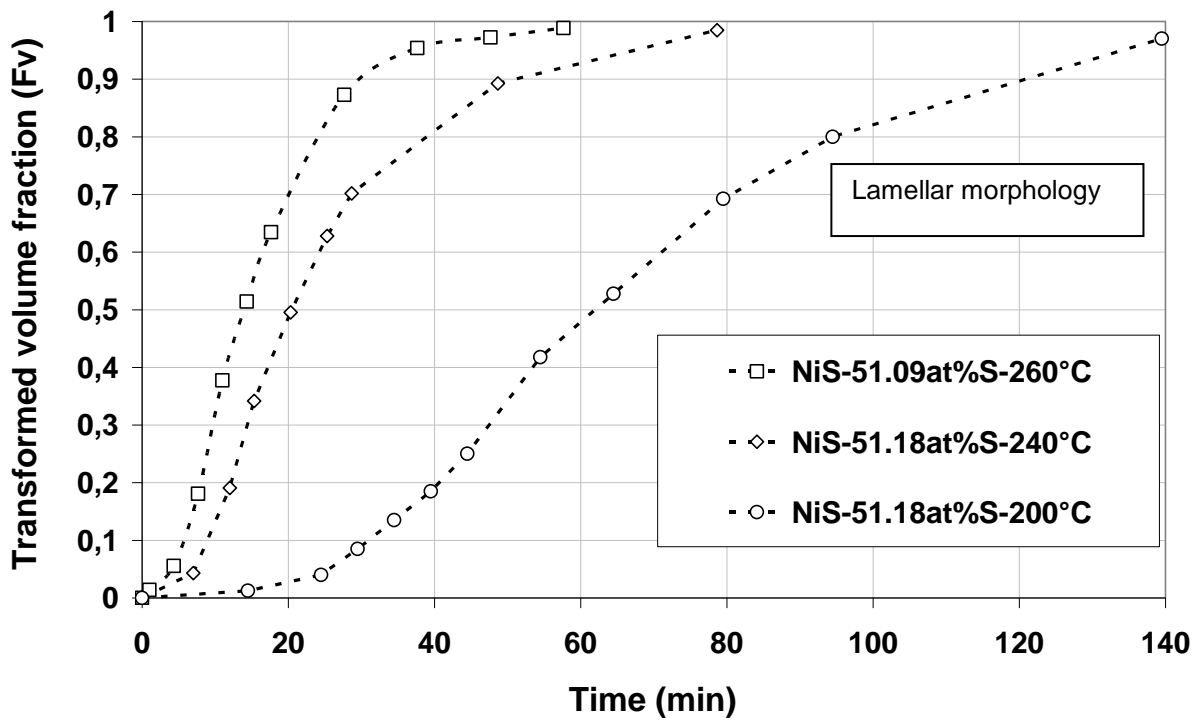
V.3.2 Quantitative study of the phase transformation for the different morphologies

The sequence of images describing the transformation will be now used to extract quantitative information on the transformation mechanisms and kinetic laws as can be done through the measurement of the transformed volume fraction F_v , the nuclei density N_v and the velocity of the interface V_i .

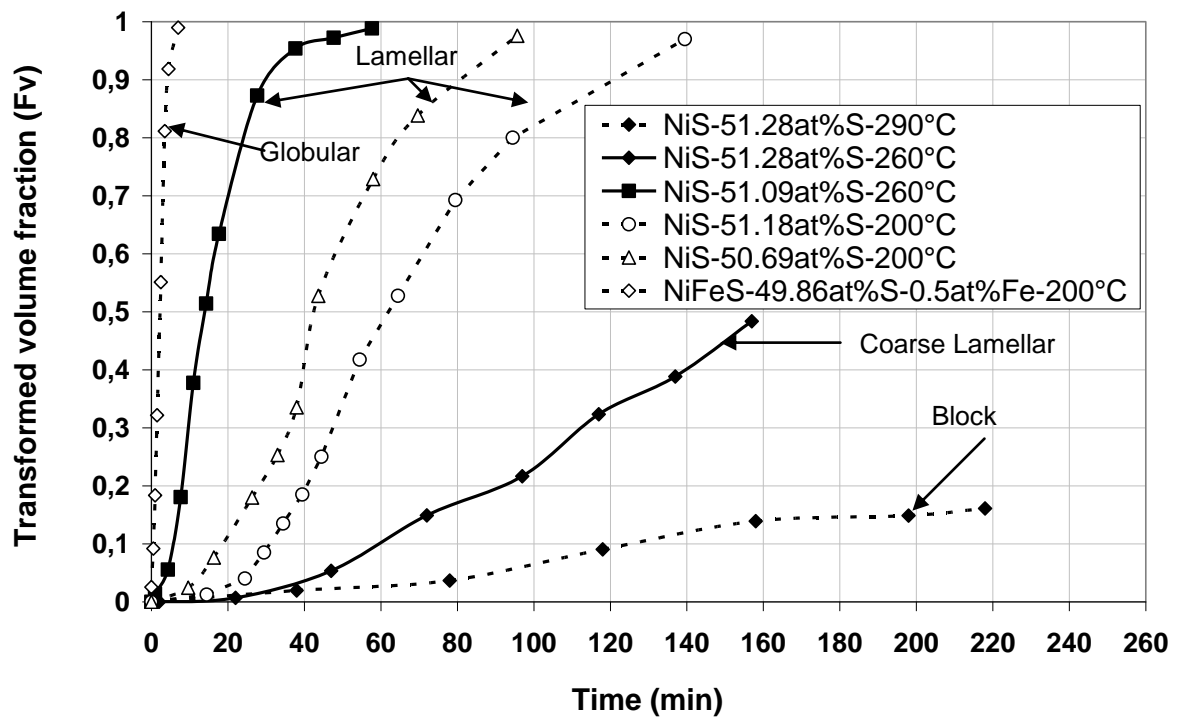
a. Transformed volume fraction

The transformed volume fraction can be obtained using image analysis of the *in situ* sequence as mentioned earlier. The results for different compositions and temperatures are shown in Figure 54. Figure 54a illustrates the strong influence of temperature on the transformed volume fraction for samples characterized by an overstoichiometric composition (around 51.1at%S). These curves are in good agreement with the one obtained from analysis of isothermal DSC curves. Figure 54b displays the evolution of the transformed volume fraction with composition for samples of different overstoichiometry at a constant temperature together with curves corresponding to very overstoichiometric samples at higher temperature (260°C- 290°C). These curves for the 200°C isotherms clearly illustrate the deceleration of the transformation when increasing overstoichiometry. The ones corresponding to higher temperatures provide a comparison of the impact of composition with that of temperature: for the high overstoichiometry 51.28at%S, it will be necessary to raise the temperature to 260°C or even 290°C to have a transformed volume fraction comparable to the one of the overstoichiometric sample at 200°C.

V.3 In situ observations of the phase transformations



(a): Temperature effect on the evolution of the transformed volume fraction for the lamellar morphology. The transformation time range of these 3 overstoichiometric samples was compared to TTT diagram (section III.4.2): a very good agreement between DSC and *in situ* observation is obtained.



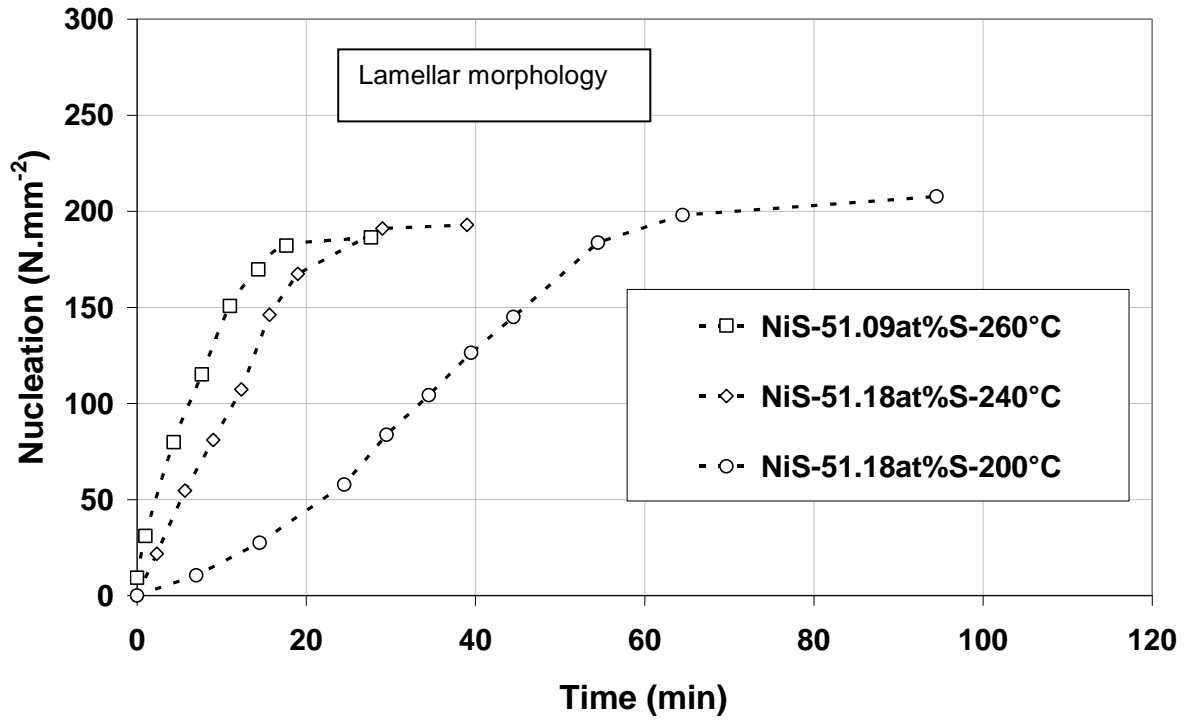
(b) Fv evolution for the globular lamellar block and coarse lamellar morphologies

Figure 54: Transformed volume fraction obtained from *in situ* observations for the typical morphologies (the sample NiFeS is used to illustrate the near stoichiometric evolution)

b. Nucleation rate

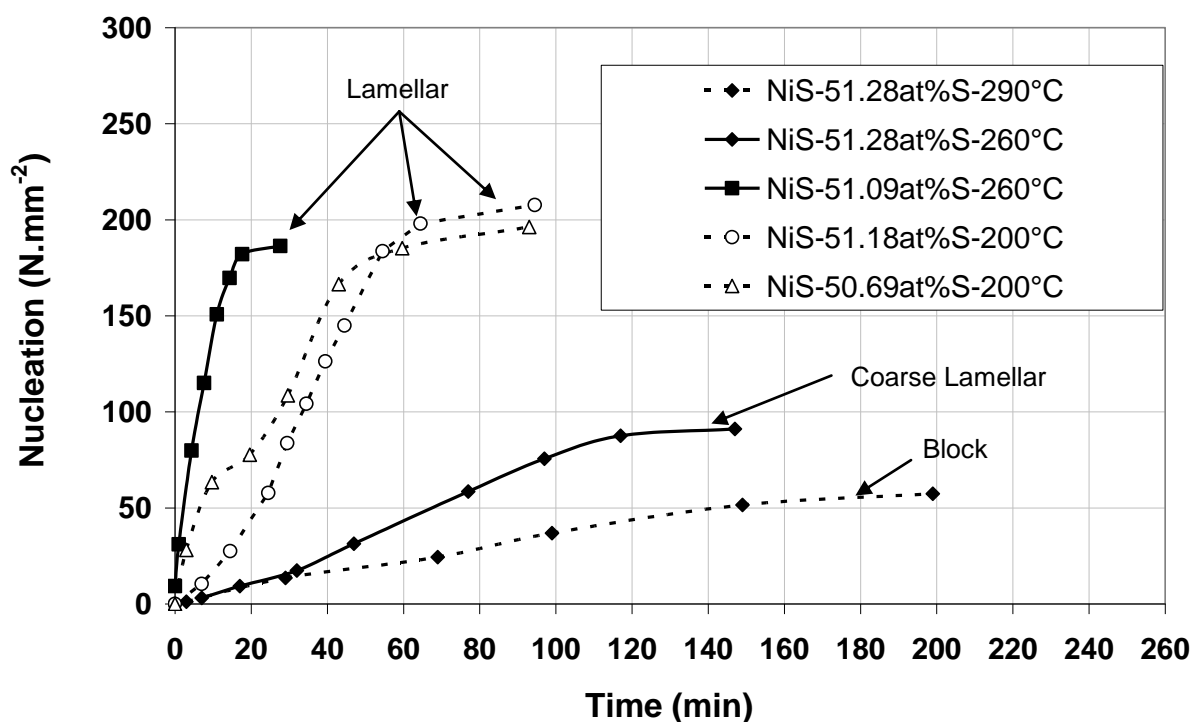
The nucleation rate has been measured from the sequence of images. First a surface density of β phase grains $N_s(t)$ can be measured along the transformation and it is further transformed into a bulk density. In the following we will concentrate on the overstoichiometric sample since for the near stoichiometric sample, the nucleation occurs at the beginning of the transformation (around 1250 /mm²) and no new nuclei subsequently appear.

For overstoichiometric samples, the $N_s(t)$ curves in Figure 55 all show two steps in the nucleation regime: a first step with continuous increase of the number of nuclei and a second one with negligible nucleation. The increasing number of nuclei at the beginning of the transformation can be described by a constant nucleation rate. Figure 55a displays the curves $N_s(t)$ describing the nucleation during the transformation for an overstoichiometric sample (around 51.1at%S corresponding to lamellar morphology) and for different temperatures. Obviously when increasing the temperature, the nucleation rate increases. But as illustrated by Figure 55b, the nucleation density saturates at lower value while increasing overstoichiometry.



(a) Surface nucleation obtained from *in situ* observations for the lamellar morphology (overstoichiometric sample around 51.1at%S)

V.3 In situ observations of the phase transformations



(b) Surface nucleation evolution for the lamellar, block and coarse lamellar morphologies

Figure 55: Surface nucleation obtained from *in situ* observations for the typical morphologies (for the globular morphology constant nuclei density during the transformation)

A significant reduction of the total number of nuclei to about one half is observed when the overstoichiometry changes from 51.1at%S to 51.28at%S at 260°C. The number of nuclei is also reduced of about one half when the temperature is increased from 260 to 290°C for 51.28at%S sample. This significant reduction of the nucleation rate and nuclei number is one of the reasons of the transformation drastic slowing down when the overstoichiometry increases.

The measured nucleation density and nucleation rate are consistent with the JMAK analysis of the DSC curves (Chapter 3). According to this analysis, the obtained Avrami exponents could correspond to a mechanism with increasing or constant nucleation rate for overstoichiometric compositions or to a mechanism with a zero nucleation rate for near stoichiometric samples. The relevant information here is that nucleation rate is larger when temperature is increased and when the overstoichiometry is decreased.

It is worth noticing that the sample containing 50.69at%S exhibits a nucleation curve with a kind of intermediate plateau (Figure 55). This low overstoichiometry sample shows as expected a high nucleation rate. Therefore such a nucleation plateau could be explained by the successive activation of nucleation sites of different energy. The first stage will then result from the saturation of the lower energy nucleation sites. This is an illustration of the information on the mechanisms which is contained in the nucleation density evolution during the transformation.

In principle, a physically based model for phase transformation should comprise a model for nucleation. However, classical nucleation models are notoriously inaccurate [50]. Therefore the strategy chosen in the present study will be to develop a model for growth rate, and to use as an input the nucleation rate observed experimentally, in order to obtain a macroscopic kinetic law. In order to do so, we need to derive, from the nucleation rate measured at the surface, a bulk nucleation rate. A simple derivation is as follows: if N_s and N_v are the number of grains per unit surface and per unit volume respectively, one has the following relation:

$$N_s = N_v \cdot L \quad \text{eq 10}$$

With L a characteristic size of the shape (for example $2R$ for spherical shape and the length for cylinder) and called here depth value. The L value should take into consideration the nuclei size and the anisotropy of the morphology. The experimentally observed number of grains per unit surface is reasonably described as linear with time:

$$N_s(t) = b \cdot t \quad \text{eq 11}$$

b is the slope of the surface nucleation curves of Figure 55 at a given composition and temperature.

Table 6 summarizes the nucleation rate obtained during this study at different conditions of composition and temperature (Figure 55). It is worth noticing that, for the lamellar morphology, a temperature dependence of nucleation could be measured and could be accounted for using an Arrhenius law $b = b_0 \exp(-E/RT)$ (Figure 56).

Mor- phology	Globular (200°C)	Block (290°C)	Coarse lamel- lar (260°C)	lamellar		
				200°C	240°C	260°C
N_s ($\mu\text{m}^{-2}\text{s}^{-1}$)	$125 \cdot 10^{-5}$ (cst)	$5.8 \cdot 10^{-9}$	$1.23 \cdot 10^{-8}$	$5.6 \cdot 10^{-8}$	$14.6 \cdot 10^{-8}$	$17.8 \cdot 10^{-8}$
L (μm)	10	15	50	50	50	50
N_v ($\mu\text{m}^{-3}\text{s}^{-1}$)	$125 \cdot 10^{-6}$ (cst)	$3.88 \cdot 10^{-10}$	$2.46 \cdot 10^{-10}$	$1.12 \cdot 10^{-9}$	$2.93 \cdot 10^{-9}$	$3.56 \cdot 10^{-9}$

Table 6: Volume nucleation rate for the typical morphologies measured from the surface one

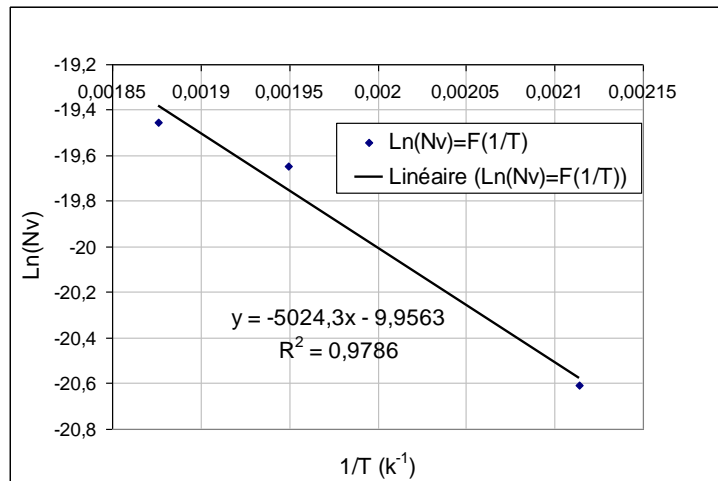


Figure 56: Temperature dependence of nucleation density for lamellar morphology:
Arrhenius law $N_v = N_{v0} \exp(-E/RT)$; $N_{v0} = 4.710^{-5} \mu\text{m}^{-3}\text{s}^{-1}$; $E = 41.7 \text{ kJmol}^{-1}$

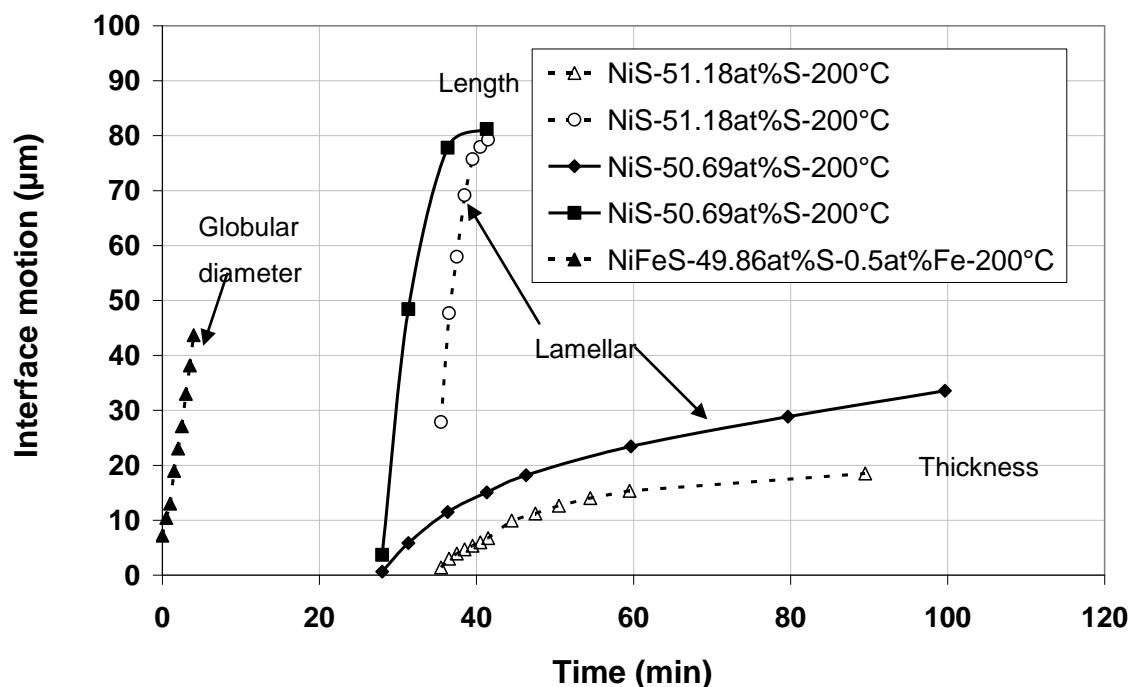
V.3 In situ observations of the phase transformations

c. Interface velocity

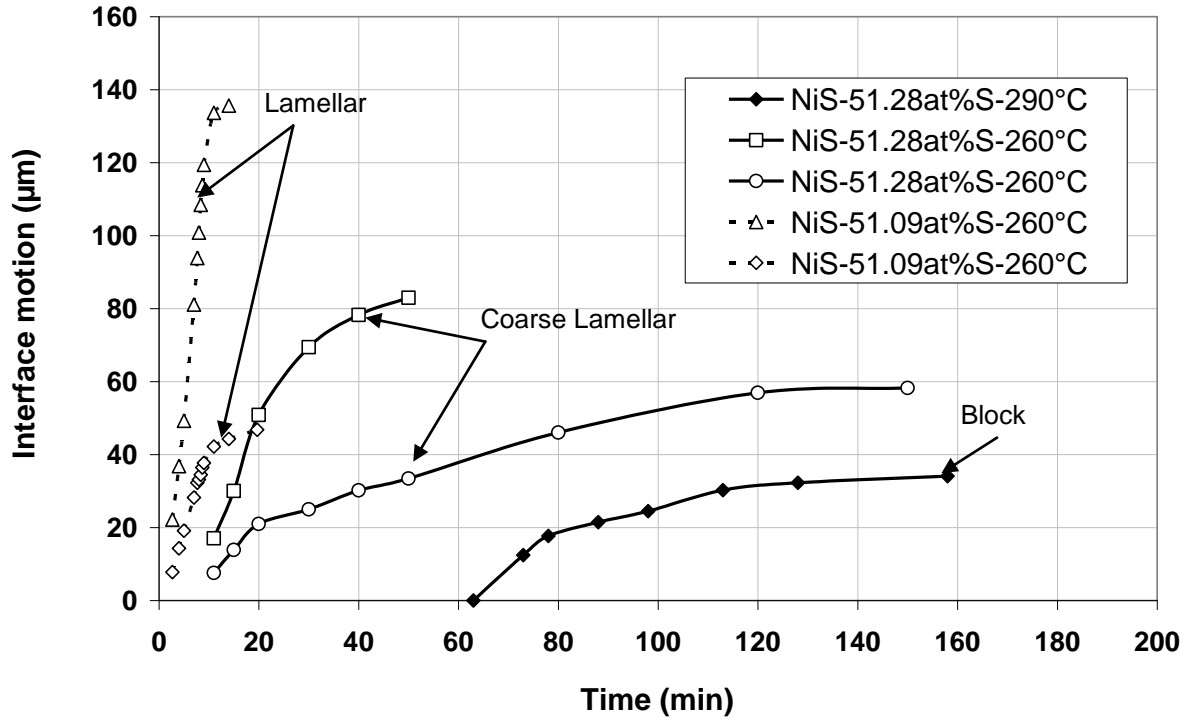
In situ optical microscopy allows an accurate measurement of the growth rate. Of course, for isotropic morphology (globular and block morphology) only one dimension characterizes the growth rate while for anisotropic morphology (lamellae) two dimensions must be considered corresponding to the large and small dimensions. It is worth noticing that, in addition to providing values for the velocity, the interface motion which is directly related to the mechanism controlling the growth also indicates the type of mechanisms involved. For instance, for a globular shape with a near-planar interface, a linear dependence indicates a transformation controlled by interface mechanism and a quadratic evolution indicates a long range diffusion controlled mechanism

Figure 57 displays the results for interface motion measured in samples of different compositions and temperatures. The shift along the time axis corresponds to the nucleation starting time. Figure 57a and b, show decreasing slopes with increasing overstoichiometry and with decreasing temperature. In other words, the velocity of the interface decreases with decreasing temperature and increasing overstoichiometry which again contributes (together with the effect on nucleation notices above) to the slowing down of the transformation with increasing stoichiometry.

Regarding the globular morphology, the interface position shows linear evolution with time. For the lamellar morphology a linear evolution with time is observed for the lengthening but the thickening follows a quadratic law. Regarding the block and the coarse lamellar morphology, a quadratic evolution is observed for the growth in the two directions. Therefore we conclude that two models are necessary in order to take in account the quadratic and the linear particle growth law.



(a) Interface motion obtained from *in situ* observations for the lamellar and globular morphology at T=200°C. (A near stoichiometric NiFeS sample is used to illustrate the interface motion for the globular morphology)



(b) Interface motion for the lamellar block and coarse lamellar morphologies at high temperature

Figure 57: Interface motion obtained from *in situ* observations for the typical morphologies

V.4 Modelling of the phase transformation

At this stage we have all the experimental information required to model the transformation. First we have identified the mechanisms partitioned or partitionless depending on composition and temperature which means that we have knowledge on the time dependence of interface migration. When the transformation is globular and massive (i.e. without partition), dimensions increase linearly with time. When lamellar growth occurs, associated with partition, the diffusion controlled kinetics is expected to give a linear lengthening and a quadratic thickening. In addition, the *in situ* study of the transformation provides the experimental data to describe the nucleation. Then modelling of the transformed volume fraction (F_v) requires to integrate all these information along the transformation time range. In the following, the modelling of the interface velocity and later the calculation of the transformed volume fraction for each morphology will be carried out. It must be kept in mind that we restrict ourselves here to the evolution of the formation of the β phase since the Ni_3S_4 phase form after the β phase and represents only about 10% of the total volume fraction.

V.4 Modelling of the phase transformation

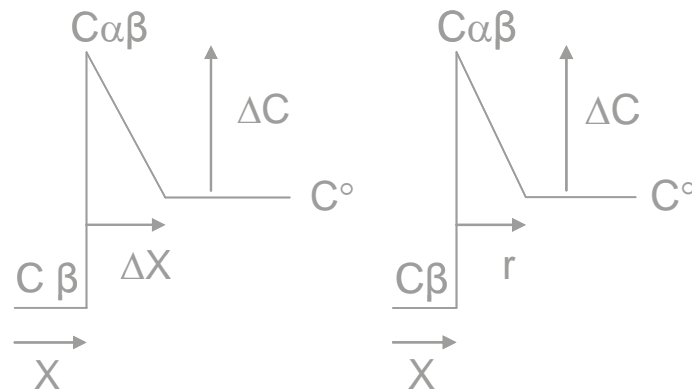
V.4.1 Modelling of the Interface velocity

Modelling the interface velocity is a key point because it will take in account the composition and temperature since concentration and interdiffusion coefficient are controlling the interface migration. It is worth noticing that since we are dealing with a binary system, partitioning is limited to only one element but may occur on a short or a long range.

For a globular morphology with partition of the solute elements, an appropriate model due to Zener model [51] is sketched Figure 58a. The interface migration is controlled by the composition of the initial α phase (C_α^0), the β phase composition C_β , and the composition at the interface $C_{\alpha\beta}$. The $C_{\alpha\beta}$ and C_β concentrations will be determined from the phase diagram. The interdiffusion coefficient D is known from the diffusion couple experiments (Chapter 4). The Zener model accounts for a long range partitioning of the elements. For lamellar growth controlled by diffusion, the Zener-Hillert model [37-39] sketched in Figure 58b should be considered. Interface migration is controlled by the concentrations and diffusion coefficient as in the Zener model but the diffusion distance is characteristic length r , which correspond to the interface curvature radius. This radius will be estimated for each morphology of the growing particle. In each case the equation governing the interface motion have been already established [37-39, 51] and writes as follow:

- For the Zener model:
$$X^2 = \frac{D(\Delta C)^2}{(C_{\alpha\beta} - C_\beta)(C_\alpha^0 - C_\beta)} \cdot (t - t_1)$$

- For the Zener-Hillert model:
$$V = \frac{D}{2 \cdot r} \cdot \frac{(C_{\alpha\beta} - C_\alpha^0)}{(C_{\alpha\beta} - C_\beta)}$$

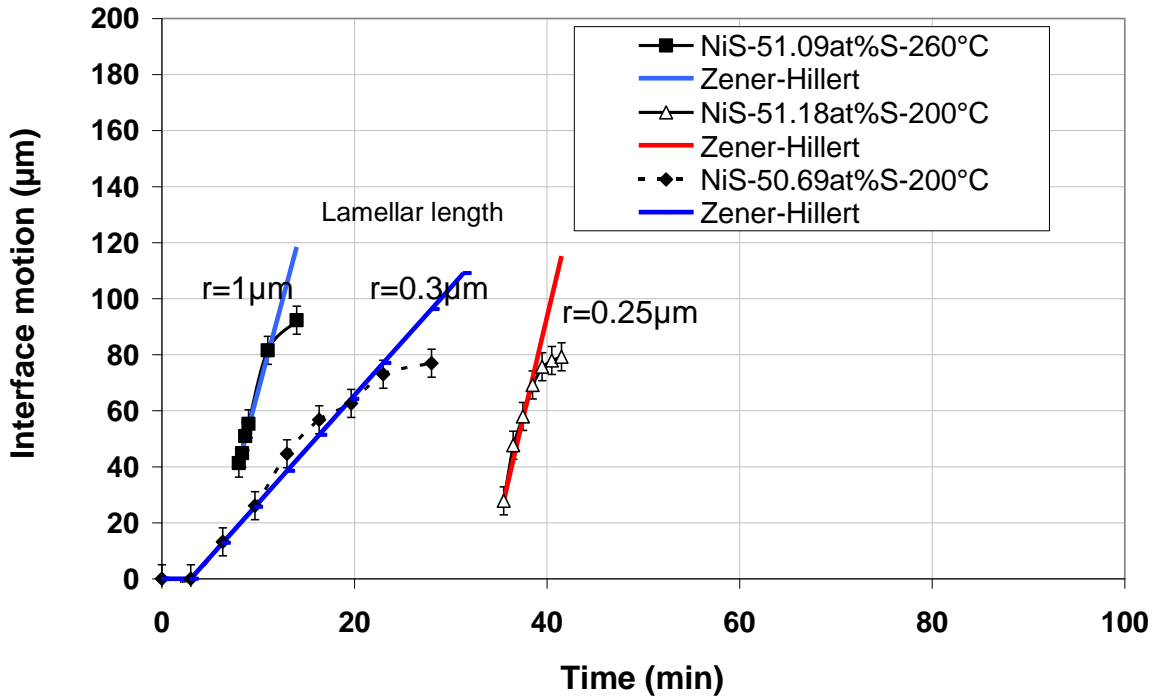


(a)-Zener: long range partitioning

(b) Zener-Hillert: short range partitioning

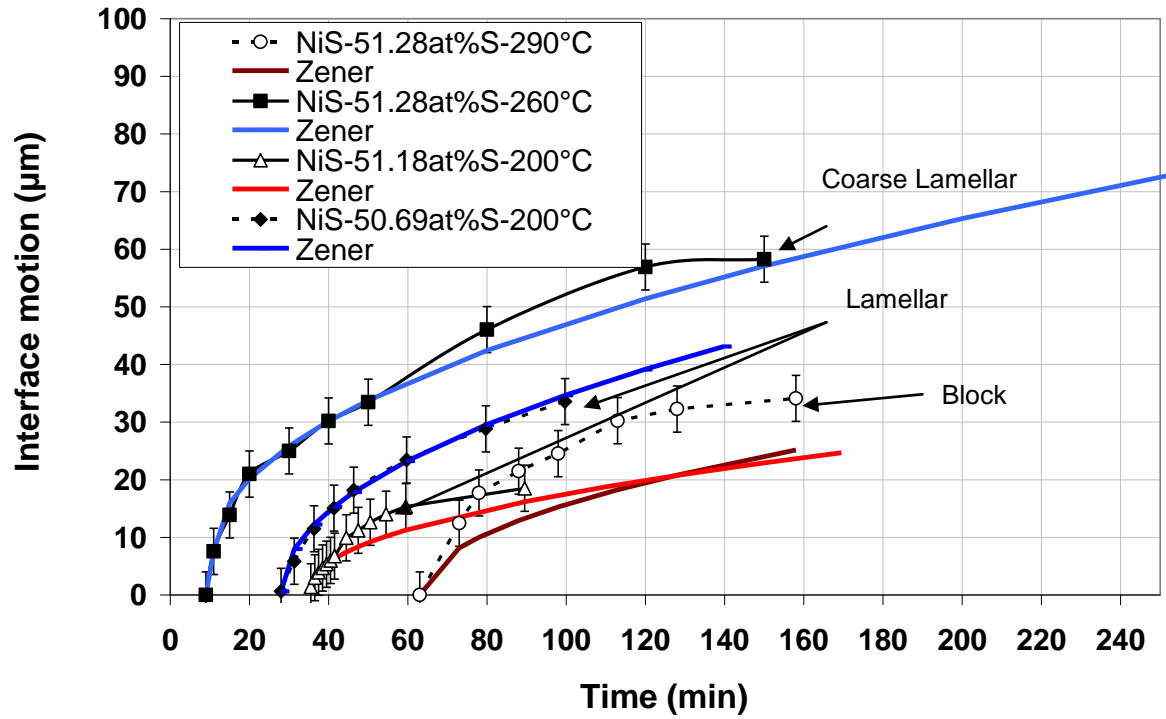
Figure 58: schematic representation of the phase composition near the moving interface for: (a) a long range diffusion controlled mechanism (b) short range diffusion controlled mechanism

These interface migration models can be used to describe the growth of the phases of different morphology identified for the NiS phase transformation. Actually only the morphologies corresponding to diffusion controlled mechanism can be accounted by Zener or Zener-Hillert models. For the globular morphology, since it results from a massive transformation, the interface velocity is constant and growth is linear along one dimension. Whether interface migration is described by a Zener or Zener-Hillert model can be directly obtained the experimental *in situ* observations. For instance the experimental interface migration shown in Figure 59 indicates quadratic or linear dependence which reveals respectively a Zener and a Zener-Hillert behavior. For the block, lamellar and coarse lamellar morphologies these models have been used to describe the interface migration. Figure 59a compares experimental and calculated migration laws for each morphology. Figure 59b corresponds to the Zener-Hillert case: a good agreement between experimental and model is obtained but in this case the tip radius is an adjustable parameter: r is about 300nm at 200°C and 1 μ m at 260°C which are in reasonable agreement with the values for tip radius. On the other hand, Figure 59a compares the Zener model to the experimental data: an excellent agreement is here observed without any adjustable parameters.



b) Lamella morphology lengthening: Comparison between experimental data and the calculated ones from the Zener-Hillert model

V.4 Modelling of the phase transformation



(a) Comparison experimental data showing a quadratic thickening of the lamella block and coarse lamellar morphology with the evolution given by Zener model.

Figure 59: Comparison between the Interface motions obtained from *in situ* observations and Zener or Zener-Hillert model

It must be noticed that the deviation of the lamellar growth rate from Zener Hillert model at long transformation times is likely to come from the soft impingement of diffusion fields which slows down the growth kinetics of the needles

V.4.2 Modelling of transformed volume fraction on isothermal heat treatment

To obtain the transformed volume fraction as function of time it is necessary to integrate over time the nucleation and growth of particles (particle growth being controlled by their shape and the related interface velocity; the nucleation rate being experimentally measured). Of course impingement has to be taken in account by a continuous reduction of the available volume during the transformation [20, 44], in the spirit of the JMAK formalism. Since each morphology has its own characteristic nucleation and interface migration rate they will be described separately in the paragraphs below.

a. Globular morphology

For the globular morphology, we will consider a spherical nuclei which diameter grows with a linear law because of the massive transformation mechanism. Nucleation being instantaneous, a constant density measured in the previous section is considered. After integration the transformed volume fraction is given by:

$$f = 1 - \exp\left(-\frac{4}{3} N_v \cdot \Pi \cdot d^2 \cdot t^3\right) \quad \text{eq 12}$$

d and N_v respectively correspond to the interface velocity and the nuclei density measured from *in situ* experiments. Figure 60 compares the modelled volume fraction to the one measured by the *in situ* experiment. An excellent agreement is obtained with a N_v density estimated using a depth value of $15\mu\text{m}$ which is a reasonable value with respect to the nuclei size.

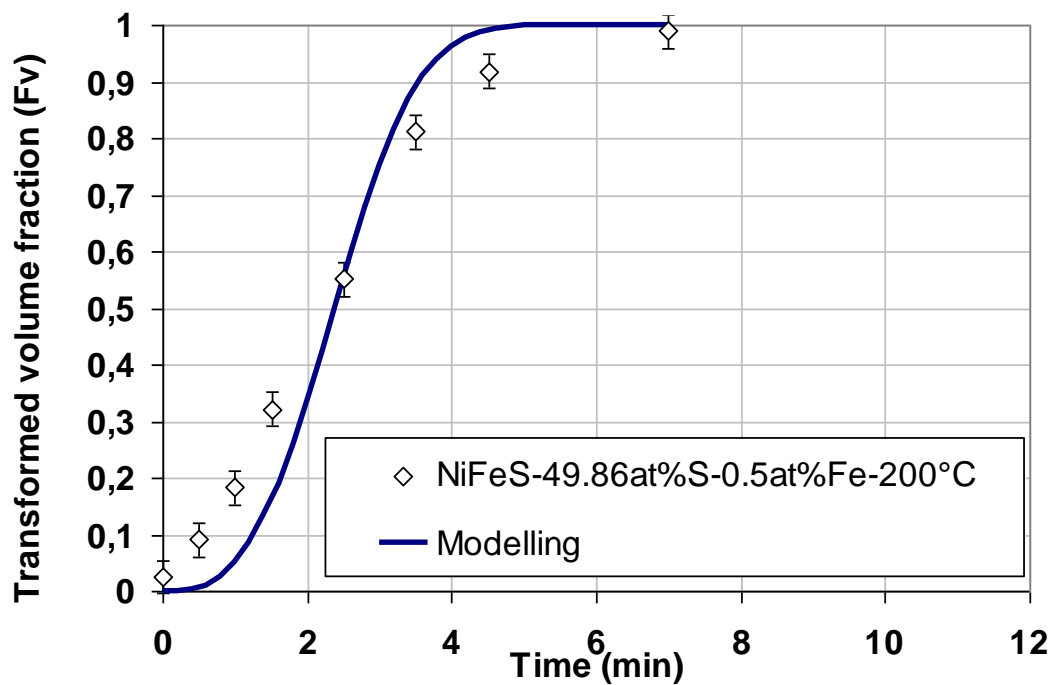


Figure 60: Globular morphology: comparison between calculated and measured Fv

V.4 Modelling of the phase transformation

b. Block morphology

The block morphology can be described by spheroidal shape, starting from spherical nuclei, and growing with a diffusion controlled kinetic. According to *in situ* observations, the interface migration follows a quadratic growth well accounted by the Zener model. This provides the evolution law of the particle diameter. On the other hand, the nucleation phenomenon, which occurs continuously during the transformation, is described by a linear law ($N_v = N_v \cdot t$) also derived from *in situ* observations reported in previous section. The transformed volume fraction is then given by the following law:

$$f = \frac{1 - \exp - \left[\frac{8}{15} N_v \cdot \Pi \cdot D^{3/2} \cdot \left(\frac{(C_{\alpha\beta} - C_{\alpha}^0)^2}{(C_{\alpha\beta} - C_{\beta})^{3/2} (C_{\alpha}^0 - C_{\beta})^{1/2}} \right) t^{5/2} \right]}{5} \quad \text{eq 13}$$

N_v is the volume nucleation rate.

Since the block morphology is obtained in a field of the phase diagram field corresponding to a partial transformation, the transformed volume fraction is normalized to the β phase volume fraction at equilibrium. As illustrated by Figure 61, a good agreement is found between the experimental data (obtained with *in situ* measurements) and the modelled volume fraction using a depth value of 15 μm . The calculated volume fraction is also consistent with that obtained by DSC for a 750 min at 290°C ($F_v = 21\%$). Unfortunately, the comparison between modelling and DSC results cannot be made for smaller volume fractions because the DSC signal was too small to be quantitatively exploited.

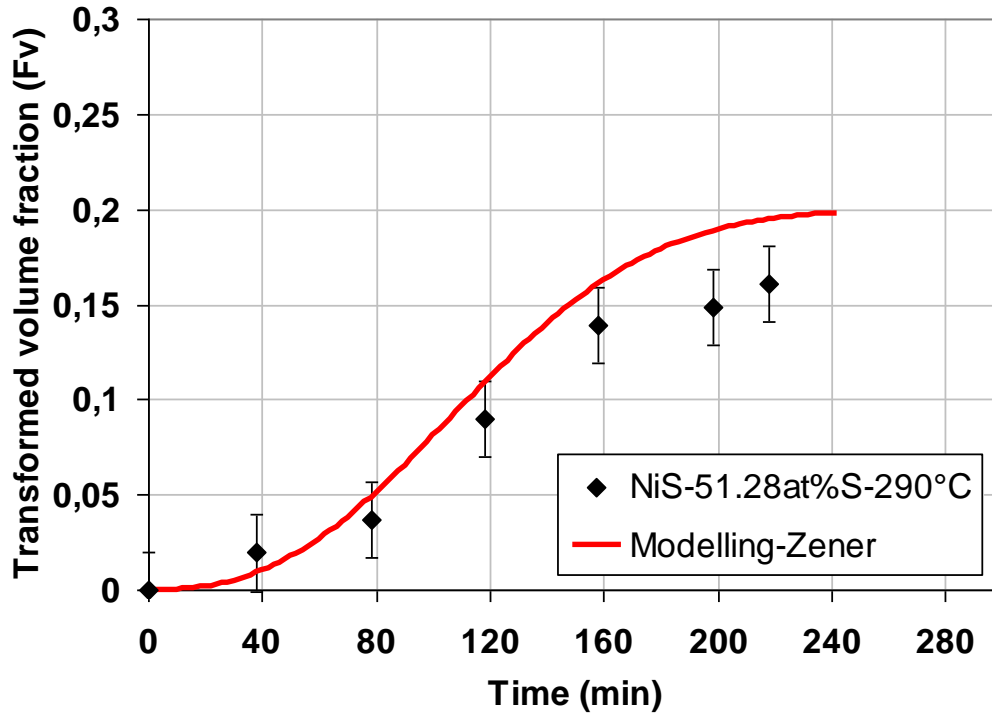


Figure 61: Block morphology: comparison between calculated and measured F_v ; a good agreement is obtained

c. Lamellar morphology

Regarding the lamellar morphology, its anisotropic shape is due to the nuclei shape and to the different growth rate in the different directions. According to *in situ* observations the plate lengthening is linear in time and then will be accounted with a Zener-Hillert model. On the other hand, the plate thickening is quadratic in time and is accounted then with a Zener model. As shown by the *in situ* experiment a constant nucleation rate has to be considered. Assuming that the nuclei are platelets with length and thickness governed by respectively linear and quadratic laws, we obtained for the transformed volume fraction:

$$f = \frac{1 - \exp - \left[\frac{2}{7} \Pi \cdot N_v \cdot \left(\frac{C_\zeta - C_\beta}{C_\zeta - C_\alpha^0} \right) \left(\frac{D}{2 \cdot r} \cdot \frac{(C_{\alpha\beta} - C_\alpha^0)}{(C_{\alpha\beta} - C_\alpha^0)} \right)^2 \cdot \left(\frac{D(C_{\alpha\beta} - C_\alpha^0)^2}{(C_{\alpha\beta} - C_\beta)(C_\alpha^0 - C_\beta)} \right)^{1/2} \cdot t^{7/2} \right]}{\left(\frac{C_\zeta - C_\alpha^0}{C_\zeta - C_\beta} \right)} \quad \text{eq 14}$$

N_v is the volume nucleation rate and r the tip radius. C_ζ is the Sulphur concentration of the Ni_3S_4 phase. The transformed volume fraction is normalized to the equilibrium volume fraction of the β phase.

For the case shown in Figure 62 a good agreement is obtained between the calculated fraction and the *in situ* experiment one with a depth = 50 μm and a tip radius = 0.55 μm . This depth, which is higher than the one used for the block morphology (10 μm), is indeed consistent with a plate morphology. In other words, because of the anisotropy of the lamella, a higher depth should be considered to transform the surface density in a volume density. These parameters have been further used to test the modelling on two states (51.18at%S-200°C, 51.09at%S-260°C) for which we have the *in situ* measurements and the DSC ones. For the sample 51.18at%S-200°C, we note a rather good agreement using the parameters above ($r = 0.55 \mu\text{m}$, $d = 50 \mu\text{m}$) between the *in situ* experiment and the model. For the sample 51.09at%S-260°C, the calculated volume do not fit with the experimental for the set of parameters ($r = 0.55 \mu\text{m}$, $d=50 \mu\text{m}$). But if the radius tip r is changed (1.3 μm instead of 0.55 μm) a good agreement is obtained with the *in situ* measurement and a reasonable one with the DSC measurements.

In both cases, we note that the depth parameter is quite a robust parameter: as long as the morphology is the same, the depth parameter can be used. On the other hand, the tip radius parameter is somewhat variable. This is not surprising since it is highly related to the lamella size and to the grain size. In addition, this sensitivity should increase with temperature since it accelerates the lamella growth.

V.4 Modelling of the phase transformation

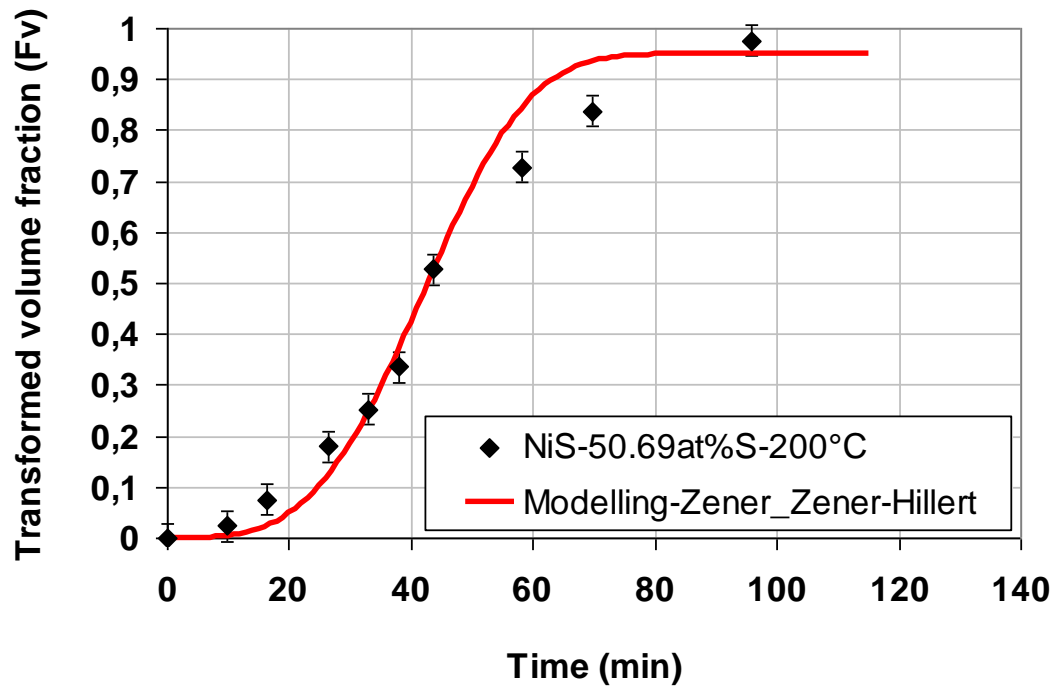


Figure 62: Lamellar morphology: comparison between calculated and measured Fv; a good agreement is obtained with $r=0.55 \mu\text{m}$ and depth value= $50 \mu\text{m}$.

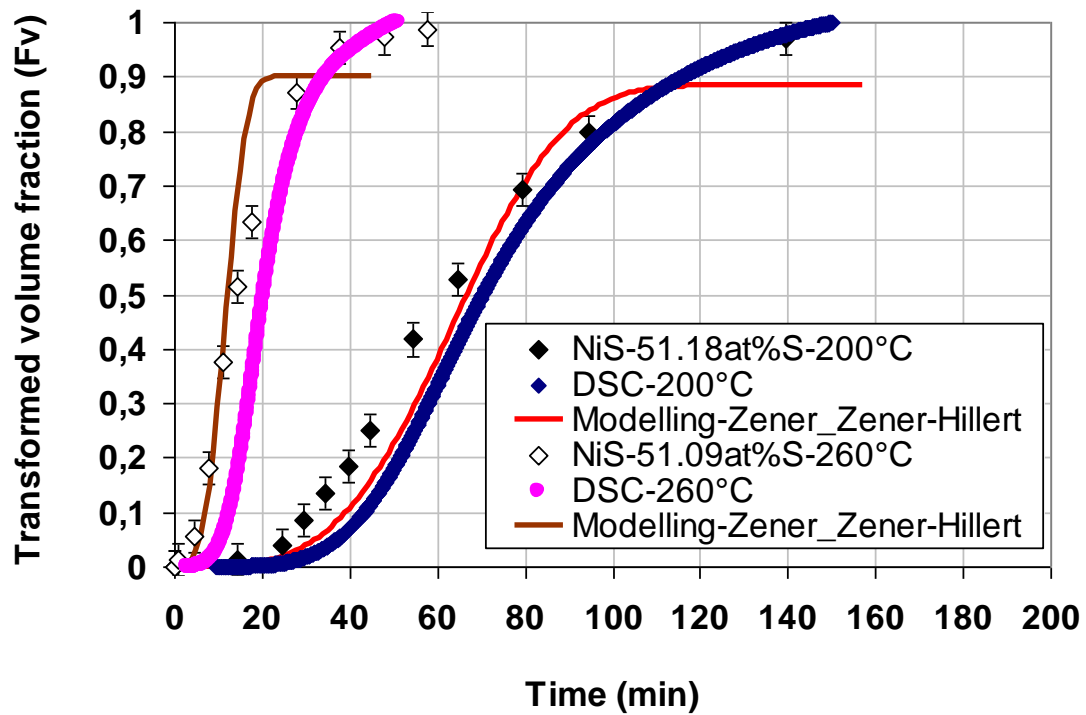


Figure 63: Lamellar morphology: comparison between calculated and measured Fv; a good agreement is obtained with a depth value= $50 \mu\text{m}$ and $r=0.55 \mu\text{m}$ at 200°C and $r=1.3$ at 260°C

To conclude concerning the modelling of the lamellar morphology, it can be said that the model accounts well for the transformed volume fraction with a set of two parameters, each having a simple physical meaning. The depth parameter, which allows us to relate the apparent nucleation rate observed at the surface with the true bulk nucleation rate, can be taken as constant for the lamellar morphology and is close to the lamella average length. The tip radius which is a very local quantity is more sensitive to the growth, the microstructure and temperature and needs to be adjusted according to experimental data. Regarding this adjustment, it should be insisted that DSC measurements are always more reliable than *in situ* measurements. In fact the *in situ* result slightly overestimates the transformed volume fraction. This may be due to the acceleration of the transformation mainly because of some surface nucleation effect. Unfortunately, DSC measurements are not always available since slow transformations kinetics do not give detectable signal.

V.5 Discussion and concluding remarks:

The modelling of the phase transformation proposed here is based on classical theory of phase transformation and validated here mostly on the *in situ* measurement. It is worth noting that very good agreement is found for globular, block and lamellar morphology with a limited number of adjustable parameters. These parameters which all have a transparent physical meaning are: a depth value which allows to transform the nuclei surface density in volumic information, a radius of curvature which mainly accounts for the lamellar morphology as its tip. The depth values we have to use in the model are consistent with nuclei size and shape factor. We note that the tip radius necessary to account for the modelling of the interface velocity of lamellae is different from the one used for the modelling of the transformation. This difference is attributed to the fact that the migration velocity at the beginning of the transformation is free of impingement. On the contrary, the transformed volume fraction integrates the growth of lamellar for which impingement due to other lamella or grain boundary has occurred. Actually it could be more appropriate in modelling to keep the same tip radius and account for impingement by a specific factor.

Regarding the experimental data provided by the *in situ* experiment, only the one which were consistent with the DSC measurement have been used. For instance, we did not consider the modelling the case of the coarse lamellar morphology because the volume fractions measured optically and by DSC were too different (which can be due to a strong surface effect biasing the *in situ* measurement). This points out the limit of *in situ* measurement for the determination of the modelling parameters. For the transformed volume fraction it would be always safer to rely on DSC measurements.

The present modelling includes information on composition and temperature dependence naturally via interdiffusion coefficients and phase diagram information. The dependence of the nucleation rate with temperature and composition has to be determined experimentally. This model is able to predict isothermal transformations and should be able to predict non isothermal heat treatments, provided a minimum of information of the characteristic morphology in the domain of interest is available.

V.5 Discussion and concluding remarks:

It should be mentioned that only the formation of the β phase has been addressed, without taking in account the Ni_3S_4 phase. Actually the Ni_3S_4 precipitation occurs only for the lamellar morphology, and at a certain point of growth of the lamellae: this in itself reveals the partition of Sulphur so that the local concentration can allow for this precipitation. In addition, even at the end of transformation, the Ni_3S_4 phase represents only 10 % of the total volume fraction. Therefore since we were interested by the transformed volume fraction due to β phase formation the Ni_3S_4 phase precipitation has been neglected here. A full modelling of the phase transformation should of course take it in account.

Chapitre VI. Proposition to improve the efficiency of the Heat Soak Test

VI.1 Introduction:

Nickel sulphide inclusions are known to cause spontaneous fracture of toughened glass due to the volume increase (~4%) of this inclusion [4, 14] caused by $\alpha \rightarrow \beta$ -NiS phase transformation. Against this, the European standard EN14179-1 was developed and implemented (as prEN) in 2002, and was formally installed as a standard in 2006. It prescribes the toughened glass to be heated up to $(290 \pm 10^\circ\text{C})$, and this temperature to be kept constant during at least two hours in order to provoke the $\alpha \rightarrow \beta$ -NiS transformation before implementation of glasses on building. This strongly reduces the fracture probability so that glasses can be used in façades practically without risk of failure. Six years of practical experience with this HST showed that indeed the fracture rate is now very low. In contrast to the time before implementation of the new HST standard, apparently no more breakage of tested glass was reported. However, such efficiency suggests that the glass processed in this way could be somewhat “over-safe”, i.e. the HST might destroy more glass sheets than would have broken on a building. It is possible that the conditions of the HST might be slightly modified in order to optimize it in terms of safety, efficiency and cost. There are already some studies concluding that the HST temperature might be too high and proposing to use lower temperatures and shorter times [42, 52, 53].

Indeed the efficiency of the HST treatment is strongly related to the mechanisms controlling the kinetics of the $\alpha \rightarrow \beta$ -NiS phase transformation together with the inclusion compositions which are known to have an impact on the transformation [3, 8, 10]. Hence, phase transformation mechanisms in NiS inclusions should be first investigated in order to propose new HST conditions. The optimal HST should ensure that no phase transformation occurs within the life time of the mounted glass and that the test is at the lowest cost: i.e. the shortest time for the lowest temperature. Such an optimization requires mainly the identification of the NiS transformation mechanisms and the measurement and/or modelling the laws governing the transformation kinetics as a function of temperature and inclusion composition. Hence, knowledge of the natural inclusion composition is necessary in order to identify

the composition which will be the limiting steps determining the HST conditions. Using the whole set of information we have obtained from the study of synthetic Ni(Fe)S specimens with different stoichiometry and containing different level of iron contamination as reported in the previous Chapters and completed by dedicated experiments, we will propose a modification of the present HST conditions.

VI.2 Microstructures and mechanism for the $\alpha \rightarrow \beta$ -NiS transformation

The objective here is to identify mechanisms controlling the kinetics of the phase transformations. Contrary to previous studies [3, 17] which took essentially a macroscopic point of view, the transformation mechanism is here investigated based on a detailed microstructural characterization during phase transformation and its evolution as a function of temperature and Sulphur composition. The microstructural investigation was carried out on isothermal heat treatment which allowed the separation of temperature and time effects on microstructural evolution.

The $\alpha \rightarrow \beta$ -NiS phase transformation was studied for different α phase overstoichiometry and for temperature range from 200 \rightarrow 300°C. It was pointed out that, according to temperature and initial α -NiS composition, five typical microstructures are developed. In addition, from the microstructural characterization, we have concluded that two transformation mechanisms are involved: a massive mechanism for the near stoichiometric samples and a diffusive one with Sulphur partition for overstoichiometric samples. The massive transformation is done without long range diffusion and compositional change between, the daughter phase and the mother phase; it follows a linear growth kinetics. Regarding overstoichiometric samples, the composition of the daughter phase is different from the mother one indicating clearly that a partition mechanism has occurred. The growth of the β grain for these morphologies requires the long range diffusion of Sulphur and Nickel in the α phase which then causes a deceleration of the growth kinetics as a consequence of a parabolic growth kinetics.

VI.3 Kinetic law of NiS phase transformation and HST optimization

The microstructural study was successful in identifying the morphology evolution as a function of temperature and composition, and in aiding to understand the kinetic evolution of the different morphology by massive and partition diffusive mechanism. However, it remains important to know whether these mechanisms are relevant for the optimization of the HST. First, these mechanisms having very different kinetics, the HST optimization should be done on the slowest one which actually corresponds to inclusions with the highest amount of Sulphur and iron impurities. We have analyzed by EPMA the composition of natural Nickel sulphide inclusion (Figure 64a and Annexe A). It comes out that the average composition varies between 50.10 at%S and 52.7at%S. The iron quantity varies between 0.11 at% and 1.62at%. The majority of inclusions presents a Fe content close to 0.2at%. The high overstoichiometry given by EPMA for some inclusions is confirmed by the high volume fraction of Ni₃S₄ phase precipitates (Figure 64b). Therefore for overstoichiometric composition, the partitioning diffusive mechanism for the transformation should be involved.

VI.3 Kinetic law of NiS phase transformation and HST optimization

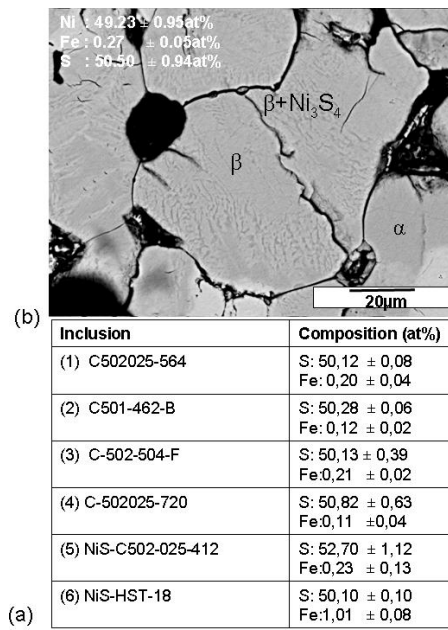


Figure 64 : (a) EPMA analysis for 5 typical NiS inclusions (b) SEM micrograph of natural inclusion: the precipitation of the Ni_3S_4 phase confirms the overstoichiometric composition measured by EPMA.

After the HST, the $\alpha \rightarrow \beta$ transformation should be complete, therefore the temperature domain of the heat treatment should allow for a full $\alpha \rightarrow \beta$ transformation. The NiS phase diagram [22] indicates that, for a full transformation to occur, the maximum temperature is 280°C, the eutectoid temperature. Above 280°C and for overstoichiometric composition, the transformation will be partial. In order to confirm these features, two heat treatments were carried out on a 51.14at%S sample at 300°C and 260°C (Figure 65). The micrograph in Figure 65 exhibits a full transformation for T=260°C and a partial one (~30%) at T=300°C as expected by the phase diagram. Having in mind that the compositions of the NiS inclusion are overstoichiometric, to obtain a full transformation, the temperature of the heat treatment should not exceed 280°C.

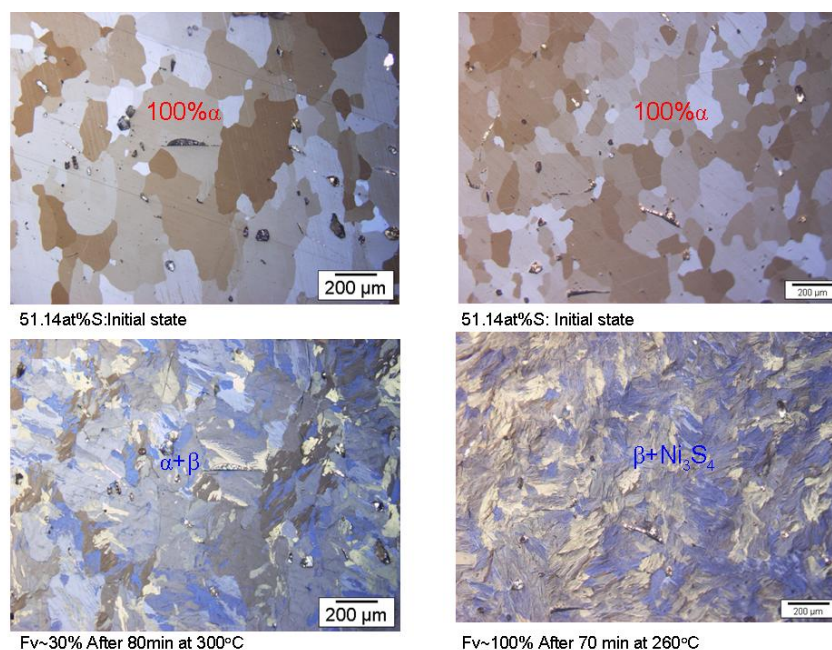


Figure 65: Optical micrograph illustrating complete transformation at 260°C and partial one at 300°C: the transformed volume fraction decreases when increasing temperature above 280°C

The last parameter required for the HST optimization is the composition limit. Since the transformation kinetics decelerates with increasing stoichiometry, for some NiS inclusions the transformation may be so slow that the glass never breaks during the lifetime on site. The HST can be then optimized using a composition limit which is relevant with respect to the lifetime of the mounted glass. The determination of this composition limit requires knowledge of the transformation kinetic at room temperature. The information we have obtained consists in the evolution during 30 months at room temperature for different sample composition. Figure 66a, b and c illustrate the microstructures observed after 30 months in NiS samples of different overstoichiometry. Figure 66d, e and f report similar observations for iron contained sample. For near stoichiometric sample, Figure 66a shows that about 60% of the α phase is transformed after 30 months. However, a transformed volume fraction smaller than 5% and 1% are transformed respectively for the 51.14at% and for 51.28at%S samples. Since the transformation, for such compositions, is controlled by diffusive mechanisms then the transformation kinetics is slower than what would be expected from a linear kinetics. For a linear growth kinetic, at room temperature the transformation would take 25 years and 125 years to reach 50% transformed volume fraction respectively for 51.14at% and for 51.28at%S samples. Hence the 51.28at%S inclusions can be clearly considered as not dangerous for all practical purposes. However no conclusion could be taken here for 51.14at%S. Regarding the transformation time range for these compositions at high temperature, microstructural study has shown that complete transformation takes about 2h for 51.14 at%S. However, after 600 min at 200°C, only 30% of the α phase is transformed for 51.28at % sample (30% after 330min at 260°C). Thus the transformation in the 51.14at% sample follows a relatively rapid kinetics at high temperature with respect to the HST conditions. Thus considering this overstoichiometry as the composition limit guarantees that no inclusion untransformed during the HST could transform within the life time of glass. In the following the optimization of the HST will be carried out on this composition.

VI.3 Kinetic law of NiS phase transformation and HST optimization

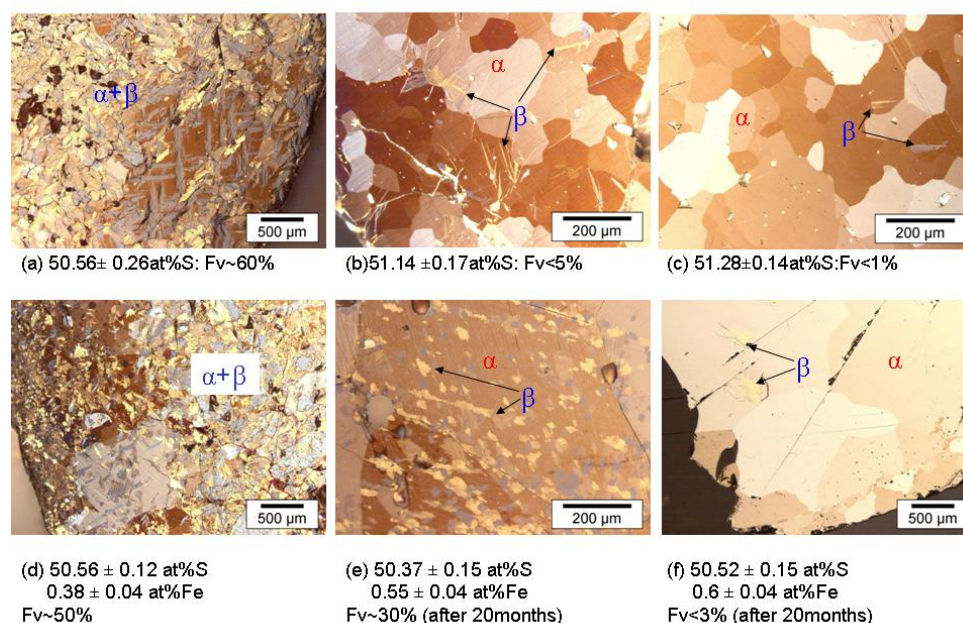


Figure 66: Optical microscopy observations of phase transformation behavior occurring at room temperature for Ni(Fe)S sample of different composition: for very overstoichiometric sample (51.28at%S) the transformation is very slow that only less than 1% of the α phase are transformed at room temperature during 30 months..

VI.3.1 Kinetics aspect of the $\alpha \rightarrow \beta$ -NiS transformation: TTT diagram

The objective now is to determine the optimal heat treatment conditions which allow to provoke the complete transformation at the lowest temperature and shortest time for the composition limit i.e. 51.14at%S. As the $\alpha \rightarrow \beta$ transformation is diffusion controlled, it can be described by a sequence of nucleation and growth mechanisms. Then the kinetic acceleration can be obtained by increasing temperature or the nucleation rate; thus the temperature and nucleation rate effect on kinetics are studied. First, a kinetic study, based on isothermal heat treatment, is carried out in the temperature field $T < 280^\circ\text{C}$ in order to build the Time Temperature Transformation (TTT) kinetic diagram which describe quantitatively the transformation time range as function of temperature for a given volume fraction. Second, in order to study the effect of “pre-nucleation” on further transformation kinetics, a two stage heat treatment consisting in a low temperature step to enhance nucleation and a high temperature step to enhance the growth is carried out. The kinetic results are obtained using DSC (Chapter 3) together with *in situ* observation of phase transformation in optical microscopy (Chapter 5).

The TTT curves (established in Chapter 3) are very appropriate tool to synthesise all the information on the temperature and composition effect. For near stoichiometric sample (50.4at%S), Fv~90% is reached after about 17 min at 200°C and 3 min at 260°C ; for the overstoichiometric sample 51.14at%S after 115 min at 200°C and about 40 min at 260°C . The acceleration with temperature increase is clearly illustrated by the reduction of the time range: from 125min at 200°C to 50min at 260°C . The same remark holds for the composition effect: for an increase of 1 at%S the

transformation time range increases from about 20 min to about 110min. According to the TTT curves of Figure 67, the transformation time range is less than 60min for temperature between 240°C and 280°C and for all studied composition. Of course at temperature higher than 280°C, as the transformation becomes partial, the time of transformation is not mentioned. The rather flat shape of the TTT curve at low temperature indicates a strong effect of temperature on the reduction of the time range. On the contrary, the curved shape at higher temperature corresponds to a smaller effect of the temperature on the transformation time range.

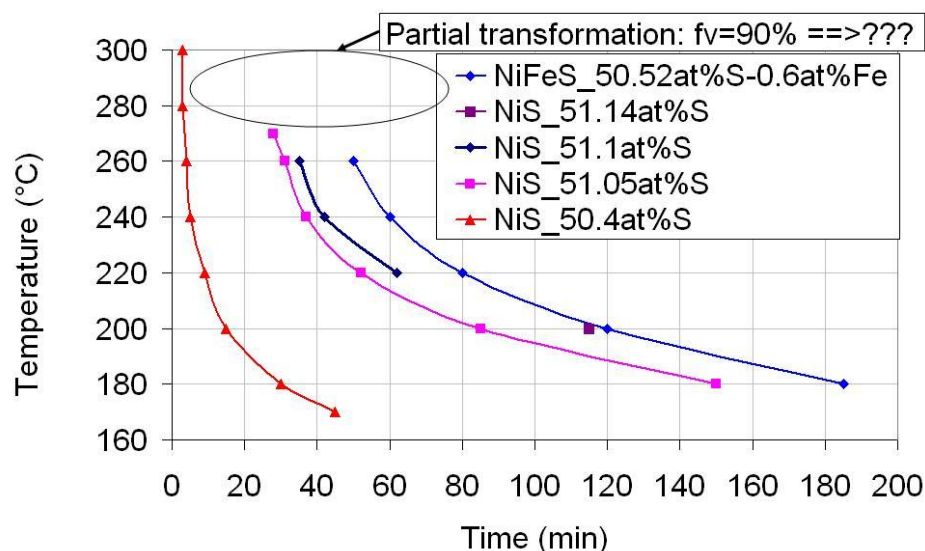


Figure 67: Time Temperature Transformation (TTT) diagram for Ni(Fe)S sample of different composition for $F_v=90\%$: the transformation time range for the composition limit, corresponding to $F_v=90\%$, is about 1h for $T>240^\circ\text{C}$.

VI.3.2 Kinetic results on two stage heat treatments

The study of the nucleation rate effect has been obtained by comparison of DSC curves recorded on isothermal heat treatments in two samples with the same composition but with different initial states. The first one corresponds to a sample in the α phase state while the second already contains β nuclei. The β nuclei are here obtained after heat treatment during 1h at 160°C - 190°C . Figure 68 shows two DSC curves recorded during the isothermal steps with a plateau temperature of 220°C . According to the DSC curve in Figure 68, transformation starts after a delay of about 15 min for the sample without β phase nuclei. On the contrary, for the sample with pre-existing β phase nuclei, the transformation starts at the beginning of the second isothermal plateau. This illustrates that transformation is accelerated when the sample already contains β phase nuclei. The maximum reduction of time (of about 50%) is obtained after the nucleation plateau at 190°C .

VI.3 Kinetic law of NiS phase transformation and HST optimization

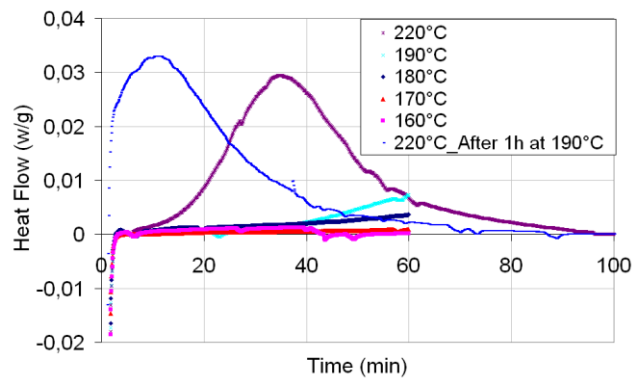


Figure 68 : (a) DSC curves $\Delta H=f(t)$ recorded during isothermal heat treatments at 220°C on sample with different initial state showing the acceleration of the transformation due to pre-existing β nuclei.

The second relevant point is now to gather quantitative information on the evolution of the nucleation as a function of temperature and time. A qualitative description is given by the DSC curve as illustrated by Figure 68 by curves recorded during the nucleation step. The area under the DSC curve increases when increasing temperature and time and then the same should hold for nucleation. Since DSC gives global information, the calorimetric signal does not separated the contribution of nucleation with respect to growth. Thus it is more appropriate to use here the quantitative information obtained by *in situ* optical microscopy observation of the transformation. Figure 69a shows the evolution of the number of nuclei recorded after two temperatures and for two overstoichiometric compositions 50.82at%S and 51.09at%S. For the overstoichiometric composition 50.82at%S the nuclei number, as a function of time, increases at 160°C and 180°C. In addition, the nucleation rate increases when increasing temperature and reaches saturation after about 10 min at 180°C. Regarding the overstoichiometric sample, the recorded nucleation curves show similar saturation after about 30 min. The increase of nuclei numbers during transformation shows that the nucleation continuously occurs during the transformation. However, the saturation of nucleation indicates that the plateau holding time should not exceed 30min at 180°C for overstoichiometric composition 51.09at%S. The most important finding here is the confirmation of the effect of nucleation on the acceleration of the transformation kinetics in the NiS transformation. In addition, the nucleation rate depends on temperature and composition. The higher the temperature, the higher is the nucleation rate. In parallel the lower the overstoichiometry, the higher is the nucleation rate.

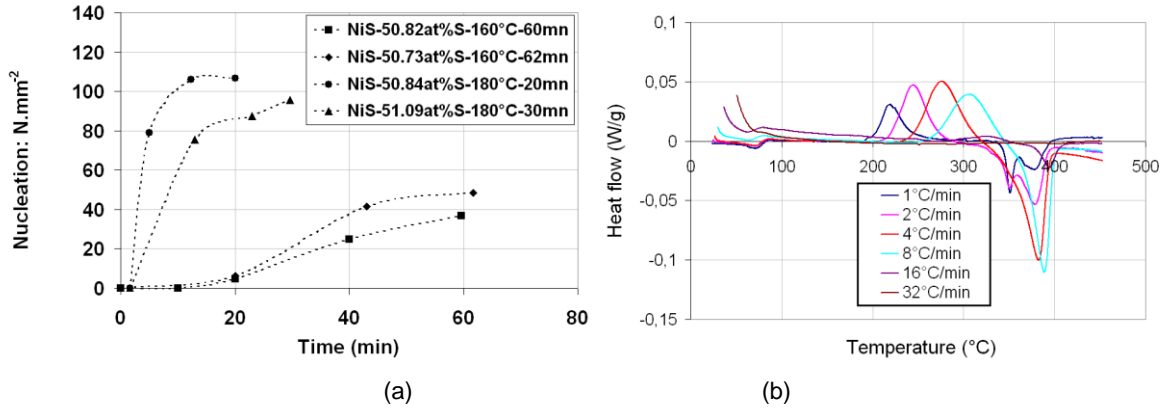


Figure 69 : (a) Evolution of number of β phase nuclei during the transformation obtained from *in situ* observation in optical microscopy: nucleation continuously occurs during phase transformation. (b) Recorded DSC curves (heat flow against temperature) obtained after several heating rate (1, 2, 4, 8, 16 et 32 $^\circ\text{C/min}$) from 25 to 450 $^\circ\text{C}$ on sample $\text{Ni}_{48.86}\text{S}_{51.14}$: for heating rates higher than 2 $^\circ\text{C/min}$ the transformation is partial.

VI.4 Summary and conclusion:

Regarding the identification of key parameters for HST optimization, the major points of the present study are i. the composition of the overstoichiometric inclusion which should be considered to devise the HST. ii. the identification for this composition of the controlling mechanisms (nucleation growth type and diffusion). iii. a decisive piece of information is the critical composition of 51.14at%S above which inclusions will not transform during the glass life time, iv. for complete transformation, the temperature must be kept below 280 $^\circ\text{C}$. The kinetic study has shown that nucleation and temperature play strong roles in the acceleration of the transformation kinetics. Such results improve the understanding of the transformation mechanisms and kinetic and thus will be used in order to enhance the industrial HST conditions.

The current HST European standard EN14179-1 prescribes the toughened glass to be heated up to $290 \pm 10^\circ\text{C}$, and to be held at this temperature during at least 2h to assure HST. However it is not excluded that some dangerous inclusions survive this test. Indeed, for overstoichiometric compositions we have observed that the transformation is partial (Figure 69b) for heating rate higher than 2 $^\circ\text{C}$ (in the temperature range from 200 to 300 $^\circ\text{C}$) and that transformation is partial if the temperature is over 280 $^\circ\text{C}$. Therefore, regarding the current HST, when the heating rate is higher than 2 $^\circ\text{C/min}$, the transformation for some inclusions will be partial after the HST even for long holding time since the temperature plateau (290 $^\circ\text{C} \pm 10$) corresponds to field in which the equilibrium state involves two phases. However this case is not very frequent as it corresponds to extreme conditions of the heat soak test parameter: overstoichiometric inclusion (the majority of inclusion are near stoichiometric), heating rate higher than 4 $^\circ\text{C/min}$ and effective plateau temperature of 290-300 $^\circ\text{C}$. But the probability of such case is not negligible and attention should be paid to such a case. According to the EN14179-1 standard, the heating rate can be variable, however in practice, depending on the furnace; the heating rate may be rather low. According to the present study, without this slow heating, the holding

VI.4 Summary and conclusion:

at 290° alone would allow many dangerous inclusions to survive the test. Hence, the experimental conditions of this standard (plateau temperature 290°C) are not appropriate with respect to inclusions with compositions which should be eliminated during the heat soak test and then amelioration should be brought to HST.

A first modification could be to limit the plateau temperature to less than 280°C. Indeed the kinetic study prescribes that the transformation time range is less than 1 hour for $T > 240^{\circ}\text{C}$. Therefore a HST consisting of two hours holding at a temperature plateau of $260 \pm 10^{\circ}\text{C}$ assures that all dangerous inclusion will transform (Figure 70b). No particular heating rate has to be followed since the transformation is done in the complete transformation domain. Contrary to the actual HST standard EN14179-1 (Figure 70a), which prescribes 320°C as an absolute temperature in furnace, no restriction on a maximum furnace temperature has to be mentioned here. Only the holding at $260 \pm 10^{\circ}\text{C}$ during at least 2 hours has to be respected.

To reduce the de-tempering effect, a second heat treatment is proposed which allows the decrease of the holding time at high temperature (Figure 70c): a two stage HST consisting on a first step at low temperature 180-200°C during 30-60min to enhance nucleation followed by a second step at $260^{\circ}\text{C} \pm 10^{\circ}\text{C}$ 1 hour. Since it is very difficult to introduce a second step during HST, a realistic solution could be to substitute the holding step at low temperature by a slow heating from 170 to $260 \pm 10^{\circ}\text{C}$ at $1^{\circ}\text{C}/\text{min}$ and a holding during 1h and 30 min at this temperature. In addition, according to our study, the heat treatment we proposed to achieve complete transformation of dangerous inclusions is not sensitive to the fluctuations of thermal conditions in furnace.

Finally the proposed HST conditions which ensures safety can be also more economic because of a reduction by 30°C of the temperature and of 2 hours of the HST time (at temperature above 180°C). This reduction of the HST temperature allows at the same time an increase in the efficiency of the HST and a reduction of the de-tempering effect. It is worth noticing that a detailed investigation of natural inclusions (reported in Appendix A) and of the Ni-S phase transformation in synthetic NiS samples has lead to the necessary understanding which can be used to propose a new more efficient HST processing.

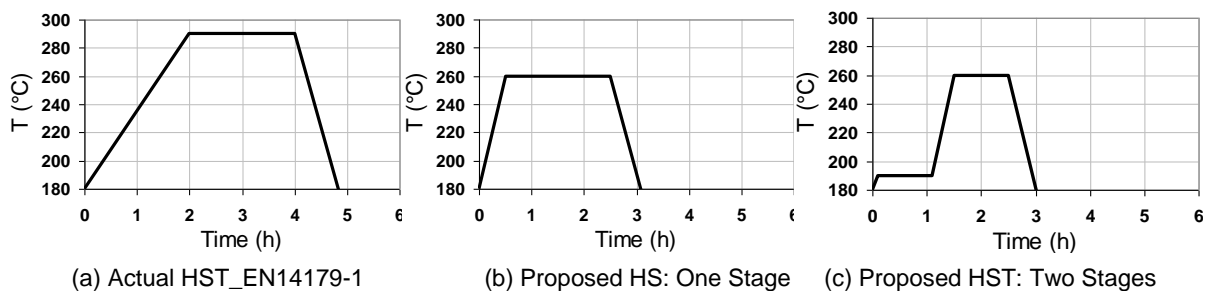


Figure 70 : Comparison between the actual HST (following EN14179-1) and the proposed heat treatment. The modified plateau temperature is below the eutectoid (280°C) to ensure complete transformation. A two stages heat treatment is proposed to reduce the de-tempering effect.

Chapitre VI. Proposition to improve the efficiency of the Heat Soak Test

Chapitre VII. Conclusion

Cette étude a été conduite afin de répondre au problème industriel de rupture des verres trempés causée par la transformation de phase différée des inclusions de sulfure de Nickel (NiS) dont la présence est inévitable dans les verres. Une solution efficace est déjà appliquée afin de répondre à cette problématique. Elle consiste en un traitement thermique (Heat Soak Test - HST) accélérant la transformation. Autant cette solution donne satisfaction en terme d'élimination des vitrages à risque, autant elle l'est moins en terme de coût résultant de la température et de la durée du traitement thermique industriel. Le fait que les conditions de ce traitement thermique aient été déterminées à partir des études macroscopiques (essentiellement par calorimétrie différentielle et diffraction des Rayons X) laissait suggérer que l'optimisation du traitement industriel était possible à partir d'une connaissance détaillée des mécanismes de transformation de phase $\alpha \rightarrow \beta$ -NiS. Ainsi, partant de ce problème industriel, nous avons conduit une étude académique visant à la compréhension de la transformation de phase en termes de mécanismes et cinétiques de transformation, conduisant en retour à proposer de nouvelles solutions industrielles en termes de traitements thermiques optimisés.

La présente étude a été basée sur une caractérisation microstructurale de la transformation de phase. Cette vision « métallurgique » permet de progresser dans l'identification des mécanismes de transformation de phase jusqu'à la modélisation de la fraction volumique transformée. D'une part, les observations métallographiques complétées par des caractérisations fines ont permis d'identifier les mécanismes de transformation. D'autre part, l'observation *in situ* en microscopie a permis d'étudier les aspects cinétiques de la transformation de phase. Nous avons ainsi pu déterminer les éléments nécessaires pour modéliser la loi de transformation $F_v(t)$. Les principaux résultats de l'étude microstructurale sont les suivants :

- compréhension des mécanismes de transformation et leur dépendance en fonction de la composition et la température (un mécanisme sans partition, massive, pour les faibles surstœchiométries et un mécanisme avec partition à longue distance pour les fortes surstœchiométries).
- identification des mécanismes contrôlant le déplacement des interfaces pour les différentes morphologies,
- quantification du taux de germination pour chaque morphologie avec dans le cas de la morphologie lamellaire la dépendance en température et en composition.

Cette étude microstructurale a été complétée par une étude en calorimétrie qui a servi à déterminer les durées de transformation pour tracer le diagramme TTT (Temps, Température Transformation) pour différentes compositions. Des expériences de couples de diffusion ont été réalisées pour mesurer les coefficients de diffusion nécessaires pour rendre compte des transformations diffusives.

L'ensemble de ces résultats a fourni les bases de la modélisation de la fraction volumique transformée pour des traitements isothermes. Des modèles cinétiques classiques, construit à partir d'un taux de germination et une croissance des grains, ont été utilisés pour modéliser la fraction volumique transformée. D'une part, le taux de germination est directement issu des données obtenues expérimentalement des observations *in situ*. D'autre part, des modèles à base physique ont été utilisés afin de décrire les vitesses de déplacement des interfaces. En l'occurrence, il s'agit d'un modèle de Zener pour décrire le déplacement des interfaces contrôlé par la diffusion à longue distance et d'un modèle de Zener-Hillert pour le déplacement contrôlé par la diffusion à plus courte distance. Cette modélisation a été effectuée pour les différentes morphologies. Le modèle cinétique permet une prédiction quantitative de la fraction volumique transformée $F_v(t)$ pour différentes conditions de température et composition dans le cas de la morphologie lamellaire qui s'avère la plus intéressante pour l'aspect industriel.

D'autre part, plus proche de la situation industrielle, une caractérisation des inclusions « naturelles » de NiS a été conduite pour déterminer les paramètres nécessaires pour proposer des améliorations sur le Heat Soak Test (HST) : notamment les compositions des inclusions naturelles et plus particulièrement la composition limite qui doit être considérée. Ainsi l'analyse des inclusions naturelles a montré qu'elles peuvent présenter des compositions surstœchiométriques en Soufre. L'examen de la cinétique de transformation à haute température complété par le comportement à basse température a permis de conclure que la composition limite est 51.14at%S. Cette composition correspond à une transformation caractérisée par une morphologie lamellaire. De plus, en se basant sur des considérations microstructurales, sur le diagramme TTT et sur le diagramme de phase, nous avons proposé de réduire la température maximale du HST à 280°C pour être dans les conditions de transformation complète et de faire un palier isotherme de 2 heures à une température de l'ordre de 260°C. La durée du palier peut être réduite en ajoutant un second palier isotherme, favorisant la germination, à plus basse température (170-190°C).

La modélisation de la transformation de phase a débouché dans le cas de la morphologie lamellaire à des modèles avec deux paramètres ajustables ayant un sens physique. Il s'agit, d'une part, du rayon de courbure des lamelles qui a été ajusté sur des résultats expérimentaux de l'allongement des lamelles ; d'autre part d'un paramètre qui rend compte de « l'impingement ». Ce paramètre est sensible aux différentes causes du phénomène: c'est-à-dire ici la taille des grains et le blocage de la croissance d'une lamelle par les lamelles environnantes. Les inclusions naturelles qui ont des petites tailles ~50-500µm peuvent être considérées comme monocristallines, « l'impingement » dû à la croissance des autres lamelles est alors dominant. Pour adapter la modélisation aux inclusions naturelles, on utilisera donc les paramètres ajustés sur des échantillons synthétiques à taille de grain équivalente à la taille des inclusions naturelles.

Chapitre VII. Conclusion

Bien entendu la modélisation proposée dans cette étude n'est qu'une première approche. Bien que suffisante pour prédire les fractions transformées, elle ne décrit que des transformations isothermes. Or le traitement industriel impose une étape de chauffage lente, l'optimisation du HST nécessite donc une modélisation de la cinétique pour des traitements anisothermes. C'est une des prolongations envisagées à ce travail pour mieux l'adapter à l'application industrielle.

Dans l'objectif d'une étude complète de la transformation de phase, il manque des connaissances sur l'étape de germination. Au cours de la présente étude, il n'a pas été possible de faire des observations en microscopie électronique en transmission sur la phase α -NiS pour des questions de préparation des lames minces. Néanmoins, en fin de l'étude, nous avons obtenu par la méthode FIB (Focussed Ion Beam) des lames minces de qualité qui rendraient possible l'étude de la germination. Par ailleurs, la composition limite entre transformation massive et diffusive n'a pas été abordée dans cette étude par manque d'un ensemble d'échantillons décrivant le domaine de composition d'intérêt. Pour déterminer cette concentration limite, on peut envisager de réaliser des échantillons avec un gradient de composition en Soufre ce qui peut être obtenu, soit par une désulfuration par analogie avec la décarburation dans le système Fe-C, soit par des couples de diffusion permettant d'obtenir un gradient de composition dans la phase α -NiS.

Au-delà du cadre industriel associé à cette étude, le système NiS présente un intérêt pédagogique pour former à l'étude des transformations de phase. Les transformations de phase dans le système NiS se passent à basse température tout en présentant autant de richesse et de variété des mécanismes que celles des aciers ce qui fait de ce système un cas d'école pour l'étude des transformations de phase. En effet, la transformation peut être suivie par des observations *in situ* en microscopie optique pendant un traitement thermique. Concrètement, il est d'ailleurs prévu d'en faire une séance de travaux pratiques pour initier les élèves-ingénieurs de première année de l'école PHELMA à l'étude des transformations de phase.

Les microstructures caractéristiques des transformations de phase dans le système NiS ont montré des similitudes très fortes avec celles du système Fe-C. Ce parallèle entre microstructures, et partant, entre les mécanismes sous jacents, a largement facilité la modélisation en nous permettant d'utiliser les concepts des transformations de phase dans les aciers. Ce travail qui illustre un exemple concret de l'intérêt de l'étude académique pour résoudre un problème industriel, montre aussi l'apport d'une approche de métallurgiste à un problème jusque là considéré en chimiste et sur des bases de comportement macroscopique.

Bibliographie

- [1] **[Ballantyne ER. 1957]**, Cracking of coloured glass used as a wall cladding. In: Secondary editor^editors. Architecture in Australia 46, p. 72.
- [2] **[Ballantyne ER. 1961]**, Fracture of toughened glass wall cladding, ICI house, Melbourne. In: Secondary editor^editors. Div. Build. Res. Melbourne (Australia), p.1.
- [3] **[Kasper A, Bordeaux F. 2000]**, Nickel sulphide: New Results to Optimise the Heat Soak Test for Tempered Building Glasses. Glastech. Ber. Glass Sci. Technol. ;73 130.
- [4] **[Swain MV. 1981]**, NiS Inclusions in Glass: An Example of microcracking induced by a volumetric expanding Phase. J. Mat. Science 151.
- [5] **[Laffitte M, Crousier, J.-P. 1958]**, Etude cristalochimique et thermodynamique des monosulfures de Nickel NiS et de cobalt.: Faculté des Sciences de l'Université de Paris.
- [6] **[Laffitte M, Crousier, J.-P. 1964]**, Etude de la sulfuration du nickel entre 400 et 650°C. C.R.Acad.Sc. ;Groupe 8:1.
- [7] **[Kasper A. 2000]**, Stability of Nickel Sulfide Stones in Glass Melts. Glastech.Ber. Glass Sci.Technol.;73:341.
- [8] **[Kasper A, Stadelmann H. 2002]**, Chemical behavior of nickel sulfide in soda lime glass melts Glass Sci. Technol.;75:1.
- [9] **[Lin RY, Hu DC, Chang YA. 1978]**, Thermodynamics and phase relationships....: The Ni-S system. Metall Trans.B;98:531.
- [10] **[Kasper A, Moschek, S., Stadelmann H., Zeihe R. 2003]**, Composition and Structure of NiS Inclusions in Float Glass, and their Impact on the Heat Soak Process. In: Secondary editor^editors. Proceedings of the Glass Processing Days, p.pp.692.
- [11] **[Hsiao CC. 1977]**, Spontaneous fracture of tempered glass Fracture. In: Secondary editor^editors. ICF4, vol. Vol.3. Waterlow, Canada, p.985.
- [12] **[Barry CJ. 1993]**, A study of Nickel Sulphide stones in tempered Glass. Ultramicroscopy 52:297.

- [13] **[Kim B, Chou C-C, Wayman CM. 1992]**, The alpha to beta transformation in stoichiometric Nickel sulfide. In: Secondary editor^editors. Proceedings of the International Conference on Martensitic Transformations 7th. Monterey, Calif: Monterey Institute of Advanced Studies, p.701.
- [14] **[Swain MV. 1980]**, A fracture mechanics description of the microcracking about NiS inclusions in Glass. J. Non-Cryst. Solids;38&39:451.
- [15] **[Kasper A. 1999]**, Advances in Testing Tempered Glasses in Heat Soak Ovens. In: Secondary editor^editors. Proceedings of the 5th Glass Processing Days, p.71.
- [16] **[Bishop DW, Thomas PS, Ray AS. 1999]**, α - β Phase re-transformation kinetics in Nickel sulphide. J. Thermal Analysis Calorimetry;56: 429.
- [17] **[Bishop DW, Thomas, P.S., Ray, A.S., Simon, P. 2001]**, Two-stage model for the a - b phase recrystallisation in nickel sulphide. J. Thermal Analysis Calorimetry;64:201.
- [18] **[Kasper A. 2000]**, Stability of Nickel Sulfide Stones in Glass Melts. In: Secondary editor^editors. Advances in Fusion an Processing of Glass. Ulm (Germany), p."Abstracts" 109.
- [19] **[Thomas P, Simon P, Ray A. 2003]**, The effect of thermal history on the morphology of nickel sulfide. J. Thermal Analysis and Calorimetry;72.
- [20] **[Christian JW. 1975]**, The theory of transformation in metal and alloys, Part 1: equilibrium and general kinetic theory: Pergamon Press.
- [21] **[Christian JW. 1986]**, In Encyclopedia of Materials Science and Engineering. London: Permagan Press.
- [22] **[Nash P, et al. 1991]**, Phase diagrams of binary nickel alloys.:394.
- [23] **[Aaronson HI. 2002]**, Mechanisms of the Massive Transformation. Metallurgical and Materials Transactions A;Volume 33A, :2285.
- [24] **[Aaronson HI, Vasudevan, V.K. 2002]**, General Discussion Session of the Symposium on "The Mechanisms of the Massive Transformation". Metallurgical and Materials Transactions A 33A:2445.
- [25] **[Aaronson HI, Mahajan S, Purdy GR, Hall MG. 2002]**, Origins of Internal Structure in Massive Transformation Products. Metallurgical and Materials Transactions A Volume 33A:2347.
- [26] **[Borgenstam A, Hillert M. 2000]**, Massive transformation in the Fe-Ni system. Acta Materialia.;48:2765.
- [27] **[Hillert M. 1984]**, Thermodynamics of the massive transformation. Metallurgical Transactions A: Physical Metallurgy and Materials Science;15A:411.
- [28] **[Hillert M. 2002]**, Critical limit for massive transformation. Metallurgical and Materials Transactions A: Physical Metallurgy and Materials Science;33A:2299.
- [29] **[Karlyn DA, Cahn JW, Cohen M. 1969]**, Massive transformation in copper-zinc alloys. Transactions of the Metallurgical Society of AIME;245:197.
- [30] **[Massalski TB. 1984]**, Distinguishing features of massive transformation. Metal.Trans.A;15a:421.

Bibliographie

- [31] **[Massalski TB. 2002]**, Massive transformations revisited. Metallurgical and Materials Transactions A: Physical Metallurgy and Materials Science;33A:2277.
- [32] **[Massalski TB, Perepezko JH, Jaklovsky J. 1975]**, Microstructural study of massive transformations in the iron-nickel system. Materials Science and Engineering;18:193.
- [33] **[Hillert M. 1984]**, Thermodynamics of the massive transformation. Metallurgical Transactions A: Physical Metallurgy and Materials Science 15A(3):411.
- [34] **[Porter DA, Easterling KE. 1992]**, Phase Transformations in Metals and Alloy.
- [35] **[Bhadeshia HKDH. 1985]**, Diffusional formation of ferrite in iron and its alloys. Progress in Materials Science;Vol. 29:321.
- [36] **[Van der Ven A, Delaey L. 1996]**, Models for precipitate growth during the $\gamma \rightarrow \alpha + \gamma$ transformation in Fe-C and Fe-C-M alloys. Progress in Materials Science;Volume 40:181.
- [37] **[Hillert M. 1957]**. Jernkont Ann;141:757.
- [38] **[Hillert M, Höglund L, Ågren J. 2003]**, Diffusion-controlled lengthening of Widmanstätten plates. Acta Materialia. ;volume 51:2089.
- [39] **[Zener C. 1946]**. Trans AIME;167:550.
- [40] **[Quidort D, Brechet Y. 2001]**, Isothermal growth kinetics of bainite in 0.5% C steels. Acta Materialia. ;Volume 49:4161.
- [41] **[Kullerud G, Yund RA. 1962]**, The Ni-S-System and related Minerals J. Petrology 3:126.
- [42] **[Sakai C, Kikuta M. 1999]**, Adapted Heat treatment for phase transformation of NiS inclusions in the heat strengthened and tempered glass. In: Secondary editor^editors. Proceedings of the 6th Glass Processing Days, p.pp.76.
- [43] **[Kissinger HE. 1956]**, Variation of peak temperature with heating rate in DTA. J. Res. Nat. Bur. Stand.;57:217.
- [44] **[Avrami M. 1939]**, Kinetics of phase change. J. Chem. Phys. ;7:1103.
- [45] **[Philibert J. 1985]**, Diffusion et transport de matière dans les solides.
- [46] **[GUIRALDENQ. P.]**, Diffusion dans les métaux. In: Secondary editor^editors: Techniques de l'Ingénieur.
- [47] **[Oukassi. S, Hodaj., F. 2009]**, Reactive Diffusion in Ni-Si Bulk Diffusion Couples. Journal of Phase Equilibria and Diffusion;Basic and Applied Research: Section I.
- [48] **[Laffitte M, Crousier, J.-P. 1956]**, Origine des variations de composition du NiS hexagonal. C.R.Acad.Sc.;243:1.
- [49] **[Rau H. 1975]**, Range of homogeneity and defect interaction in high temperature Nickel sulfide Ni_{1-x}S . J. Phys. Chem. Solids;Vol 36:1199.
- [50] **[Hirth JP, Pound. GM. 1963]**, Evaporation, Nucleation and growth kinetics. Progress in Materials science.
- [51] **[Zener C. 1949]**. Journal of applied Physics;20:950.

- [52] **[Sakai C. 2001]**, Effective Reduction of Nickel Sulfide Stones in Heat-strengthened and Tempered Glass. In: Secondary editor^editors. Glass Processing Days, p.98.
- [53] **[Sakai C, Kikuta, M. 2007]**, Heat soak test (HST) with high reliability. In: Secondary editor^editors. Glass Performance Days, p.698.
- [54] **[J.C. Barry SF. 2001]**, An electron microscopic study of nickel sulfide inclusions in toughened glass. JOURNAL OF MATERIALS SCIENCE 36:3721
- [55] **[Seim H, Fjellvag H, F.; G, Stolen S. 1995]**, Metastable Nickel sulfides with composition close to Ni₇S₆ - Stability and structural properties. Journal of Solid State Chemistry;121:400.
- [56] **[Collin G. CC, Comès R. 1983]**, Structure and planar faults in the defective NiAs-type compound Ni₁₇S₁₈. Acta crystallographica B39:289.

Annexes

Annexe A: Composition and microstructure of Nickel sulphide stones found in tempered glass

A.I. Introduction:

Nickel sulphide inclusions present in very small proportion in glass (1inclusion/300m²) [8] can lead after several years and under local conditions for the state of stress to a delayed glass fracture. This fracture is due to the phase transformation of the metastable high temperature α -NiS phase present in the inclusions into the low temperature β -NiS structure. The α phase is hexagonal and the β phase is rhombohedral and the transformation from one to the other is accompanied by a volume change of about 4%. This change in volume leads to the nucleation of small cracks around the particles [4, 14]. Tempered glasses, which exhibit tensile stresses in the core zone of glass plate, are specially concerned by this problem of delayed fracture, since the cracks initiated by the phase transformation can propagate in a catastrophic manner.

According to different authors (e.g. [8] and references herein) inclusions originate from Sulphur and Nickel impurities found in raw material such as calcite, dolomite and recycled glass. In addition materials handling with stainless steel tools introduce metal particles that contribute to Fe and Ni impurity content in glass. Analysis of the stones always indicates Nickel and Sulphur as major element in addition to very small quantities of other metals such as Iron or Copper [8]. It should be mentioned that only 1 g of Nickel can produces up to 70 000 inclusions of 200 μ m diameter [3]. This may break the entire ten day's production of a float glass line (i.e. 5600t of 8mm thick glass in 4 m² sheets). Unfortunately the total elimination of Ni and S impurities is impossible, due to the process of glass production; only reducing their quantity is possible. To overcome the NiS inclusion problem an industrial test, the so called Heat Soak test HST (EN14179-1 norm for European country), was developed in order to provoke the phase transformation before glass mounting on buildings. It consists in a heat treatment, at $290 \pm 10^\circ\text{C}$ during at least two hours, accelerating the phase transformation and during which all "contaminated" glasses should break.

The formation mechanism of Nickel sulphide inclusion can be explained as follows [8]. During glass production, the initial mixture is heated until 1200-1400°C. At this temperature the mixture melts but Nickel, being non soluble in glass, forms small melt metal zones which react with O₂ and SO₃, dissolved in molten glass, thus forming Nickel sulphides and oxides [8]. Since the liquid phase is Nickel rich [9], upon cooling, it can crystallize into NiS and Ni₇S₆ structures. The Ni₇S₆ phase further decomposes during cooling into Ni₉S₈ + Ni₃S₂. Generally speaking, crystallization can follow different path leading to variety of inclusions with different phases as (α - β) NiS, Ni₇S₆, Ni₉S₈, Ni₃S₂ and also pure Nickel. This diversity from one stone to another [8, 10, 54] is due to the difference in initial Ni:S

ratio at the beginning of the crystallization of liquid Ni-S, a ratio which results from the impurities distribution in raw materials.

Among all inclusions, α -NiS containing stones are the most likely to provoke delayed fracture. After quenching, inclusions presents crystallographic structure known as α -NiS, stable at high temperature but metastable at room temperature. Thus transformation to β -NiS phase is expected but the kinetics of transformation can be very slow. Though the transformation is rapid in stoichiometric NiS, overstoichiometric inclusions and those containing high iron impurity content may take so long to transform that the glass may never break within the lifetime of the building [10]. Thus composition of the α -NiS containing inclusion is an important parameter for the optimization of the industrial test used to detect these inclusions and to eliminate contaminated glasses.

Therefore a study of Nickel sulphide stones collected from glasses fractured on building or after the HST is carried out. This characterization was carried out using optical and SEM microscopy together with electron probe microanalysis (EPMA). The main point of the present study was to use EPMA instead of Energy Dispersive X ray (EDX) analysis in order to have precise information in the composition. Moreover, a special interest was paid to microstructure as signature of the phase transformation.

A.II. Characterization of Nickel sulphide stones

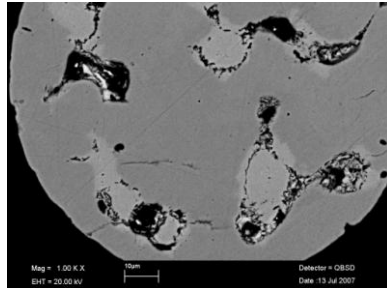
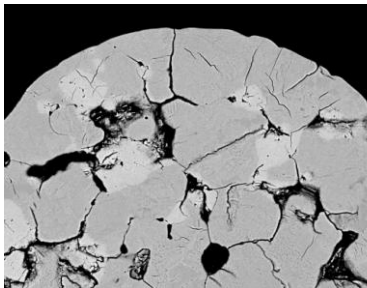
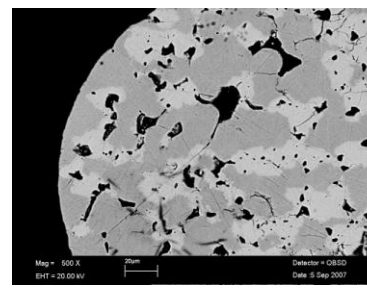
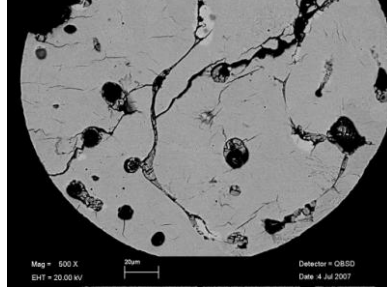
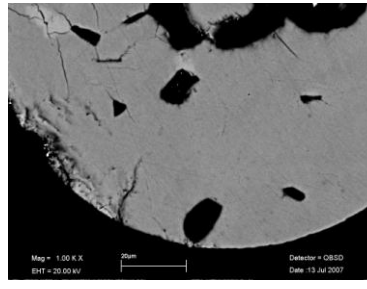
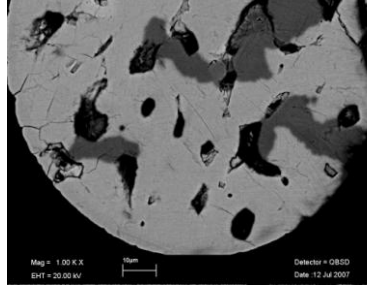
This characterization is carried out on several aspects of inclusions: phase structure and composition, microstructure of the natural inclusions. This extensive description of stones is meant to have a better understanding of their behavior. This study was carried out on 22 inclusions: half of the stones are found in the initiation site of fracture of glass plates after HST and the second half are collected from plates which have broken on site, on façades. All samples were observed by optical microscopy. The most representative were selected for SEM microscopy (17/22) and composition analysis by EDX-SEM (17/22) and by EPMA (13/22). Grains size of α phase was difficult to estimate because in most cases the stones are already transformed into β phase. Also, the stones are likely to be monocrystalline inclusion as they have small sizes (~ 50 - $600\mu\text{m}$) and are formed in the glass starting from liquid state.

A.II.1 Phases and microstructure in Nickel sulphide stones

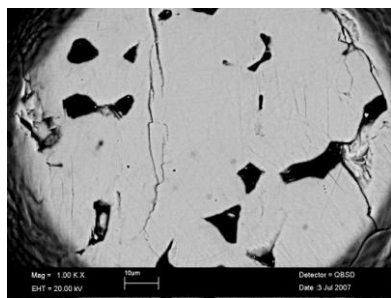
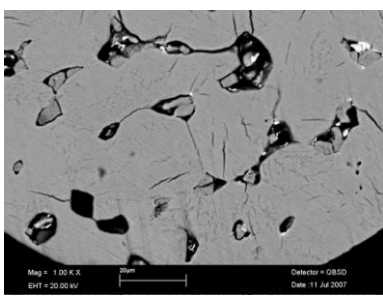
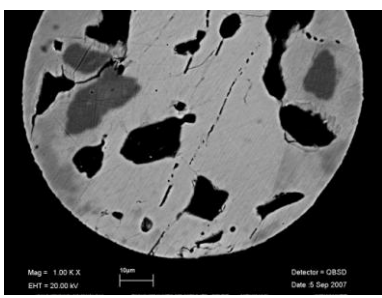
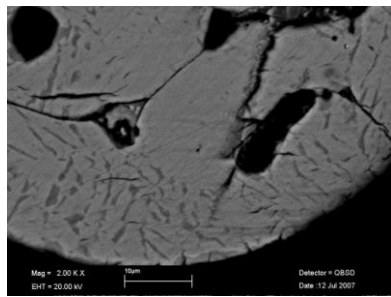
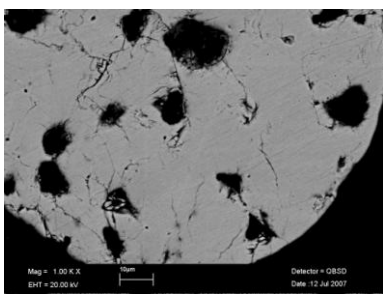
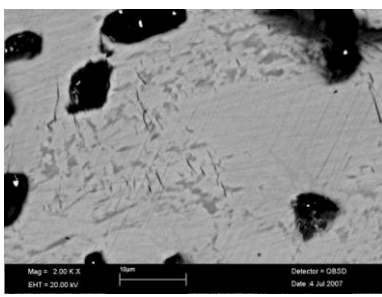
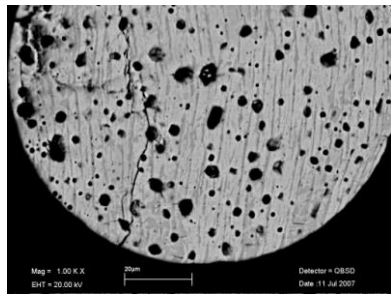
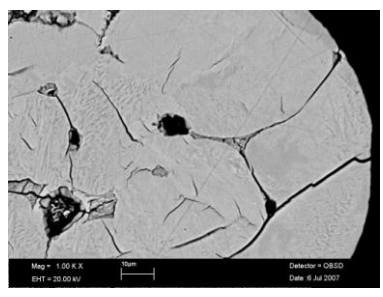
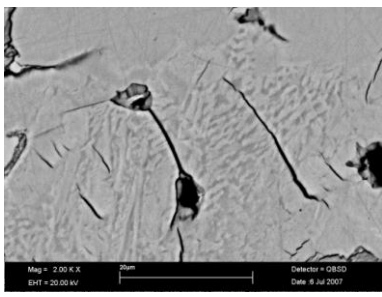
Inclusions are first observed using polarized light microscopy which is of interest here because of the crystallographic anisotropy of the α and β structure. The different phases display a color contrast which allows to identify them without ambiguity. In addition, SEM imaging using the backscattered electrons mode and EDX analysis completes the phase identifications.

Figure 71 shows SEM observation of natural stones. The darkest zones correspond to areas where concentrate impurities such as: Si, O, C, S, Ca, Fe and Ni. The dark lines are fractures in the stones. On SEM image in Figure 71, the clear zones correspond to Ni_9S_8 and the gray one to NiS phases (α , β) and possibly some Ni_3S_4 . We note that the set of natural stones separates into two families: one containing Ni_9S_8 (8/17) (Figure 71a) and one with no Ni_9S_8 (9/17) (Figure 71b).

Annexes

		
<p>C501-462-B</p> <p>Grey zones → Ni: 49.62 ± 0.09 Fe: 0.12 ± 0.02 S: 50.28 ± 0.06</p> <p>Clear zones → Ni: 52.00 ± 0.37 Fe: 0.06 ± 0.02 S: 47.93 ± 0.35</p>	<p>Balk3</p> <p>Grey zones → Ni: 49.23 ± 0.95 Fe: 0.27 ± 0.05 S: 50.50 ± 0.94</p> <p>Clear zones → Ni: 52.14 ± 0.10 Fe: 0.11 ± 0.01 S: 47.75 ± 0.10</p>	<p>NiS-HST-18</p> <p>Grey zones → Ni: 48.92 ± 0.13 Fe: 1.01 ± 0.08 S: 50.10 ± 0.10</p> <p>Clear zones → Ni: 51.39 ± 0.18 Fe: 0.68 ± 0.08 S: 47.93 ± 0.17</p>
		
<p>C-502-504-E</p> <p>Grey zones → Ni: 49.24 ± 0.16 Fe: 0.2 ± 0.01 S: 50.56 ± 0.16</p>	<p>C502025-564</p> <p>Grey zones → Ni: 49.68 ± 0.09 Fe: 0.20 ± 0.04 S: 50.12 ± 0.08</p>	<p>C-502-504-O</p> <p>Grey zones → Ni: 49.26 ± 0.17 Fe: 0.21 ± 0.05 S: 50.53 ± 0.13</p>

a: Ni₉S₈ contained stones

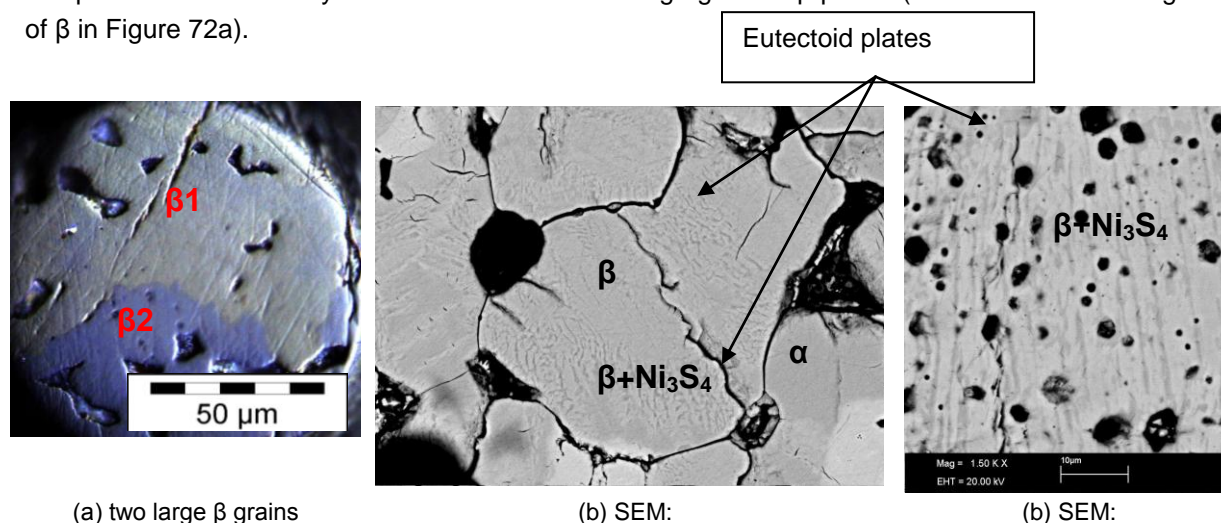
		
<p>Balk1</p> <p>Grey zones → Ni: 49.39 ± 0.18 Fe: 0.14 ± 0.02 S: 50.47 ± 0.17</p>	<p>NiS-C502-104Prob HST</p> <p>Grey zones → Ni: 49.65 ± 0.28 Fe: 0.15 ± 0.03 S: 50.20 ± 0.30</p>	<p>NiS-HST-C501-408-A</p> <p>Grey zones → Ni: 47.96 ± 0.53 Fe: 1.62 ± 0.08 S: 50.38 ± 0.56</p>
		
<p>C-502-504-F</p> <p>Grey zones → Ni: 49.66 ± 0.38 Fe: 0.21 ± 0.02 S: 50.13 ± 0.39</p>	<p>C-502-504-N</p> <p>Grey zones → Ni: 49.51 ± 0.13 Fe: 0.19 ± 0.03 S: 50.29 ± 0.12</p>	<p>C-502025-720</p> <p>Grey zones → Ni: 49.03 ± 0.66 Fe: 0.11 ± 0.04 S: 50.82 ± 0.63</p>
		
<p>NiS-C502-025-412</p> <p>Grey zones → Ni: 47.24 ± 1.06 Fe: 0.23 ± 0.13 S: 52.70 ± 1.12</p>	<p>NiS-C703055-01_Prob Building</p>	<p>NiS-C703055-01_Prob Building</p>

b: stones without Ni_3S_8

Figure 71 : SEM observation of the series of natural inclusion (dark zones correspond to fractures in stones; clear zones correspond to Ni_3S_8 and the gray one to NiS phases (α , β) and possibly some Ni_3S_4). For each natural stones inclusion, EPMA analysis (in at%) are given below the SEM images. the majority of stones show composition around $50.3 \pm 0.15 \text{at}\% \text{S}$ and Fe impurities of about $0.2 \text{at}\%$, i.e. these inclusions have not the NiS stoichiometry)

Annexes

A detailed investigation was performed on the grey zones which reveal the fine microstructure shown in Figure 72. Figure 72a shows the microstructure frequently observed in the Ni_9S_8 containing samples: the stone is fully transformed and shows large grain of β phase (For instance the two grains of β in Figure 72a).



(a) two large β grains

(b) SEM:

(c) SEM:

Figure 72 : Optical and SEM observation of NiS stones illustrating 3 typical morphology: (a) a coarse morphology, (b) Coarse morphology+ lamellar eutectoids, (c) lamellar eutectoids alone

Figure 72b illustrates a microstructure frequent in the stones which are not containing Ni_9S_8 phase. It consists in to a partially transformed inclusion showing the coexistence of three phases α , β and Ni_3S_4 , the β phase regions being surrounded by $\beta+\text{Ni}_3\text{S}_4$ area. In this mixed zone, the microstructure is characterized by a rather coarse morphology surrounded by area reminding a lamellar eutectoid one. The Ni_3S_4 phase have small size ($\sim 0.5\mu\text{m}$) and occupies generally a small volume fraction (less then 10%) while β phase grains are larger and display various orientations. Figure 72c shows a specifically spectacular morphology which has been observed in only one stone. It displays a typical eutectoid microstructure made of $\beta+\text{Ni}_3\text{S}_4$ parallel plates which have developed along the same direction in the whole inclusion. The existence of such a microstructure indicates that the initial composition of the α phase can reach the eutectoid composition known from the phase diagram[22] to be $(\text{Ni}_{48.45}\text{S}_{51.55})$.

The development of so different microstructures (namely a coarse morphology, coarse morphology+ lamellar eutectoids, and lamellar eutectoids alone) indicate that the initial composition of the α phase often departs from the stoichiometric NiS composition, opening the possibility for different transformation mechanism. This is very reminiscent of the classic situation in carbon steels where depending on the composition, austenite decomposes in ferrite, or in a mixture ferrite + carbides, or in a lamellar eutectoid called perlite. This motivates the investigation of the stone composition for each of the observed morphology. This was done with precision using EPMA.

It should be stressed here that β -phase coexisting with Ni_3S_4 phase in natural stones were not reported in the past because neither optical microscopy nor SEM observations in specific contrast conditions had ever been carried out. Therefore the stones were usually thought to be homogeneous NiS stones.

A.II.2 Phase compositions

It is worth noticing that, inclusion being heterogeneous (after transformation, both α β and Ni_3S_4 may be present), the compositions given in Figure 71 correspond to an average on about 10 punctual analyses taken in the grey contrast zone in Figure 71. The microstructures scale being smaller or of the same order as the probe size ($\sim 2\mu\text{m}$), this average composition measures the composition of the inclusion before transformation.

According to composition analysis measured by EPMA reported in Figure 71, the average composition varies between 50.10 and 52.7at%. The Fe content varies between 0.11 and 1.62at% with a majority of the samples having a Fe content close to 0.2at%. Only two samples present a strong Fe content: 1.01 and 1.62 at %. In the clear contrast zones like in Figure 71a, we note that the Sulphur content is close to 47.85at%. This composition is close to that of Ni_9S_8 which is the stable phase at low temperature according to the Ni-S phase diagram (Figure 73b). The dissolved quantity of Fe in Ni_9S_8 phase of the different sample varies between 0.06 and 0.68 at%.

In summary, NiS zones in different stones present composition variability from 50.1 toward 51.5at%S. The majority of inclusions are low overstoichiometric one. Their average composition is around $50.2 \pm 0.15\text{at}\%\text{S}$ and 0.2at%Fe. There exist also inclusions with higher Sulphur content around 50.5 at%S. Remarkably, two inclusions show very overstoichiometric composition with 50.82 and 52.70 at%S. These two compositions are indeed consistent with the microstructure typical of the eutectoid decomposition reported in Figure 72c.

A.III. Discussion

Earlier studies of Ni-S stone had already provided characterization about phase nature but composition of NiS zones was always difficult to investigate essentially because of the precision required with respect to the small range of composition of the phase involved. However Kasper *et al* [10] has shown that a majority of inclusion has near stoichiometric composition : the average composition was $(\text{NiFe})\text{S}_x$ $x=0.99\pm 0.03$ ($\sim \pm 0.75\text{at}\%$ error including dispersion and experimental accuracy). It is worth noting that this average composition was given by the mean value obtained on a set of stones. In the present study, we noted that some stones seem to be very overstoichiometric. Indeed possible overstoichiometry was already pointed out by Barry [54] using EDS spectra and comparing the ratio of Ni and S peak in contrast to the ratio found for the standard Millerite. These studies [10, 54] have motivated the present analysis which focus on the composition of each stone and was performed with EPMA instead of EDX analysis to have a better precision necessary to account for the actual composition diversity. The measured overstoichiometries are consistent with the observation of Kasper and Barry [10, 54] with the advantage of being obtained with a precise analytical method. In addition the microstructural observations carried out in parallel had confirmed that some stones can reach the eutectoid composition which rules out any doubt on composition analysis.

Annexes

Actually the overstoichiometry of NiS stones are of interest since the diversity of composition could explain the glasses breakage rate recorded during HST [3]. Indeed we observed that: i the stone composition is ranging from 50.10 and 52.7at% ,i.i. the microstructure after transformation is different depending on composition (changes from a coarse morphology for near stoichiometric composition, toward lamellar eutectoids morphology for high overstoichiometry). It means that the transformation involved different mechanisms with their own kinetic law. In particular, the observation of Ni_3S_4 phase indicated that long range Sulphur diffusion must occur during the transformation of the overstoichiometric stone. In this case, the transformation kinetics is expected to be much slower than the one when no long range diffusion is involved. As the majority of stones have low overstoichiometry, most of the NiS stones will be certainly rapidly transformed. However, the transformation from α to β is likely to involve a short range partitioning of S across the moving transformation interface. As a consequence the remaining α phase will progressively get enriched in Sulphur up to a point where the eutectoid transformation takes over. All these processes involve diffusion on short distances coupled with interface migration, which are relatively rapid processes. This explains qualitatively the reason why 80% of glasses fractured during heating step of HST. On the contrary, for the overstoichiometric stones and the ones with a high amount of Fe, the diffusion processes being long ranged, the transformation is more sluggish and the glass fracture occurs during the isothermal step. Thus the optimization of HST needs to extend the kinetic study of the $\alpha \rightarrow \beta$ -NiS phase transformation kinetics in the range of overstoichiometric composition.

According to the EPMA analyses and the microstructure characterization results, the composition of α phase in stones, after preparation, is not NiS stoichiometry (even in the presence of the Ni_9S_8 phase) and present a broad composition range. This result apparently disagrees with the phase diagram which predicts a NiS stoichiometric composition of the α phase at low temperature. Actually, in order to understand the origin of this deviation from stoichiometry, it is useful to examine the thermal cycle followed during the solidification of NiS inclusions.

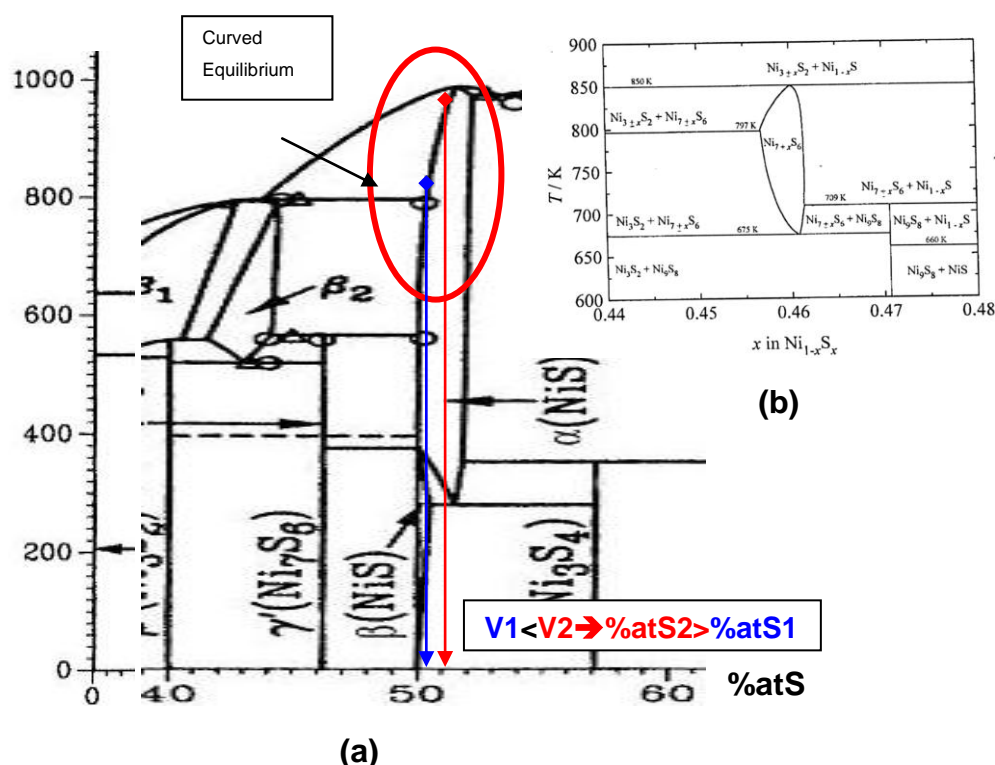


Figure 73 : Ni-S phase diagram: after Nash, P. *et al* (1991)[22] (b) Ni-S phase diagram after Seim *et al* (1995) [55] showing that Ni₉S₈ is the stable phase at low temperature instead of Ni₇S₆.

As described in the introduction, the initial composition of α phase within the stones is dependent of the liquid one. The study of the NiS phase diagram has shown [7-9] that Nickel sulphide zones containing a quantity of Sulphur higher than stoichiometry 1:1 are not stable in the liquid state and then decompose to form sulphides rich in Nickel (Ni_{1+x}S) occurs. According to the phase diagram near the stoichiometric composition (Figure 73), the α phase domain boundary is a straight line below 700°C and becomes curved for $T > 700^\circ\text{C}$. Therefore during glass cooling, the first step is the formation of solid α NiS phase which is overstoichiometric. As cooling is going on, the initial overstoichiometric NiS phase is enriched in Ni up to stoichiometric NiS. This solidification path is illustrated in Figure 73 by the lines corresponding to different cooling rates ($V1$, $V2$). The final composition of α phase in a given inclusion depends on the cooling rate seen by this inclusion. This cooling rate depends on the stone position in the glass plate with respect with the surface. The faster the cooling is, the more overstoichiometric in S the α phase will be, as sketched in Figure 73. Consequently, for a given average composition, it is expected that overstoichiometric inclusions will be close to the surface where the cooling rate is the highest. Since the cooling rate in glass production process is usually very high (30 min from 1000°C to 25°C), according to the above reasoning, many inclusions are expected to be overstoichiometric in S. This expectation is in agreement with the fact that the majority of near stoichiometric inclusions are found in the inner zones of glass section.

A.IV. Conclusion

The main point of the study was to consider the composition analysis as well as microstructural characterization of NiS zones using the combination of optical microscopy and SEM. The composition analysis was carried out with EPMA to obtain the precise results required for the small composition range exhibited by the NiS zone in Ni-S inclusion. The study reported in this paper confirmed that α -phase is not of NiS stoichiometry. The majority of studied stones show composition around $50.2 \pm 0.15 \text{ at\%S}$ and Fe impurities of about 0.2 at\% . There exist also stones with very overstoichiometric composition.

Not only has this detailed study evidenced that composition is significantly changing from one stone to another, but it has significant consequences for the transformations morphologies. Natural stones show the development of three microstructures according to stones compositions which clearly indicate that the transformation mechanism changes with composition. According to our microstructural observation, a 0.5 at\% difference on composition of the inclusion have a strong effect on the transformation microstructures and consequently on the mechanisms. Therefore the optimization of HST needs to consider the effect of overstoichiometry on transformation mechanism and further its impact on the kinetics of the phase transformations.

Annexe B : Cristallographie et relation structurale entre les phases α et β

Dans ce paragraphe, on décrira les structures cristallographiques des phases α & β -NiS en proposant une description simplifiée en couches plus ou moins planes de ces structures. On donnera aussi une analyse structurale qui peut rendre compte des relations d'orientation entre les phases α et β -NiS observées en EBSD

Dans ce paragraphe, on décrira les structures cristallographiques des phases α & β -NiS. Les autres phases mentionnées dans le diagramme de phases ne seront pas elles étudiées en détail.

Le Table 7 présente les structures cristallographiques des différentes phases du système Ni-S.

Formule	Classe cristalline	Groupe d'espace (Symbole Pearson)	Paramètres de maille (nm)	Fiches ASTM ou JCPDS
α -NiS	Hexagonale	$P6_3/mmc$ (hP4)	$a=0,343$ $c= 0,535$	2-1273 65-0395 89-1957
β -NiS Millerite	Rhomboédrique	$R3m$ (hR6)	$a=0,962$ $c= 0,315$	12-041 65-3686
Ni_7S_6	Octaédrique	$Cmcm$ (oC56)	$a = 0,3274$ $b = 1,1359$ $c = 1,6157$	24-1021
Ni_3S_4 Polydymite	Cubique	$Fd-3m$ (cF56)	$a = 0,9476$	8-106 43-1469
Ni_9S_8 ou Ni_7S_6 basse T°	Orthorhombique	$C222$ (oC68)	$a = 0,93359$ $b = 1,12185$ $c = 0,943$	22-1193
$Ni_{17}S_{18}$	Orthorhombique	$P3_121$ (hP105)	$a = 1,0290$ $c = 1,5993$	Collin <i>et al.</i> (1983)[56]
Ni_3S_2	Rhomboédrique	$R32$ (hR5)	$a = 0,57454$ $c = 0,7135$	8-126 44-1418

Table 7 : Structures cristalline des phases du système Ni-S

Les phases α et β sont, respectivement, de structure hexagonale et rhomboédrique. Elles sont présentées en Figure 74 et Figure 75. Sur la Figure 75, la phase β est représentée par sa maille primitive rhomboédrique. Par la suite, comme tous les auteurs, nous utiliserons de préférence la maille hexagonale dérivée de cette maille primitive. La maille hexagonale est obtenue en triplant le volume de la maille primitive. C'est pourquoi la maille hexagonale de la phase β a de grands paramètres de

maille dans le plan de base ($a = 0,962 \text{ nm}$), ceci ne résulte pas de motifs plus complexes que ceux de la phase α mais de l'utilisation d'une maille non-primitive.

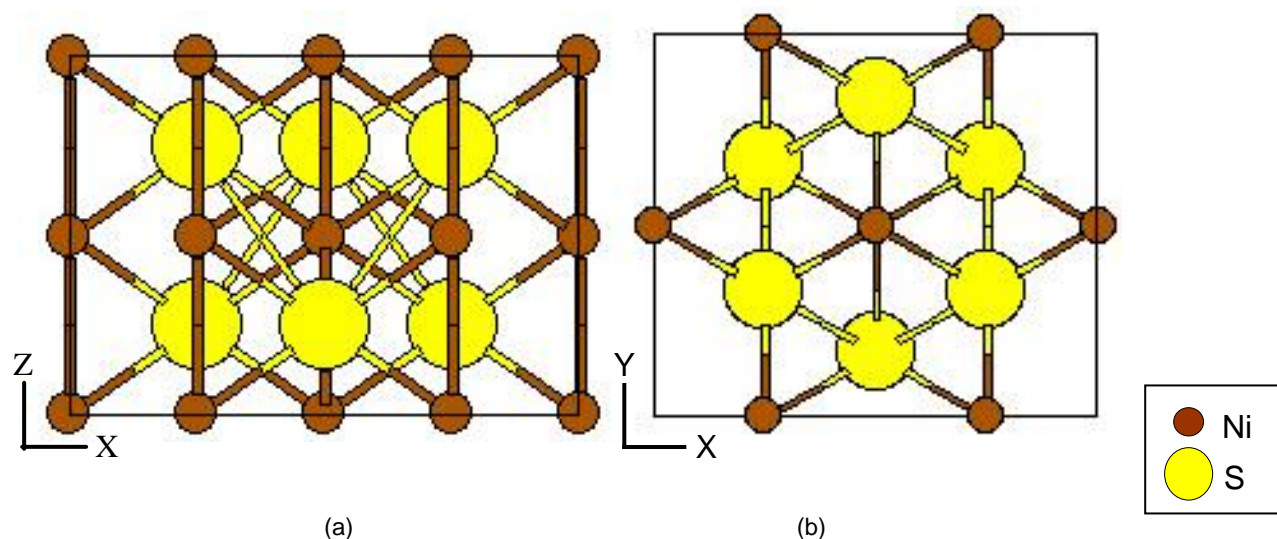


Figure 74 : Représentation de la maille de la phase α vue selon deux directions de projection simples :
(a) en projection selon une direction (010) (b) en projection selon une direction (001)

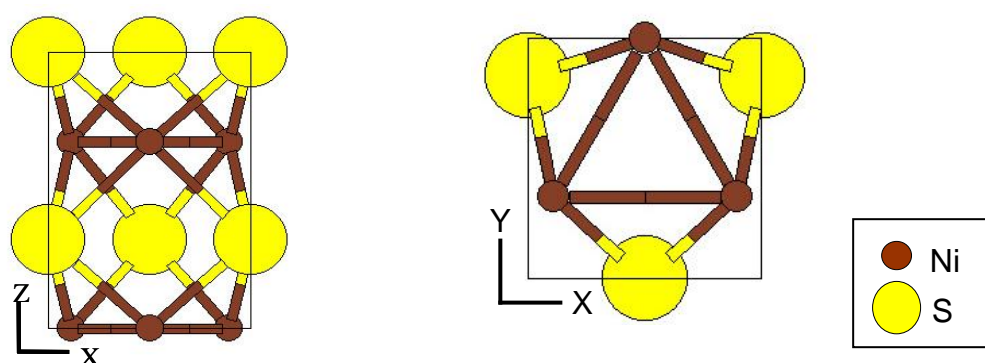


Figure 75 : Représentation de la maille de la phase β vue selon deux directions de projection simples :
(a) en projection selon une direction (010) (b) en projection selon une direction (001)

La comparaison des structures des phases α et β -NiS a fait apparaître qu'il était possible d'adopter une description simplifiée en couches de la phase α mais aussi de la phase β -NiS. La phase α étant de structure hexagonale, il est facile d'en faire une description en couches parallèles aux plans de base. Cette démarche de description en couches a été étendue à l'examen de la phase β . Les deux descriptions obtenues peuvent de plus être reliées entre elles de façon assez simple.

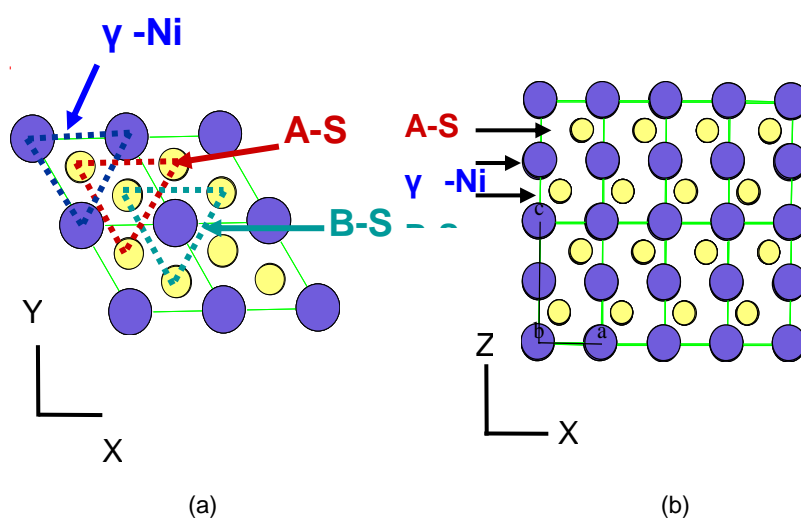
La phase α qui est présentée en projection selon l'axe c dans la Figure 76a et perpendiculairement à cet axe en Figure 76b peut se décrire en alternance de plans purs en atomes de Nickel et de plans

Annexes

d'atomes de Soufre. Ces plans forment un pavage triangulaire régulier d'atomes de Nickel ou d'atomes de Soufre.

Les plans de Nickel se reproduisent de façon identique le long de l'axe c (Figure 76). En revanche les plans de Soufre sont décalés de façon à se trouver à l'aplomb des centres des triangles de Ni. Il y a deux décalages possibles pour réaliser ce centrage par rapport au triangle de Nickel. Les plans de Soufre présentent alternativement chacun des décalages possibles.

En résumé, la maille de la phase α est donc constituée de deux plans de Nickel sans décalage et de deux plans de Soufre décalés entre eux et par rapport aux plans de Ni. Le décalage entre les plans de Soufre est décrit par une translation suivant le vecteur $(1/3, -1/3, 1/2)$.



Paramètres de maille de la phase α : $a = 0,343\text{nm}$ $c = 0,535\text{nm}$ $\gamma = 120^\circ$

Figure 76 : Représentations de la maille hexagonale de la phase α selon deux directions cristallographiques simples (projection selon l'axe c en Figure 76a et projection selon une direction de base de l'hexagone en Figure 76b).

Les plans de Soufre forment des pavages triangulaires empilés selon l'axe c . Les plans de Soufre notés A-S et B-S sont décalés comme l'indique la Figure 76(a). Les plans de Nickel noté γ -Ni forment un pavage triangulaire se reproduisant de façon identique selon l'axe c

En Figure 76, les vues en projection permettent de visualiser l'arrangement sous forme de pavage triangulaire dans les couches de Nickel et de Soufre. Les couches en atomes de Nickel correspondent à un alignement des colonnes de Ni (pavage en traits pointillés bleus) alors que la vue en projection selon l'axe (100) met en évidence les décalages des plans de S visibles aussi sur la projection selon (001) (pavage en traits pointillés rouges et verts).

La phase β vue en projection selon l'axe c présentent aussi des motifs en triangles d'atomes de Nickel et de Soufre. Les plans de S sont aussi décalés et les atomes de S se trouvent à l'aplomb des centres des triangles de Ni (Figure 77 a projection suivant l'axe c). La structure en couches de la phase β peut être mises en évidence en reportant sur la structure les coordonnées selon l'axe c (Figure 77a). Il apparaît ainsi clairement une répartition en couches de motifs triangulaires.

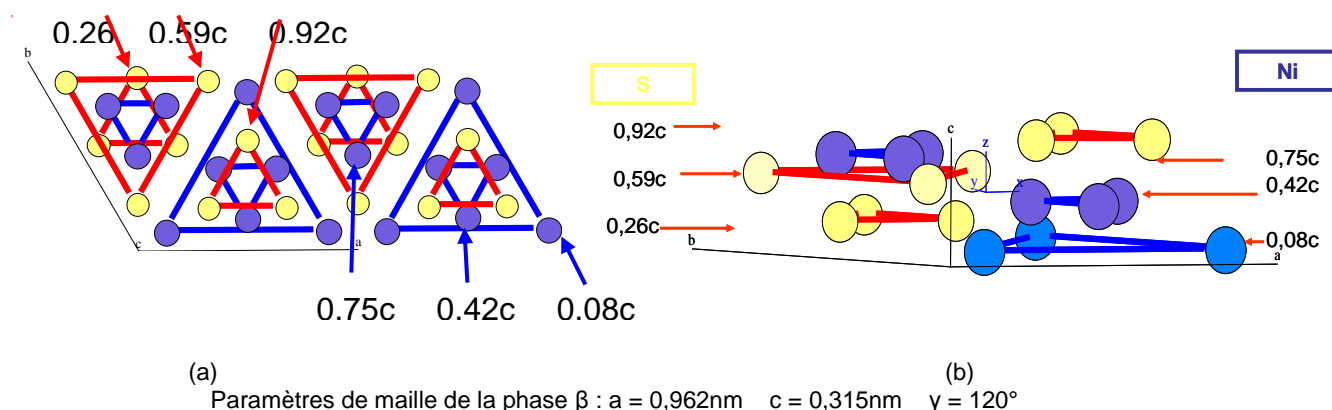


Figure 77 : Représentations schématiques de la maille rhomboédrique de la phase β vues en projection suivant l'axe c Figure (a) et de biais Figure (b) .

Les atomes sont reliés sur ce schéma en fonction de leurs coordonnées selon l'axe c . Des motifs triangulaires formés de Nickel ou de Soufre sont visibles mais ils ne constituent pas des plans « pur Ni » ou « pur S » à pavages triangulaires mais plutôt des couches ondulées

Il est possible de décomposer la phase β en couches triangulées d'atomes de Nickel et de Soufre mais contrairement à la phase α , ces couches ne sont pas planes mais présentent un aspect ondulé dû aux écarts en coordonnées z des motifs d'atomes de Nickel et de Soufre.

La Figure 78 donne une représentation des couches triangulées formées d'atomes de Soufre qui décrivent l'arrangement des atomes de Soufre dans la phase β .

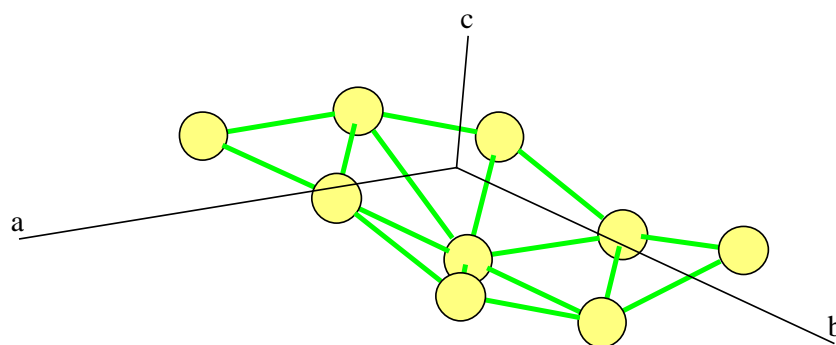


Figure 78 : Couche ondulée formée par les atomes de Soufre en reliant les atomes à $z = 0,26$ et $z = 0,59$. Le paramètre de maille selon l'axe c étant $c = 0,315\text{ nm}$, l'amplitude de l'ondulation de la couche est de l'ordre de $0,1\text{ nm}$.

La même représentation en couches ondulées peut être construite avec les atomes de Nickel. Il faut souligner que contrairement à la couche d'atomes de Soufre formées de motifs triangulaires presque identiques, la couche de Nickel est formée de motifs imbriquant un grand triangle et un petit triangle.

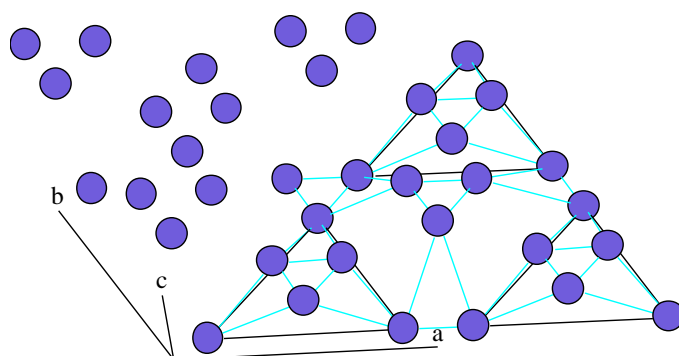


Figure 79 : Couche ondulée formée par les atomes de Nickel en reliant les atomes de coordonnées $z=0,08$, $0,42$ et $z = 0,75$. Le paramètre de maille selon l'axe c étant $c = 0,315$ nm,

La maille de la phase β est donc constituée d'une succession de plans de Ni et plan de S ondulés. Il existe un décalage entre les couches de Nickel et de Soufre de façon à centrer les atomes de Nickel sur le centre du triangle de Soufre mais à la différence de la phase α , dans la phase β les couches Nickel (respectivement de Soufre) se reproduisent à l'identique le long de l'axe c .

En résumé, les structures des phases α et β peuvent se décrire simplement par une alternance de couches à pavage triangulaire d'atomes Ni et de couches à pavage triangulaire d'atomes S. Les couches sont très semblables en termes de densité atomiques et de motifs triangulaires. Mais dans la phase α , les couches sont planes et formées de triangles réguliers. En revanche dans la phase β , les couches sont ondulées et formées de triangles légèrement déformés (distance Ni-Ni = $0,344$ nm dans la phase α , distances Ni-Ni = $0,253$ nm et $0,373$ nm dans la phase β). Dans les deux phases, les couches de Ni se reproduisent de façon identique perpendiculairement à l'axe c . Dans la phase α , les plans d'atomes de Soufre présentent des décalages entre eux et par rapport aux couches de Nickel. Dans la phase β , les couches d'atomes de Soufre sont en décalage par rapport aux couches de Nickel mais se reproduisent de façon identique le long de l'axe c .

En se limitant aux atomes de Soufre, on pourrait décrire la phase α par un empilement de type A-B alors que la phase β correspond à un empilement de type A-A. Les atomes de Nickel forment des couches γ -Ni qui s'insèrent entre les couches de type A ou B. Les couches γ -Ni sont décalées par rapport aux couches de Nickel de type A ou B de façon à placer les colonnes de Nickel à l'aplomb du centre des triangles formés par les atomes de S.

On retient donc comme différences marquantes entre les phases α et β -NiS :

- les couches d'atomes de Soufre en décalage dans la phase α et sans décalage dans la phase β
- les déformations locales plus ou moins importantes des couches atomiques dans la phase β par comparaison aux plans pavés de triangles réguliers dans la phase α .

La description en couches des structures des phases α et β met l'accent sur les similitudes et différences entre ces phases. Elle suggère des stades précurseurs possibles pour la phase β à partir de la phase α . En effet, une faute d'empilement dans la phase α qui conduira localement à une séquence A-A-A qui a une structure proche de la phase β . Cette remarque implique des relations d'orientation classique entre les phases α et β -NiS ($C\alpha//C\beta$). Néanmoins cette observation ne correspond pas avec les OR observées dans les transformations de phase dans NiS et notamment avec celles observées dans les morphologies lamellaires et globulaires.

Cependant on a observé que la relation d'orientation entre les phases α et β (globulaire et lamellaire) est telle que les densités atomiques dans les plan prismatique de β $(100)\beta$ et le plan de base de α $(001)\alpha$ (Figure 80) sont respectivement : $217 \cdot 10^{-3} \text{ (Ni+S) / \AA}^2$ et $198 \cdot 10^{-3} \text{ (Ni+S) / \AA}^2$. En plus la comparaison des distances entre ces couches (Figure 80) montre une proximité structurales (Distance entre plans : $(001)\alpha = c/2 = 2,68 \text{ \AA}$; $(100)\beta = 2,77 \text{ \AA}$). Cette proximité structurale et de densité montre que la relation d'orientation observée en EBSD est compatible avec une transformation sans changement de composition avec déplacement courte distance ce qui est caractéristique de la transformation massive.

Ainsi l'étude des proximités structurales entre les phases α et β a montré que les relations d'orientation ne peuvent pas être anticipée seulement à partir de considérations cristallographiques. La détermination des relations d'orientation EBSD a montré ici clairement que la relation cristallographique la plus simple n'est pas celle observée.

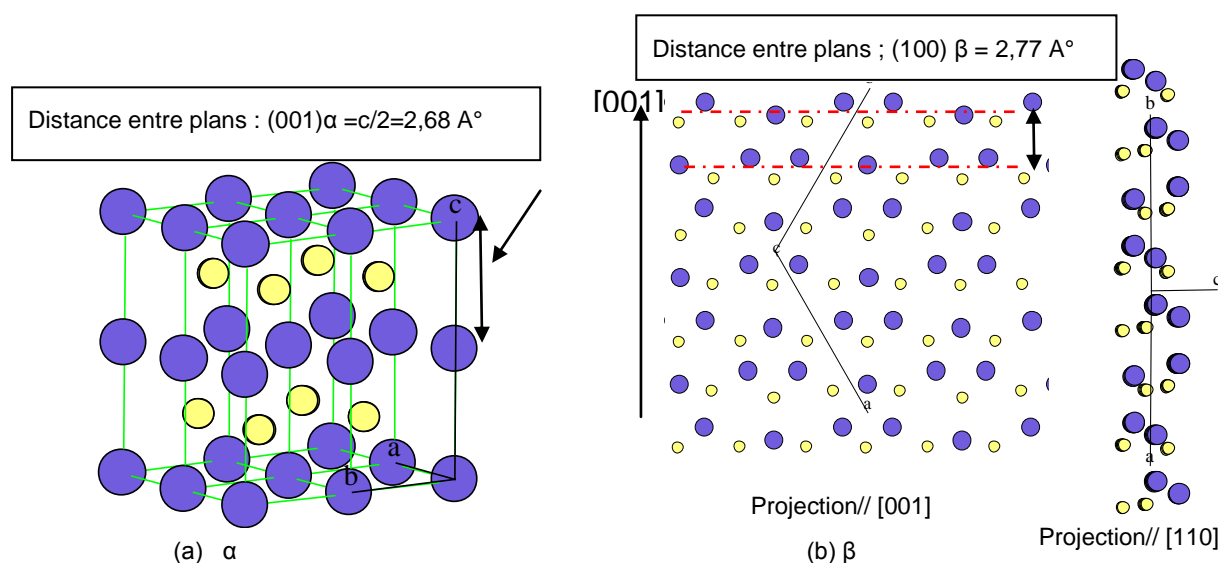


Figure 80 : Représentations schématiques de la maille (a) hexagonale de la phase α ; (b) rhomboédrique de la phase β vues en projection suivant l'axe $[001]$ Figure 10(b) et $[110]$.

Densité des plans : $(001)\alpha = 217 \cdot 10^{-3} \text{ (Ni+S) / \AA}^2$; $(100)\beta = 198 \cdot 10^{-3} \text{ (Ni+S) / \AA}^2$

Annexe C : Observation en Microscopie électronique (MEB) avec chauffage *in situ* de la transformation $\alpha \rightarrow \beta$ -NiS

Avant les observations en microscopie optique *in situ*, nous avons d'abord fait un essai en MEB avec chauffage *in situ*. La microscopie électronique avec chauffage *in situ* permet d'enregistrer des séquences de formation des phases notamment en ce qui concerne la formation de la phase Ni_3S_4 ce qui n'est pas possible en optique vue la taille des précipités de la phase Ni_3S_4 . De plus nous utilisons une imagerie en contraste chimique (électrons rétrodiffusés détecteurs QBSD) qui permet de distinguer la phase Ni_3S_4 des phases α et β NiS. Les expériences, réalisées dans un MEB munie d'une platine chauffante, ont montré la faisabilité de ces expériences.

Deux résultats importants ont été observés. D'une part, une séquence complète de croissance de la phase β dans la morphologie lamellaire i.e. croissance d'une lamelle β suivie de la précipités de Ni_3S_4 a été obtenue (Figure 81a). D'autre part, concernant la morphologie globulaire pour laquelle il n'y a pas de précipitation Ni_3S_4 ni de contraste chimique (phases α et β NiS), on observe un changement de l'état de surface du à un relief et la formation de fissure (Figure 81b).

L'étude *in situ* a été conduite sur un échantillon partiellement transformé (éch $\text{Ni}_{48,86}\text{S}_{51,14}$ 200°C-45mn). Les micrographies en Figure 81a présentent différents états d'avancement de la transformation, sur la même zone, pour un traitement isotherme à $T=200^\circ\text{C}$. Ces micrographies permettent de suivre l'évolution de la croissance d'une lamelle de phase β . On note que la germination a lieu après quelques minutes à 200°C suivie d'une deuxième étape de croissance assez rapide de la lamelle de phase β . Ensuite la croissance des lamelles ralentit et on observe le début de précipitation de la phase Ni_3S_4 à l'interface α/β (après ~30mn de maintien). La croissance de phase β est quasiment arrêtée à ce stade. On assiste alors à une croissance de la phase Ni_3S_4 certainement par consommation du Soufre rejeté à l'interface α/β vers les zones α non encore transformées. Cet enrichissement en Soufre de la phase α explique le ralentissement de la croissance de la phase β dans cette zone.

Ceci montre que la précipitation de la phase Ni_3S_4 intervient après un stade très avancé de la croissance des lamelles β . Ceci conforte l'hypothèse que la fraction transformée résulte principalement des lamelles β .

Ces observations de la transformation en MEB avec chauffage *in situ* ont donné des résultats intéressants. Cependant l'observation reste assez difficile: d'une part la qualité des images est affectée par le chauffage (instabilité du détecteur des électrons rétrodiffusés) et d'autre part il est difficile de différenciation en MEB les phases α et β -NiS en imagerie MEB. Pour une étude *in situ* donnant une description plus complète de la transformation de phase, nous avons opté pour la Microscopie optique avec chauffage *in situ* pour laquelle l'observation des phases α et β -NiS est plus facile grâce au bon contraste des phases en mode lumière polarisée.

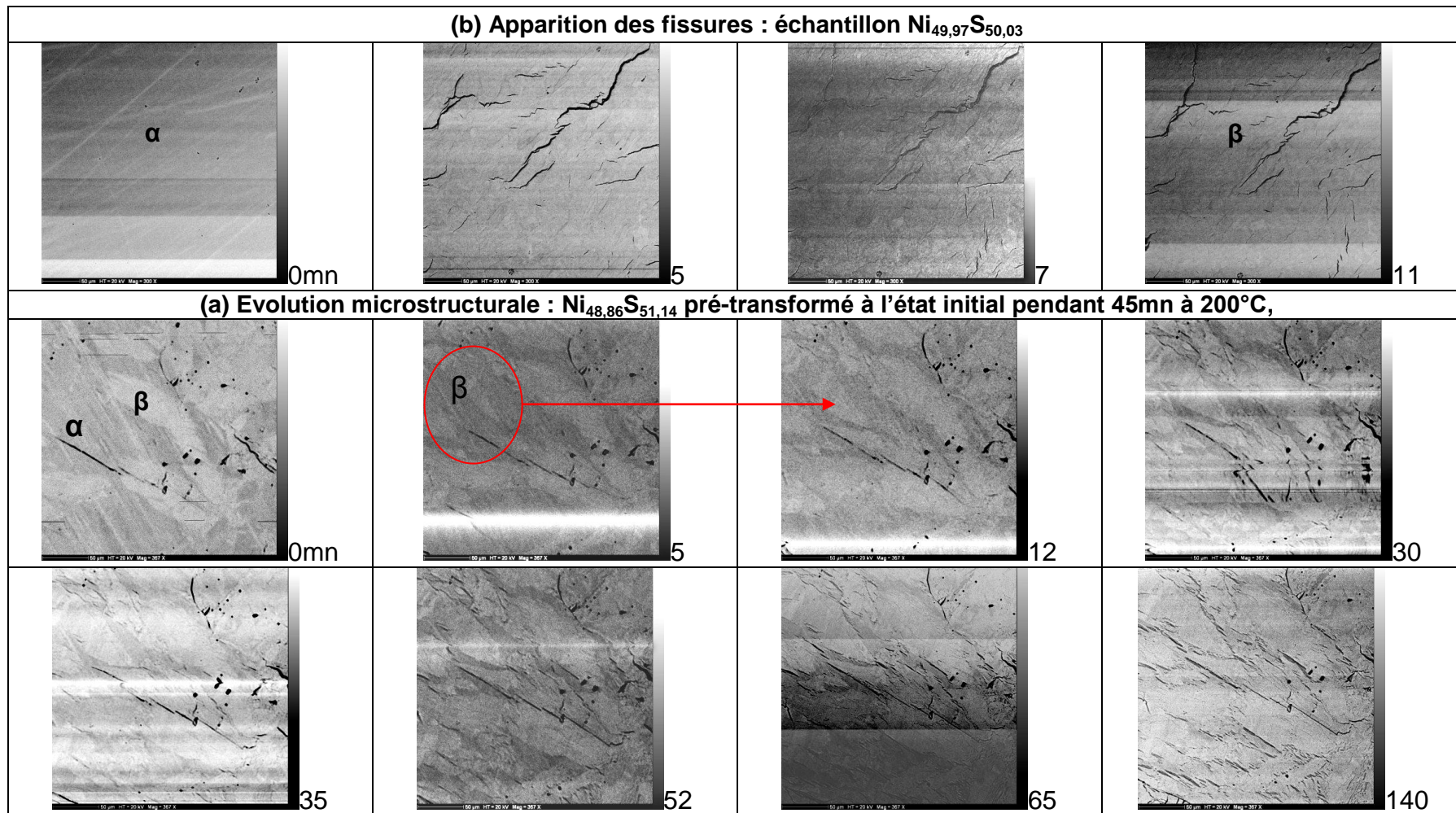


Figure 81 : Observation au MEB avec chauffage *in situ* de la transformation $\alpha \rightarrow \beta$ -NiS : apparition des fissures et évolution microstructurale ($T=200^\circ\text{C}$).

Annexe D : Caractérisation par dilatométrie de la transformation de phase

Nous avons remarqué dans la littérature une différence entre les valeurs du changement de volume, reliées à la transformation de phase $\alpha \rightarrow \beta$ -NiS, calculées suivant différentes méthodes : ~4,6% par dilatométrie et ~2% à partir des paramètres de maille. Afin de déterminer l'origine de cette différence, un suivi par dilatométrie de la transformation de phase en parallèle avec une caractérisation de l'état de surface avant et après la transformation a été réalisé.

La Figure 82 montre les courbes enregistrées en dilatométrie au cours de la transformation pour trois compositions différentes. D'après ces courbes le changement de volume final est de l'ordre de 12% pour l'échantillon 50.39at%S et celui contenant du Fe. Par contre il est de l'ordre de 4.7% pour l'échantillon très surstœchiométrique 51.14at%S. Ces résultats montrent que dans tous les cas le changement de volume total est différent de celui estimé à partir des paramètres de maille. Ceci suggère l'existence d'un lien entre le changement de volume total et les morphologies. Ce lien pourrait être déterminé à travers une caractérisation de l'évolution de l'état de surface pendant la transformation pour les différentes morphologies.

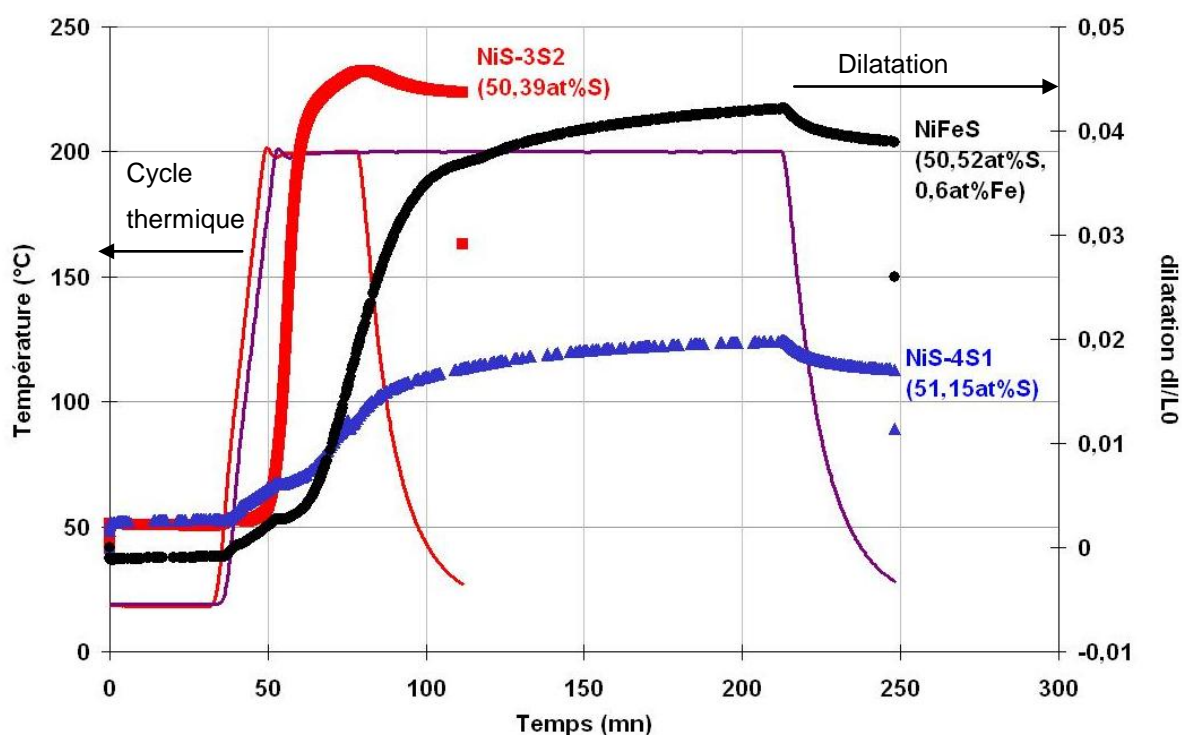


Figure 82 : suivi par dilatométrie de la transformation de phase : illustration du changement de volume pour plusieurs composition de l'échantillon initial Ni(Fe)S : le changement de volume final dépend de la vitesse de transformation et est supérieur à celui dû juste au changement de cristallographie (~2%).

La Figure 83 présente différents états d'avancement de la transformation obtenus sur l'échantillon de composition $\text{Ni}_{49}\text{Fe}_{0,6}\text{S}_{50,42}$ pour un traitement isotherme *in situ* à $T=200^\circ\text{C}$ après 0, 20 et 106mn. D'après les micrographies on n'observe aucun changement de microstructure après 20mn (Figure 83(b)) par rapport à l'état initial de l'échantillon (Figure 83(a)) : la transformation n'a pas encore commencée. Par contre, après 106mn, fin de transformation, la micrographie de Figure 83(c), montre l'apparition des fissures. Ces observations mettent en évidence d'une part l'apparition des fissures pendant la transformation de phase et qu'elle est directement liée à la transformation de phase et ainsi au changement de volume. L'observation de l'apparition des fissures au cours de la transformation de phase permet d'expliquer les différences entre les valeurs bibliographiques de changement de volume. En effet la dilatométrie donne une mesure globale du changement de volume rassemblant à la fois l'effet de changement de cristallographie et l'apparition de fissures alors que le calcul cristallographique ne prend pas en compte la contribution des fissures.

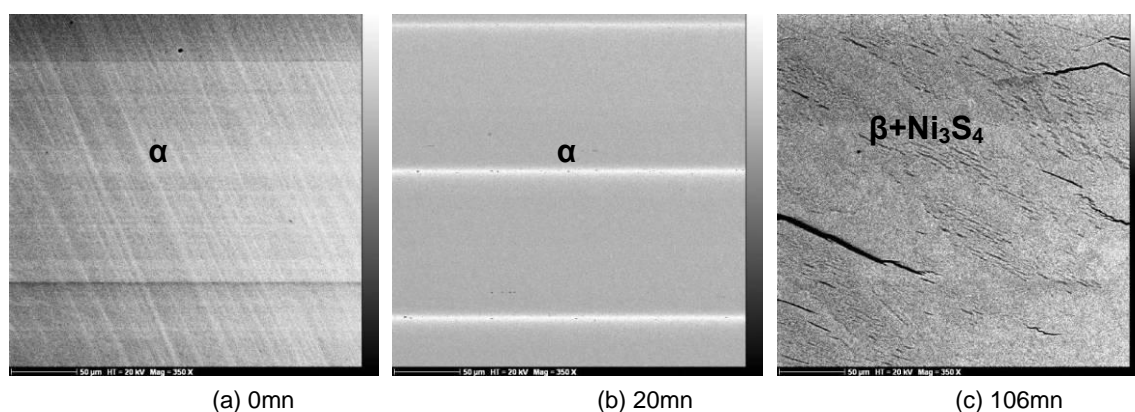
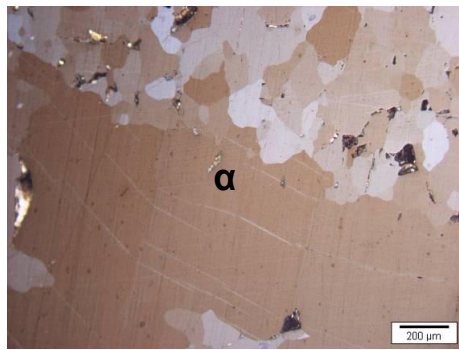


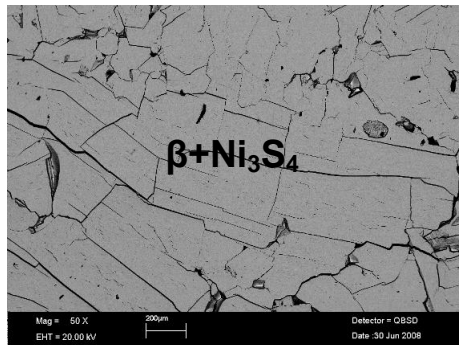
Figure 83 : Observation MEB *in situ*: apparition des fissures du à la transformation de phase $\alpha \rightarrow \beta\text{-NiS}$
Les fissures qui apparaissent suite à la transformation de phase sont à l'origine de cette différence.

Les micrographies de la Figure 84 montrent que la concentration de fissures est plus importante dans un échantillon pour lequel la transformation est rapide (Figure 84a) par rapport à l'échantillon transformation lente (Figure 84b). Ce qui peut expliquer les différences de changement de volume obtenues entre les échantillons de la Figure 82.

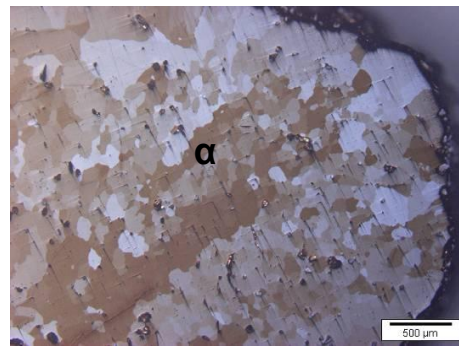
Annexes



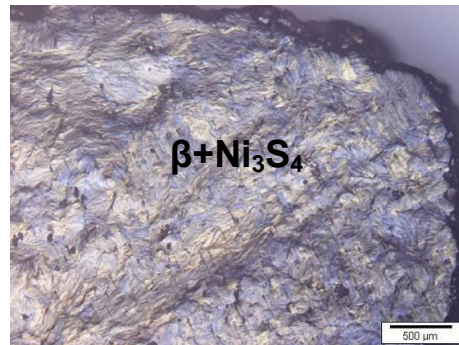
Etat initial



NiS-1S1 : 50,57at%ST=260°C;
t=5mn (pour une transformation totale)



Etat initial



NiS: 51,14at%ST=200°C;
t=140mn (pour une transformation totale)

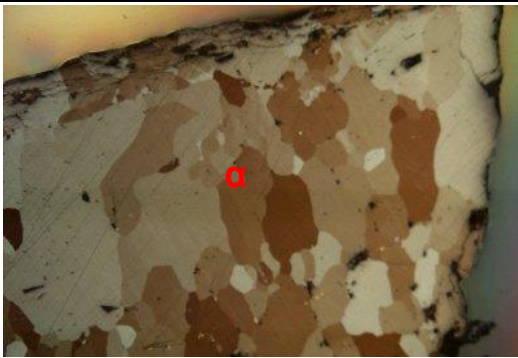
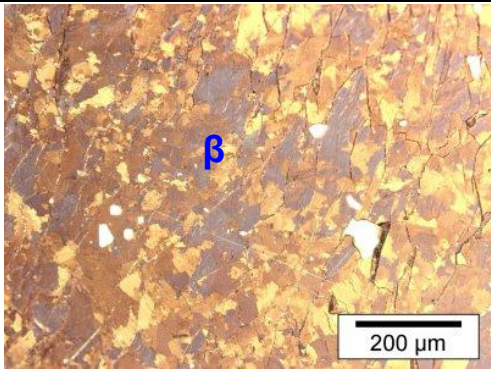
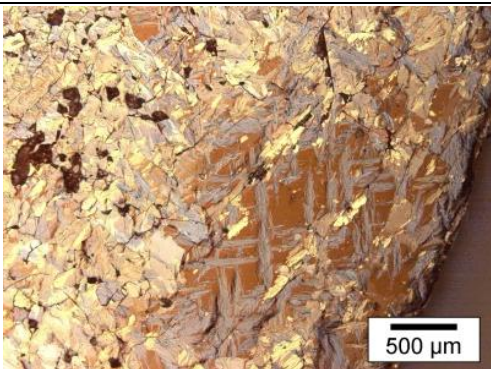
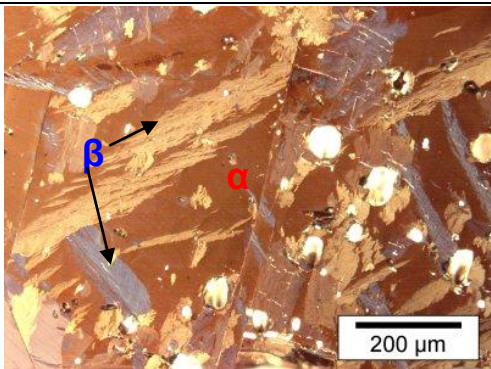
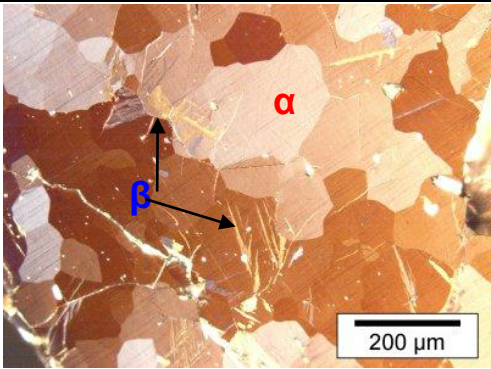
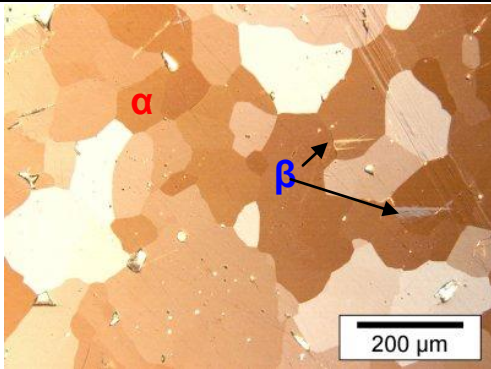
Figure 84 : Comparaison de l'état de surface avant et après transformation: apparition des fissures du à la transformation de phase $\alpha \rightarrow \beta$ -NiS et qui est d'autant plus prononcées quand la cinétique est rapide.

Annexe E : Transformation de phase des sulfures de Nickel et évolution à température ambiante

Les inclusions de sulfure de Nickel sont connues pour être à l'origine de la rupture retardée des verres trempés dus à la transformation de phase $\alpha \rightarrow \beta$ dans l'inclusion. La particularité de cette transformation est qu'elle peut se produire à température ambiante et avec des vitesses variables (en fonction de la composition de l'échantillon) ce qui donne un caractère imprévisible au phénomène de rupture. Nous rapportons dans cette annexe les observations faites sur des échantillons partiellement transformés et vieillis à l'ambiante sur plusieurs années (la durée de la thèse).

E.I. Effet de la composition sur la cinétique de Transformation de phase à température ambiante

Les micrographies de la Figure 85 b-f, illustrent la microstructure observée après vieillissement, à température ambiante, dans des échantillons NiS de différent surstoechiométrie (Figure 85 g-k, pour des échantillons contenant des impuretés de fer). Pour l'échantillon proche stoechiométrique NiS (~50.13at%S), Figure 85b montre que la totalité de la phase α est transformée après 30 mois. Cependant, moins de 5% et 1% sont transformés respectivement pour 51.14at% et pour les échantillons 51.28at%S. Ces résultats sont à la fois compatibles avec le ralentissement de la transformation prévue à la température ambiante pour des échantillons de composition très surstoechiométrique et ceux qui contiennent le montant élevé de fer. De plus, l'observation d'une transformation complète pour une durée de 30 mois dans un échantillon proche de la stoechiométrie est en accord avec le délai de la première casse observée dans les verres trempés pour lesquels le HST n'a pas appliqué (généralement entre 1 et 3 ans) [2, 15, 17].

Echantillon proche de la stœchiométrie NiS		
	(a) Initial surface aspect	(b) 50.04 ± 0.08: après 30 mois
		
	(c) 50.57±0.26at%S: après 30 mois	(d) 50.39±0.16at%S: après 20 mois
Echantillon surstœchiométrique		
	(e): 51.14±0.17at%S: après 30 mois	(f): 51.28±0.14at%S: après 30 mois

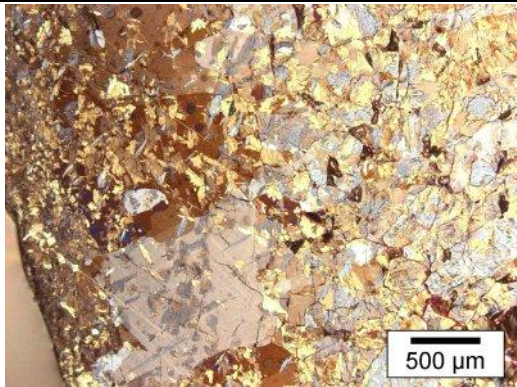
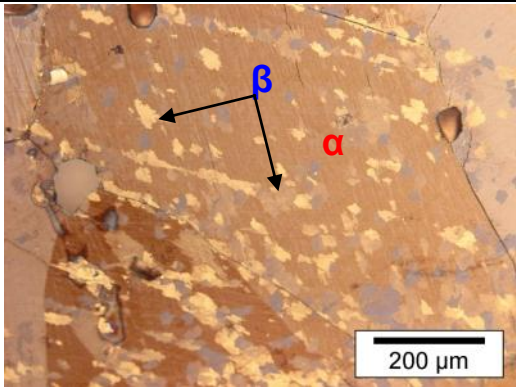
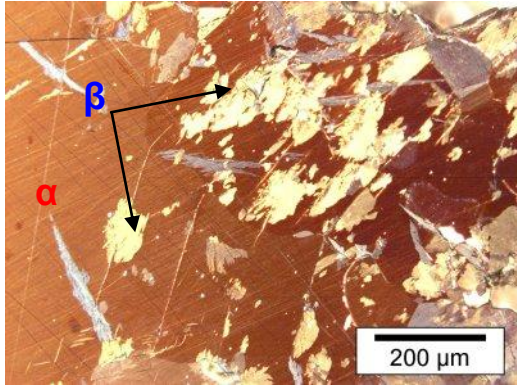
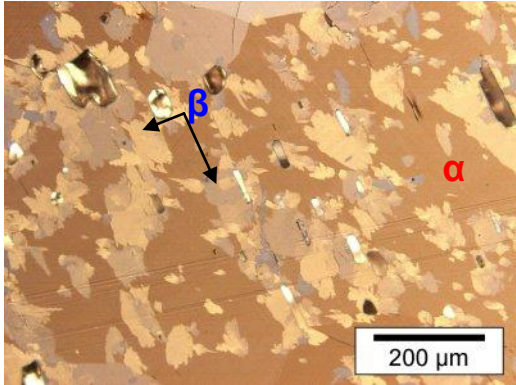
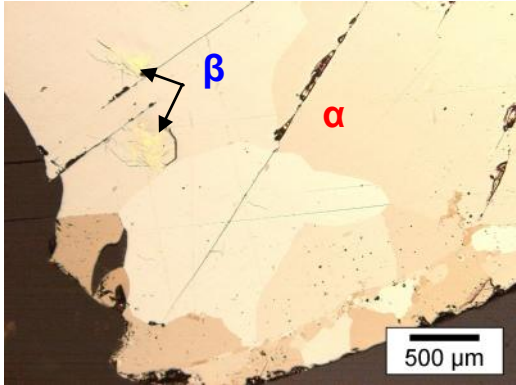
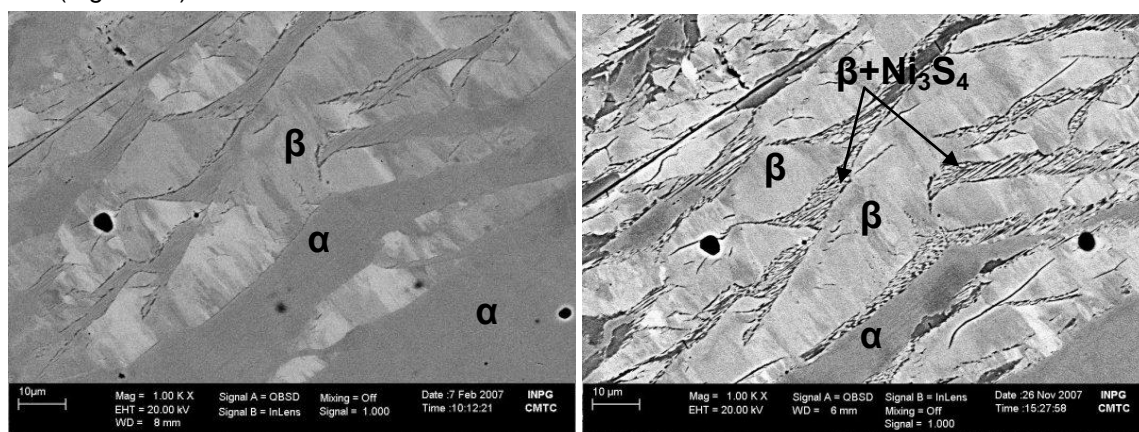
Echantillon contenant des impureté de Fe		
	(g): $50.56 \pm 0.12 \text{at}\% \text{S}$; $0.38 \pm 0.04 \text{at}\% \text{Fe}$ après 30 mois	(h): $50.37 \pm 0.15 \text{at}\% \text{S}$; $0.55 \pm 0.03 \text{at}\% \text{Fe}$ après 20 mois
		
	(i): $50.63 \pm 0.13 \text{at}\% \text{S}$; $0.49 \pm 0.03 \text{at}\% \text{Fe}$ après 30 mois	(j): $50.42 \pm 0.45 \text{at}\% \text{S}$; $0.49 \pm 0.02 \text{at}\% \text{Fe}$ après 20 mois
		
		(k): $50.52 \pm 0.12 \text{at}\% \text{S}$; $0.6 \pm 0.03 \text{at}\% \text{Fe}$ après 20 mois

Figure 85 : Observations en microscopie optiques de la transformation de phase se produisant à la température ambiante pour des échantillons Ni(Fe)S de composition différente : pour l'échantillon très surstœchiométrique (51,28at%S) la transformation est très lente que seulement moins de 1% de la phase de α sont transformé à la température ambiante pendant 30 mois.

E.II. Effet de la composition sur la microstructure de la Transformation de phase à température ambiante

Dans cette partie, nous étudions l'évolution de la microstructure de la transformation à température ambiante à partir des échantillons partiellement transformé à haute température. Ceci permettra de comparer les deux microstructures développées à hautes températures (200°C-300°C) et à celles des billes naturelles. Cette étude a été conduite sur un échantillon partiellement transformé à haute température puis laissé à l'ambiante : échantillons $\text{Ni}_{48,86}\text{S}_{51,14}$ transformé pendant 30 mn à 200°C (Figure 86).

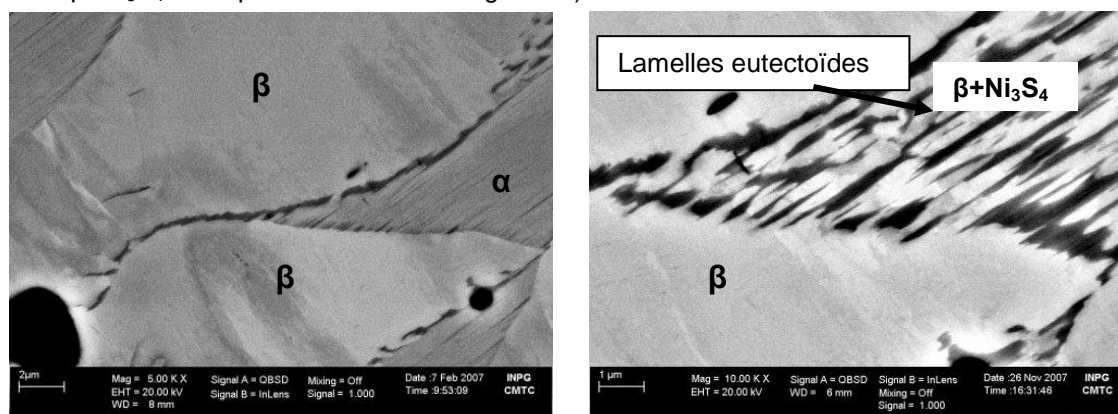


(a) microstructure après transformation partielle 30 mn à 200°C

(b) la même zone après 10 mois à T ambiante

Figure 86 : évolution de la microstructure à T ambiante (échantillon $\text{Ni}_{48,86}\text{S}_{51,14}$)

Les Figure 86 (a) et (b) montrent une même zone, dans l'échantillon $\text{Ni}_{48,86}\text{S}_{51,14}$, observée après un traitement à 200°C pendant 30mn et de nouveau observé après 10 mois à T ambiante respectivement. Cette comparaison montre clairement le développement d'une microstructure lamellaire $\beta+\text{Ni}_3\text{S}_4$ à température ambiante Figure 87).



(a) Microstructure après transformation partielle
Lamelles fines (30mn à 200°C)

(b) La même zone après 10 mois à T ambiante

Figure 87 : évolution de la microstructure à T ambiante (échantillon $\text{Ni}_{48,86}\text{S}_{51,14}$) : développement d'une microstructure lamellaire $\beta+\text{Ni}_3\text{S}_4$.

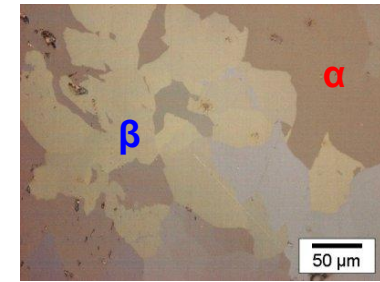
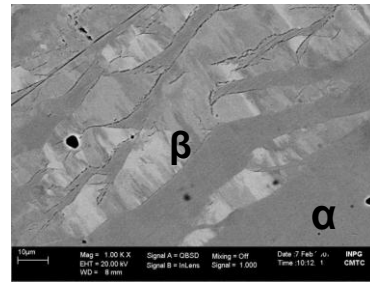
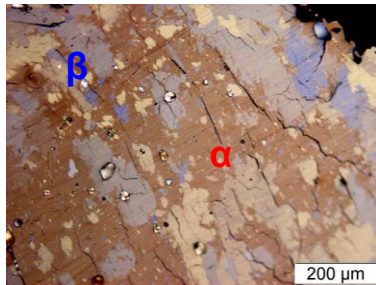
Annexes

Le changement microstructural observé indique que la transformation a continué à température ambiante. Comme il y a formation de Ni_3S_4 , il y a donc eu diffusion du Soufre au sein de la phase mère à l'ambiante ce qui suggère que le mode de diffusion du Soufre est très rapide. Le fait même que cette transformation se produise semble indiquer que la phase mère après transformation était sursaturée en Soufre (au moins par rapport à la teneur en Soufre correspondant à la limite de solubilité à l'ambiante)

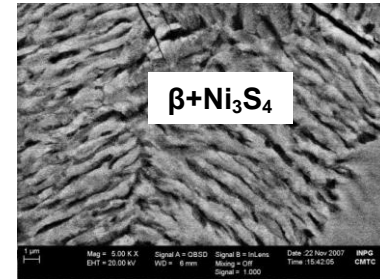
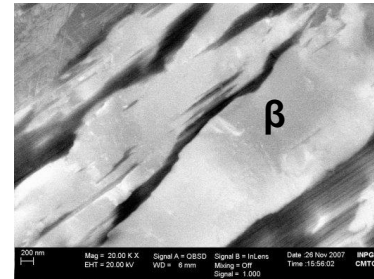
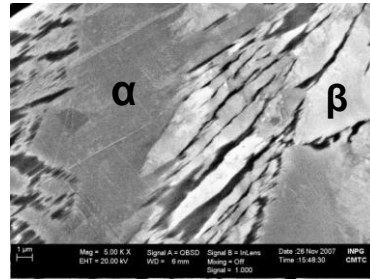
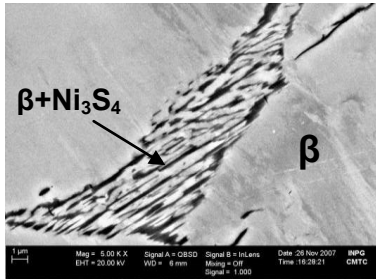
Par la suite, nous comparons les microstructures développées à hautes températures à celles développées à température ambiante (Figure 88). Il en résulte qu'à température ambiante les échantillons surstœchiométriques présentent des microstructures plus fines (Figure 85). Par contre elles gardent les mêmes caractéristiques pour les échantillons de composition proche de la stœchiométrie NiS (Figure 85). Ceci s'explique par l'effet de la température sur le phénomène de partition de Soufre pendant la transformation. En effet, pour les échantillons surstœchiométriques, le ralentissement de la diffusion à température ambiante conduit à une partition à courte distance entre les phases α et $\beta\text{-NiS}$ ce qui amène à la formation des microstructures fines. En revanche dans les échantillons de composition proche de la stœchiométrie NiS , la diffusion n'étant pas un paramètre limitant car la transformation est sans partition, et ainsi la taille des grains de phase $\beta\text{-NiS}$ n'est pas trop influencée par la température.

Annexes

Microstructure à Haute Température



Microstructure à température ambiante → transformation partielle à T=200°C suivi d'une évolution à l'ambiante



Microstructure inclusions naturelles

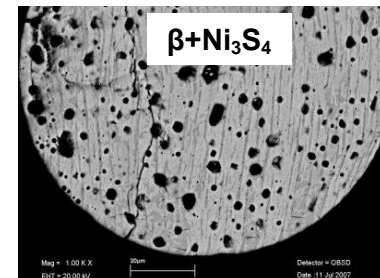
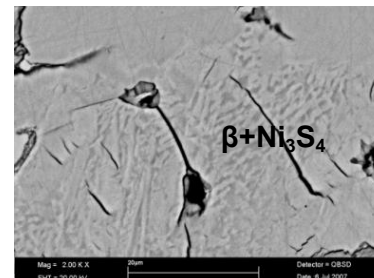
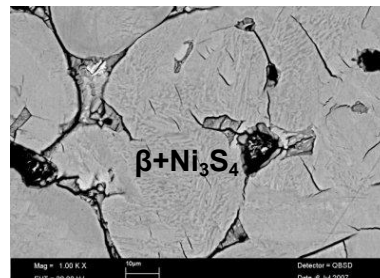
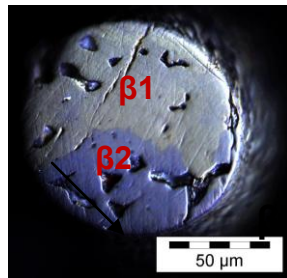


Figure 88 : Observation en microscopie optique et au MEB (mode électrons retrodiffusés) de la transformation $\alpha \rightarrow \beta$ -NiS : Comparaison de la microstructure à haute T / T ambiante / inclusions naturelles :

Annexe F : Illustration de la microstructure lamellaire à différentes températures

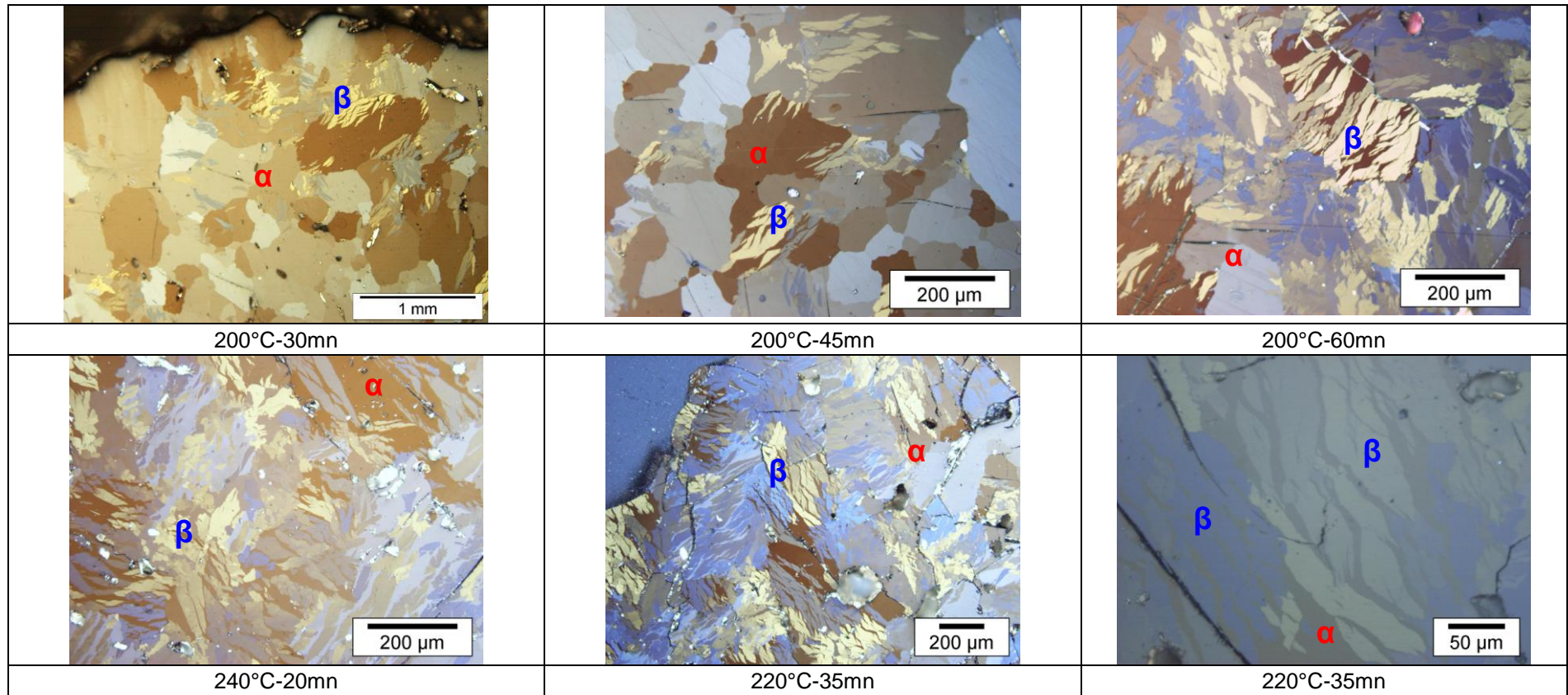


Figure 89 : Suivi en microscope optique de la morphologie lamellaire à différente Température $T = 200 - 220 - 240^{\circ}\text{C}$ sur l'échantillon $\text{Ni}_{48,86}\text{S}_{51,14}$ -surstoechiométrique et à petits grains . Les grains de phase β correspondent aux zones de couleurs jaune et bleu.

Annexes

Observations MEB : précipitation de la phase Ni_3S_4

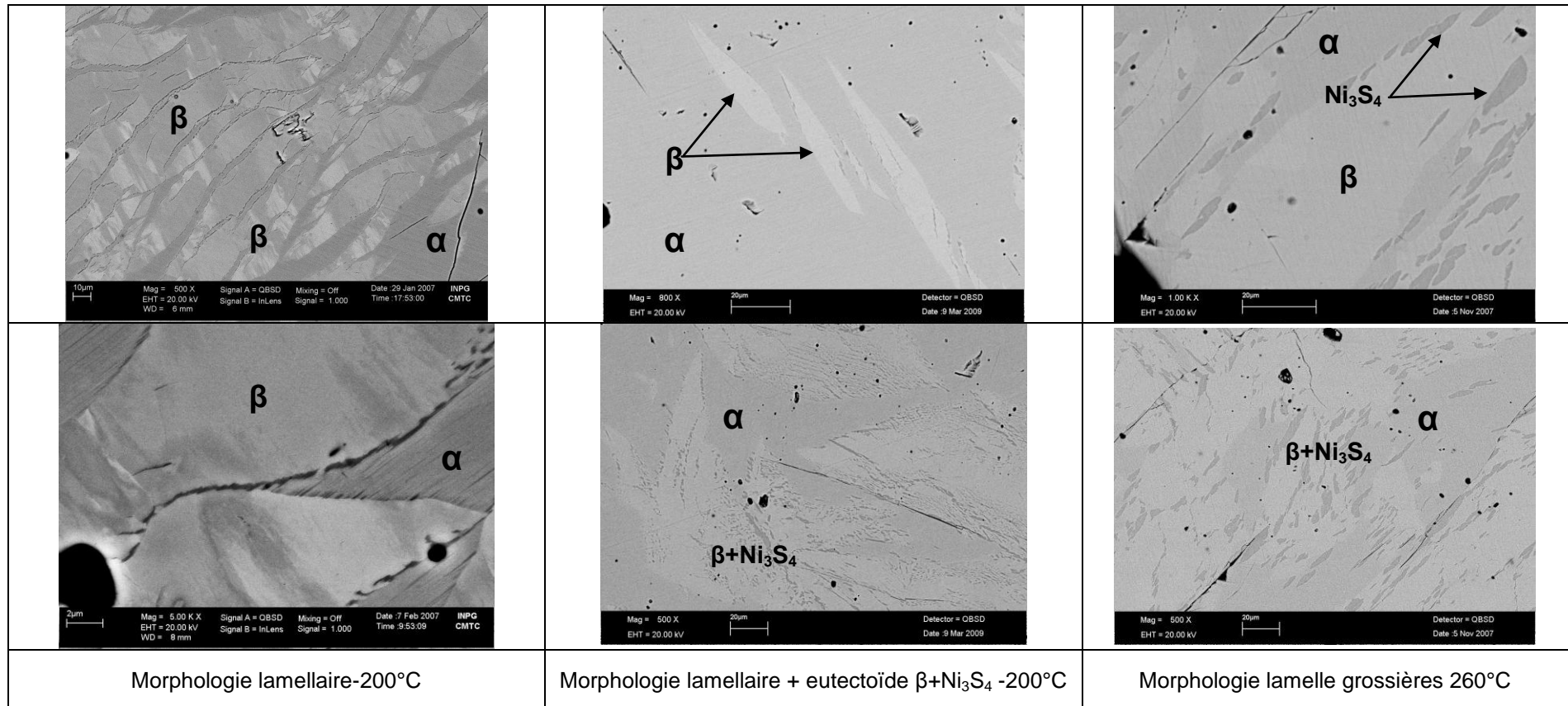


Figure 90 : Observation au MEB de la morphologie lamellaire et lamelle grossière : illustration de la précipitation de la phase Ni_3S_4 ; la taille des précipités est de l'ordre de $0.5\mu\text{m}$ à 200°C (morphologie lamellaire) et de $3\mu\text{m}$ à 260°C . (morphologie lamelle grossière).